Cell Size Control in Fission Yeast

Kally Pan

Submitted in partial fulfillment of the
requirements for the degree of
Doctor of Philosophy
in the Graduate School of Arts and Sciences

COLUMBIA UNIVERSITY

2013

ABSTRACT

Cell Size Control in Fission Yeast

Kally Pan

Among all living organisms, there is almost much variety in cell size as there is for cell function and cell type. However, within each cell type, cells stay remarkably faithful to a defined size over generations. Many factors have been found to influence this ability to specify and maintain cell size, yet clear mechanisms have yet to be elucidated. The fission yeast *Schizosaccharomyces pombe* is an ideal model organism whose simple but conserved cell biology has led to the identification of many important cell size regulators common to all eukaryotes. In this thesis, I have quantitatively analyzed the dynamics and localization of several key players of cell size regulation, which lead to a new physical model on cell size regulation based on the localization and accumulation of a size sensing kinase cdr2p. In this model, cdr2p molecules accumulate in proportion to cell size into complexes called midsomes, which localize to the cortex at the central section of the cell. Upon reaching the desired cell size, cdr2p accumulation surpasses a concentration threshold and the cell will divide. This accumulation is partly facilitated by the key negative regulator pom1p, which prevents midsome formation at the cell tip. Evidence also suggests that the ER serves a role in confining midsome localization to the medial plasma membrane, perhaps by providing a physical link to the nucleus. Together, this work elucidates a mechanistic understanding of how cell size can be determined and controlled.

Table of contents

Tables

List of Figures

Acknowledgements

I would like thank and acknowledge Drs. Tim Saunders and Martin Howard for devising the analytic methods that described the pom1p gradient as well as the mathematical models constructed for pom1p gradients, their clustering, cdr2p signaling mechanisms, and the positioning of midsomes in the ER membrane. I would also like to acknowledge Drs. Yinghua Guan and Jagesh Shah for their expertise in FCS imaging and for their analytic work in interpreting that data. Additional acknowledgement goes to Drs. Padte and Sophie Martin for their original work on pom1p gradients which inspired this project, and for strains and reagents created that became useful in my work. I would also like to acknowledge Jerome Zon and Angel Andrew for initializing the work into the cortical cell tracking software. Thanks go to the other members of the Chang laboratory for thoughtful discussion and advice. I would like to thank my members of my thesis committee, Drs. Jonathan Dworkin, Nick Rhind, Rodney Rothstein, and Mimi Shirasu-Hiza. Their patience and advice was instrumental to the completion of this thesis. Finally, I would like to acknowledge Dr. Fred Chang, who has served as a mentor throughout my graduate career, and without whom this work would have not have been possible.

Chapter One: Overview

Introduction

Cells are the fundamental unit of life. Though different cells can vary greatly in size, it has been long observed that cells of the same type have their own characteristic size to which they strictly adhere. Maintaining cell size over many generations is critical to cellular function in multicellular organisms and to its fitness in unicellular organisms (Jorgensen and Tyers, 2004). To accomplish this, cell growth and cell division must be coordinated.

How is size determined by the cell? What are the mechanisms that translate a spatial cue to a decision for the cell to divide? In this thesis, I will go through some of the background historic findings of cell size control and lay out a current model in cell size determination in fission yeast by which size is determined by a kinase signal whose accumulation eventually triggers mitosis. Mainly, I will attempt to present evidence for a molecular counting mechanism that acts as a marker for cell size and discuss some of the implications such a mechanism may have on the workings of the cell.

The regulation of cell division

Cells that are dividing typically do so through the cell cycle, where the cell need to grow, duplicate its DNA, and initiate cell division, or mitosis. However, the timing of these divisions seems to follow several different patterns that were determined through the study of several model organisms.

In budding yeast, small daughters have a longer G1 phase than their mothers, because they need time to grow to a minimum size before traversing START at G1/S. Once pass START, the cell cycle will irreversibly continue forward until mitosis. Passage through the START checkpoint is influenced by many other factors such as nutrient availability, presence of mating factor, and amount of stress (Morgan, 2007). Progression through the G1/S transition requires the activation of transcription by the SBF and MBF complexes, which are inhibited by Whi5. Removal of this key inhibitor from the nucleus is necessary if cell cycle progression is to occur (Doncic et al., 2011). (Figure 1.1a)

In fission yeast, there is little to no G1 phase, but a long G2 phase where most of the growth occurs. There appears to be a minimal size requirement at G2/M. In the size mutant *wee1-50*, the G2 growth phase is considerably reduced and the cells are much shorter upon division as a result. In cells that are starved, the G2 phase remains similar to wildtype, but the G1 phase is extended, while cell size are reduced. This suggests that the cell size threshold is reset in starved conditions to compensate for slower growth. (Figure 1.1b)

In somatic animal cells, regulation of cell division becomes more complicated. In addition to G1, S, and G2 phases, most somatic cells enter a quiescent stage (G0) after differentiation and do not divide. Unlike in yeast, there does not seem to be such a strict connection between cell size and cell division as growth and cell division are found to be independently regulated in some cases. This may not be surprising considering that multicellular organisms have specialized cell types that may need to grow or divide independently of nearby cells. In general, exposure to growth factors drive cell growth and exposure to mitogens drive division (Conlon and Raff, 1999). While there have been some evidence that cell size influence the cell cycle, there have also been evidence to the contrary (Conlon et al., 2001; Saucedo and Edgar, 2002).

In embryonic cell divisions in some animals, fertilization of the egg is followed by a series of multiple divisions without G1 or G2 phases, producing many small cells from one large one. (Novak and Tyson, 1993). In the period of 1970-1990s, key regulators of the cell cycle were found to be conserved in practically all eukaryotes. The primary discoveries came from converging studies in many model organisms such as budding yeast, fission yeast, and oocytes.

In oocytes, it was found that the cytoplasm of hormonally stimulated frog oocytes had an activity that could induce another oocyte to enter meiosis when injected (Masui and Markert, 1971; Smith and Ecker, 1971). This activity was named maturation (or M-phase) promoting factor or MPF, but for many years the molecular nature of this factor was unknown. More than ten years later, cyclins were identified in marine oocytes as proteins whose abundance oscillates with the cell cycle (Evans et al., 1983).

Concurrently, Hartwell, Nurse and colleagues used genetics to identify key cell cycle regulatory genes in budding and fission yeast (Nurse, 2002). In budding yeast, Hartwell and colleagues screened for temperature sensitive lethal mutants that arrested uniformly at certain cell cycle stages, which were identified by cell morphology. Nurse and colleagues performed a similar screen in fission yeast, screening for mutants that show abnormally long or short morphologies indicative of cell cycle timing abnormalities. Both groups independently focused on a protein kinase as a key rate-limiting factor in cell cycle progression. Cdc28 in budding yeast is implicated in G1/S control of START. Cdc2 in fission yeast showed numerous phenotypes affecting both G2/M and G1/S and cell size control. Cross complementation and sequencing showed that Cdc28, cdc2 and a human cdc2 were members of a conserved protein family of CDK kinases (Lee and Nurse, 1987; Ninomiya-Tsuji et al., 1991). Subsequent studies showed that the vertebrate Cdk1 associated with cyclin to form MPF (Gautier et al., 1988). It is now appreciated that the Cdk1 cyclin complexes trigger mitosis and other cell cycle events in every eukaryote studied (Draetta et al., 1988; Dunphy et al., 1988; Nurse, 1990). Hundreds of targets of cdk1 have been identified to play critical roles in cell cycle such as DNA replication, DNA segregation, transcription programs, and cell morphogenesis (Enserink and Kolodner, 2010; Ubersax et al., 2003).

Timers versus sizers

The paradigms of cell cycle control in yeasts and oocyte model systems have led to different concepts in how cell size is maintained. The oocyte work suggests the existence of "timers" by which oscillating internal clocks regulate division periods at regular intervals. Simulations suggest that it would be challenging for maintaining cell size using a pure timing mechanisms especially in cells that grow in at an exponential rate (Son et al., 2012).

In contrast, studies in yeasts, bacteria and somatic animal cells suggest that these cells monitor a critical cell size before committing to cell division (Jorgensen and Tyers, 2004). By definition, having a critical cell size, whether it would be a minimum size threshold or a "normalized" wildtype where every cell converges require a sizing mechanism to quantify size. But it is not clear what size means to a cell. Whether it would be volume, mass, biosynthetic status, or some other physical property of living matter, it would have to be some tangible cellular resource that is physically countable and uniform.

One type of sizing mechanism may involve the rate of protein synthesis (Unger and Hartwell, 1976). Since protein synthesis integrates many signals such as nutrient availability and production ability, it has been thought to be a good proxy for measuring growth as well. Such a reporter is thought to be unstable so that its abundance in the cytoplasm would be constantly proportional to the translation rates. Other prevalent models include nuclear cytoplasmic ratios of key proteins (Schmidt and Schibler, 1995). In this thesis, I will focus on two other sizer mechanisms, one based on cortical gradients and another on cell surface sensing.

Cell size regulation in budding yeast

In budding yeast, cells need to reach a critical cell size before entering G1/S phase. In general, the daughter cell is born smaller than the mother cells. While the mother cell quickly begins to bud and replicate its DNA after cytokinesis, the daughter cells has a longer G1 in which it grows to a minimal size before entering S phase (Dolznig et al., 2004; Donachie, 1968; Hartwell et al., 1970; Nurse, 1975). Move elsewhere Genes affecting cell size control in budding yeast include Cln3 (a G1 cyclin) and Whi5 (a transcription factor). The Cln3 is a possible example of a "sizer", a molecule that acts as a signal for the physical size of the cell. Cln3 is an upstream G1 cyclin that can trigger the Start cell cycle check point (Tyers et al., 1993). Cdk1 bound Cln3 phosphorylates its downstream target, the transcription factor inhibitor Whi5 and forces its export out of the nucleus in a dose-dependent manner (Nash et al., 1988). The transcription activators that were inhibited by Whi5 can now promote the expression of over 200 genes that start S-phase as well as activate a feedback loop between newly expressed cyclins and Cln3 (Bean et al., 2005; Dirick and Nasmyth, 1991). Cln3 levels increase linearly with the size of the cell; deleting Cln3 results in larger cells while overexpression results in smaller cells (Cross, 1988; Nash et al., 1988). More importantly, deletion of both Cln3 and Whi5 will result in cells that show a dramatic loss in its inverse relationship between birth size and growth time, indicating a weakening of the specific cell size regulatory mechanism (Di Talia et al., 2007).

The current model is that Cln3 signals size by reflecting the translational state of the cell. Unlike most cyclins whose expressions oscillate dramatically through the cell cycle, Cln3 is expressed evenly throughout the entire cell cycle (Tyers et al., 1991; Tyers et al., 1992). Second, Cln3 is an incredibly short lived protein with a half-life of less than 5 minutes (Tyers et al., 1993). This would indicate that the level of Cln3 at any moment of time is proportional to the translational capacity of the cell, which is proportional to the size of the cell. Blocking translation by successive rounds of treatment by the global translation inhibitor cycloheximide slows down the cell cycle and increases the critical cell volume (Moore, 1988; Popolo et al., 1982). This seems to suggest that reduced translation can reset the cells ability to detect size. For now, the instability of Cln3 has prevented a more rigorous quantitative study of this model. However, this simple model fails to account for the reduction in cell size seen in nutrient deprivation. In this state, translation is usually reduced, which should result in a similar scenario as a cycloheximide block. Yet cell size is reduced, not increased. Furthermore, a mechanistic explanation of this model is also lacking. If Cln3 is dose dependent, yet expression rises in proportion with cell size, the one to one increase of expression and volume would result in no effective change in protein concentration. If Cln3 signaling is kept constant, then the signal strength will never change over the cell cycle. On the other hand, if the cell uses some other factor to increase the activity of Cln3 as the cell size grow, this other factor would also be required to sense cell size.

Genome wide screening for cell size mutants have led to the inclusion Sfp1, a transcription regulator responsible for the control of at least 60 genes implicated in ribosome biogenesis (Jorgensen et al., 2002). Degradation of Sfp1 by Blm10 proteasome activator causes the repression of ribosome biogenesis during starvation (Lopez et al., 2011). This is consistent with the reduction in ribosome synthesis and cell size exhibited during nutrient deprivation (Schneider et al., 2004). In addition to this, screen for synthetically sick size mutants have identified even more potential size regulators such as Mrp149 and Cdbs1, both dependent on CLN3 but both need to be deleted to result in smaller cells (Dungrawala et al., 2012). This may indicate that size regulation may have many more nuanced components than previously thought. Recently, it was discovered that Cln3 is released from the rough ER periphery in late G1 via a chaperone dependent manner (Verges et al., 2007). This release from ribosomal ER may be the mechanism that link cell growth and cell division.

As an additional size control, the asymmetry in cell cycle regulation between mothers and daughters may arise through a system of asymmetrically localized transcription factors Ace2 and Ash1, which regulate expression of the cyclin *CLN3*. Budding yeast divide asymmetrically when a smaller daughter cell “buds” from the larger mother cell. Ace2 and Ash1 asymmetrically distribute to the smaller daughter cells and delay the activation of cell cycle progression at the G1-S transition, allowing them to grow for a longer period of time to “catch up” to their larger mother cells (Di Talia et al., 2009).

Size checkpoint in algae and the RB pathway

Chlamydomonas reinhardtii is a unicellular green alga that has been shown to dual mechanisms for size control. Cells exposed to 30ºC instead of 20ºC will grow at about 2.5 faster. Conversely, cells grown in the absence of light will drastically slow down growth. However, in either case, the first division that follows will leading to a several fold variation in size in the different scenarios (Donnan and John, 1983). This pattern follows that of a "timer" based model where the cell sense time to regulate division. However, Chlamydomonas also divides by a multiple fission mechanism where cells that have grown to many times their normal size undergo a series of rapid division cycles of S phases and mitosis to produced daughters of uniform size (Coleman, 1982; Craigie and Cavaliersmith, 1982; Donnan and John, 1983). This ability to produce similar sized daughter cells regardless of their original size indicates that Chlamydomonas can sense size to regulate division as well.

The RB gene *MAT3* was identified as a mutant defective in size control (Fang et al., 2006). *Mat3* mutants not only committed to division at a smaller size, they also undergo too many rounds of division and produce much smaller daughters. Interestingly, temporal control of the cell cycle remains normal in these mutants, suggesting that their defect lay only with size sensing (Umen and Goodenough, 2001). In mammalian cells, Rb (the *MAT3* ortholog) and its related proteins E2F and DP form the retinoblastoma (RB) tumor suppressor pathway. These are thought to act through the transcriptional repression of *cyclin E* and are in turn modulated by other cyclins and Cdks (Cobrinik, 2005; Dimova and Dyson, 2005). Deletion of RB results in smaller cells and overexpression of RB leads to larger cells indicting a conserved role in size control (Dannenberg et al., 2000; Neufeld et al., 1998). Interestingly, mutants of mat3, e2f1, or dp1 in Chlamydomonas all have no effect on the cell cycle transcription of periodic cell cycle genes (Fang et al., 2006). A further suppressor screen in Chlamydomonas yielded several more members of this size controlling pathway, including a putative small ubiquitin-like modifier (SUMO) peptidase (Fang and Umen, 2008). This hints at a larger and more complex network downstream of the RB pathway that may use sumoylation as a mechanism for cell size regulation. Additionally, the RB pathway in mammalian cells play a role in a host of intercellular growth-related regulations in development, differentiation, and cancer (David-Pfeuty, 2006). It has been proposed that RB senses cell size via the nucleocytoplasmic ratio (Umen, 2005).

Cell Size regulation in fission yeast

First isolated from East African millet beer ("pombe" is derived from the Swahili word for beer), *S. pombe* cells exhibit remarkable fidelity of size control; cells under normal conditions grow by tip extension to 14 µm with a standard deviation of 0.85 µm before entering mitosis and dividing medially (Sveiczer et al., 1996). As cells elongate continuously in interphase (but not in mitosis), the size of the cells reflect the length of time spent in G2 interphase; in effect the cells act as their own cell cycle ruler (Jorgensen and Tyers, 2004). Since growth is limited at the tips of the cell, the diameter of the cell remains constant at approximately 4 µm, and its growth follows a strict linear pattern, it is relatively easy to track and quantify growth by measuring cell length (Mitchison and Nurse, 1985).

The size of *S. pombe* cells is altered by conditions such as nutrition and ploidy. When *S. pombe* cells are shifted to a low nutrient source, growth slows and the cells divide at the shorter length. However, when cells are shifted towards a high nutrient source, cell growth became faster, but cell division lengths increased in one step instead of gradually increasing (Fantes and Nurse, 1977). If a timer was the only control of cell size, then a shift to richer medium should result in longer and longer cells if cell growth is related to length and the growth time is constant. This classic experiment demonstrated that cell division was triggered by a size threshold rather than a timing threshold. The authors proposed that this threshold could be reset by the growth rate, but did not have to divide by a strict timer. Hence, it was able to delay division and correct cell size in a step-wise manner. Then they showed that mutations in the wee1p gene produced short cells that were incapable of responding to such size threshold reset when deprived of nutrients (Fantes and Nurse, 1978).

A similar size threshold can be seen in another experiment, where *S. pombe* cells were treated with hydroxyurea, an S-phase inhibitor, so that the cells continued to grow beyond their normal maximum length. When the HU was washed out, the cells regained their normal length within a few generations by reducing the time of each cell cycle so that division occurred before cell size has doubled. This observation support the existence of a size threshold in fission yeast (Miyata et al., 1978a, b). A similar result was seen when a temperature sensitive mutant of cdc10p, which arrested in S-phase, was used. These cells continued to grow when arrested but regained their normal length with rapid division cycles as well (Fantes and Nurse, 1978).

Size control through the cdk1/wee1 pathway

Wee1p was identified through abnormally small mutants in fission yeast. It is a tyrosine kinase that restricts the activity of cdk1 by phosphorylating cdk1 tyrosine residue 15. This action is balanced by the phosphatase cdc25p, which removed this phosphate and acts as the rate limiting step for mitotic entry (Gould et al., 1990; Russell and Nurse, 1987). Wee1p is also partially redundant with another tyrosine kinase mik1 (Lundgren et al., 1991). Mutants of wee1p divide short and are insensitive to both hydroxyurea (S-phase block) and DNA damage through radiation, suggesting that it plays a role in G1-S transition as well as a DNA damage check point (Rowley et al., 1992).

Both wee1p and cdc25p proteins can be regulated by activity as well as by expression. For example, in higher eukaryotes, polo-like kinase can phosphorylate wee1and lead to degradation via SCF, an E3 ubiquitin ligase (Watanabe et al., 1995). Wee1p is phosphorylated by the Nim1-like kinase cdr1p *in vitro* and the over expression of nim1p leads to hyperphosphorylation of wee1p in its N-terminal region, resulting in the promotion of mitosis (Wu and Russell, 1993). Interestingly, cdr2p) is part of the nitrogen sensing pathway and its deletion causes cell size to be insensitive to nitrogen starvation, indicating that wee1p is a part of the response to nutrients (Feilotter et al., 1991; Ubersax et al., 2003). Wee1p may also be phosphorylated by cdc2p, which creates a positive feedback loop (Mueller et al., 1995). While it has been clear that a balance between wee1p, cdc25p, and cdk1p regulate the switch to initiate mitotic entry, the mechanism by which information about cell size may regulate this network remains unclear.

Pom1p: a spatial mechanism for size control in fission yeast

Two regulators upstream of wee1p, the pom1p and cdr2p protein kinases have been recently implicated in cell size control. Recent investigation has led to the proposal of a geometric size sensing model that is based on the distribution of a protein gradient of the protein kinase pom1p that acts as a threshold for mitosis (Martin and Berthelot-Grosjean, 2009; Moseley et al., 2009). Pom1p is a dual specificity Yak1-related kinase (DYRK) that is known as a regulator of cell polarity and cytokinesis (Bahler and Pringle, 1998; Celton-Morizur et al., 2006a; La Carbona and Le Goff, 2006; Padte et al., 2006). Pom1p deleted cells are unable to remove the rga4 GAP from the non-growing cell tip and results in monopolar cells that only grow from one end (Tatebe et al., 2008). Deleting pom1p also mislocalize mid1p and causes a drift of the positioning of the cytokinetic ring. Interestingly, a ring can still form, but now is often times set askew and offset from the center of the cell (Padte et al., 2006). Pom1p is localized largely at the tips, in gradient like distributions during interphase, but moves additionally to the division play during cytokinesis (Bahler and Pringle, 1998). Evidence suggests that polarities factors containing the complex of Tea1p and tea4p are brought to the cell tip by microtubules and recruit pom1p (Hachet et al., 2011; Huang et al., 2007).

Pom1p also affects cell size. By measuring the length of cells expressing different levels of pom1p, researcher from the Martin and Nurse labs showed that pom1p seems to be a dose-dependent inhibitor of the G2/M transition (Martin and Berthelot-Grosjean, 2009; Moseley et al., 2009). Pom1 null mutants are short, while cells overexpressing pom1 are long (Bahler and Pringle, 1998). Epistasis tests show that pom1p functions in a pathway upstream of cdr2p and ultimately acts to inhibit cdk1p activity (Martin and Berthelot-Grosjean, 2009; Moseley et al., 2009) (Figure 1.2). This link may be direct, as pom1p affects cdr2p phosphorylation and can directly phosphorylate cdr2p in vitro although the significance of these phosphorylation events remains to be established (Martin and Berthelot-Grosjean, 2009). Image analysis suggests the presence of a gradient distribution that is strongest at the cell tip, and falls off in the middle of the cell (Celton-Morizur et al., 2006a; Padte et al., 2006).

Pom1 may have some conserved function in animal cells. In animal cells it has been implicated in cell polarity, asymmetric division, and mitosis, while cells deleted for DYRKs were either small in the case of minibrain in the fly, or displayed morphological defects in the case of DYRK1a in cultured neurons (Becker and Sippl, 2011; Hammerle et al., 2011; Pang et al., 2004; Park et al., 2009). However, proper cell cycle and cell size studies have not been done except in the case of MBK2 in C. elegans where cells in the embryo were unable to properly commit to asymmetric cell division (Nishi et al., 2008).

DYRKs are uniquely characterized by their ability to catalyze tyrosine-directed autophosphorylation as well as phosphorylation of serine/threonine residues. The minibrain kinase ortholog MBK-2 in *C. elegans* is required for spindle positioning and asymmetric cell division in early development by its activation and subsequent phosphorylation of downstream targets MEI-1 and OMA-1 (Nishi and Lin, 2005; Pellettieri et al., 2003). Yak1 in budding yeast is responsible for linking growth and stress response (Lee et al., 2008). Minibrain in Drosophila is critical in the development of neurons (Tejedor et al., 1995). In humans, DRYK1a has been linked to the Downs syndrome gene and have been seen in mouse models to affect the development of the brain (Altafaj et al., 2012; Becker and Sippl, 2011; Park et al., 2009). In tissue culture, this developmental problem has been connected to the regulation of a transient expression on DYRK1A in a switch like manner that induces cell cycle exit (Hammerle et al., 2011). These wide ranging studies suggest that DYRKs may have a conserved function in cell division regulation that have become more specified in organs such as the brain.

Cdr2p and midsome proteins

Downstream of pom1p is the SAD (NIM1-like) kinase cdr2 (Breeding et al., 1998; Kanoh and Russell, 1998). Cdr2p is a serine/threonine protein kinase that is a member of the GIN4 family. Its orthologues in budding yeast and *Candida albicans* (Gin4) are regulators of septin organization (Gladfelter et al., 2004; Wightman et al., 2004). In fission yeast, cdr2p was identified by its role in nitrogen sensing similar to cdr1p. Deletion of cdr2p leads to a dramatic increase in cell length at division, and wee1p is epistatic to cdr2p (Breeding et al., 1998; Young and Fantes, 1987). It genetically interacts with wee1p (more specific) and can phosphorylate wee1p *in vitro*. It has a separate role in cytokinesis but acts independently of septins (Morrell et al., 2004). The N-terminus of cdr2p contains the kinase domain while the C-terminus is responsible for localizing it onto cortical dots (Morrell et al., 2004).

Cdr2 resides in clusters of peripheral membrane proteins located on the plasma membrane in a medial band around the middle of the cell; these clusters have been named "midsomes" or "nodes." (Almonacid et al., 2009; Morrell et al., 2004; Moseley et al., 2009; Pan and Chang, 2009). Co-localization and biochemical studies have shown that these dots or "midsomes" are made up of protein complexes containing dozens of molecules of several different proteins including the anillin-like mid1p, midsome membrane anchors blt1p and gef2p, and the kinesin like protein klp8p, and gef2p (Almonacid et al., 2009; Chang et al., 1996; Guzman-Vendrell et al., 2013; Moseley et al., 2009). Though mid1p remains the central figure in this complex, its deletion does not completely prevent the cortical localization of other proteins that make up the midsomes. Truncation studies with gef2p, cdr2p, and mid1p have revealed an interconnected series of interactions that affect midsome localization and dynamics as a whole.

However, separating the multiple functions that have been ascribed to each of these proteins remain difficult as disturbing one protein will often have unintended consequences for the others. Adding to the difficulty is separating the different roles these proteins play during interphase and during mitosis/cytokinesis. While deleting mid1p leads to severe cytokinesis defects and deleting cdr2p do not, cdr2p can have severe synthetic cytokinesis defects with ER proteins, suggesting a more subtle effect on cytokinesis (Zhang et al., 2012). Interestingly, while deletion of cdr2p leads to an increased cell division, gross overexpression is lethal, leads to an inability to divide and the development of multiple septations (Breeding et al., 1998). It might be that cdr2p operates primarily for cell size control and that its cortical localization is more important as a structural anchor for cytokinesis.

Direct interactions between the midsome components are beginning to be identified. Cdr2p anchors at the cortex and, along with interactions with gef2p, help stabilize midsome complexes through association with the mid1p N-terminus. This complex help define the localization of mid1p to the cell middle with cdr2p playing a semi-redundant role (Almonacid et al., 2009; Calonge et al., 2010; Lee and Wu, 2012; Morrell et al., 2004; Ye et al., 2012).

The pom1p/cdr2p switch

These findings lead to the proposal of a fairly simple model for cell size sensing and regulation (Martin and Berthelot-Grosjean, 2009; Moseley et al., 2009; Pan and Chang, 2009). This model postulates that a pom1p kinase gradient emanates from the cell tips and decays exponentially, thus regulating its own concentration in a length dependent manner. As the localization of the pom1p censor cdr2p is fixed as the midsomes, its distance becomes farther from the cell tip as the cell elongates. Meanwhile concentration of pom1 at the middle of the cell will proportionally decrease as the cell gets longer. Earlier during the cell cycle cells are short, pom1p concentration is high in the middle of the cell, and thus effectively inhibits cdr2p and activates wee1p, which inhibits mitosis. When the cells grow longer, the progressively decreasing pom1p concentration at the middle will eventually pass a point where it is unable to inhibit cdr2p, causing wee1p inactivation and triggering mitosis (Figure 1.3).

Gradients are an attractive biological mechanism for spatial recognition and pattern formation. The most famous example include the development of the fruit fly, where morphogenic gradients have been studied in detail and seem to determine controlled development of the body plan (Gurdon and Bourillot, 2001). Similar gradients inside of cells have been implicated in single cell functions as well, such as spindle assembly and cell polarization (Caudron et al., 2005; Chen et al., 2011; Meyers et al., 2006). However, even after more than 20 years of study of the *bicoid* gradient in the fly embryo, quantitative measurements still present a challenge for current prevailing models (Lander, 2007). Undoubtedly, quantitative measurements will shed more light onto the pom1p gradient as well.

Multiple lines of regulation for cell size

Cell size control is subject to regulation by many other factors including nutrient availability, DNA damage, and developmental factors (Cranna and Quinn, 2009; Petersen and Nurse, 2007; Pyronnet and Sonenberg, 2001). Nutrient limitation may lead to smaller cell size through the nutrient sensing pathway involving TOR/PI3K where direct changes on the pathway can lead to aberrant cell cycle timing (Petersen and Nurse, 2007; Rupes, 2002). This is thought to work on a two pronged approach where the TOR pathway links nutrient sensing directly to growth by controlling translation, while PI3K links the insulin signaling pathway to the activation of cyclins like Cln2. Inhibition of TOR signaling through inactivation of TOR or its downstream targets like S6K leads to small cells similar to that of nutrient starvation. It is likely that the signals such as nutrition modulate the same wee1p-cdk1p pathways to control cell size. Thus, size control as a whole is a function of the integration of these signals.

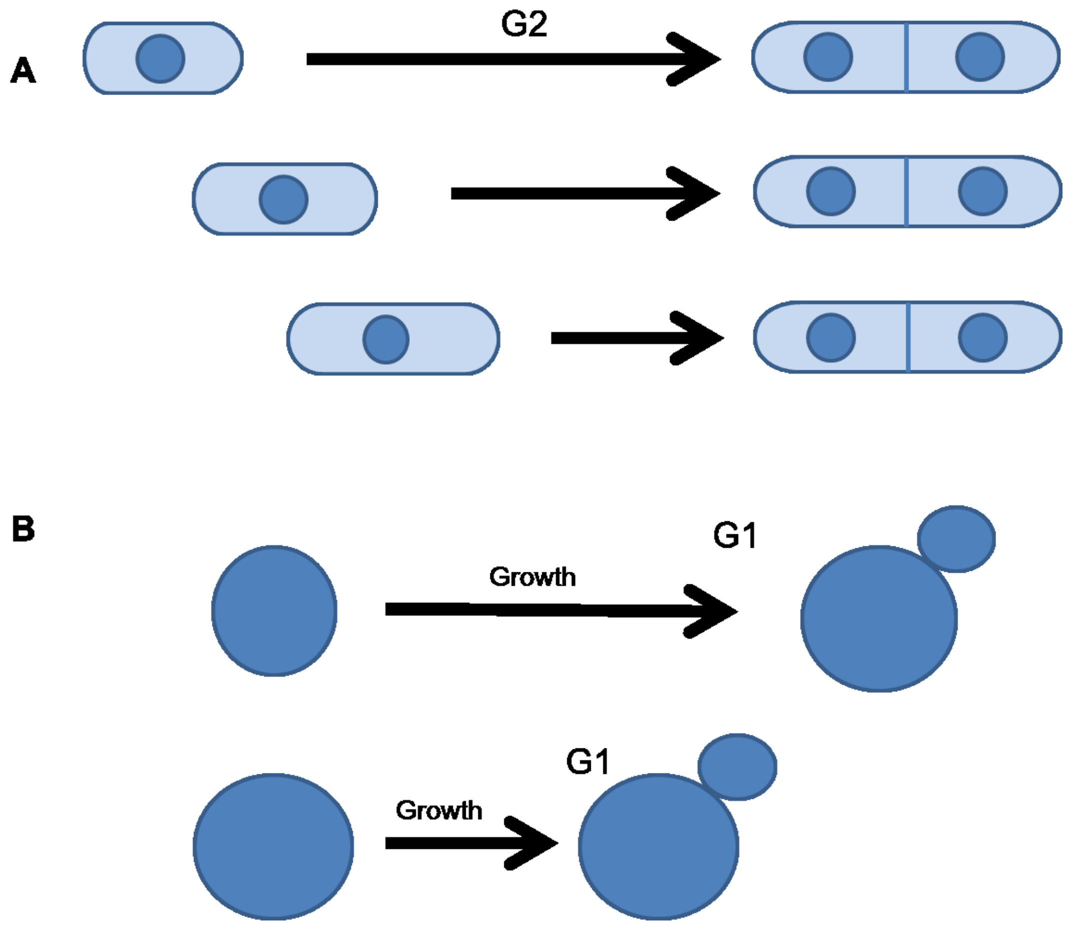

Figure 1.1. Size control at different stages of the cell cycle

A. The size control in fission yeast is at the G2/M transition, after a period of growth for the cell.
B. The size control in budding yeast is during a similar period of growth but takes place at the G1/S transition instead.

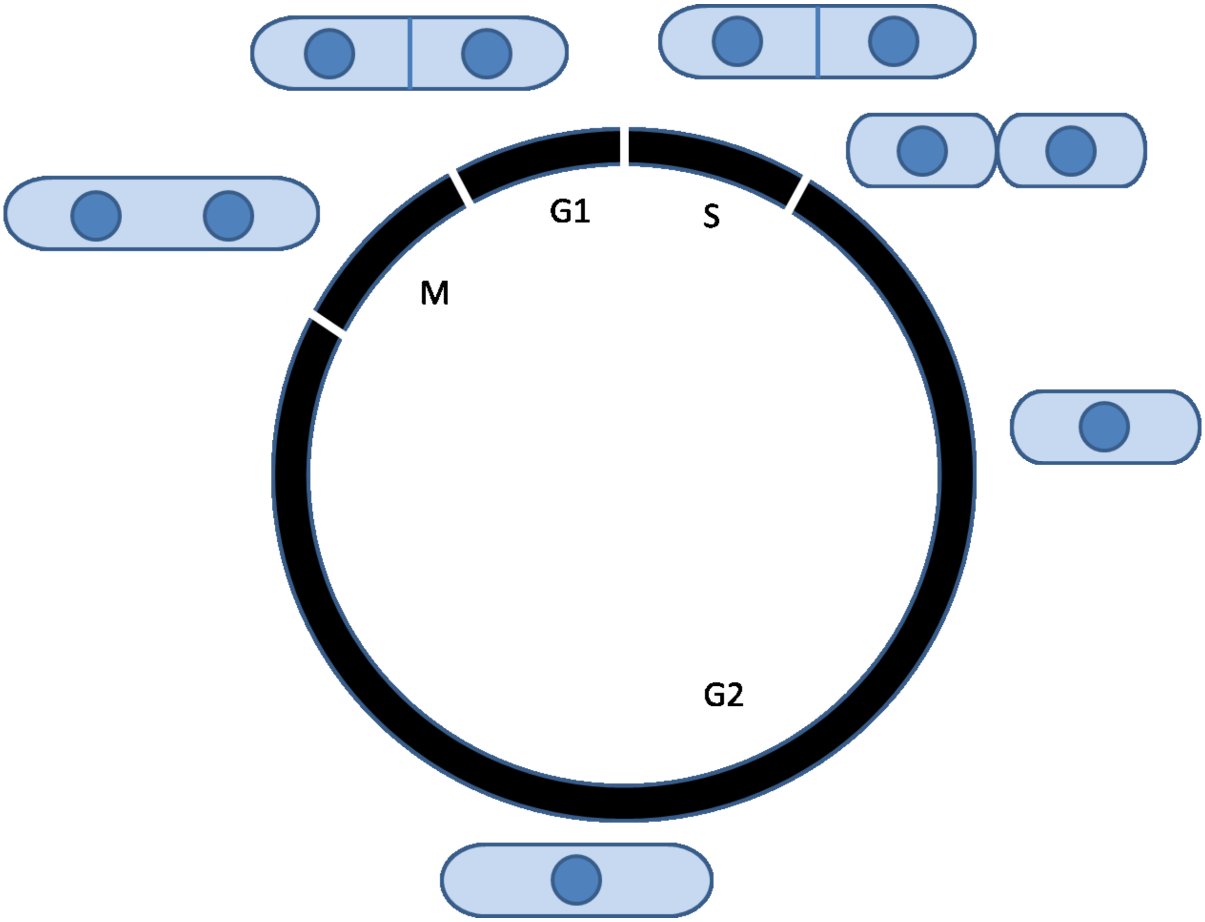

Figure 1.2 Cell cycle of *S. Pombe*

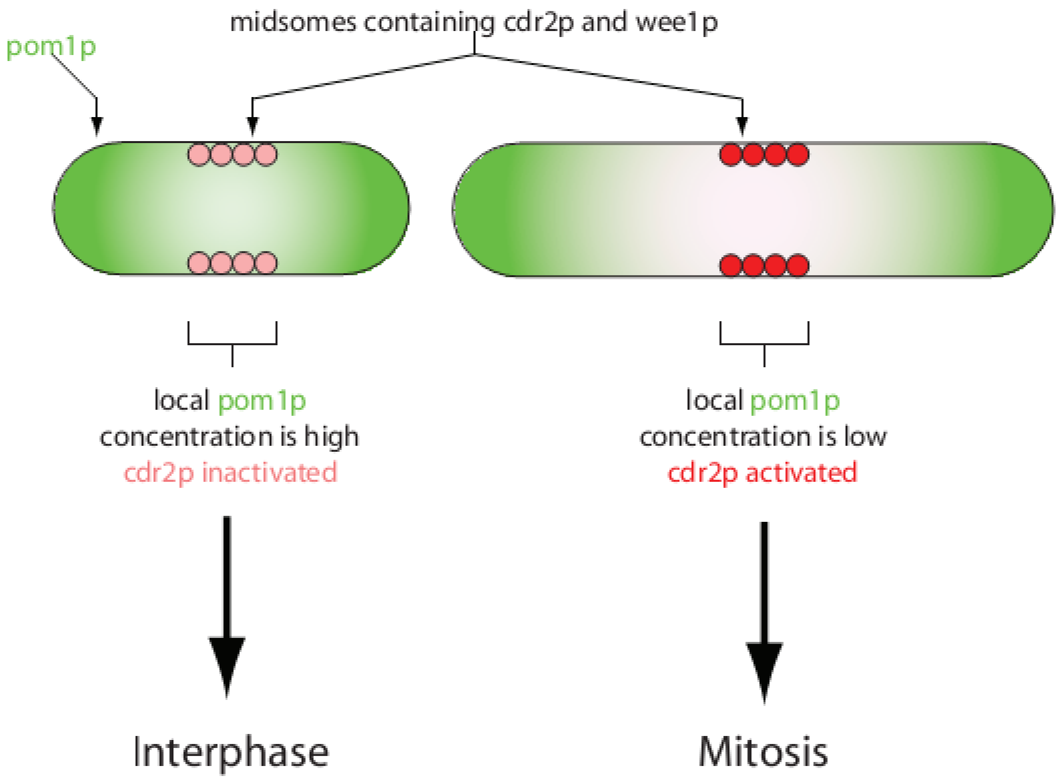

Figure 1.3. Model of cell size sensing

Pom1p localizes to gradients emanating from cell tips, while cdr2p and wee1p are in midsome structures at the cell middle. In short cells (left) pom1p concentration at the cell middle inhibits cdr2 activity and maintains the cell in G2 phase. When the cell grows to a critical length (right), pom1p concentration at the cell middle decreases and allows cdr2p activity to promote entry into M phase.

Chapter two: Noise reduction in the intracellular pom1p gradient by a dynamic clustering mechanism

Timothy E. Saunders*[2,3], Kally Z. Pan*[1], Andrew Angel[2], Yinghua Guan[4],

Jagesh V. Shah[4], Martin Howard[2] and Fred Chang[1]

Reproduced from: Noise reduction in the intracellular pom1p gradient by a dynamic clustering mechanism. Developmental Cell 2012 Mar 13;22(3) 558-72

*These authors contributed equally as co-first authors

1. Department of Microbiology and Immunology, Columbia University College of Physicians and Surgeons, New York, NY, 10032, USA
2. Department of Computational and Systems Biology, John Innes Centre, Norwich Research Park, Norwich NR4 7UH, United Kingdom
3. European Molecular Biology Laboratories, Meyerhofstrasse 1, 69117 Heidelberg, Germany
4. Department of Systems Biology, Harvard Medical School and Renal Division, Brigham and Women's Hospital, Boston, MA 02115, USA

Abstract

Chemical gradients can generate pattern formation in biological systems. In the fission yeast *Schizosaccharomyces pombe*, a cortical gradient of pom1p (a DYRK-type protein kinase) functions to position sites of cytokinesis and cell polarity, and to control cell length. Here, using quantitative imaging, fluorescence correlation spectroscopy and mathematical modelling, we study how its gradient distribution is formed. Pom1p gradients exhibit large cell-to-cell variability as well as dynamic fluctuations in each individual gradient. Our data lead to a two-state model for gradient formation where pom1p molecules associate with the plasma membrane at cell tips, and then diffuse on the membrane while aggregating into and fragmenting from clusters, before disassociating from the membrane. In contrast to a classical one-component gradient, this two-state gradient buffers against cell-to-cell variations in protein concentration. This buffering mechanism, together with time-averaging to reduce intrinsic noise, allows the pom1p gradient to specify positional information in a robust manner.

Introduction

Chemical gradients have long been hypothesized to underlie sensing and control of positional information in multi-cellular organisms and tissues (Lander, 2007). Gradients such as those formed by the *Drosophila* morphogen Bicoid can provide positional information with less than a 2% relative positional error (Gregor et al., 2007b). Gradients also provide spatial information inside single cells for processes such as morphogenesis, mitosis and cell cycle regulation (Brown and Kholodenko, 1999; Chen et al., 2011; Fuller et al., 2008; Kalab and Heald, 2008; Meyers et al., 2006; Niethammer et al., 2004). The mechanisms behind the formation and maintenance of protein gradients remain elusive. Although it has been assumed that many gradients are formed through a classic mechanism based on simple diffusion (Ashe and Briscoe, 2006; Crick, 1970), more complex variations are likely to underlie gradients in many biological contexts (Eldar et al., 2002; Gregor et al., 2007a; Spirov et al., 2009).

A poorly understood aspect of gradients is how they are able to provide sufficient precision in face of substantial biological noise. The stochastic nature of biological processes may contribute significant differences between individual cells (cell-to-cell or extrinsic noise), as well as fluctuations over time and space even within a single cell (intrinsic noise). Studies have revealed high variability among individual cells for processes such as gene expression (Elowitz et al., 2002; Raj et al., 2010; Raser and O'Shea, 2004). Noise could potentially disrupt the precision of gradient-based mechanisms that are based upon fine differences in protein concentration or activity (Gregor et al., 2007b; Saunders and Howard, 2009; Tostevin et al., 2007). It is not yet well understood what mechanisms might mitigate the effects of extrinsic and intrinsic fluctuations, although several mechanisms have been proposed, including time-averaging

(Gregor et al., 2007a; Tostevin et al., 2007), spatial averaging (Erdmann et al., 2009; Gregor et al., 2007a) (both for intrinsic noise) and self-enhanced ligand degradation (Eldar et al., 2003) (for extrinsic noise).

In the fission yeast *Schizosaccharomyces pombe*, precise spatial information must be established for proper cell morphogenesis and cell division. These rod-shaped cells grow during interphase from their cell tips to around 14 μm in length, before entering mitosis and dividing medially (Mitchison and Nurse, 1985). The Dual-specificity tyrosine phosphorylation regulated kinase (DRYK) pom1p has been implicated in the regulation of polarity, division plane placement, and cell length sensing (Bahler and Pringle, 1998; Celton-Morizur et al., 2006b; Martin and Berthelot-Grosjean, 2009; Moseley et al., 2009; Niccoli et al., 2003; Padte et al., 2006). Pom1p localizes to cell tips in a gradient-like distribution (Bahler and Pringle, 1998; Padte et al., 2006). For the regulation of cytokinesis, pom1p regulates the localization of mid1p, an anillin-like cytokinesis factor responsible for division site positioning. Mid1p localizes to a band of cortical dots near the nucleus, but in *pom1* mutant cells these dots are spread over half of the cell cortex, and, as a consequence, the cells often divide slightly asymmetrically (Celton-Morizur et al., 2006b; Padte et al., 2006). This phenotype suggests that pom1p is a cell tip inhibitor that prevents mid1p from accumulating at one of the cell tips (the non-growing one). Pom1p has additional mid1p-independent functions in preventing contractile rings from forming at the very ends of cells (Huang et al., 2007) and in the regulation of cell polarization, possibly through effects on the rhoGAP rga4p (Tatebe et al., 2008).

Recently, the pom1p gradient has been proposed to act as a ruler for signalling the length of fission yeast cells (Martin and Berthelot-Grosjean, 2009; Moseley et al., 2009; Moseley and Nurse, 2010; Pan and Chang, 2009), where the cells are able to sense that they are 14 μm long before entering mitosis. Pom1p contributes to the regulation of mitotic entry as part of a regulatory network of protein kinases that includes cdr2p, wee1p, and cdk1 (cdc2p). The gradient-like distribution of pom1p from cell tips and the very different localization of its targets such as mid1p and cdr2p that are in cortical dots near the middle of the cell, suggests a model for cell length control: in short cells, the pom1p gradient inhibits cdr2p activity, inhibiting entry into mitosis. As cells grow longer, the source of the pom1p gradient at the cell tips moves away, leading to a drop in the effective pom1p concentration at the medial site, and allows for the activation of cdr2p and entry into mitosis. Thus pom1p may form a morphogen-like gradient that is used to sense distances in the cell.

Here, we present a quantitative analysis of the pom1p gradient. Using a combination of experimental and computational analyses, we elucidate a mechanism for how the pom1p gradient is generated. The gradient is constructed and maintained through a highly dynamic process of pom1p associating to the plasma membrane at the cell tip, followed by diffusion on the plasma membrane. However, instead of a simple diffusion process, fission yeast employs a more complex mechanism that involves the formation of pom1p clusters on the membrane. This clustering provides a mechanism to buffer against fluctuations in concentration levels. Together with intrinsic noise reduction via time-averaging, this pom1p gradient is then able to impart significantly more precise positional information.

Results

Pom1p localizes in noisy cortical gradients

We imaged pom1p in *S. pombe* cells expressing a pom1-tomato-dimer fusion (Figure 2.1A) (Martin and Berthelot-Grosjean, 2009). This fusion protein is expressed as the only pom1 protein in the cell, from the $pom1^{+}$ chromosomal locus under the control of the endogenous promoter; it was found to be functional based on its ability to regulate cell length and cdr2p and mid1p localization. To quantitatively measure the distribution of pom1p on the cortex, we developed custom software that derives image masks around the cortex, allowing us to plot fluorescence intensities as a function of *d*, the distance along the cortex from the center of a cell tip (Figure 2.1B, see also Supplemental Information).

Pom1p localized on the cell cortex in a gradient-like distribution, with the highest concentrations at the cell tips and dropping to low but detectable levels at the cell middle (Figure 2.1A, S2.1A) (Martin and Berthelot-Grosjean, 2009; Moseley et al., 2009; Padte et al., 2006). Pom1p was present in the cytoplasm at low levels in a homogeneous distribution and was not detected in the nucleus (Figure 2.1A, S2.1A). On the cortex, the distribution of mean pom1p intensities showed a gradient-like profile that could be fitted to an exponential decay function $I_a\, e^{-|d-d_0|/\lambda}$ between $1.5\ \mu\text{m} < d < 4\ \mu\text{m}$ (Figure 2.1B), where d is the distance along the cortex from a tip, $d_0 = 1.5\ \mu\text{m}$, λ is the decay length and I_a is the intensity of pom1p 1.5 µm from the cell tip. Of individual profiles, a large subset (85% ; n=396) were well-fitted to this exponential decay function ($r^2=0.94\pm0.06$), with a characteristic length scale $\lambda = 1.5\pm0.4\ \mu\text{m}$. The small subset of profiles with poor fits ($r^2<0.9$, 15%) had low intensity values at $d=1.5\ \mu\text{m}$ (on average 40% lower than for the large subset). These measurements show that pom1p exhibits an exponential decay profile that is often characteristic of gradients.

Pom1p exhibited high cell-to-cell variability. By comparing the fluorescence intensity of pom1-GFP with other GFP-fusions as standards (see Figure S2.1B) (Wu and Pollard, 2005), we estimated that there are approximately 5000 ±1900 molecules of pom1p per cell, with approximately 2500 molecules located at the cell tips (a tip region is defined here as the 10% of the cell closest to a cell tip). There was, however, a significant amount of cell-to-cell variability in total pom1p levels (Figure 2.1C, D). We tested whether this variability could be due to changes in pom1p levels during the cell cycle. In fission yeast, the cell cycle phase can be related to the length of the cell because cells grow continuously during interphase. Measurements of an asynchronous population of cells showed a weak correlation of total pom1p intensity in the cell rising with increased cell length with substantial variability ($r^2 = 0.32$; Figure 2.1D, red), suggesting that the total (including cytoplasmic) concentration of pom1p stays relatively constant. The intensity of pom1p in the tip regions exhibited high variability and little correlation of intensity values with cell length ($r^2 = 0.002$; Figure 2.1D, blue). We also examined if the shape of the gradient changed as a function of cell length. In the fits to exponential decay functions, we found no significant correlation of λ with cell length (Figure 2.1E; see Figure S2.1C for parameter distribution). These data suggest that the pom1p distribution at cell tips does not exhibit systematic changes with cell length and is consistent with a notion that these gradients provide absolute rather than relative positional information.

We next analyzed variability within individual cells. In each cell, there are two pom1p gradients (one at each cell tip), which were often unequal in intensity. These differences were variable, as plotted in Figure 2.1F. This suggested that variation in pom1p was not derived solely from differences in global expression level, but also depended on properties specific to each tip. Time-lapse images revealed no oscillations between the two tips or large changes in pom1p distributions over the 1 to 10 min time scale.

Pom1p intensities within each gradient exhibited rapid intrinsic fluctuations on a second time scale. For instance, in single images (500 ms acquisition), pom1p exhibited an irregular distribution that changed on a second time scale (Figure 2.1G, left image). However, when multiple images of the same cell acquired over 25 s of total imaging time were computationally summed, the distribution presented a smoother gradient-like profile (Figures 2.1G, right image). This smooth pattern suggested that pom1p is capable of occupying all cortical locations. These data suggest that intrinsic fluctuations are potentially significant, but could be substantially reduced by a mechanism that incorporates time-averaging.

FRAP measurements of pom1p dynamics

A current model of pom1p gradient formation is that pom1p associates with the plasma membrane at cell tips via the tea1p-tea4p-dis2p complex and then diffuses on the plasma membrane before disassociating (Hachet et al., 2011). Consistent with this model, we confirmed that the peaks of pom1p and tea1p coincide at the cell tip (Figure S2.2A,B), and that pom1p spreads over a broader area on the cell tip than tea1p (Figure S2.2C-E). While this work was in review, the tea1p-tea4p complex was shown to induce the membrane association of pom1p by regulating its phosphorylation state (Hachet et al., 2011). The phosphorylated form of pom1p is cytoplasmic, and is converted at the cell tip into a unphosphorylated form by the dis2p phosphatase associated with the tea1/tea4 complex. The unphosphorylated form of pom1p then binds to the plasma membrane via a basic phospholipid binding domain, and diffuses in the membrane to form the gradient. Pom1p may disassociate from the membrane upon autophosphorylation. The gradient distribution is independent of actin, microtubules and endocytosis (Figure 2.2A), as well as protein degradation (Hachet et al., 2011), suggesting that a transport mechanism based primarily on protein diffusion in the membrane is indeed plausible.

To test this model, we sought to quantitate key parameters such as the rate of pom1p membrane disassociation and diffusion constants. First, we performed fluorescence recovery after photo-bleaching (FRAP) experiments (see Methods and Supplemental Information). We first photo-bleached the pom1-tomato signal over one entire cell tip. The recovery profile of the total pom1p intensity in the tip region could be fitted with a $t_{1/2}$ of 30±10 s (Figure 2.2B). Most of the recovery came from the cytoplasmic pool, as the second unbleached tip did not change in fluorescence intensity. These results suggest that pom1p molecules remain on the plasma membrane for roughly 30 s. Second, we photo-bleached pom1-tomato over half of a cell tip (Figure 2.2C. Although the recovery profiles were noisy, the average fluorescence recovery occurred with a $t_{1/2}$ of 8±3 s. This faster half-tip FRAP time suggests that, in this case, recovery is not only from association of unbleached cytoplasmic pom1p to the cell tip, but also, more importantly, from diffusion on the membrane from the other half of the tip. Consistent with this, in some cases, pom1p appeared to spread from the unbleached zone into the bleached zone (Figure 2.2D). Assuming that the movement in the membrane is diffusive, our half-tip FRAP measurements provided an initial rough estimate for the diffusion constant of pom1p: the half-tip is repopulated primarily by diffusion over a distance of about 1.2 μm in around 8 s. Hence, using $x_{\mathrm{rms}}^2 \approx 2D_{\mathrm{half\text{-}tip}}t$, we find $D_{\mathrm{half\text{-}tip}} \approx 0.1\ \mu\mathrm{m}^2\,\mathrm{s}^{-1}$. These results provide initial evidence that pom1p diffuses in the plane of the plasma membrane.

Characterization of motile cortical pom1p clusters

To further observe the dynamics of pom1p, we imaged cells in the cortical focal plane using spinning disc confocal microscopy (Figure 2.3A). We found pom1p in discrete clusters that were distributed all over the cortex and enriched at the cell tips. These clusters were seen with pom1-tomato-dimer, pom1-GFP, and pom1-monomeric GFP fusions. Among clusters that could be tracked (primarily those located some distance away from the cell tips), these had an average lifetime of about 4 s (Figure 2.3B,C; mean lifetime $\tau = 3.7 \pm 2.0$ s (standard deviation)). In general, clusters gradually formed from a "cloud" into a discrete entity, and then gradually disassembled, although there were substantial variations in behaviors (Figure 2.3B). No movement of clusters into the cell interior was seen. Fluorescence intensity measurements estimate that detectable clusters contained on average about 20 pom1p molecules (Figure S2.3A,B), and that clusters assemble and disassemble at similar rates of 14 ±12 molecules/s (Figure S2.3C).

These transient clusters exhibited small (usually sub-micron) movements on the membrane that appeared non-directional (Figure 2.3D). We observed no systematic pattern of movements either away or toward cell tips. The appearance and movement of clusters were unchanged upon treatment with actin or microtubule inhibitors. The cluster displacement histogram was consistent with a model of purely diffusive cluster motion (Figure 2.3E and Supplemental Information). The mean root-mean-square displacement was $x_{\mathrm{rms}} \approx 0.40 \pm 0.36$ μm. Using, $x_{\mathrm{rms}}^2 \approx 2D_{\mathrm{clus}}\tau$, we estimate a diffusion constant of these clusters to be $D_{\mathrm{clus}} \approx 0.02 \pm 0.03$ $\mu m^2 s^{-1}$. On average, larger clusters (higher intensity in regions away from the cell tip) diffused slower than smaller ones (lower intensity) (Figure 2.3F). Cluster formation was also independent of tea1p, tea4p and pom1p kinase activity (Hachet et al., 2011; Padte et al., 2006).

We next used Fluorescence Correlation Spectroscopy (FCS)(Botvinick and Shah, 2007) to further investigate the different states of pom1p . We assayed pom1-GFP behaviors at different cellular sites and orientations in wildtype and *tea* mutants (see Supplementary Information; Figures 2.4 and S2.4). In the cellular interior, the predominant state detected was a cytoplasmic component (Species S1), which diffused with a diffusion constant of $D_1 \approx 1.5\ \mu m^2 s^{-1}$; this suggests that cytoplasmic pom1-GFP is in a form larger than a monomer (e.g. intracellular soluble GFP had a diffusion constant of $7.5\ \mu m^2 s^{-1}$) (Figure S2.4B) and has a similar behavior as the 20S anaphase promoting complex (YG and JVS, unpublished observation). We detected at least two cortical states: 1) A Species S2 with a diffusion constant $D_2 \approx 0.026\ \mu m^2\ s^{-1}$ (diffusion time ≈ 0.65s, Figures 2.4B, S2.4C), which has a similar diffusion constant to the clusters observed through time-lapse imaging. 2) A very slow Species S3, with a diffusion constant $D_3 \approx 0.006\ \mu m^2\ s^{-1}$ (diffusion time > 2.85s, Figures 2.4B, S2.4C). This very slow state is enriched at the cell tip regions (Figures 2.4B, S2.4D), and may represent pom1p in complex with cortical tea1p. This state was not measured in the earlier time-lapse analysis probably because the clusters were too dense for tracking in the tip region. Overall, these FCS studies therefore independently validate and characterize multiple pom1p states.

We noted that our measurements on pom1p clusters are significantly different from those on more general cortical pom1p fluorescence measured by FRAP. The cluster lifetime of 4 s is much shorter than the 30 s estimated from FRAP for the pom1p membrane lifetime. The diffusion constant extracted from cluster tracking (a value also found in the FCS analysis) was 5 times smaller than that estimated previously using half-tip FRAP. These discrepancies suggested that the clusters alone do not account for the whole gradient distribution and thus indicate that the measured cortical gradient includes an additional fast moving state of pom1p, such as pom1p monomer, that is not resolved as a discrete entity using light microscopy. We note that this more rapid state was also not easily identified in FCS, as its presence is likely to be masked by the brighter, slower clusters (Tcherniak et al., 2009). Taken together, these results prompted us to consider that pom1p exists in multiple states on the cortex.

A two-state model for gradient dynamics

To rationalize the results of the above experiments and to mechanistically understand the formation of the pom1p gradient, we turned to mathematical modeling. A classical model for gradient formation is based on the localized introduction of a chemical species, after which it can diffuse before disassociation (an SDD model: source, diffusion, disassociation) (Gregor et al., 2007b). Such a model has previously been applied to the pom1p system (Padte et al., 2006; Tostevin, 2011; Vilela et al., 2010). However, such a model with only a single membrane diffusion constant and membrane lifetime is clearly inconsistent with our experimental results (see paragraph above). We therefore considered whether pom1p might exist in at least two membrane-bound forms, each with its own diffusion constant and characteristic timescale. Consequently, we developed and tested a two state (TS) gradient model.

We assume that hypophosphorylated pom1p associates with the membrane at sites marked by tea1p (Hachet et al., 2011), with a rotationally-symmetric pom1p membrane association function (peak value *J*) parameterised by a Gaussian fit to the tea1p spatial distribution. The membrane-associated pom1p then diffuses in the plasma membrane (assumed in the model to consist of two hemispherical caps with a connecting cylinder of radius 1.75 μm) as two interchanging states. The first state consists of slow-diffusing, short lifetime (~4 s) pom1p clusters with a diffusion constant of 0.02 $\mu m^2 s^{-1}$. The second state consists of faster-diffusing pom1p, with a diffusion constant of 0.2 $\mu m^2 s^{-1}$ and with a membrane disassociation timescale of around 30 s. This second state needs to be more rapidly diffusing with a longer lifetime in order to be consistent with the FRAP data. The diffusion constant of 0.2 $\mu m^2 s^{-1}$ is larger than the earlier estimate $D_{half\text{-}tip} \approx 0.1\ \mu m^2 s^{-1}$, due to the presence of the additional slow-diffusing state. The TS model assumes that molecules of pom1p can transition between the clustered and faster-diffusing forms while on the membrane. Simpler models with transfer only in one direction between the clustered and faster-diffusing forms did not fit the data as well (see Supplemental Information). Furthermore, while cluster fragmentation was assumed to be a linear process, we employed nonlinear cluster growth dynamics, proportional to the product of the densities of the clusters and faster-diffusing state. Such dynamics is appropriate for an aggregation phenomenon where slow-diffusing pom1p clusters can absorb colliding fast-diffusing pom1p. Moreover, such a nonlinearity ensures that as the levels of pom1p rise, the proportion of pom1p in the clustered form can increase to an even greater extent. As we will see below, this nonlinear cluster growth is the key to the noise-buffering properties of the model; two state models with a linear growth term do not exhibit this feature and fit our experimental data less well (see Supplemental Information and Figure S5). Finally, we assume that faster-diffusing pom1p can spontaneously disassociate from the membrane into the cytoplasm. Although we do not explicitly include pom1p autophosphorylation (Hachet et al., 2011) in our model, such dynamics is implicit through a long (~30s) pom1p membrane dwell time prior to disassociation, a timescale potentially created through slow pom1p auto-phosphorylation followed by rapid disassociation. Importantly, constructing a simple model of autophosphorylation, but without clustering, could not explain our data (see Supplemental Information). The reaction scheme, model equations and parameter values (together with the experiments from which the parameter values were extracted) are shown in Figure 2.5A. A more detailed mathematical analysis is presented in the Supplemental Information.

We numerically solved the steady-state differential equations (Figure 2.5A) for the TS model. The TS model contains nine parameters (Figure 2.5A), which we inferred in the following way (see Supplemental Information for full procedure): cell radius (direct measurement), association width (tea1p spatial distribution), membrane disassociation rate (full-tip FRAP), cluster fragmentation rate (cluster lifetime) and cluster diffusion constant (cluster tracking, FCS). The diffusion constant of the faster-diffusing component was then constrained by the mean pom1p profile (to which a good fit was obtained, see Figure 2.5B). We note that the initial estimate of the diffusion constant from the half-tip FRAP data was not used in our detailed quantitation. To constrain the relative membrane association of the two states, and the cluster aggregation parameter, we measured and then fitted the TS model to the relative fraction of clustered pom1p as a function of position (Figure 2.5C), where overall around half of membrane pom1p was in the clustered form. The total number of pom1p molecules on the cortex was then used to constrain the maximum membrane association parameter. We then validated our model parameterisation by comparison with directly measured cluster assembly/disassembly rates (Figure S2.3C), and by generating TS model half-tip FRAP recovery profiles and comparing with our experiments. We find that the TS model is consistent with all of our previously presented experimental data, including the full and half-tip FRAP (Figure 2.5D, E). As detailed below, the TS model can also make testable predictions about the robustness of the pom1p gradient to cell-to-cell variations.

Mechanism for buffering cell-to-cell variations

One attractive property of this TS model is that it provides an inherent mechanism for buffering against cell-to-cell variations in concentration levels. This feature could be important as our experimental measurements show that the intensities of pom1p at the cell tip vary greatly. The model predicts that if more pom1p is introduced onto the membrane at the cell tip, a larger proportion of pom1p close to the cell tips can be in the clustered form due to the nonlinearity of cluster growth. As the pom1p clusters diffuse more slowly than the faster-diffusing component (Figure 2.3F), these gradients would have shorter decay lengths λ, i.e. an anti-correlation could exist between the peak pom1p concentration and λ. Thus, in the TS model, differences in the concentration of pom1p at certain distances away from a cell tip can be reduced, as illustrated in Figure 2.6A. We tested this prediction *in silico*. We first examined the effects of variations in the membrane association parameter. We chose to examine large variations in association, because of the large cell-to-cell variation in the tea1p tip intensity (Figure S2.2E). Accordingly, the maximum membrane association parameter in the TS model was drawn from a Gaussian distribution with 20% (standard deviation) variation relative to the mean. The resulting individual pom1p profiles were then fit to an exponential function over the range d=1.5-4 μm. For 100 such profiles, Figure S6A confirms the predicted anti-correlation between the pom1p peak concentration and λ. Similarly, cell-to-cell variation in the membrane pom1p diffusion constants also generated a similar anti-correlation (Figure S2.6B, 10% relative variation in diffusion constants). Such an anti-correlation is not, however, significantly generated by cell-to-cell variations in the membrane disassociation rate (Figure S6C, 10% relative variation in the disassociation rate), nor by cell-to-cell variations in the aggregation constant or fragmentation rate. To test for an overall anti-correlation, we simultaneously drew parameter values from

Gaussian distributions with standard deviations relative to the mean of 10% (diffusion, aggregation, fragmentation, disassociation) and 20% (association). Figure 2.6B shows the pom1p peak concentration plotted against λ for 100 such simulated profiles, with a clear anti-correlation in the TS model. The SDD model with equivalent parameter variations did not exhibit such an anti-correlation (see Figure S2.6D), nor did simple linear models that incorporated pom1p phosphorylation but without clustering dynamics (see Supplemental Information).

To test these model predictions with our *in vivo* data, we re-examined our experimental pom1p profiles (Figure 2.6C). Indeed, profiles with high pom1p concentrations at the cell tip tended to decay more rapidly with distance compared to those cells with lower tip pom1p concentrations (Figure 2.6C). To substantiate this finding quantitatively, we used our earlier fits (with $r^2>0.9$) of individual pom1p profiles (one from each individual cell) to exponentially decaying functions. These experimental data (Figure 2.6D) show an I_a-λ anti-correlation, in quantitative agreement with the prediction of the TS model (and in disagreement with the SDD model). This striking property of the *in vivo* gradients provides strong support for our TS model by conforming to an important TS model prediction.

As illustrated in Figure 2.6A, the anti-correlation could potentially reduce the cell-to-cell variations in the pom1p gradient. To examine this possibility, we generated two sets of data from our experiments: pairs of I_a and λ in the first set were from the same original profile, whereas in the second set each I_a was paired with a randomly chosen λ. The data set incorporating the anti-correlation significantly reduced relative cell-to-cell variations (defined as the standard deviation in the pom1p intensity from Figure 2.1B divided by the mean intensity) as compared to the randomised data set (Figure 2.6E), even though the mean profiles in the two data sets were almost identical (Figure 2.6E, inset). We observe that the anti-correlation can decrease cell-to-cell variations by up to 40%.

To verify that the observed anti-correlation was not a general artifact of our measurements (for instance in image analysis), nor a non-specific property of tip gradients (for instance due to heterogeneity in membrane composition), we analyzed the profile of the protein kinase ssp1-GFP, which also forms a cortical concentration gradient from the cell tip, but without visible clustering (Figure S2.6E)(Rupes et al., 1999). In this case, no such anti-correlation was observed (Figure S2.6F).

Intrinsic fluctuations are significant and can be reduced by time-averaging

Pom1p profiles exhibited large intrinsic fluctuations, in part because of the effects of dynamic clustering and movement. This finding poses the question of how cells are able to sense pom1p concentrations with high precision (Tostevin et al., 2007). Intrinsic noise can be reduced by time-averaging, where the downstream "targets" of pom1p could be less dynamic than pom1p, and thus able to integrate the variations in pom1p over time. Indeed, FRAP studies show that two putative pom1p targets, cdr2p and mid1p, have $t_{1/2} > 90$ s (KP, unpublished observations) (Zhang et al., 2010). Although the utility of time averaging has been proposed previously in theoretical papers (see, for example, (Tostevin et al., 2007)), we sought to quantify experimentally the size of the intrinsic noise, and estimate the reduction in overall noise levels potentially provided by time-averaging. Such measurements have not previously been obtained for any intracellular gradient.

We analyzed time-lapse images of single cells to determine the magnitude of the intrinsic fluctuations δI_{int} as a function of camera imaging (averaging) time in individual measuring volumes of width ≈ 200 nm along the cortical mask. Here, δI_{int} is determined from the difference between the pom1p profile averaged over the first τ seconds, and the profile averaged over the full 90 s time series (see Supplemental Information for full protocol). In Figure 2.7A, δI_{int} is plotted as a function of averaging time at various locations along the membrane: in all cases time-averaging resulted in a significant decrease in fluctuations. At 5 μm from the cell tip, we found a five-fold reduction in δI_{int} over 90 s of averaging. A simple time-averaging theory predicts that after τ seconds of time-averaging, δI_{int} should be reduced by $1/\sqrt{\tau}$ (see Supplemental Information) (Tostevin, 2011; Tostevin et al., 2007). This prediction agrees with our data (Figure 2.7A). The TS model also generated explicit predictions about the magnitude of the intrinsic noise as a function of position for fixed τ, predictions that we also confirmed (see Supplemental Information and Figure S2.7). We did detect discrepancies in intrinsic noise levels between theory and experiment near cell tips (first two frames in Figure 2.7A), which could potentially be explained by bursty pom1p association dynamics. Overall, our analysis suggests that time averaging can provide significant intrinsic noise-reduction.

Noise reduction increases the positional precision of the gradient

We next determined the extent to which the mechanisms that reduce cell-to-cell/intrinsic noise can improve the positional precision of the gradient. We first examined the relative importance of cell-to-cell variations as compared with intrinsic noise after varying periods of imaging (time-averaging). Near the cell tip, the majority of the observed variations in pom1p intensity are due to cell-to-cell variations, even after only short averaging periods (blue line, Figure 2.7B). Near the cell middle, intrinsic noise is more significant, and hence time averaging is more important in reducing fluctuations (red line, Figure 2.7B). After 30 s of time averaging, however, cell-to-cell variations are the dominant source of error in all locations.

We then experimentally quantified the positional error for the pom1p gradient. We first assumed that pom1p is used as a classical "morphogen" gradient that defines position in the cell through a threshold mechanism. In Figure 2.7C, we show the positional precision as function of position, after 3 s or 90 s of time-averaging. We see that time-averaging significantly improves the positional precision of the pom1p profile.

Second, we examined the role of pom1p as an inhibitor that prevents proteins such as mid1p, cdr2p and rga4p from binding at the cell tip (Celton-Morizur et al., 2006b; Padte et al., 2006; Tatebe et al., 2008). We examined the probability that the pom1p concentration is above a given threshold (taken to be the mean cytoplasmic intensity) everywhere in a region close to a tip (Figure 2.7D). With 3 s of averaging, the entire tip region for $d < 2.7$ μm can be distinguished from the cytoplasm in 90% of cells. With 90 s of averaging, a larger tip region of $d < 3.6$ μm can be distinguished, or, alternatively, the same $d < 2.7$ μm region can be distinguished, but now in 99% of cells. Thus, noise buffering by time averaging can substantially improve the precision of the system.

Discussion

In this work, we develop a quantitative mechanistic model for the dynamic formation of the pom1p kinase gradient distribution. Previously, we and others have proposed a simple SDD-like model of pom1p gradient formation (Padte et al., 2006; Tostevin, 2011; Vilela et al., 2010). Upon more detailed analysis, however, we find that the mechanism is more complex. We propose that pom1p associates onto the plasma membrane close to a cell tip at sites marked by the tea1p complex and remains on the membrane for about 30s. This membrane association is regulated by a cycle of pom1p dephosphorylation and autophosphorylation (Hachet et al., 2011). During its time on the membrane, pom1p undocks from tea1p and then diffuses on the membrane. As it is diffusing, pom1p also forms larger clusters that form transiently and then fall apart into a faster-diffusing state. This clustering activity modulates the diffusion constants and the properties of the gradient profile. Based upon our empirical measurements of many of the key parameters, we present a quantitative two state (TS) computational model for gradient formation. Although this model is still a simplification of the *in vivo* mechanism, it has significant predictive power. More sophisticated models, such as an aggregation-fragmentation model (Wattis, 2006), that use a larger number of pom1p components with varying diffusion constants, would generate similar results but with many more fitted parameters. However, even our relatively simple TS model demonstrates how mechanisms for gradient formation in biology are likely to be more complex than previously imagined.

This work also elucidates mechanisms of how gradients buffer against noise. There is a growing appreciation that there are substantial fluctuations in biological systems. Fluctuations in gradients are likely to arise from stochasticity in gene expression, as well as in processes involved in gradient construction such as diffusion, membrane association, and local tea complex levels. Given this noise, it has not been clear how a gradient is able to generate a precise functional spatial pattern. Although issues of noise in subcellular gradients have been discussed previously at a theoretical level (Tostevin et al., 2007), we provide here quantitative measurements of such fluctuations *in vivo* (both cell-to-cell and intrinsic fluctuations). We propose that two mechanisms, cluster formation and time-averaging, work together to reduce the effects of noise in the pom1p system. We find that inherent in our two-state model, with nonlinear cluster growth, is a prediction that it buffers against cell-to-cell variations in concentration levels (of, for example, pom1p). Both *in silico* predictions and verification by *in vivo* data show an anti-correlation between pom1p intensity levels and gradient decay length: even as the pom1p concentration at the cell tips varies, the variation in the gradient at distances away from the cell tips is buffered. This anti-correlation relies on the property that higher (lower) pom1p concentrations form proportionally more (fewer) clusters, which leads to overall slower (faster) diffusion on the membrane. Previously, in a developmental biology context, other mechanisms proposed to buffer variations of this kind (Eldar et al., 2003) relied on self-enhanced degradation, leading to algebraically-decaying profiles.

We also propose that, in the pom1p system, a time-averaging mechanism can significantly reduce the large intrinsic fluctuations generated by the stochastic dynamics of gradient formation, including, for example, slow cluster diffusion. *In silico* time-averaging of experimental pom1p signal intensities on the order of 30-90 s produces a much smoother gradient distribution. Time-averaging can be implemented if the targets of pom1p are able to integrate the pom1p concentration over time. Consistent with this proposal, cdr2p, a possible target of pom1p, resides at the cortex near the middle of the cell with a $t_{1/2}$ of greater than 90 s (our unpublished data); cdr2 molecules could thus theoretically sense pom1p concentrations at the cortex over these time scales. Overall, our analysis measures the extent to which clustering/time-averaging enhance robustness to cell-to-cell/intrinsic noise, with the clustering-induced anti-correlation, for example, reducing cell-to-cell fluctuations by up to 40%.

Our studies provide quantitative measurements of the key parameters responsible for pom1p gradient formation. The average membrane disassociation rate, as measured by whole-tip FRAP, shows turnover on the order of about 30 s, indicating that much of the more rapid pom1p dynamics occurs on the plasma membrane. Measurements using multiple assays with differing resolutions suggest that pom1p molecules exist in at least four distinct “states,” each with its own diffusion constant. FCS and imaging both show a state with a diffusion constant of around 0.02 $\mu m^2 s^{-1}$; these correspond to the clusters moving on the membrane. It is not known whether these clusters, which contain roughly 20 pom1p molecules at their peak, consist solely of pom1p or some assemblage of pom1p with other proteins. However, tea1p and tea4p do not appear to be a major component of these cortical clusters away from the cell tip. Gradient profiles, as well as the half-tip FRAP results strongly suggest the existence of a faster diffusing state with an estimated diffusion constant of 0.2 $\mu m^2 s^{-1}$. This component may represent a pom1p monomer, or a small pom1p complex, diffusing on the membrane. It may appear as a haze in fluorescence imaging, and its presence in FCS may be masked by the brighter and slower clusters (Tcherniak et al., 2009). In addition, FCS shows a very slow membrane-associated state with diffusion constant of 0.005 $\mu m^2 s^{-1}$, located primarily at cell tips. This slow cortical state may represent a subset of pom1p docked at the cell tips with tea1p dots, which also move slowly (KP, unpublished observations). FCS also suggests that cytoplasmic pom1p is part of a larger complex.

The placement of the pom1p gradient relies on a well-studied microtubule-based morphogenetic program in fission yeast (Chang, 2001; Chang and Martin, 2009; Piel and Tran, 2009). Self-organizing microtubule bundles orient along the long axis of the cell. The growing MT plus ends transport and deposit tea1p-tea4p complexes at the cell tip, thereby indirectly helping to position the source of the pom1p gradient. We note that transient disruption of MTs has only mild effects on the pom1p gradient, as the tea proteins continue to persist at the cell tips even without MTs (Bicho et al., 2010).

This work illustrates how in biology gradients are likely to use more complex mechanisms than simple SDD-based models in order to deal with noise. Similar quantitative analyses of other biological gradients have also revealed complexities not easily explained by simple models. In the Bicoid gradient, large discrepancies in diffusion constants derived from different approaches challenge previous models and suggest more complex underlying mechanisms (Abu-Arish et al., 2010; Gregor et al., 2007b). In polarization of budding yeast, formation of a cortical gradient of the small GTPase Cdc42 relies on the interplay of regulators including GAPs and GEFs, as well as actin-dependent membrane trafficking (Marco et al., 2007; Slaughter et al., 2009). Further studies on gradients will undoubtedly forge further understanding of the mechanisms underlying the spatial regulation of development and morphogenesis at the level of molecules.

Methods

S. pombe cell preparation

Standard methods for *S. pombe* growth and genetics were used (Moreno et al., 1991). Strains are listed in Supplemental Information, Table S1. Cells were grown in liquid YE5S media at 25˚C with shaking in exponential phase before imaging. Cells were generally mounted in liquid YE5S media directly on glass. 1% agarose YE5S pads were used for long-term imaging. For some of the FRAP experiments, cells were mounted on lectin-coated chambers. Imaging was done at 23-26˚C.

Microscopy

Images were generally acquired using a spinning-disc confocal fluorescence microscope system (Nikon, Perkin-Elmer, Solamere Technology) with an EM CCD camera (Hamamatsu) and a 100x 1.4 N.A. objective. Full tip FRAP experiments were performed with a LSM710 Meta scanning confocal microscope (Zeiss). Half-tip FRAP experiments reported were performed with an Ultraview Vox spinning disc microscope system with a photo-bleaching unit (Perkin-Elmer). We confirmed that both imaging systems provide comparable results.

Image Analysis

ImageJ (NIH) and custom MatLab (Mathworks) software were used for analysis. ImageJ plugins used include MtrackJ (Erik Meijering) and Manual Tracking (Fabrice Cordeleires). For gradient profiles, generally, fluorescence intensity values around the cortex of cells were measured from images of cells in a medial focal plane, using custom MatLab software for the automated generation of a one-pixel wide mask around the cell cortex, followed by manual correction. Protein counts were estimated by quantitative fluorescence intensity with standard proteins that had been quantitated previously (Wu and Pollard, 2005). The cortical clusters were analyzed manually from spinning disc confocal images taken in a cortical focal plane. See Supplementary information for additional information.

Fluorescence correlation spectroscopy (FCS)

Two-photon FCS was performed on a custom-built microscopy setup. Autocorrelation profiles were fit to a sum of 2D and 3D diffusion models and yielded particle residence times (Haustein and Schwille, 2007). Each particle is summed with its brightness squared as a pre-factor into the autocorrelation profile. Thus, the presence of bright, slow species as seen in this study makes dimmer, faster species (e.g. monomeric pom1p) difficult to detect. Diffusion constants of the slow species are overestimated due to the long residences times in the excitation volume, whereas the diffusion constant for the faster species is underestimated due to the complex mixtures of large and small clusters in the volume (Tcherniak et al., 2009). Fission yeast cells were measured at different cellular positions to identify diffusing pom1p species. See Supplementary Information for details.

Mathematical modeling

The cell geometry was taken to be a capsule, with two hemispherical caps connected by a cylinder of equal radius. Pom1p dynamics was described using reaction-diffusion equations, which were solved numerically using Matlab. To compare the model with the experimental full-tip FRAP data, the model initial conditions had no pom1p present at a cell tip. Model comparison to the half-tip FRAP data was more complicated due to the lack of rotational symmetry about the cell's long axis. Here, 1D approximations were used in this case to analyze the model behavior. Model parameter fitting was made in 3 stages. First, experimental results limited the range of certain parameter values (for example, the pom1p membrane lifetime was constrained by the full-tip FRAP). Second, parameters were fit to four further experiments: pom1p average profile; relative distribution of slow-diffusing pom1p clusters; total pom1p copy number; and full-tip FRAP results. Finally, once satisfactory fits to the above data were obtained, the model was compared with the half-tip FRAP results and estimates of cluster assembly/disassembly rates for consistency.

Acknowledgements

I would like to thank N. Padte and S. Martin for constructing many of the strains used in this project. I would also like to acknowledge J. V. Zon and Angel Andrew for initializing the work into the cortical cell tracking software. As usual, additional thanks for the members of the Chang laboratory for thoughtful discussion and advice.

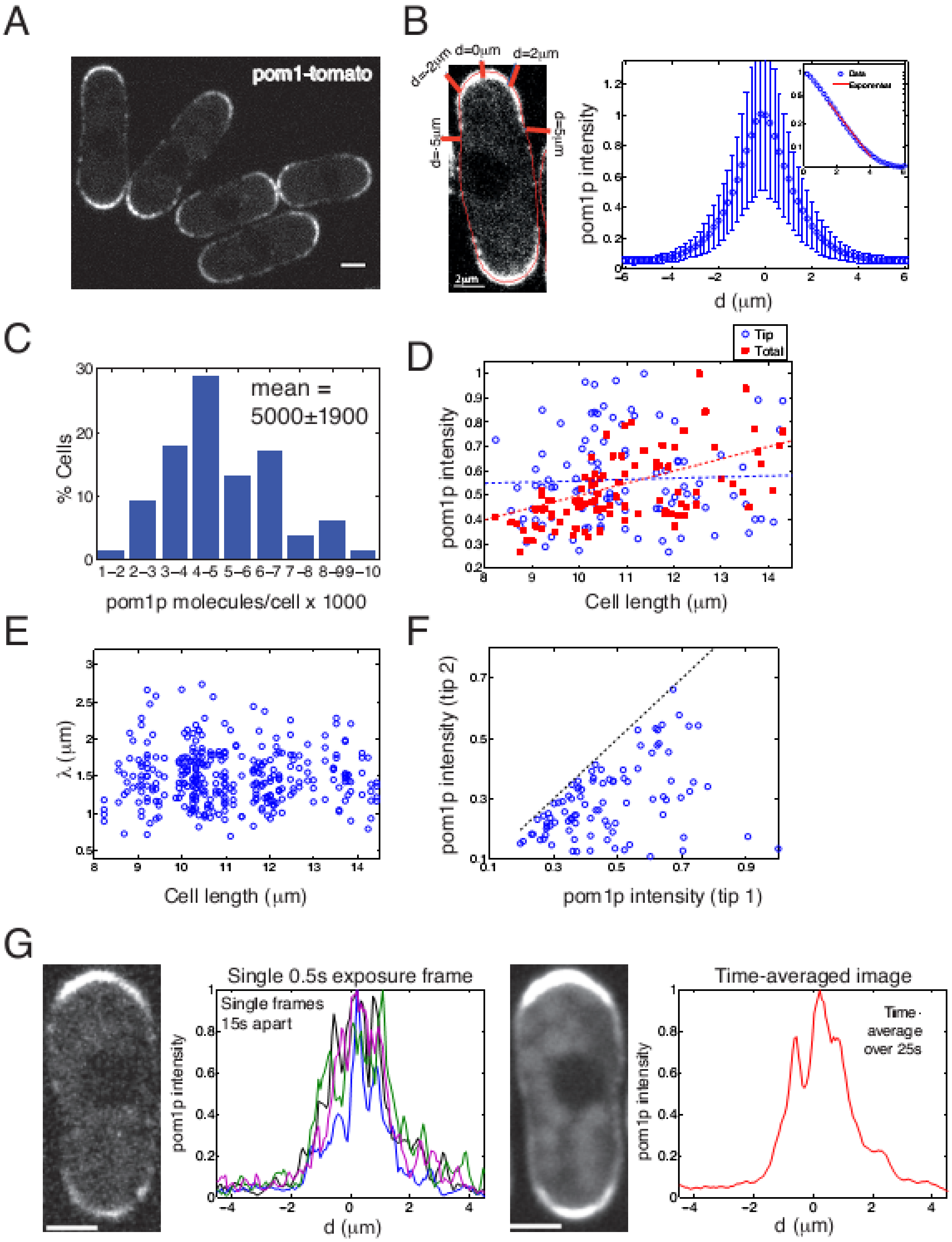
A
pom1-tomato
B
d=-2μm
d=0μm
d=2μm
d=-5μm
d=5μm
2μm
pom1p intensity
d (μm)
Data
Exponential
C
mean =
5000±1900
% Cells
pom1p molecules/cell x 1000
1–2
2–3
3–4
4–5
5–6
6–7
7–8
8–9
9–10
D
Tip
Total
pom1p intensity
Cell length (μm)
E
λ (μm)
Cell length (μm)
F
pom1p intensity (tip 2)
pom1p intensity (tip 1)
G
Single 0.5s exposure frame
Single frames
15s apart
pom1p intensity
d (μm)
Time-averaged image
Time-
average
over 25s
pom1p intensity
d (μm)

Figure 2.1 Pom1p forms a dynamic and noisy gradient along the cell cortex

A. Confocal image of wildtype cells expressing pom1-tomato in a medial focal plane. Scale bar = 2 μm.
B. Left: Measuring cortical intensities. A cortical mask (red) superimposed on a cell is used for measuring cortical intensities. *d* is defined as the distance along the cortex from the center of a cell tip. Right: Mean pom1-tomato intensity profile. Mean pom1p intensities are derived from 196 profiles from 98 cells, with each profile obtained from time lapse images acquired over 90 s. Mean maximal intensity normalized to unity. Error bars are standard deviation. Inset: Same profile but on logarithmic intensity scale. Red line is a fit to an exponentially decay curve. (Analysis by Tim Saunders)
C. Distribution of total number of pom1-GFP molecules per cell (number of cells analyzed=82), estimated from fluorescence intensities (see Supplemental Methods).
D. Pom1p intensity is variable; total, but not tip-region, levels correlate with cell length. Using medial slice, summed pom1-tomato intensities in cortical tip region (from tip to d=±1 μm; blue circles) and from the whole cell including cytoplasm (red squares) are plotted against cell length (n=98 for both). Each data set is normalized to maximum value independently. Data for each point is from images acquired over 90 s. For cell of length L, best fit for normalized total intensity = 0.05L, with $r^2 = 0.32$ (dotted red line). Best linear fit for normalized tip intensity = 0.51 + 0.005L, with $r^2 = 0.002$ (dotted blue line). (Analysis by Tim Saunders)
E. The decay length of the gradients does not correlate with cell length. Decay length λ was derived by fitting individual pom1p profiles imaged over 90 s to an exponential decay function. Fitted profiles with $r^2<0.9$ excluded, giving n=161 from 98 cells. (Analysis by Tim Saunders)
F. Comparison of pom1p cortical cell tip region intensities (from tip to d=±1 μm) on the two cell tips in the same cell (n=98). The dashed line corresponds to equal tip intensities. (Analysis by Tim Saunders)
G. Time averaging can significantly decrease the effects of dynamic pom1p fluctuations. Left: single 0.5 s exposure of cell expressing pom1-tomato. Adjacent graph shows four separately normalized pom1p cortical intensity profiles from 0.5 s exposures taken 15 s apart in same cell. Right: Summed time-lapse images of the same cell taken with overall 25 s exposure time. Adjacent graph shows corresponding normalized pom1p intensity profile. Scale bar: 2 μm. See also Figure S1. (Analysis By Tim Saunders)

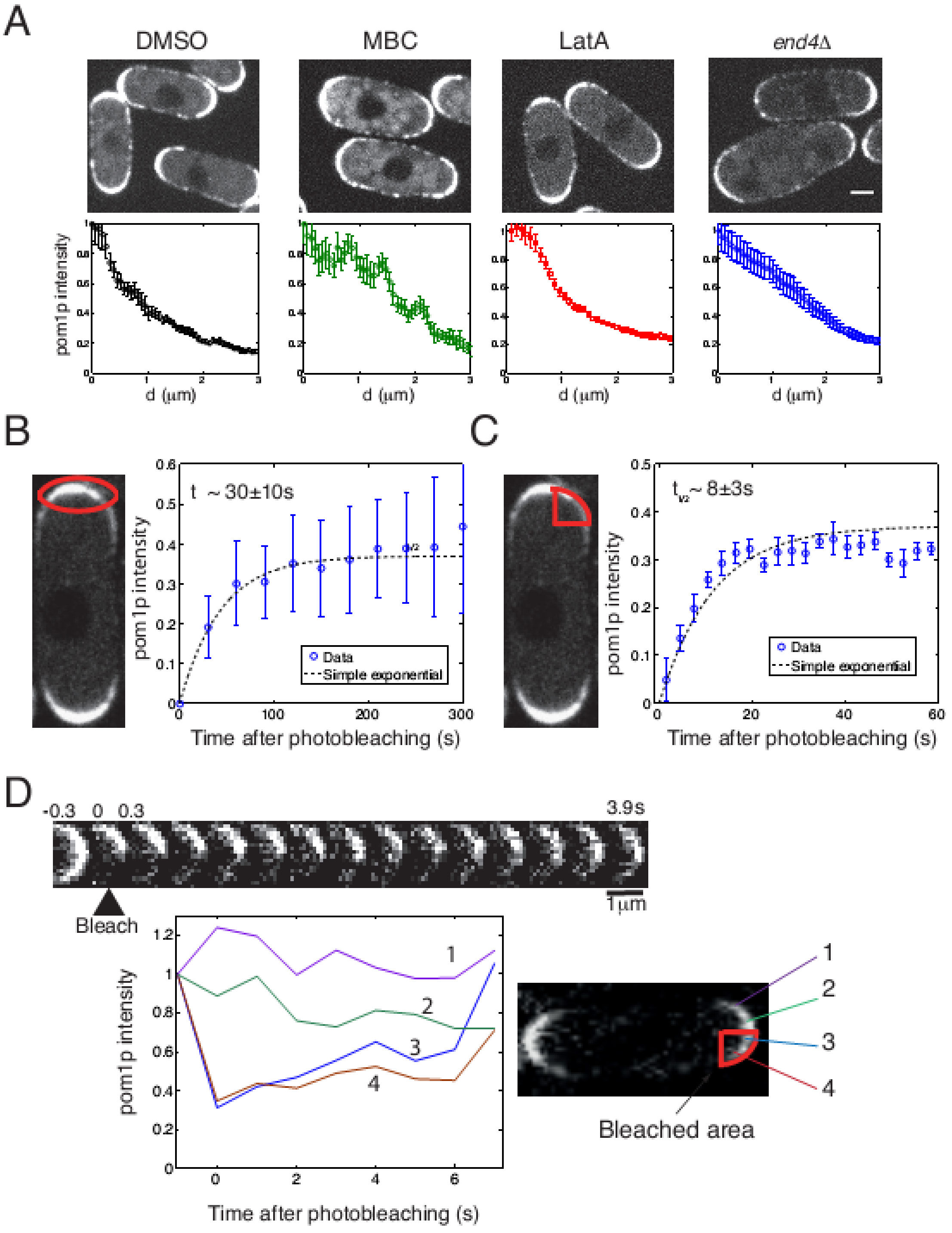
A
DMSO
MBC
LatA
end4Δ
pom1p intensity
d (µm)
B
t ~30±10s
Data
Simple exponential
pom1p intensity
Time after photobleaching (s)
C
$t_{1/2}$ ~ 8±3s
Data
Simple exponential
pom1p intensity
Time after photobleaching (s)
D
-0.3
0
0.3
3.9s
Bleach
1µm
pom1p intensity
Time after photobleaching (s)
1
2
3
4
Bleached area

Figure 2.2 The pom1p gradient could be formed by diffusion

A. Pom1-tomato was imaged in cells treated with 25 μg/ml MBC (a microtubule inhibitor), 200 μM Latrunculin A (F-actin inhibitor), or DMSO (control), and in an *end4Δ* cell (endocytosis mutant). Graphs show mean cortical intensity profiles, with maximum normalized to unity, as function of distance *d* (data from 16 profiles for each condition, each imaged over 25 s); error bars: standard error of mean. Scale bar = 2 μm. (Analysis By Tim Saunders)

B. Whole-tip region FRAP of pom1-tomato. Left: photo-bleached area is outlined. Right: Graph shows recovery of mean tip-region fluorescence intensity in 13 cells over time. Blue circles are experimental data, and dashed black line is a fit to $c_0(1-(1/2)^{t/\tau})$, with $\tau = 30$ s. Error bars are standard deviation.

C. Half-tip region FRAP of pom1-tomato. Left: photo-bleached area is outlined. Right: Graph shows recovery of mean half-tip region fluorescence intensity in 14 cells. Blue circles are experimental data, and dashed black line is fit to $c_1(1-(1/2)^{t/\tau})$, with $\tau = 8$ s. Error bars are standard deviation.

D. Movement of pom1p on cell surface contributes to fluorescence recovery. Pom1-tomato on half a cell tip was photo-bleached at 0 s. Images every 0.3 s are shown. Graph shows pom1p intensity changes at different positions in the tip region. Note that the fluorescence in region 3 recovers faster than that in region 4, and conversely, fluorescence in region 2 loses intensity faster than region 1. See also Figure S2.

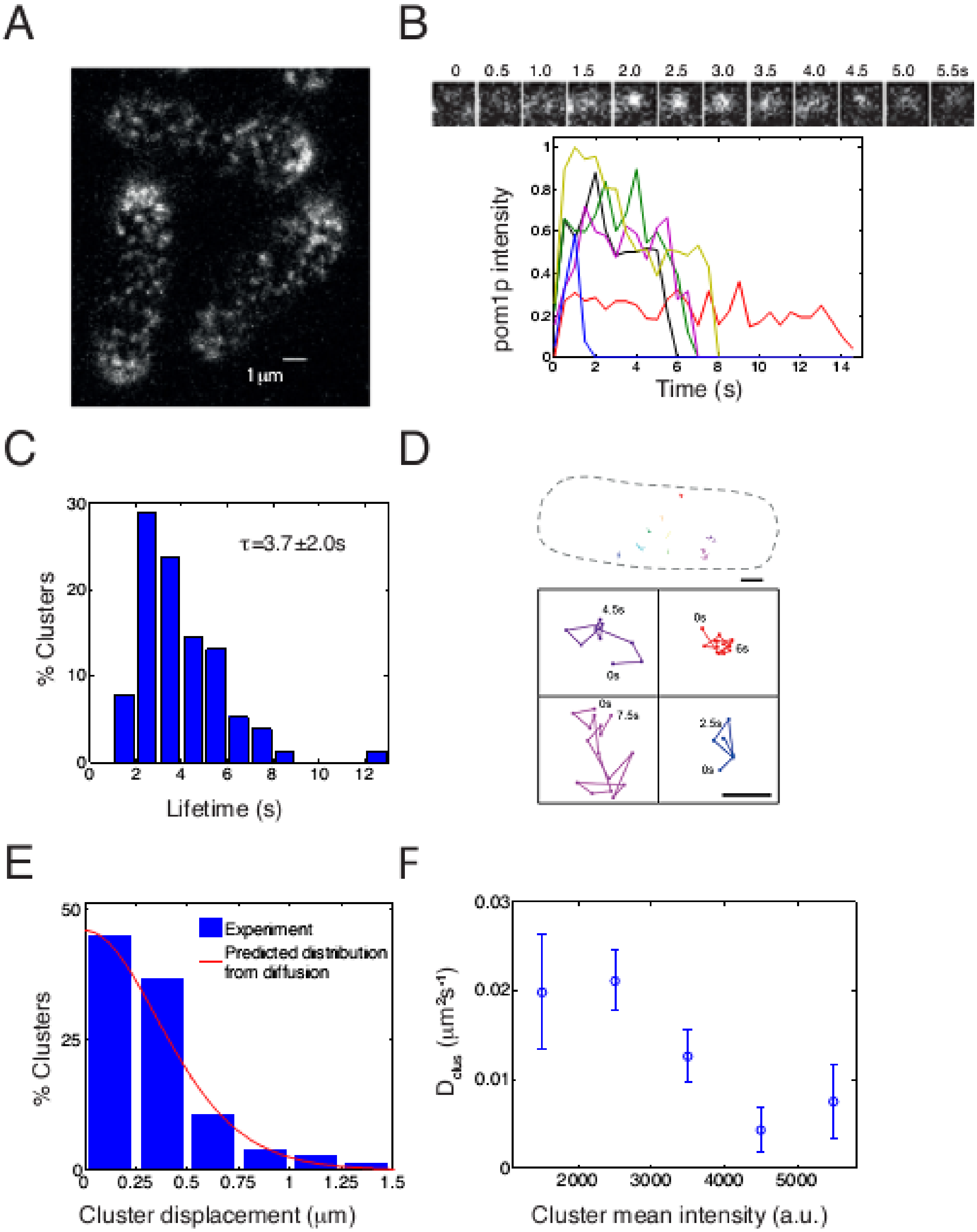
A
1 μm
B
0
0.5
1.0
1.5
2.0
2.5
3.0
3.5
4.0
4.5
5.0
5.5s
pom1p intensity
Time (s)
0
0.2
0.4
0.6
0.8
1
2
4
6
8
10
12
14
C
τ=3.7±2.0s
% Clusters
Lifetime (s)
0
10
20
30
2
4
6
8
10
12
D
4.5s
0s
0s
6s
0s
7.5s
2.5s
0s
E
Experiment
Predicted distribution from diffusion
% Clusters
Cluster displacement (μm)
0
25
50
0.25
0.5
0.75
1
1.25
1.5
F
D$_{clus}$ (μm^{2}s^{-1})
Cluster mean intensity (a.u.)
0
0.01
0.02
0.03
2000
3000
4000
5000

Figure 2.3 Pom1p forms dynamic clusters on the plasma membrane.

A. Confocal image of a cortical section along top of a cell expressing pom1-tomato (0.5 s exposure).
B. Time-lapse images showing the behavior of a single pom1p cluster. Graph shows intensity tracings over time of representative clusters (normalized by maximum intensity value measured).
C. Distribution of individual cluster lifetimes (198 clusters analyzed from 7 cells). (Analysis By Tim Saunders)
D. Tracks of cluster movements. Top: Outline of cell with 9 cluster tracks shown. Scale bar =1 μm Bottom: Magnified view of tracks. Times mark start and finish of each track in seconds. Scale bar =0.25 μm
E. Histogram of cluster displacements (198 clusters tracked from 7 cells). Red line: predicted distribution of cluster displacements from simple diffusion (see Supplemental Information). (Analysis By Tim Saunders)
F. Estimated diffusion constant (extracted from overall mean square displacement) from clusters with different average intensities (116 clusters analyzed from 6 cells), showing that brighter clusters diffuse more slowly. Error bars: standard error of mean. See also Figure S3. (Analysis By Tim Saunders)

A

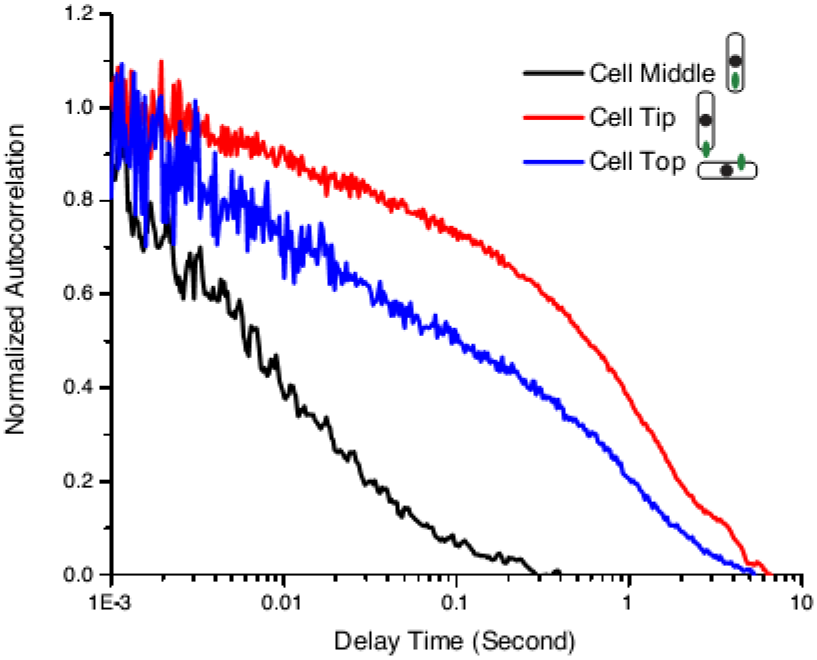

B

Species	Diffusion Time (s)	Diffusion Constant ($\mu m^2 s^{-1}$)	Location	WT	*tea1Δ*	*tea4Δ*
S1	0.011	1.5	Cytoplasm	+	+	+
S2	0.65	0.026	Membrane	+	+/-	-
S3	2.85	0.006	Membrane	+	+/-	-

Figure 2.4 Fluorescence correlation spectroscopy analysis reveals multiple species

(Experiments by Yinghua Guan, Jagesh Shah and myself , analysis by Yinghua Guan and Jagesh Shah)

A. Autocorrelation curves of pom1-GFP. FCS measurements were made at multiple sites within wild-type cells. Each curve represents the average of six measurements in one cell. Measurements in the cell interior show rapid decay of the autocorrelation function, which can be fit to a three-dimensional diffusion model, with a cytoplasmic pom1p diffusion coefficient D_1=1.5 $\mu m^2 s^{-1}$ (Species S1). Measurements at the cell surface show slower decay in the autocorrelation function corresponding to increased residence time in the FCS volume. These results reveal the presence of membrane-associated species whose relative abundance changes as the probe is moved towards a cell tip.

B. Summary of pom1-GFP species detected by FCS. See also Figure S4.

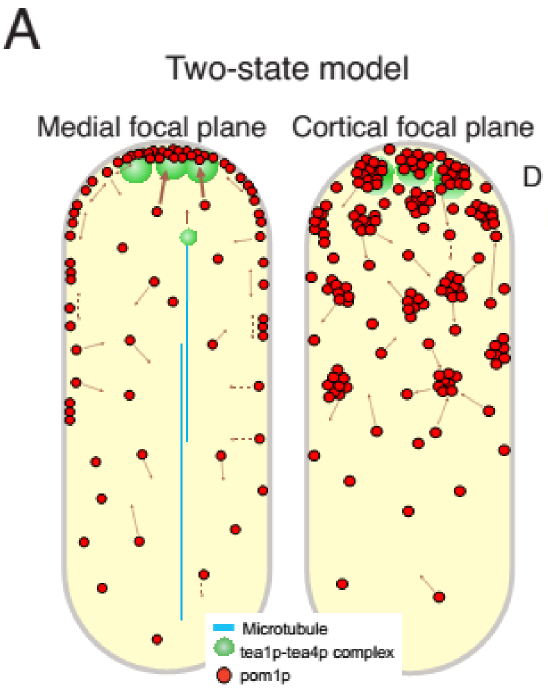

Association: $\emptyset \overset{\epsilon J f(d/\sigma)}{\rightarrow} [SLOW]$; $\emptyset \overset{(1-\epsilon) J f(d/\sigma)}{\rightarrow} [FAST]$

Interaction: $[SLOW] \overset{\alpha}{\rightarrow} [FAST]$;

$[SLOW] + [FAST] \overset{\beta}{\rightarrow} [SLOW] + [SLOW]$

Disassociation: $[FAST] \overset{\mu}{\rightarrow} \emptyset$

Equations:
$$\begin{aligned}\partial_t[SLOW] =& D_s\nabla^2[SLOW] - \alpha[SLOW] \\ &+ \beta[SLOW][FAST] + \epsilon J f(d/\sigma)\end{aligned}$$
$$\begin{aligned}\partial_t[FAST] =& D_f\nabla^2[FAST] + \alpha[SLOW] \\ &- \beta[SLOW][FAST] - \mu[FAST] + (1-\epsilon) J f(d/\sigma)\end{aligned}$$

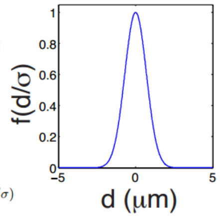

Parameter	Symbol	Value	Evidence
Pom1p membrane association	J	$12\mu m^{-2}s^{-1}$	Total pom1p molecule number
Diffusion constant of slow state	D_s	$0.02\mu m^2 s^{-1}$	Cluster tracking and FCS
Diffusion constant of fast state	D_f	$0.2\mu m^2 s^{-1}$	Mean pom1p profile
Disassociation rate	μ	$0.035 s^{-1}$	Full-tip FRAP
Fragmentation rate of slow state	α	$0.26 s^{-1}$	Cluster lifetime
Aggregation constant	β	$0.006\mu m^2 s^{-1}$	Fraction of high intensity pom1p clusters
Width of pom1p association region	σ	$0.75\mu m$	Width of tea1p intensity profile
Fraction of pom1p associating in slow state	ϵ	0.7	Fraction of high intensity pom1p clusters
Cell radius	R	$1.75\mu m$	Direct measurement

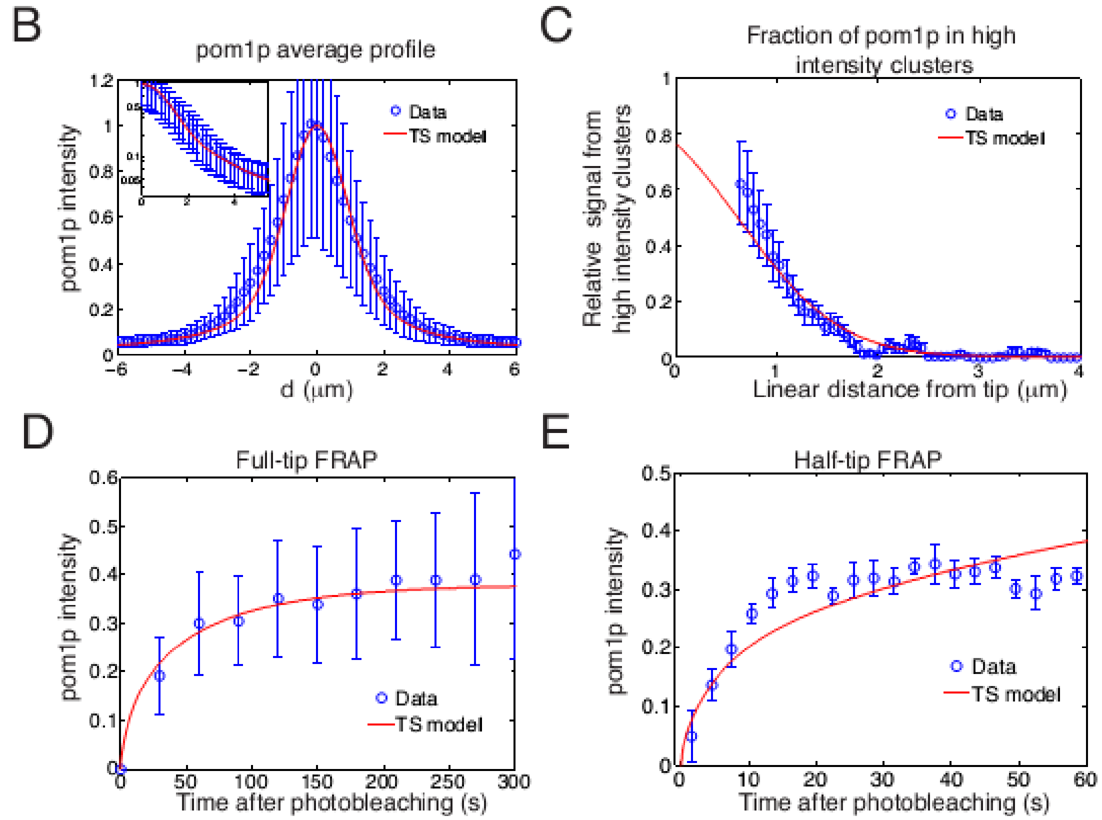

Figure 2.5 Two state mathematical model of pom1p gradient formation

(Analysis and some imaging By Tim Saunders)

A. Pictorial summary of the two-state (TS) model of pom1p gradient formation. Also shown are the TS model reactions, equations, parameter values (together with the experiments from which the values were extracted) and the Gaussian form of the membrane association function f.
B. Fit of TS model to normalized mean pom1p intensity profile (experimental data from Figure 1B). Inset: same profile but on logarithmic intensity scale.
C. Contribution of pom1p clusters to the total cortical pom1p intensity as a function of linear distance from tip (see Supplemental Information). Data from 9 profiles from 9 cells. Red profile is fit from TS model.
D. Full-tip FRAP recovery data (as in Figure 2B) but with fit from TS model (red line).
E. Half-tip FRAP recovery data (as in Figure 2C) but with fit from 1d TS model (red line), see Supplemental Information. See also Figure S5.

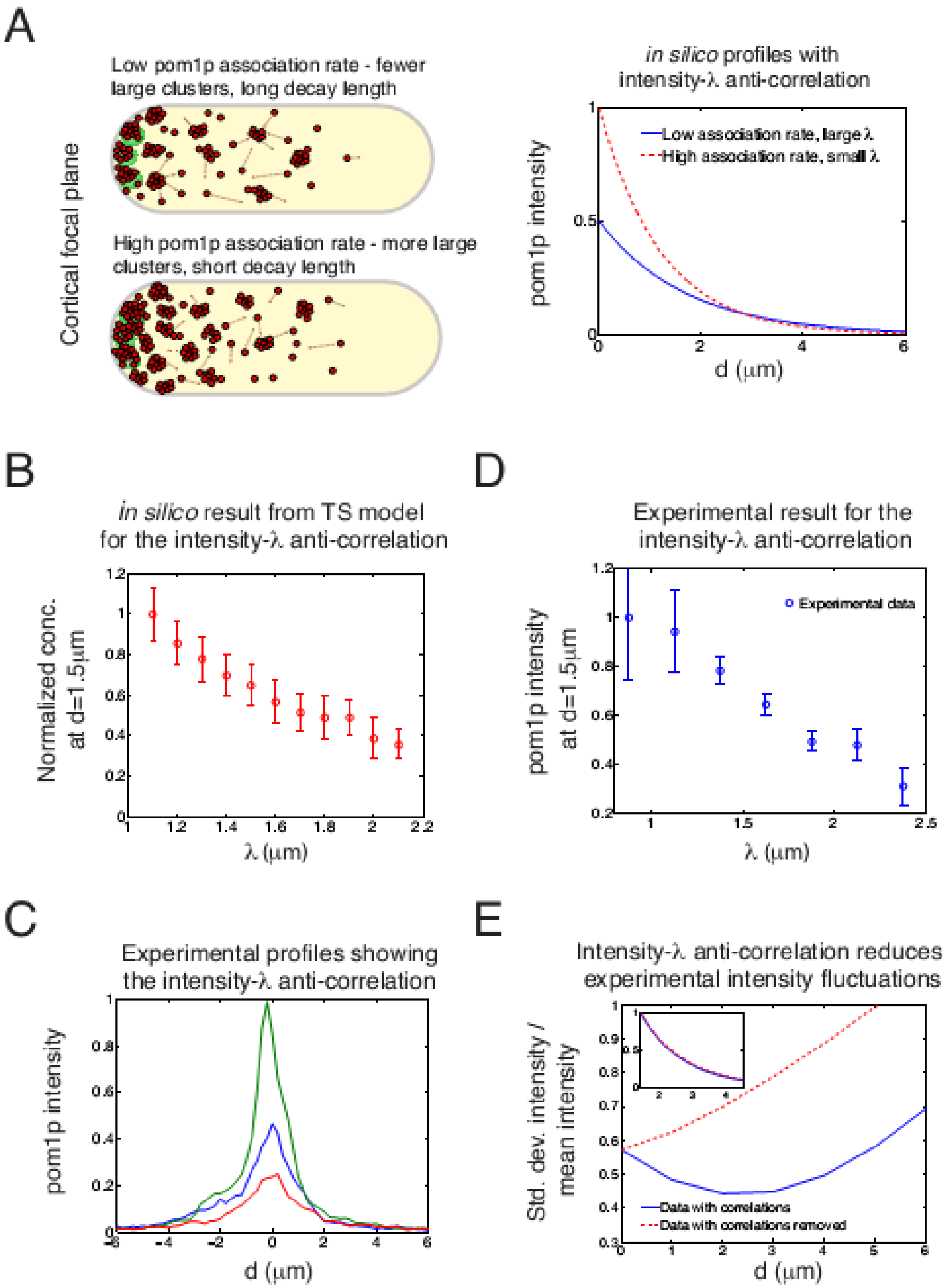
A
Low pom1p association rate - fewer large clusters, long decay length
High pom1p association rate - more large clusters, short decay length
Cortical focal plane
in silico profiles with intensity-λ anti-correlation
Low association rate, large λ
High association rate, small λ
pom1p intensity
d (μm)
0
0.5
1
0
2
4
6
B
in silico result from TS model for the intensity-λ anti-correlation
Normalized conc. at d=1.5μm
λ (μm)
0
0.2
0.4
0.6
0.8
1
1.2
1
1.2
1.4
1.6
1.8
2
2.2
D
Experimental result for the intensity-λ anti-correlation
Experimental data
pom1p intensity at d=1.5μm
λ (μm)
0.2
0.4
0.6
0.8
1
1.2
1
1.5
2
2.5
C
Experimental profiles showing the intensity-λ anti-correlation
pom1p intensity
d (μm)
0
0.2
0.4
0.6
0.8
1
-6
-4
-2
0
2
4
6
E
Intensity-λ anti-correlation reduces experimental intensity fluctuations
Std. dev. intensity / mean intensity
d (μm)
Data with correlations
Data with correlations removed
0.3
0.4
0.5
0.6
0.7
0.8
0.9
1
0
1
2
3
4
5
6
0
0.5
1
2
3
4

Figure 2.6 The two state (TS) model buffers against cell-to-cell variations

(Analysis By Tim Saunders)

A. The TS model predicts that gradients with higher membrane association will have a steeper decay. Left: schematic picture of how I_a-λ anti-correlation is generated through cluster dynamics. Right: Demonstration of the effects of this anti-correlation on gradient profiles. Two *in silico* exponential profiles, with I_a=0.5 and λ=1.7 µm (blue) and I_a=1 and λ=1.2 µm (dashed red).

B. TS model anti-correlation between pom1p peak concentrations and *λ* (red circles) from 100 simulated profiles. Shown are effects of fluctuations in pom1p association (relative standard deviation 20%) and diffusion, aggregation, fragmentation, disassociation (all with relative standard deviation 10%). Pom1p concentration normalized to unity at smallest value of *λ*. Error bars: standard deviation.

C. In vivo pom1p profiles exhibit I_a-λ anti-correlation. Three representative profiles with different pom1p peak intensities (imaged over 90 s) are shown. Pom1p intensity is normalized to the highest peak. Note decay length of the gradient changes with these different peak intensities.

D. Experimentally measured anti-correlation between fitted values of I_a and λ (profiles used in fitting were time-averaged for 90 s). Error bars: standard deviation. Fitted profiles with $r^2<0.9$ were excluded, giving 90 profiles analyzed from 90 cells.

E. Standard deviation in pom1p intensity divided by mean intensity*,* as derived from experimentally measured I_a and λ from 90 fitted profiles from 90 cells (blue line), compared to case where each I_a is paired with a randomly chosen *λ* (red dashed line). Inset: normalized mean pom1p profile unchanged between two data sets. See also Figure S6.

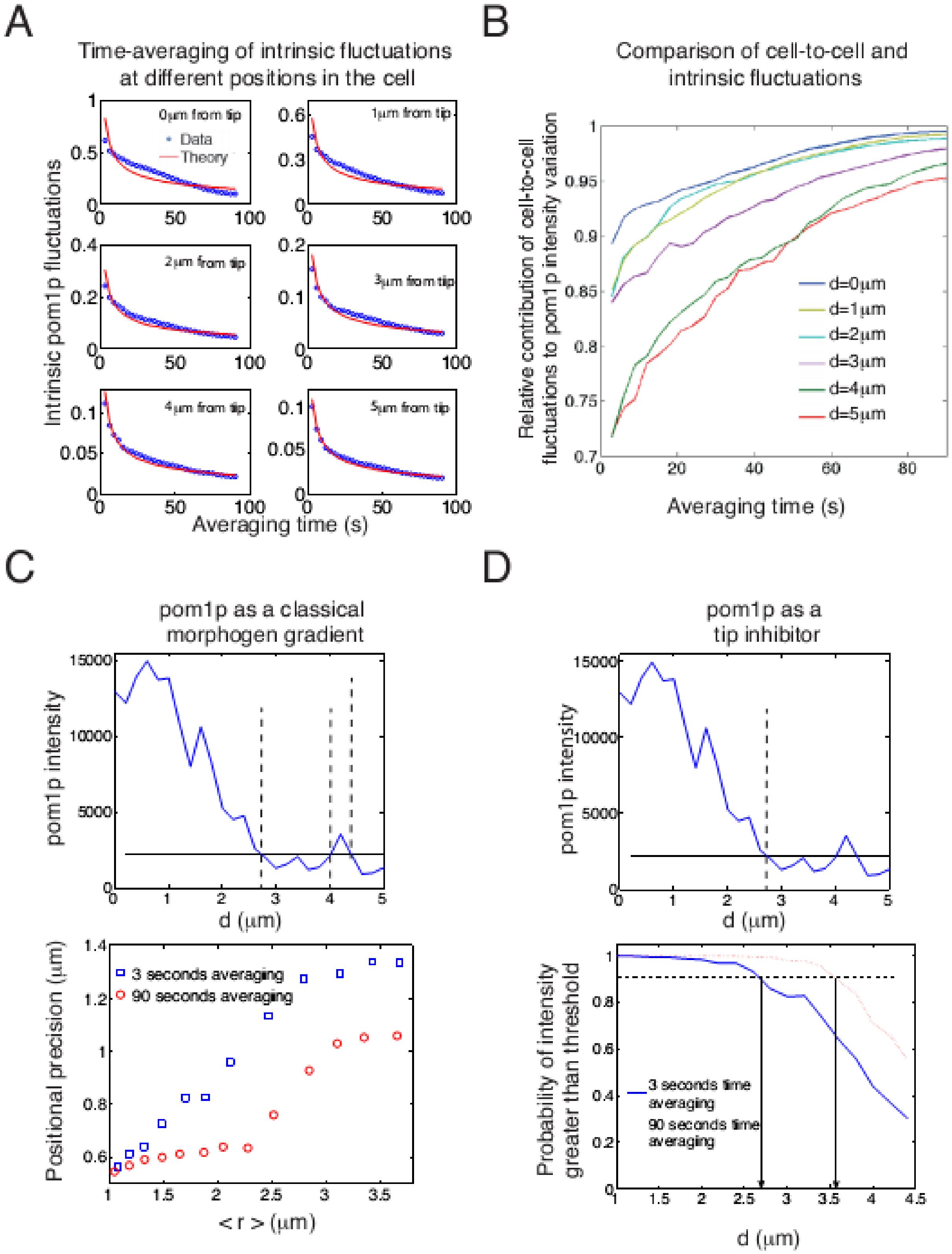
A
Time-averaging of intrinsic fluctuations at different positions in the cell
Intrinsic pom1p fluctuations
0μm from tip
Data
Theory
1μm from tip
2μm from tip
3μm from tip
4μm from tip
5μm from tip
Averaging time (s)
B
Comparison of cell-to-cell and intrinsic fluctuations
Relative contribution of cell-to-cell fluctuations to pom1p intensity variation
d=0μm
d=1μm
d=2μm
d=3μm
d=4μm
d=5μm
Averaging time (s)
C
pom1p as a classical morphogen gradient
pom1p intensity
d (μm)
Positional precision (μm)
3 seconds averaging
90 seconds averaging
< r > (μm)
D
pom1p as a tip inhibitor
pom1p intensity
d (μm)
Probability of intensity greater than threshold
3 seconds time averaging
90 seconds time averaging
d (μm)

Figure 2.7 Effects of noise on the overall positional precision of the pom1p gradient
(Analysis By Tim Saunders)

A. Standard deviation in pom1p intensity due to intrinsic fluctuations (arbitrary units) as function of averaging time at different positions along the gradient (196 gradients analyzed from 98 cells). Red curves are fit from time-averaging theory (see Supplemental Information).
B. Relative contribution of cell-to-cell fluctuations to total observed variation in pom1p intensity as a function of averaging time (196 gradients analyzed from 98 cells). Lines correspond to different distances *d* away from a tip.
C. Top: An example of a noisy pom1p intensity profile acting as a morphogen-like gradient. With little time-averaging, at a given threshold intensity (set here at 2250 in arbitrary intensity units, solid line), a noisy gradient determines position of a boundary (dashed lines; mean threshold intercept position at 3.5 μm). Bottom: Effect of time-averaging for 3 s (blue) and 90 s (red) on positional precision (standard deviation of threshold intercept positions) of the gradient for different thresholds, and therefore different mean intercept positions <r> (188 gradients analyzed from 94 cells).
D. Top: An example showing how pom1p might act as a tip-excluder with a minimum threshold intensity (solid line). Bottom: effect of time averaging on the probability of being able to distinguish cortical pom1p intensity from cytoplasmic pom1p intensity as a function of distance *d* (188 gradients analyzed from 94 cells). See also Figure S7.

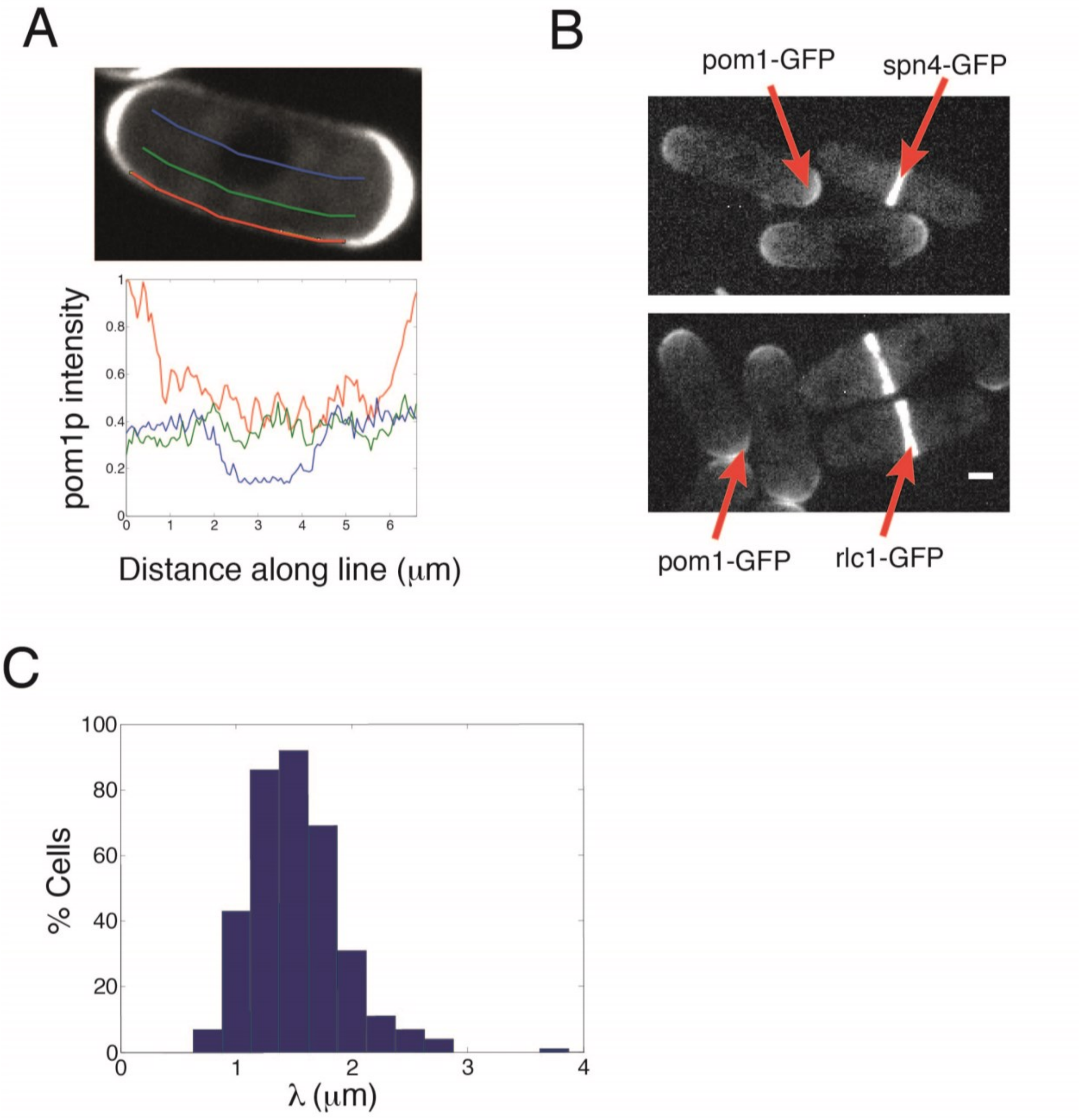
A
pom1p intensity
0
0.2
0.4
0.6
0.8
1
0
1
2
3
4
5
6
Distance along line (μm)
B
pom1-GFP
spn4-GFP
pom1-GFP
rlc1-GFP
C
% Cells
0
20
40
60
80
100
0
1
2
3
4
λ (μm)

Figure S2.1 Pom1p forms a cortical gradient

A. Top. Wildtype cell expressing pom1-tomato was imaged in a single focal plane using a spinning disc confocal microscope. Image shows a projection of images acquired over 90s. Bottom. Intensity profiles along the cortex (red), cell interior (green), and cell interior including the nucleus (blue) (intensities normalized by maximum value on the cortex). The profiles correspond to those along the colored lines in the top frame. These data show that pom1p is in a gradient distribution on the cortex, but not in the cytoplasm.

B. To estimate the number of pom1p molecules in the whole cell, we compared pom1-GFP fluorescence to that of rlc1-GFP and spn4-GFP. Images of pom1-GFP, spn4-GFP, and rlc1-GFP cells taken with same exposures. Scale bar is 2μm.

C. Quantitation of gradient profiles. Distribution of measured λ values from fitting pom1p intensity profiles in individual cells with exponentially-decaying profiles. We exclude fits with $r^2 < 0.9$, giving 161 profiles analyzed from 98 cells. (Analysis done by Tim Saunders)

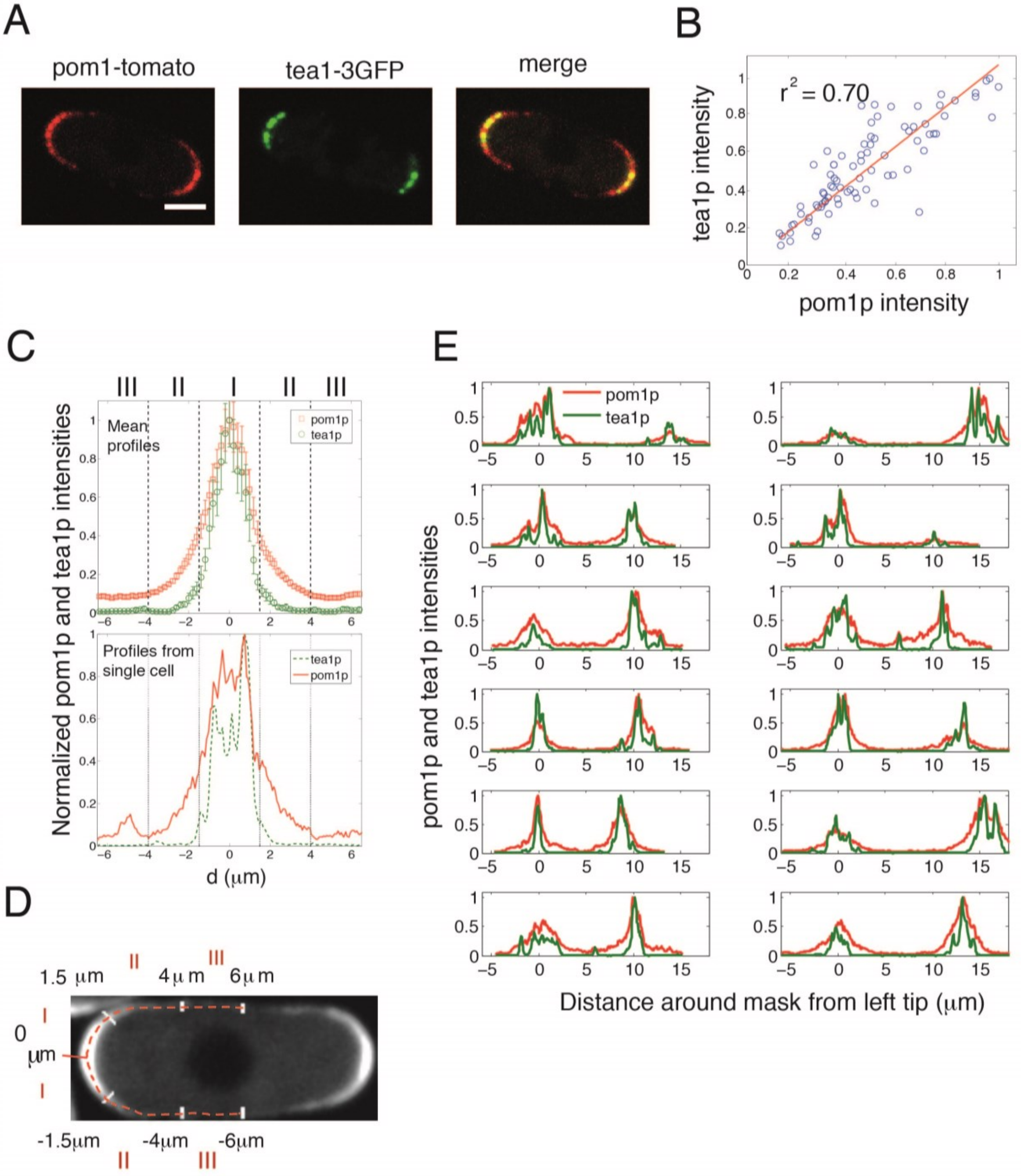
A
pom1-tomato
tea1-3GFP
merge
B
r² = 0.70
tea1p intensity
pom1p intensity
C
III
II
I
II
III
Mean profiles
pom1p
tea1p
Profiles from single cell
tea1p
pom1p
Normalized pom1p and tea1p intensities
d (μm)
D
1.5 μm
4 μm
6 μm
0 μm
-1.5μm
-4μm
-6μm
I
II
III
E
pom1p
tea1p
pom1p and tea1p intensities
Distance around mask from left tip (μm)

Figure S2.2 Role of tea1p in forming the pom1p gradient

A. Image of a cell expressing pom1-tomato and tea1-3GFP. Scale bar is 2 µm.
B. Pixel by pixel comparison of maximum pom1p and tea1p intensities at each tip (data from 90s imaging, of 82 tips from 41 cells, with intensities normalized by largest value in each data set). Straight line is a least squares fit, constrained to pass through the origin. (Analysis done by Tim Saunders)
C. Top: Mean intensity profiles of pom1-tomato (red) and tea1-3GFP (green) (data from 36 cell tip regions, each imaged over 90s). Mean maximal intensity separately normalized to unity for each protein profile). Error bars are standard deviations. I, II, and III denote regions in the gradient, as described in Supplementary text. Bottom: Normalized profiles from a single representative cell tip (imaged over 90 s). (Analysis done by Tim Saunders)
D. Extent of regions defined in (**C**) overlaid on a pom1-tomato cell image.
E. Additional examples, similar to (**C**), of normalized pom1p and tea1p spatial profiles in individual cells (profiles obtained from imaging over 90s).

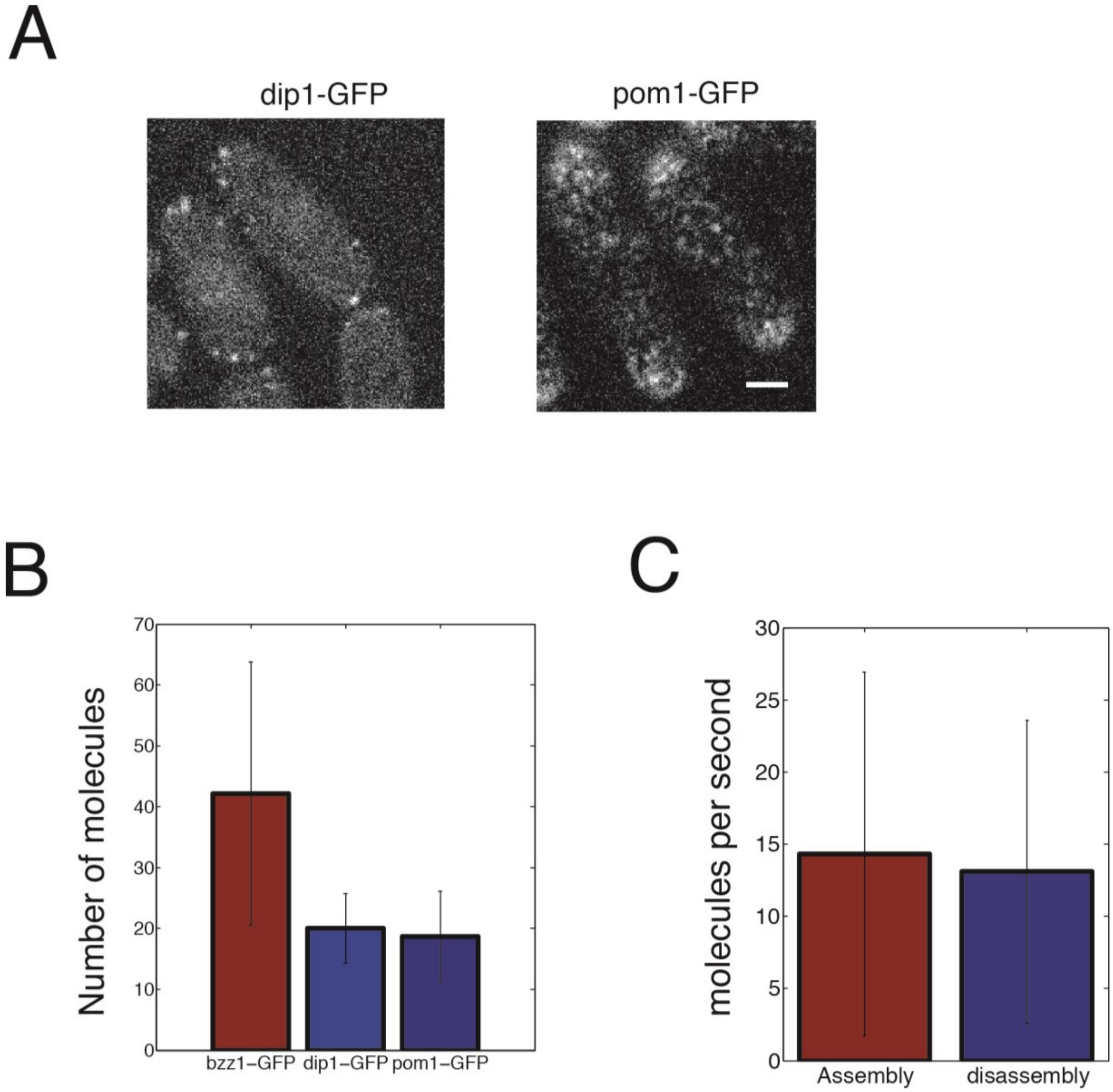
A
dip1-GFP
pom1-GFP
B
Number of molecules
0
10
20
30
40
50
60
70
bzz1−GFP
dip1−GFP
pom1−GFP
C
molecules per second
0
5
10
15
20
25
30
Assembly
disassembly

Figure S2.3 Quantifying the number of pom1p molecules in a cluster

A. To estimate the number of pom1p molecules in a cluster, we compared cluster fluorescence to that of dip1-GFP and the actin patch marker bzz1-GFP. Images of pom1-GFP and dip1-GFP cells taken with same exposures. Scale bar is 2µm.
B. Average number of molecules per cluster of pom1p and dip1p endocytic patches as calculated from intensities. These are normalized using the assumption that each dip1 patch represents 20 molecules. Error bars are standard deviations. n = 50 clusters/patches.
C. Average rate of pom1p cluster assembly and disassembly. Error bars are standard deviations. n = 15 clusters.

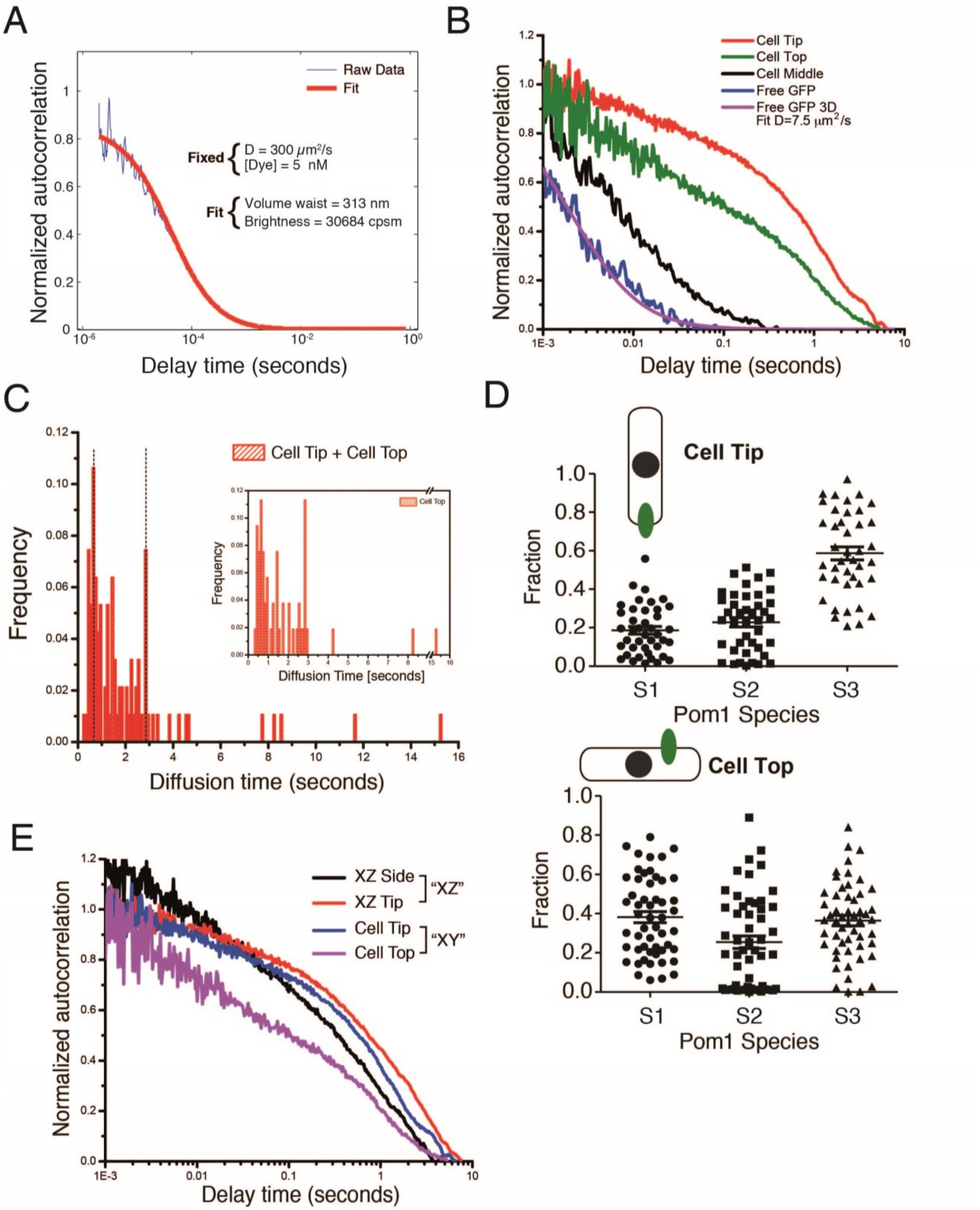
A
Normalized autocorrelation
Delay time (seconds)
Raw Data
Fit
Fixed
D = 300 μm²/s
[Dye] = 5 nM
Fit
Volume waist = 313 nm
Brightness = 30684 cpsm
B
Cell Tip
Cell Top
Cell Middle
Free GFP
Free GFP 3D Fit D=7.5 μm²/s
Normalized autocorrelation
Delay time (seconds)
C
Cell Tip + Cell Top
Frequency
Diffusion time (seconds)
Cell Top
Frequency
Diffusion Time [seconds]
D
Cell Tip
Fraction
S1
S2
S3
Pom1 Species
Cell Top
Fraction
S1
S2
S3
Pom1 Species
E
XZ Side
XZ Tip
"XZ"
Cell Tip
Cell Top
"XY"
Normalized autocorrelation
Delay time (seconds)

Figure S2.4 FCS analysis

(Experiment and analysis done by Yinghua Guan and Jagesh Shah)

A. Calibration curve for FCS volume. Fluorescein dye in PBS was prepared to 5 nM and an autocorrelation curve measured. Given the fixed concentration and known diffusion constant (300 $\mu m^2 s^{-1}$), a beam waist of 313 nm was calculated. In addition, the molecular brightness of the dye was also calculated to be 30,684 counts/sec/molecule.

B. FCS curves for free cellular GFP compared with pom1 curves (as shown in Figure 4A). Fission yeast cells expressing untagged GFP were placed in the vertical position and cellular measurements of GFP diffusion obtained. GFP diffusion is plotted alongside the average of the cytoplasmic, cell tip and cell top FCS curves. Free GFP diffuses much faster than cytoplasmic pom1. Fitting to a 3D diffusion model yields a diffusion constant of 7.5 $\mu m^2 s^{-1}$.

C. FCS measurements performed at the cell tip and the cell top positions were fit for one cytoplasmic component (D_1 = 1.5 $\mu m^2 s^{-1}$) and one membrane component (free D_2). A histogram of diffusion times ($\tau_D = \omega_{xy}^2 / 8D$) fit to the membrane species resulted in two predominant species: one with τ_D = 0.65s and one with τ_D = 2.85s (vertical dashed lines). Inset shows histogram of diffusion times for cell top measurements only.

D. FCS autocorrelation curves were fit for three diffusion times and relative species abundance derived. Measurements at the cell tip demonstrated the predominance of the slowest moving membrane species (S3), whereas measurements at the cell top show a more even distribution between the three species.

E. Geometrical artifacts in FCS. Measurements made in alternative geometries result in distortion of the autocorrelation function. XZ measurements are made by placing cells horizontally under the coverslip and positioning the excitation volume either at the tip (XZ Tip) or side (XZ Side) of the cell (side is halfway between cell tip and center). The change in autocorrelation function is most obvious in comparing the XZ Side and XY top. The observed difference is due to the change in membrane overlap, making the use of the standard membrane FCS equation inappropriate.

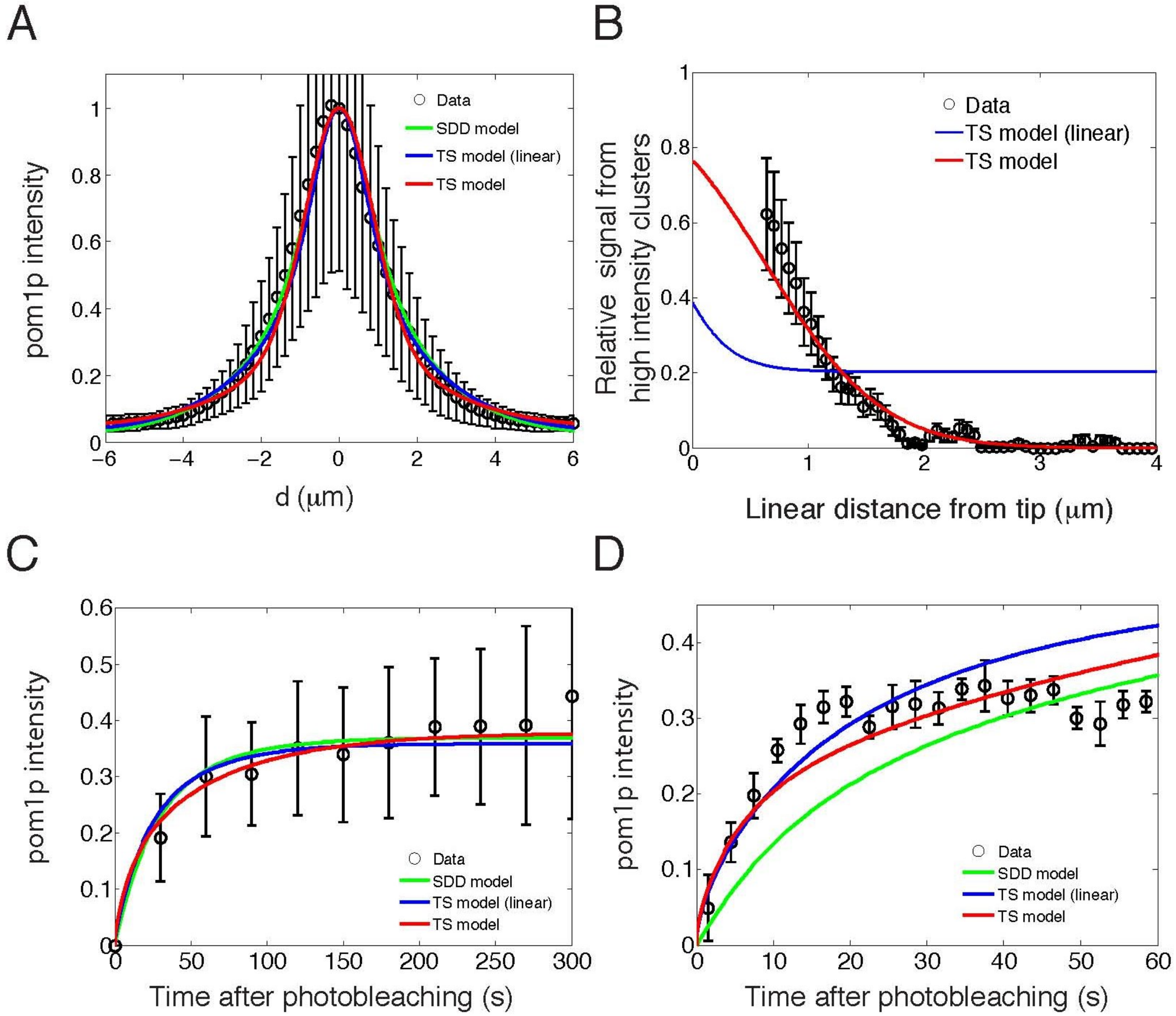
A
pom1p intensity
d (μm)
0
0.2
0.4
0.6
0.8
1
−6
−4
−2
0
2
4
6
Data
SDD model
TS model (linear)
TS model
B
Relative signal from high intensity clusters
Linear distance from tip (μm)
0
0.2
0.4
0.6
0.8
1
0
1
2
3
4
Data
TS model (linear)
TS model
C
pom1p intensity
Time after photobleaching (s)
0
0.1
0.2
0.3
0.4
0.5
0.6
0
50
100
150
200
250
300
Data
SDD model
TS model (linear)
TS model
D
pom1p intensity
Time after photobleaching (s)
0
0.1
0.2
0.3
0.4
0
10
20
30
40
50
60
Data
SDD model
TS model (linear)
TS model

Figure S2.5 Comparison of different models for pom1p gradient formation

(Analysis done by Tim Saunders)

A. Fit of TS model (both linear (blue curve) and non-linear (red curve) forms) and SDD model (green curve) to normalized mean pom1p intensity profile (experimental data from Figure 1B). See Supplementary Theoretical Analysis for description of each model.
B. Contribution of pom1p clusters to the total cortical pom1p intensity as a function of linear distance from tip. Data (black circles) from 9 profiles from 9 cells. Red (blue) curves correspond to the expected fraction of measured pom1p intensity due to clusters for the non-linear (linear) TS model (not plotted for SDD model, as SDD model does not have multiple states of pom1p).
C. Full-tip FRAP recovery data (as in Figure 2B) with fits from TS model (linear and non-linear forms) and SDD model (color scheme as in (**A**)).
D. Half-tip FRAP recovery data (as in Figure 2C) with fits from 1d TS model (linear and non-linear forms) and SDD model (color scheme as in (**A**)).

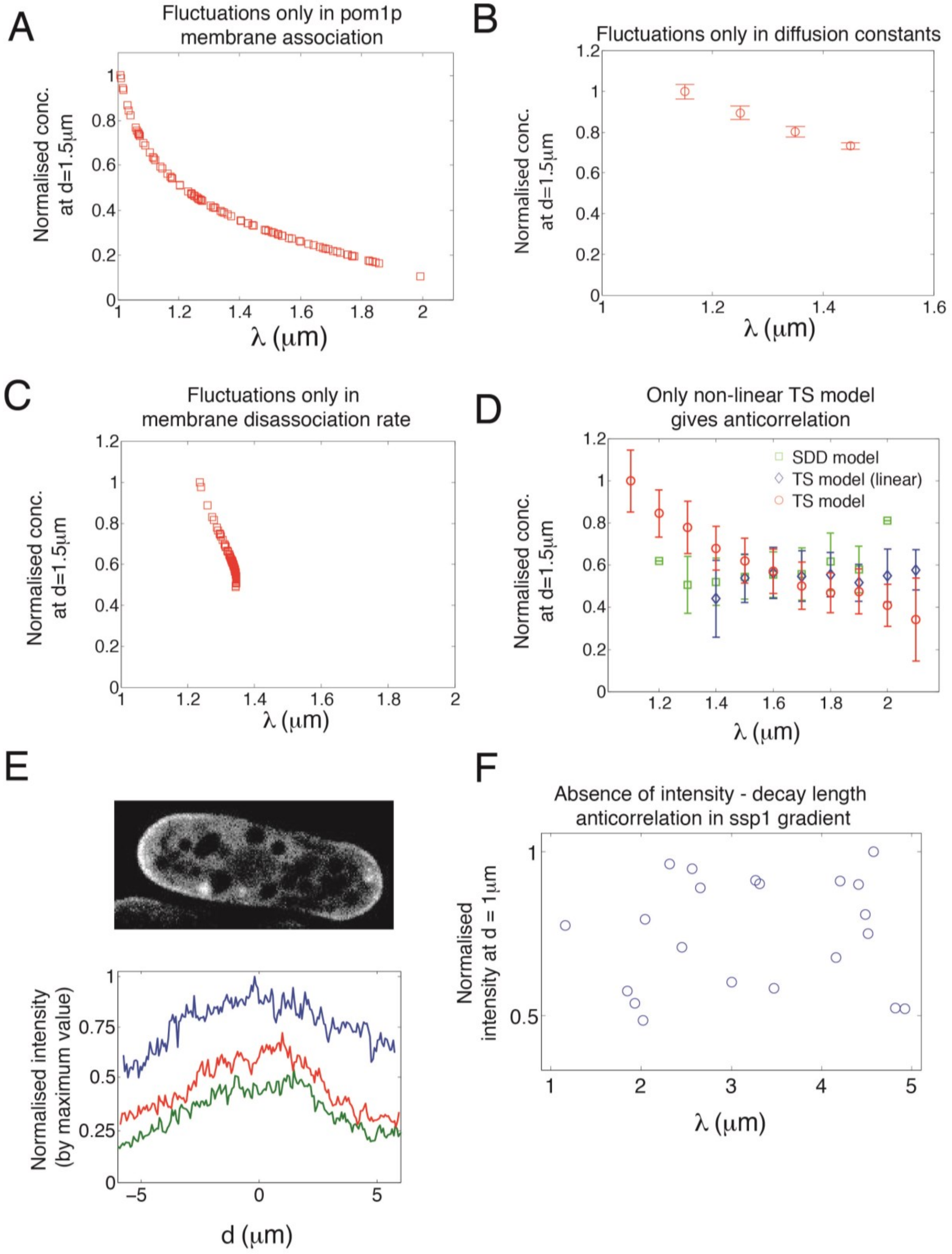
A
Fluctuations only in pom1p membrane association
Normalised conc. at d=1.5μm
λ (μm)
B
Fluctuations only in diffusion constants
Normalised conc. at d=1.5μm
λ (μm)
C
Fluctuations only in membrane disassociation rate
Normalised conc. at d=1.5μm
λ (μm)
D
Only non-linear TS model gives anticorrelation
SDD model
TS model (linear)
TS model
Normalised conc. at d=1.5μm
λ (μm)
E
Normalised intensity (by maximum value)
d (μm)
F
Absence of intensity - decay length anticorrelation in ssp1 gradient
Normalised intensity at d = 1μm
λ (μm)

Figure S6 Relationship between pom1p peak concentration and decay length of the gradient

A. Pom1p peak concentration-λ anti-correlation from 100 simulated profiles for TS model with 20% (standard deviation) relative fluctuations only in the association parameter, with other parameters remaining fixed. (Analysis done by Tim Saunders)
B. Pom1p peak concentration-λ anti-correlation from 100 simulated profiles for TS model with 10% (standard deviation) relative fluctuations only in the diffusion constants, with other parameters remaining fixed. Data has been binned according to λ, with bin width of 0.1 μm. Error bars are standard deviation of concentration values within each bin. (Analysis done by Tim Saunders)
C. Absence of significant pom1p peak concentration-λ anti-correlation from 100 simulated profiles for TS model with 10% (standard deviation) relative fluctuations in the membrane disassociation rate, with other parameters remaining fixed. (Analysis done by Tim Saunders)
D. Pom1p peak concentration-λ anti-correlation for the non-linear TS model (parameter variation described in main text) compared with the predicted results from the SDD and linear TS models. (Analysis done by Tim Saunders)
E. Characterization of an *S. pombe* cell tip gradient that does not exhibit clustering or intensity-decay length anti-correlation. Ssp1p is a protein kinase involved in regulation of cell polarity and actin (Rupes et al.,1999). Cells were transformed with a pIR2-22 plasmid expressing ssp1-GFP driven by an *nmt1* promoter, and expression was induced by incubating in minimal media without thiamine at 30^{o}C for 16h. Confocal image of representative interphase cell in the medial focal plane is shown. Lower panel shows three experimental gradient profiles at different levels of ssp1p intensities. Imaging at the cortical plane showed no clustering.
F. Absence of intensity-decay length anti-correlation from experimental ssp1-GFP gradients. Only ssp1-GFP profiles which were well fitted ($r^2 > 0.7$) by a.exp(-d/λ) + b and λ < 5 μm were included (n = 21). These data are consistent with a gradient constructed by an SDD mechanism with large variations in J, μ and D. No anti-correlation was present. These data demonstrate that the anti-correlation property of pom1p gradients is not a non-specific property of every cell tip gradient. (Analysis done by Tim Saunders)

Figure S7

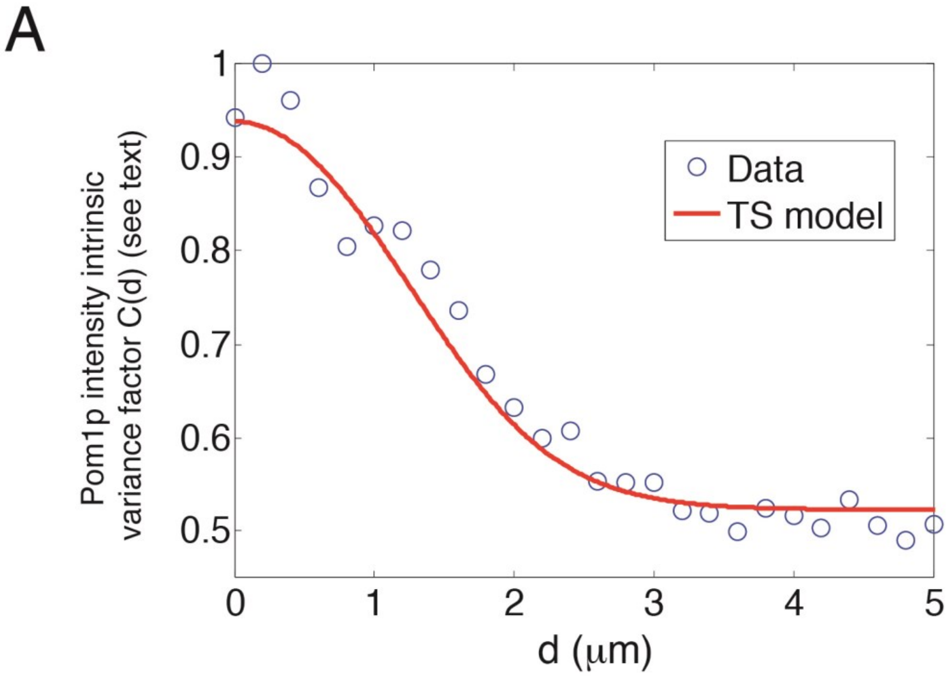

Figure S2.7 Measurement of pom1p intrinsic variance and comparison with TS model (Analysis done by Tim Saunders)

Pom1p intensity intrinsic variance factor C(d) (see Supplementary Experimental Procedures, Theoretical Analysis, Section 7) against position along the membrane. Circles are experimentally derived values from 196 gradient profiles from 98 cells. Red line is fit from TS model. Experimental data is normalized to the maximum measured value.

Supplementary Information

1. Supplementary theoretical analysis: Cell geometry and boundary conditions

We now discuss in more detail the theoretical model outlined in the main paper. First, we outline the geometry and boundary conditions with which we solve the model. We consider the cell to be a capsule, with two hemispherical caps connected by a cylinder of equal radius. We take the radius of the hemispherical caps to be R = 1.75 μm. We model the pom1p gradient formation using reaction-diffusion equations. Such equations include a ∇^2 term (the Laplacian) due to diffusion. ∇^2 has different forms in spherical polar coordinates (suitable for solving equations on hemispherical caps) as compared to cylindrical polar coordinates (suitable for solving equations on the cylindrical body) (Riley et al., 1998). In particular, on the hemispherical caps, we consider a rotationally symmetric pom1p density about the long axis of the cell, with distance expressed in terms of the arc length *l* from a cell tip. On the cylindrical region, distance is expressed in terms of z, the coordinate along the long axis of the cell. Therefore, on the hemispherical surface $\nabla^2 = \partial_l^2 + 1/(R\tan(l/R))\partial_l$ (van Zon et al., 2009) and on the cylindrical body axis $\nabla^2 = \partial_z^2$. From now on, we simply refer to ∇^2, though its form at a particular position depends on the local cell geometry. Furthermore, we use *d* in formulae to denote the distance along the membrane from a cell tip, where for $d < R\pi/2$ it describes an arc length on the hemisphere, while for $d > R\pi/2$ it denotes the hemispherical arc length plus a length along the cylindrical body. The boundary conditions between the hemispherical and cylindrical body domains are such that the pom1p concentration (henceforth denoted by ρ) and slope ($\nabla\rho$) are equal at the boundary between the domains. The boundary conditions at the cell tips are that the concentration gradient ($\nabla_d \rho |_{d=0}$) is zero. Note that this final boundary condition is not valid in the half-tip FRAP, an issue we discuss further below.

2. Supplementary theoretical analysis: Numerical integration

In general, the reaction-diffusion equations discussed here (and below) cannot be solved exactly and instead we use numerical integration in Matlab utilizing the Matlab function *pdepe*. Within 1μm of each cell tip, the space was discretized into 0.01μm size bins. For the rest of the cell, space was discretized into 0.1μm bins. We solved the models over a period of 500s. Initially, the concentrations were set to zero (except for the solutions of the FRAP, see later). We checked that the solution of the equations reached after 500s agreed with the solution found by solving directly the steady-state equations (using the Matlab function *bvp4c*). Time steps of 0.01s, 0.1s and 1s were all tested. Typically, we solved the equations for a cell half-perimeter length of 14µm (using 12µm or 16µm did not significantly alter our results).

3. Supplementary theoretical analysis: SDD model

Before discussing the two-state model outlined in the main paper, we briefly discuss the source/diffusion/disassociation (SDD) model that provides a simple mechanism for creating a concentration gradient. Within the SDD model, we assume that pom1p associates to the membrane (i.e. a source of pom1p) close to the cell tips (with a maximum amplitude J pom1p molecules injected per μm^2 per second). Membrane associated pom1p can then diffuse (with diffusion constant *D*) and unbind (disassociate) from the membrane at a rate **μ**. In such a scenario, the pom1p concentration is described by

$$\partial_t \rho = D\nabla^2 \rho - \mu\rho + Jf(d/\sigma), \tag{1}$$

where f(d/σ) = $e^{-d^2/2\sigma^2}$ describes the spatial profile of pom1p association. f(d/σ) is rotationally symmetric about the long axis of the cell and hence the solution for ρ on the cell membrane has the same symmetry. In steady-state, and only on the cylindrical membrane, and only if σ << d << L, where L is the cell length measured along the membrane, then the solution is given by

$$\rho_{SDD}(d) \approx \rho_0 e^{-(d-d_s)/\lambda}, \tag{2}$$

where ρ_0 is the pom1p concentration at $d = d_s = \pi R/2$ and $\lambda = \sqrt{D/\mu}$, the characteristic length scale of the pom1p profile. For best parameter fits to the data we find σ≈0.7**μ**m < d_s ≈ 2.75μm < L ≈ 14**μ**m. In general, we solve Eq. 1 numerically (see above). As shown in Figure S5A, with appropriate parameters the solution of Eq. 1 can give a good fit to the observed pom1p profiles. However, the SDD model has only a single membrane diffusion constant and membrane timescale, in disagreement with cluster tracking, FRAP and FCS. Moreover, as shown in Figure S5B,D and Figure S6D, the SDD model cannot replicate various other experimental results.

4. Supplementary theoretical analysis: Two-state models of pom1p gradient formation

In this section we build two-state models of pom1p gradient formation. First, we discuss simpler two-state models and demonstrate that they are insufficient to explain our experimental data. We then describe our final nonlinear two-state model.

4.1. Non-interacting two-state model

From the discussion presented in the main paper, a natural way to explain our experimental pom1p data is to consider a two-state model. One state represents slow diffusing, high intensity clusters predominantly located near the cell tips. The second state represents faster-diffusing pom1p. Without interactions between the two states, the concentrations of the fast (ρ_f) and slow (ρ_s) forms of pom1p are given by

$$\partial_t \rho_s = D_s \nabla^2 \rho_s - \mu_s \rho_s + \varepsilon J f(d/\sigma), \qquad (3)$$

$$\partial_t \rho_f = D_f \nabla^2 \rho_f - \mu_f \rho_f + (1-\varepsilon) J f(d/\sigma), \qquad (4)$$

where *J* is the maximum association of pom1p per μm^2 per second at the cell tip. $f(d/\sigma) = e^{-d^2/2\sigma^2}$ is as above for the SDD model. Since we do not separately know the association parameters of the two pom1p states (parameterized by ε, with $0 \leq \varepsilon \leq 1$), we leave this as a fitting parameter in the model. We observe that high intensity clusters are most common near the tips, suggesting that ε is more than ½. From our cluster tracking, μ_s is on the order of $(1/4)s^{-1}$ and hence we require $\mu_f \sim (1/30)s^{-1}$ to be consistent with the full-tip FRAP results. This model can fit some of our data, but is unable to accurately reproduce the observed FRAP recovery profiles, while still being qualitatively consistent with the average pom1p profile and distribution of high-intensity clusters. In particular, since $\lambda_s = \sqrt{D_s / \mu_s} << \lambda_f = \sqrt{D_f / \mu_f}$, we find that a majority of pom1p must be in the fast form in order to reproduce the wide spatial extent of the gradient. However, to fit the observed fraction of high intensity clusters (Figure 5C) requires ε to be close to unity, which is in contradiction with the previous requirement. Furthermore, if ε is close to unity then the full-tip FRAP recovery curve is too fast since the majority of pom1p then exists in the slow-diffusing, clustered form near the tip (which has $\mu_s \sim (1/4)s^{-1}$ in order to agree with the measured cluster lifetimes).

4.2. Two-state model with one-way interactions

The next simplest approach is to consider slow-diffusing, high intensity pom1p clusters breaking up into the faster-diffusing form of pom1p. This process can be represented by an interaction rate α between the two pom1p states:

$$\partial_t \rho_s = D_s \nabla^2 \rho_s - \alpha \rho_s + \varepsilon J f(d/\sigma), \tag{5}$$

$$\partial_t \rho_f = D_f \nabla^2 \rho_f + \alpha \rho_s - \mu \rho_f + (1-\varepsilon) J f(d/\sigma). \tag{6}$$

The numerical solutions to these equations can fit the average profile, but not reproduce the observed fractions of slow- and fast-diffusing states whilst also fitting the observed FRAP data. To be consistent with the measured cluster lifetimes, $\alpha \sim (1/4)\mathrm{s}^{-1}$, while $\mu \sim (1/30)\mathrm{s}^{-1}$. Due to the interaction between the slow- and fast-diffusing pom1p states, there can be a larger proportion (compared to the non-interacting two-state model) of the slow pom1p state near the tips, whilst still ensuring sufficient levels of the fast pom1p state away from the tips. Therefore, this model provides an improved fit to our experimental data when compared to the non-interacting two-state model. However, we still have problems when trying to fit all the data sets: mean pom1p profile, high-intensity cluster fraction, full-tip FRAP recovery and half-tip FRAP recovery. One particular problem is that the decay length of the slow state is very short, $\lambda_s = \sqrt{D_s / \alpha} \approx 0.3$ μm. In order to have a sufficient fraction of the pom1p signal from the slow state away from the tips (to be consistent with the cluster fraction data), requires most pom1p association to be in the slow form (i.e. ε close to unity). However, such a high proportion of the slow state results in a poor fitting to the average profile and the FRAP data, particularly for the half-tip recovery.

We can also alter the above model so that transitions occur only from the fast- to slow-diffusing state:

$$\partial_t \rho_s = D_s \nabla^2 \rho_s + \kappa \rho_f - \mu \rho_s + \varepsilon J f(d/\sigma), \qquad (7)$$

$$\partial_t \rho_f = D_f \nabla^2 \rho_f - \kappa \rho_f + (1-\varepsilon) J f(d/\sigma). \qquad (8)$$

Again, numerical solutions of such a model are unable to explain all our experimental results. In particular, we cannot fit the FRAP recovery curves (Figures 2B and 2C) whilst qualitatively being consistent with the proportion of high intensity clusters near the tips (Figure 5C). Finally, we note that including disassociation from the membrane for both states does not alter any of the above conclusions.

4.3. Linear two-state model

An important piece of evidence needed to finalize the two-state model comes from cluster tracking. As shown in Figure 3B, the intensity of clusters clearly varies, both up and down. This suggests that pom1p may well be able to transition between the two states in addition to the processes present in Eqs. (5)-(6). Furthermore, the cluster intensity time-courses shown in Figure 3B demonstrate that this interaction occurs on second timescales. This conclusion is further supported by the estimated rates of cluster assembly and disassembly (Figure S3C). Accordingly the above models can be combined into a linear two-state model, with fast and slow diffusing states, and with transitions between the two states that only depend linearly on the concentrations of the respective states:

$$\partial_t \rho_s = D_s \nabla^2 \rho_s - \alpha \rho_s + \kappa \rho_f + \varepsilon J f(d/\sigma), \qquad (9)$$

$$\partial_t \rho_f = D_f \nabla^2 \rho_f + \alpha \rho_s - \kappa \rho_f - \mu \rho_f + (1-\varepsilon) J f(d/\sigma). \tag{10}$$

Such a linear two-state model can reproduce the mean pom1p profile and full-tip FRAP recovery curves well (Figure S5A and S5C). However, using parameters that fit the average profile and full-tip FRAP recovery curves well; we do not replicate the observed distribution of high intensity aggregates, Figure S5B. It is also clear from Figure S5D that the fit to the half-tip FRAP is not satisfactory. Furthermore, such a linear model does not reproduce the observed anti-correlation between the pom1p peak concentration and gradient decay length (Figure S6D). Overall, therefore, a linear two state model for pom1p gradient formation is insufficient to reproduce our experimental results.

4.4. Final nonlinear two-state model

A potentially more realistic two-state model could allow the slow diffusing state to grow by aggregation of the faster diffusing state. A simple way of describing such an aggregation process is through the non-linear term $\beta\rho_f\rho_s$. This non-linear interaction is clearly a simplification of the potential *in vivo* biochemistry, but it turns out to provide a simple model that is consistent with much of our experimental data. Our final nonlinear two-state model is therefore given by

$$\partial_t \rho_s = D_s \nabla^2 \rho_s - \alpha \rho_s + \beta \rho_s \rho_f + \varepsilon J f(d/\sigma), \tag{11}$$

$$\partial_t \rho_f = D_f \nabla^2 \rho_f + \alpha \rho_s - \beta \rho_s \rho_f - \mu \rho_f + (1-\varepsilon) J f(d/\sigma). \tag{12}$$

The solutions to these equations and the fits to our experimental data are as described in the main paper, with the parameter values given in Figure 5A. While our quantitative results do depend on the functional form of f(d/σ) (taken to have a Gaussian profile), our qualitative conclusions hold for other reasonable forms of f(d/σ) (where f is a monotonically decreasing function equal to unity at d = 0), such as could be used to fit individual pom1p profiles in single cells. Finally, we have also verified that including membrane disassociation for the slow-diffusing pom1p clusters does not alter any of our results.

4.5. Phosphorylation model of pom1p gradient formation

A recent study (Hachet et al., 2011) has investigated the role that phosphorylation of membrane-bound pom1p plays on the rate of pom1p disassociation from the membrane. So, is it possible that the results we observe can be explained by phosphorylation of pom1p, without the need for clustering? A simple model that is consistent with the results presented in Hachet et al., is to assume pom1p has two states, an unphosphorylated state A, and a phosphorylated state A*. Pom1p is unphosphorylated when it associates to the membrane. At a rate $\tilde{\alpha}$, the pom1p becomes phosphorylated. The phosphorylated form of pom1p disassociates from the membrane at a rate $\tilde{\mu}$. We allow the phosphorylated and unphosphorylated states to have different diffusion constants. The dynamics of this system can be described by

$$\partial_t A = D_A \nabla^2 A - \tilde{\alpha} A + J f(d/\sigma), \qquad (13)$$

$$\partial_t A^* = D_{A^*}\nabla^2 A^* + \tilde{\alpha} A - \tilde{\mu} A^*. \qquad (14)$$

Using these equations, we can fit the mean pom1p profile. This is unsurprising, since Eqs. 13 and 14 have very similar forms to Eqs. 5 and 6 discussed earlier (the only difference is in the pom1p association). As discussed in Section 4.2, such a model of pom1p gradient formation cannot satisfactorily explain all of our data. Finally, we have also confirmed numerically that considering only pom1p phosphorylation dynamics (without clustering) does not reproduce the pom1p intensity-λ anti-correlation, and associated buffering of cell-to-cell variations, observed experimentally. This is due to the linear dependence of the pom1p concentration on J in the above model.

5. Supplementary theoretical analysis: FRAP analysis

The experimental FRAP methods are described in the Methods section of the main paper. Here, we briefly outline our approach to fitting our models to the FRAP data. In our whole-tip FRAP recovery data, we do not see a dip in intensity of the unbleached tip. Moreover, in the FRAP procedure, the vast majority of the fluorescence intensity at one end of the cell is removed. Hence, diffusion either from the unbleached tip, or from remaining gradient signal outside of the bleached region, is likely to be unimportant. Therefore, repopulation of the bleached cell tip is likely to come primarily from association of pom1p from the cytoplasm. In order to simulate whole-tip FRAP within the TS model, we numerically solved the TS reaction-diffusion equations using Matlab starting from the steady-state and then setting $\rho_f = \rho_s = 0$ for $d < 2.75$ μm. This procedure was relatively straightforward as whole-tip FRAP preserves rotational symmetry.

Mathematical modeling of the half-tip FRAP is considerably more complex, since bleaching only a half-tip destroys the rotational symmetry about the long axis of the cell. However, our aim here is to see if the TS model can account for the rapid half-tip FRAP recovery. To this end, solving the half-tip FRAP scenario in one-dimension, with coordinate x, is insightful. In particular, the one-dimensional solution includes diffusive repopulation into the bleached region from both the unbleached half-tip and non-tip regions (as well as pom1p membrane association/disassociation and cluster aggregation/fragmentation). We first solved the one-dimensional TS model in steady-state and then set both $\rho_f = \rho_s = 0$ in the region $0 < x < R\pi/2$. We then resolved the equations, with the resulting intensity recovery curve for the bleached region shown in Figure 5E. Parameters are as given in Figure 5A (see also below), with $D_f \approx 0.2$ $\mu m^2 s^{-1}$, except for $J_{1d} = 0.55J$ (determined such that the steady-state profile was similar to the full two-dimensional solution). This one-dimensional solution will tend to overestimate the diffusion constants, since it neglects diffusion of pom1p from the unbleached half-tip around the two-dimensional hemispherical cap into the bleached half-tip. In the main paper, we also present a simple calculation to estimate the diffusion constant needed to repopulate a half-tip (giving $D_{half\text{-}tip} \approx 0.1$ $\mu m^2 s^{-1}$). This is an underestimate of D_f as it does not account for the two states of pom1p, one of which diffuses much more slowly. Given these two bounds, we can be confident that the TS model can explain the half-tip FRAP data and that the diffusion constant of the faster state, D_f, is in the range 0.1 - 0.2 $\mu m^2 s^{-1}$.

6. Supplementary theoretical analysis: Parameter fitting

Fitting of the model parameters proceeded as follows. First, a selection of parameters that were directly measured or bounded experimentally were set: D_s (from FCS, cluster tracking); α (mean cluster lifetime); μ (full-tip FRAP); σ (tea1p spatial distribution) and R (width of cell). Note that μ here is obtained from fitting the formula $A(1-e^{-\mu t})$ to the data in Figure 2B. This value will actually be a lower bound on the real membrane disassociation rate in the TS model due to the additional cluster aggregation/fragmentation dynamics. The same is true for our value for α, since the estimate neglects processes that cause cluster intensities to increase. Parameters were allowed to vary within the range of their experimental standard deviation (or in the case of α and μ, they could increase up to twice the experimentally measured standard deviation, but not decrease below the mean measured values). The next step was to solve the TS model such that the mean steady-state profile (Figure 5B) was well-fitted. In general, a range of values were capable of fitting this profile. However, fitting the mean profile did constrain D_f in order to get the correct profile across the whole of the cortex. β and ε were then adjusted to give good agreement with the experimentally measured relative fraction of high intensity pom1p clusters, Figure 5C. μ was adjusted to ensure that the full-tip FRAP recovery curve (Figure 5D) was well-fitted by the model. We then calculated the total number of pom1p molecules on the cortex within the 10% of the cell length closest to a tip, and constrained this to be 1300, in agreement with our experimental quantification, thereby constraining J. The above parameter alterations were performed iteratively until a good fit to the data was achieved. For example, altering J resulted in a change to the shape of the average profile that then had to be corrected for by adjusting other parameters. Though α was not directly fitted to a single experiment, it was tuned to ensure a good fit of the model to the data whilst ensuring that it was approximately consistent with the measured cluster lifetime.

To validate our fits, we then computed the half-tip FRAP recovery profiles, and compared to experiment, and also compared our values of the cluster assembly/ disassembly rates with those measured directly in experiments (Figure S3C), with reasonable results. Importantly, in our parameter fitting we used some experimental results as inputs (e.g. D_s from FCS, cluster tracking) and some experiments for model verification (half-tip FRAP, observed cluster assembly/disassembly rates). We note that generally there was a large (20-30%) flexibility in most parameter values. However, the solution was sensitive to the value of β. Since our fitted β value implied a cluster assembly rate of the same order as that measured experimentally (Figure S3C), we have confidence in our fit. Furthermore, the behavior of the intrinsic noise (see below) and the pom1p peak concentration-λ anti-correlation (Figure 6B) were model predictions (not fits) that were then experimentally tested and confirmed. More sophisticated methods of parameter fitting were not required as there were relatively few free parameters. Furthermore, most parameters were already constrained, at least to an order-of-magnitude, by our experiments.

7. Supplementary theoretical analysis: Intrinsic noise

In our models, diffusion, association and membrane disassociation are Poisson processes. Therefore, if we exclude interactions between pom1p states then we expect that the instantaneous variance in the measured pom1p intensity due to intrinsic noise scales as $\delta I_{\text{int}}^2(d) \propto I(d)$, where $I(d)$ is the mean intensity and where we assume a linear relationship between intensity and particle number. In such a system, the role of time-averaging is well-understood (Tostevin et al., 2007). The timescale between statistically independent measurements is given by $\tau_0 = (\Delta x)^2 / D$, where Δx is the linear size of the measuring region. Hence, we find that the variance in pom1p intensity due to intrinsic noise $\delta I^2_{\text{int}}(d,\tau)$ after a time τ of averaging is given by

$$\delta I^2_{\text{int}}(d,\tau) = \frac{c(\Delta x)^2}{D\tau} I(d), \tag{15}$$

where c is a constant (Tostevin et al., 2007). We see that $\delta I^2_{\text{int}}(d,\tau)/I(d)$ is independent of position. A more detailed discussion of time-averaging of the pom1p gradient (as described by the SDD model), also incorporating receptor binding/unbinding, can be found in (Tostevin, 2011).

The situation is somewhat more complex in the TS model when interactions between states are included. One key difference emerges in the time-averaging. The effective timescales ($\tau_{\text{f,s}}$) over which the fast and slow forms are time-averaged are different: $\tau_{f,s} = (\Delta x)^2 / D_{f,s}$. Therefore, we see that $\tau_{\text{f}} < \tau_{\text{s}}$, i.e. it takes longer for the intrinsic fluctuations in the slow-moving clusters to be reduced by time-averaging. Assuming independent, Poisson statistics (see below), we find that the variance in the total pom1p intensity due to intrinsic noise, $\delta I^2_{TS,\text{int}}(d,\tau)$ (where $I_{\text{TS}} = I_{\text{s}} + I_{\text{f}}$), after a time τ of averaging, is given by

$$\delta I^2_{TS,\text{int}}(d,\tau) = \frac{c(\Delta x)^2}{\tau}\left(\frac{I_s(d)}{D_s} + \frac{I_f(d)}{D_f}\right). \tag{16}$$

Close to a tip, it is clear that $\delta I_{TS,\text{int}}^2(d,\tau)/I_{TS}(d)$ varies with position, whereas far from the tips, where pom1p is only present in the fast form, the intrinsic fluctuations become independent of distance. In Figure 7A, we fit $\delta I_{\text{int}}^2(d,\tau)/I(d)=C(d)/\tau$ to our intrinsic noise data and extract *C(d).* We can then compare the value of *C(d)* with that predicted by Eq. (16). As shown in Figure S7, the TS model prediction is in good agreement with our experiments. The above analysis leading to Eq. (16) does assume that the statistics of the two states are independent and well-described by Poisson statistics. These turn out to be good approximations because, for our choice of parameter values, the fluctuations in the TS model are dominated by diffusion for both the slow and fast-diffusing states.

Finally, we discuss the role of the measuring region size Δx. In our experiments, this size was around 200nm. In principle, the size of the intrinsic noise will depend on Δx. The structures that sample the pom1p gradient *in vivo*, for example cortical dots of cdr2p, are likely to be smaller in size than this. However, these smaller length scales cannot be accessed experimentally due to the diffraction limit of our equipment. Therefore, the size of the intrinsic noise relevant for the read-out measurement could potentially be altered compared to our estimates. However, the gradient of pom1p on the membrane is effectively confined to a 2D surface. When the intrinsic fluctuations in density (rather than intensity) are computed, it turns out that dependence on Δx in 2D almost completely cancels out, leaving only a slowly-varying logarithmic dependence (Tostevin et al., 2007). This result follows from larger measuring regions having smaller instantaneous density fluctuations, but also slower time-averaging (due to their larger size). For this reason we expect our measurements of the intrinsic noise, and its size relative to cell-to-cell variations, to be reasonable estimates of the relevant *in vivo* noise levels.

8. Experimental methods

8.1. Protein Counting

Numbers of molecules were estimated by comparison with fluorescence intensity of cells or structures containing proteins that have been quantified previously in fission yeast cells (Wu and Pollard, 2005). For an estimation of the number of pom1p molecules in the whole cell, we compared pom1-GFP with rlc1-GFP and spn4-GFP (see Figure S1B). Pom1p exhibited similar intensities as rlc1-GFP. Numbers of molecules within a single pom1p cortical cluster were estimated by comparison to a set of actin patch proteins (Sirotkin et al., 2010; Wu and Pollard, 2005); in particular the pom1p clusters were very similar in intensity to dip1-GFP patches, which were estimated at about 20 molecules/actin patch (R. Basu and F. Chang, unpublished) (Figure S3A,B). Although this approach certainly has limitations, including reliance on the accuracy of previous measurements, these experiments do provide at least a rough estimate.

8.2. Fluorescent correlation spectroscopy (FCS) methods

Multi-photon FCS was performed on a custom built setup based on a Nikon TE2000-U inverted microscope. A collimated IR laser beam (Mai Tai Ti:Sapphire laser with an 80 MHz repetition rate and 100 fs pulse width, Spectra Physics, CA, USA) was focused by a Nikon 100X Plan Apochromat oil immersion objective (N.A.=1.4) with the back aperture slightly overfilled, creating a diffraction-limited focal spot. The laser was tuned to 850nm for EGFP excitation and the total power was set to 2 mW to reduce photobleaching and minimize cellular autofluorescence. The emission fluorescence was collected by the same objective and was guided through a custom infinity-space port into a 30mm cage system (Thorlabs, NJ, USA). The cage system combines a band-pass filter (HQ510/50m-2p for EGFP, Chroma Tech, VT, USA) and a 30mm focus length lens (Thorlabs, NJ, USA) to focus the fluorescence through a 50 μm size pinhole to eliminate the out of focus fluorescence. The emission fluorescence is then refocused onto a photomultiplier detector (PMT, H7421-40, Hamamatsu, Japan) running in photon counting mode. The photon signal was converted to an autocorrelation function in real time using a Flex02-01D/C hardware autocorrelator (correlator.com) and transferred to a personal computer using a high speed USB port. The two-photon excitation volume was calibrated by a $5x10^{-9}$ M fluorescein solution with known diffusion constant (Figure S4A). Calibration of the FCS volume yielded an excitation volume minor axis radius (ω_{xy}) of 313 nm at wavelength 780 nm (Figure S4A) and 367 nm at wavelength 850 nm.

To measure the FCS signal *in vivo*, we assayed fission yeast cells that were positioned in horizontal and vertical orientations. Cells were grown in YE5S liquid media in exponential phase cultures and concentrated by a brief centrifugation. To orient the rod-shaped cells vertically, we placed cells in arrays of round microwells of 6 μm diameter and approximately 20 μm deep (J. He, L. Munteanu, F. Chang, M. Bathe, unpublished observations). These wells, which were micro-fabricated in polydimethylsiloxane (PDMS), were plasma cleaned and coated with polylysine and lectin to immobilize the cells. Cells were placed on the PDMS and covered with a glass coverslip. The vertical position of the cell allowed for cell middle and cell tip measurements. For the horizontal position (top), 1.3 μl of cell slurry was placed on a glass side and covered with a cover slip. The cell top measurement position in the cell was selected by placing the laser in a position halfway between the center and tip of the cell under bright field illumination. Each autocorrelation curve was collected for 30 seconds and 5-6 runs were carried out for each position in each cell. Calibration measurements in the middle position within the cytoplasm in cells expressing free GFP show an autocorrelation curve consistent with free 3D diffusion and a diffusion constant of 7.5 $\mu m^2 s^{-1}$ (Figure S4B). This diffusion is much faster than for cytoplasmic pom1-GFP.

9. Experimental Analysis

9.1. Pom1p cortical masks

In order to define the cell membrane sufficiently well to reliably measure the pom1p/tea1p spatial distributions, automated cell-membrane detection routines were coded using Matlab and the image processing toolbox. A custom graphical user interface (GUI) was also coded using Matlab to allow for correction of the automatically generated cell membrane masks. The cell-membrane detection procedure was as follows: data in the form of pom1-tomato fluorescence intensity and phase contrast grayscale bitmaps were loaded into Matlab. The phase contrast images were converted into black and white with a threshold, such that the outlines of the cells appeared as white rings. All objects (continuously connected groups of pixels) that touched the border of the image were removed to discard partially imaged cells. Any objects with total area regarded as too large or small to be a single cell were also discarded. At this point the remaining objects were assumed to correspond to cells and each was converted to a perimeter and then dilated to encompass the membrane of the cell. Each dilated perimeter was then converted into concentric single-pixel-width bands, each one a potential mask, and these were swept over the local area. The combination of band and position that gave the greatest overlap with the intensity signal was judged to be the best automated guess for the membrane. At this point, pixel-shifting could have been applied to improve small errors in the masks, but this method tended to help and hinder in equal measure. The automated system also struggled to detect cells that were close to others and would frequently only fit to the membrane for part of a cell. To allow manual correction of the masks, and addition in the case of cells that were missed completely, a Matlab GUI was created. The intensity image was displayed alongside a copy of this image with the automatically generated mask overlaid. The GUI allowed the user to drag, delete and add pixels to the masks using the Matlab GUI framework, then skeletonize, sort and save any complete loops as cell masks. Once the masks were properly defined, a tip position was identified as the pixel in the mask closest to the major axis of the cell. The distance along the cortex was then measured using the Euclidean distance to the next pixel starting from the tip pixels. The pom1p/tea1p intensity at each point along the mask was then stored as a function of this distance. Finally, for each image exposure during a time course, the mask was, if necessary, altered to allow for slight cell movement.

9.2. Defining regions of the pom1p gradient

Pom1p is regulated by the cell tip factors tea1p and tea4p (Bahler and Pringle, 1998; Martin et al., 2005; Padte et al., 2006; Tatebe et al., 2005). In a *tea1* mutant, pom1p exhibits reduced accumulation at cell tips, while in a *tea4* mutant, pom1p is predominantly cytoplasmic (Padte et al., 2006). Tea1p and tea4p, which are deposited at cell tips by plus ends of microtubules, localize to discrete dots near the center of the cell tip (Figure S2A) (Behrens and Nurse, 2002; Bicho et al., 2010; Feierbach et al., 2004; Martin et al., 2005; Mata and Nurse, 1997). We found that tea1p and pom1p partially co-localized at cell tips. Peaks of tea1p intensity often matched peaks in pom1p intensity in individual cells (Figure S2B,C,E). Pixel-by-pixel analyses revealed a high correlation between the maximum tea1p and pom1p intensity values (Figure S2B, $r^2 = 0.70$). Intensity profiles, both averaged over the cellular population (Figure S2C top) and in individual cells (Figure S2C bottom, E), showed that the pom1p profile can be divided into three regions (Figure S2C, D): Region I is a zone d = 0-1.5 μm from the center of a cell tip that contains the highest concentration of pom1p and tea1p, with significant overlap of these proteins; Region II is a zone d = 1.5 μm- 4 μm from a cell tip, in which the tea1p intensity rapidly decreases to zero, but where the pom1p intensity spreads significantly further in a gradient distribution; and Region III is a zone further than d = 4 μm from a cell tip, where there is little tea1p and a low pom1p concentration. These findings suggest a model in which pom1p associates to the membrane in a tea1p-dependent process in Region I, and then undocks from tea1p and spreads on the membrane into a gradient-like distribution in Region II, and remains at a low concentration in Region III (see also (Hachet et al., 2011)).

9.3. Pom1p cluster tracking

All analysis was performed using ImageJ. The cluster tracking procedure was as follows. First, a data set of 50 images of the cortical plane was loaded. Each image had an exposure time of 0.5

seconds: this choice resulted in sufficient intensity to make cluster identification straightforward, while the image acquisition time was still relatively short. The latter issue was important since we expected the typical cluster lifetimes to be around only 3-4s. In total, therefore, each image sequence covered 25s. Each image was consecutive in time to the previous image. A cell was then selected and rotated so that the major axis was horizontal. The ImageJ macro *photobleach correct* was then used on all 50 images. Using the ImageJ threshold function, we defined a threshold for cluster intensity to remove the majority of the cortical signal, leaving only high intensity clusters. Starting from the second image of the series, a new cluster was identified (i.e. no significant intensity could be found near the cluster's position in the previous image of the series). Here a cluster was defined as an area of five nearest-neighbor pixels above the threshold intensity. The particular threshold used does, to an extent, effect the measured lifetimes of the clusters. However, we used a low threshold that encompassed most observable clusters. Comparing cluster intensity with the displacement and lifetime found by cluster tracking (see below) revealed no strong correlation. Our qualitative results are therefore substantially independent of the choice of threshold. The chosen cluster was then tracked, with the intensity and position of the cluster center (determined by eye) recorded at each step. The cluster was deemed to have dissipated after the cluster had less than five nearest neighbor pixels above the threshold intensity. For each cluster, we calculated the mean intensity over its lifetime. After tracking a cluster, we then returned to the image where it was first identified to see if any other new clusters appeared at that time. These additional clusters were then tracked as above. Once all the new clusters in an image were identified, we then proceeded to the next image in the series and repeated the whole procedure. We continued until we reached the 50th image, where we discounted clusters that were still visible (as we could not know their future behavior). We tracked 198 clusters from seven cells, all from the same experiment, using the same cluster threshold for each cell. Most tracked clusters were away from the cell tips, as clusters near the tips were difficult to distinguish due to the large number of very high intensity pixels.

We calculated cluster displacement $r = \sqrt{(x_{start} - x_{end})^2 + (y_{start} - y_{end})^2}$ (where *x, y* represented the two-dimensional coordinates in the images). Clusters were tracked by eye (the data was too noisy for readily-available numerical methods), which made the tracking of fast-moving clusters difficult. Therefore, our methodology did introduce a bias towards slow-moving clusters away from the tips, as these clusters could be more reliably tracked. Finally, it is possible that clusters come in and out of the focal plane during their lifetime. A consequence of this would be to reduce the measured cluster lifetime. For example, a single cluster moving out of the focal plane and then back in at a later time point would be recorded as two clusters with short lifetimes rather than one with a longer lifetime. However, using maximum intensity projections of the pom1p signal from the top 4 slices of the cell, we see little difference from that using the pom1p signal in only the cortical plane. Therefore, it is unlikely that pom1p movement in and out of the focal plane is significantly altering our results.

9.4. Quantifying diffusion of pom1p clusters

From simple diffusion theory, clusters with a lifetime τ will have a spread in observed displacements given by a Gaussian probability distribution, with mean zero and variance $\omega^2 = 2D_{cluster}\tau$. In our cluster tracking experiments we measure a range of cluster lifetimes,

Figure 3C. Therefore, to estimate the predicted distribution of cluster displacements due to diffusion, we proceeded as follows: for each lifetime bin shown in Figure 3C we calculated the corresponding expected Gaussian distribution of cluster displacements. We then multiplied this distribution by the fraction of clusters belonging to that bin. We repeated this for each lifetime bin and summed the resulting distributions, shown as the red line in Figure 3E.

9.5. FCS data analysis

All FCS curves were analyzed by custom-written Matlab code (Mathworks Inc, Waltham, MA) using a nonlinear least-squares fitting algorithm from the curve fitting toolbox. The fitting formula for multi-species diffusion with different molecule brightness is (Haustein and Schwille, 2007; Kerichevsky and Bonnet, 2002):

$$G(t) = \frac{1}{\left(\sum_k Q_k N_k\right)^2} \sum_j Q_j^2 N_j \left(1 + \frac{t}{\tau_{D_j}}\right)^{-1} \left(1 + m\frac{t}{\omega^2 \tau_{D_j}}\right)^{-1/2}, \qquad (17)$$

where Q_j is the molecular brightness of species j and is the product of the absorption cross section, the fluorescence quantum yield and the efficiency of fluorescence detection in counts/molecule/second. N_j is the average particle number of species j in the sampling volume. τ_{D_j} is the residence time of species j within the sampling volume, with $\tau_{D_j} = \omega_{xy}^2 / 8D_j$, where D_j is the diffusion coefficient of species j, and $\omega = \omega_z / \omega_{xy}$ is the aspect ratio of the sampling volume. *m* is the dimension counter, *m* = 1 for three dimensions and m = 0 for two dimensional diffusing pom1 species. This formula assumes membranes are oriented in the xy plane and located near the center of the excitation volume (Ries and Schwille, 2008).

Before the fit analysis, raw FCS autocorrelation curves were denoised by a moving average filter of window span 5. Comparing the fast cytoplasmic diffusion with membrane-bound slow diffusion, we found the fast diffusion FCS curves were much noisier than the slow decaying curves. To decrease the noise, we averaged 5-6 single FCS curves and then carried out curve fitting using a single species 3D free diffusion model (k = 1, j = 1 and m = 1, with D and N as the fitting parameters). In contrast, the membrane-bound FCS curves were fit by a multi-species model (k > 1, j > 1, including a 3D species and up to two 2D species) without measurement averaging. In the two species fits (one 3D species combined with one 2D species), the diffusion coefficient for 3D was fixed to 1.5 $\mu m^2 s^{-1}$ with the membrane-bound diffusion coefficient and the molecular numbers of the 3D and 2D species being free parameters. A histogram of diffusion times was constructed to evaluate the presence of multiple species. Over many binning sizes, two characteristic timescales were identified for further analysis (τ_{D_2}= 0.65s, τ_{D_3}= 2.85s). In the three species fits (one 3D species combined with two 2D species), all diffusion coefficients were fixed with D_1 = 1.5 $\mu m^2 s^{-1}$,

D_2 = 0.026 $\mu m^2 s^{-1}$ and D_3 = 0.006 $\mu m^2 s^{-1}$, with all molecular numbers (N_1, N_2, N_3) being free parameters. The species fractions were rebuilt by the molecular number ratio, with the brightness-weighted fraction$\left(Q_i^2 N_i / \sum_j Q_j^2 N_j\right)$.

9.6. FCS Supplementary results

Through FCS measurements of the wild-type, *tea1* deletion and *tea4* deletion strains in various positions we have been able to identify at least three distinct pom1p species, including two membrane bound species and one cytoplasmic species. Initially all strains were measured in the cytoplasmic position to determine a consensus cytoplasmic component (Figure 4A, S4B). From this analysis a consensus value of 1.5 $\mu m^2 s^{-1}$ (S1) was estimated from the autocorrelation functions taken in the wild-type strain (a value later shown to be unchanged in the deletion backgrounds).

Using the cytoplasmic component, we fit the cell tip and cell top positions to identify a 2D component (Figure S4C). A wide range of diffusion times ($\tau_{D_j} = \omega_{xy}^2 / 8D_j$) for the

2D component were seen with a long-tailed bimodal distribution. Two characteristic timescales were chosen from the distribution as most representative of the observed species in both measurements (see also inset in Figure S4C). The 2D component was split into two distinct species: S2 with τ_{D_2}= 0.65s; D_2 = 0.026 $\mu m^2 s^{-1}$ and S3 with τ_{D_3}= 2.85s; D_3 = 0.006 $\mu m^2 s^{-1}$ (Figure S4C and S4D).

The brightness-weighted proportion of the three species can be calculated from the particle number derived from the FCS fit. This proportion accounts for the amount of pom1p that is present in each of the diffusing species. When measured at each of the positions, we can see that the relative proportion of each species changes as measurements become closer to the center of the cell (Figure S4D). Specifically, the cell tip is dominated by the S3 component, whereas the cell top, which is more central, has a lower proportion of S3 compared to the tip position. These data indicate that the proportion of pom1 in S2 and S3 is reduced at points closer to the center of the cell and, in fact, S3, the very slow membrane component, is highest in proportion at the tip and drops in abundance at positions closer to the center of the cell.

Long residence times in the volume, as seen for the slow diffusing pom1-GFP, were subjected to further analysis to rule out potential FCS artifacts. One such artifact can be photobleaching. While the power used is low, for long residence times the fluctuations can be due to bleaching of a non-moving component rather than slow motion. However, such artifacts can be detected by the loss of photon counts from the start versus the end of the measurement. In no cases did we observe such photobleaching in our measurements. Another potential artifact for large objects is fluctuations due to cell movement. In this case the movement is generally stochastic (i.e. variable from cell to cell) and would also differ in frequency depending on the sample. Given the consistency in the measurements of the slow diffusing pom1-GFP we can rule out cell movement as a contributing factor. Given the long diffusion times measured and the relatively short measurement time, it is likely that for the slowest diffusing species, its diffusion time is underestimated since this species has not been sufficiently sampled (Tcherniak et al., 2009). However, the estimates for the faster moving species are not affected by underestimation of the slower species. Geometric artifacts can also contribute to erroneous measurements.

Measurements made with the yeast membrane oriented in the XZ axis (e.g. by placing the tip or side of a horizontally oriented cell directly into the excitation volume) resulted in changes in the autocorrelation function (Figure S4E). These changes result from the longer diffusion time due to the larger intersection with the membrane. The equation above does not account for the increased membrane overlap. Moreover, the exact overlap can be difficult to control in these orientations.

9.7. Measuring the fraction of high intensity clusters

We analyzed the z-stacks of twenty cells (3s exposure images) using ImageJ. First, we found the cell length along the linear tip-to-tip axis by looking in the medial plane. We then investigated the pom1p intensity in the cortical plane. We subtracted the background and found the mean overall pom1p intensity in the cortical plane. A threshold for high intensity clusters was defined as four times this mean intensity. We then calculated the pom1p intensity at each position along the linear tip-to-tip axis (summing over pixels perpendicular to this axis) with and without the threshold. This procedure was carried out in each cell with the results then averaged over all cells. The high-intensity pom1p cluster fraction was defined as the relative signal due to pom1p above the threshold at each position.

Several issues arose when comparing our experimental measurements with the predictions from the TS model. The first issue was that the edge of the pom1p intensity signal in the cortical plane does not correspond to the tip of the cell; the cell profile is longer in the medial plane. We found that this difference for a typical cell was around 0.6 μm. This is why there are no data points for distances less than 0.6 μm in Figure 5C (where linear distance is measured from the cell tip, not the beginning of the cortical plane). The second issue arose due to the geometry in which we solve the TS model. We approximate the cell as a cylinder for the body-axis, with two-hemispherical caps. Therefore, distances in the TS model are expressed in terms of the distance along the hemisphere and cylinder (see Section 1 for more details). This distance measure (d), around the cortex, is different from the distance measured in the cluster fraction experiment (which is the linear distance along a plane of the cell, *x*). Therefore, we have to convert *d* into *x* in order to compare the results. We used the formula

$x = R(1-\cos(d/R))$ for $d < R\pi/2$, and $x = d - R(\pi/2-1)$ for $d \geq R\pi/2$, where R is the radius of the hemispherical cap (see Section 1). We note that the cell tip is not a perfect hemisphere and so this conversion inevitably includes a systematic error. However, we find that by comparing different possible geometries for the cell tip that this error is less than 0.2 μm.

9.8. Calculation of intrinsic fluctuations

Single cells were analyzed using a series of up to 30 images, where each image was acquired with a 3s exposure and was corrected for photobleaching and background. To calculate the intrinsic fluctuations in the pom1p profile after time-averaging for τ seconds, we require knowledge of the mean pom1p intensity profile in that cell, against which the measured intensities can be compared. For each cell the time-averaged pom1p profile $I(d,\tau_0)$ was found, averaging over the entire image series spanning a time τ_0. We also calculated the standard error of $I(d,\tau_0)$ at each position, $\delta_{I(d,\tau_0)}$. However, the fully time-averaged profile cannot be used as the mean profile, because in that case the fluctuations due to intrinsic noise would be zero when averaging over the entire image time series, which is incorrect. In reality, when averaged over the full time series the intrinsic noise is small but nonzero. Instead, we sampled the mean intensity at each position from a Gaussian distribution defined by $I(d,\tau_0)$ and $\delta^2_{I(d,\tau_0)}$. We repeatedly (50 times for each position) compared the observed intensity after a given period of time-averaging with a value randomly drawn from the above distribution. By sampling in this way, we explored the variance between the measured intensities and the distribution of possible mean pom1p intensities. This procedure was repeated for every cell, giving us the intensity variance due to intrinsic fluctuations as a function of averaging-time τ and position d in each cell. Finally, we averaged the observed variance of the intrinsic fluctuations at each position over all cells, giving $\delta I^2_{\text{int}}(d,\tau)$. This procedure was used to make Figure 7A.

9.9. Analysis of cell-to-cell variations

For each cell, we (arbitrarily) define a "left" and "right" tip. To calculate the cell-to-cell variations we separated these two data sets, in order to avoid any tip-to-tip correlations. Each individual pom1p profile was imaged (time-averaged) for 90s (with background subtraction and correction for photobleaching) and then binned into 0.2 μm bins. For each data set of pom1p profiles we found the mean and standard deviation $\delta I_{cell-to-cell}$ in each bin position. The standard deviation essentially represents the cell-to-cell variation: the intrinsic noise also contributes slightly, but 90s of time-averaging reduces the intrinsic noise to low levels, so that the cell-to-cell variation is the dominant contributor. Note that the profile shown in Figure 1B is the average pom1p profile over all profiles (including both "left" and "right" data sets). The cell-to-cell variations discussed in Figure 6 correspond to the standard deviation within a single data set. Figure 7B is derived on the basis that cell-to-cell and intrinsic fluctuations are independent. At each time-averaging step we calculated the size of the intrinsic fluctuations (see above). The total variation in pom1p intensity after τ seconds of time-averaging was given by $\delta I^2(d,\tau) = \delta I^2_{cell-to-cell}(d) + \delta I^2_{\text{int}}(d,\tau)$. The y-axis in Figure 7B is given by $\sqrt{\delta I^2_{cell-to-cell}(d) / \delta I^2(d,\tau)}$.

9.10. Additional sources of variation

The experimental analysis inevitably generates additional fluctuations. There are modest fluctuations in the background that introduce errors during background subtraction: compared to the magnitude of the intrinsic noise, the error from background subtraction is typically less than 10%, rising at most to around 30% at 5μm from a tip after 90s of time-averaging. Compared to the cell-to-cell variation, the error from background subtraction is even smaller. The photobleaching-correction methodology (as described in Methods) also introduces modest additional errors. Again, as compared to the magnitude of the intrinsic noise, the photobleach error is typically around 10%, rising to around 25% at 5 μm from a tip after 90s of time-averaging. Compared to cell-to-cell variation the relative photobleach error is again even smaller. The image analysis software also introduces additional errors when determining the precise location of the cell cortex. Again, this is a small effect, with errors on the scale of a couple of pixels (~0.1 μm since one pixel corresponds to a physical size of 65nm). This source of error is further reduced by binning of our data into 0.2 μm bins (corresponding to approximately three pixels). Finally, the camera does introduce a very small amount of shot noise, but this is completely negligible in comparison to the other sources of noise. Overall, we found our results were consistent across multiple experiments and were not significantly affected by any of the above factors.

Chapter Three: cdr2p concentrations define a cell size threshold for cell division

Kally Z. Pan[1] Timothy E. Saunders[2,3], Ignacio Flor Parra[1], Martin Howard[2] and Fred Chang[1]

1. Department of Microbiology and Immunology, Columbia University College of Physicians and Surgeons, New York, NY, 10032, USA
2. Department of Computational and Systems Biology, John Innes Centre, Norwich Research Park, Norwich NR4 7UH, United Kingdom
3. European Molecular Biology Laboratories, Meyerhofstrasse 1, 69117 Heidelberg, Germany

Abstract

Cell size is a key regulator of mitosis entry. However, the mechanism by which cells sense their size remains unclear. Recent finding suggests that in the fission yeast Schizosaccharomyces pombe, a protein gradient of the kinase pom1p may communicate cell length by signaling to the downstream kinase cdr2p which resides in a band of midsomes at medial cortex. To test this model, we quantified the amount of pom1p and cdr2p molecules at the medial cortex by quantitative fluorescent imaging in cells of varying length. Surprisingly, we find that pom1p levels at the cdr2p midsome band do not change as the cell grows, and varying the distribution of the pom1p gradient does not significantly affect cell length at division. However, cdr2p levels in the same region increase proportionally with the cell length and increasing cdr2p expression can lead to mitotic entry in shorter cells. Interestingly, small clusters of cdr2p are detected all along the cortex but are extremely unstable outside the medial cortex. These findings suggest that cdr2p concentrations at the midsome band acts as the signal for cell size and that pom1p may help to limit midsomes from forming at the cell tips.

Introduction

A critical aspect of cell division requires cells to reach a certain size before mitotic entry. However, a cell autonomous mechanism for cells to sense their size has yet to be identified. Recent studies in the rod-shaped fission yeast *Schizosaccharomyces pombe* have implicated the kinase pom1p maybe marking cell length by localizing as a dynamic gradient along the cortex of the cell. In this model, local concentrations of pom1p inhibit cdr2p, a downstream kinase that localizes in stable node-like structures at the medial cortex called midsomes and an activator of the cdk1 pathway. As cell length increases, the gradient nature of pom1p localization leads to a decrease in pom1p levels at the medial cortex, freeing cdr2p to activate cdk1 initiating mitosis.

However, both the small size of the system (cells go from a minimum of 7 μm to a maximum of 14 um at division) and the small numbers of pom1p molecules involved (approximately 2500 molecules at the cortex) result in extremely "noisy" gradients that are highly variable both in time and from cell to cell. Through our previous studies, we constructed a model based on measurements of pom1p dynamics that explored the range of differences in gradients that could result in a detectable signal through this noise. In this study, we investigate further this mechanism by focusing at areas where the pom1p/cdr2p signaling is thought to occur, at the cortex and more specifically at the midsomes where cdr2p mostly localizes. First, we tried to establish the nature of the pom1p signal as the cells get longer by quantifying the amount of pom1p at the medial cortex.

When cells are deprived of nutrients, they undergo stimulated mitotic entry and produce smaller cells (Fantes and Nurse, 1977). It was thought that smaller cells allowed for better survival under resource poor conditions. A screen for more genes in this pathway led to the identification of cdr1p and cdr2p, both of which mutants were insensitive to nitrogen starvation in terms of cell size (Young and Fantes, 1987). Additionally, when cdr2p was deleted, cells became larger than wildtype, further evidence that cdr2p may be involved in sell size regulation. A close relative of Nim1 (also known as cdr1) in fission yeast and Gin4 in budding yeast, the 775 amino acid protein has a serine-threonine kinase domain near the N-terminus. Genetic and biochemical studies found that it associates with the N-terminus regulatory domain of wee1 and negatively regulates it through phosphorylation (Breeding et al., 1998; Kanoh and Russell, 1998).

Cdr2p was shown to mainly localize in the cortical band around the middle of the cell in stable clusters called cortical nodes or midsomes during interphase and to a medial ring during mitosis (Morrell et al., 2004). Targeting its localization seems to be the responsibility of its non-catalytic C-terminus (Morrell et al., 2004). During mitosis, these midsomes are responsible for the recruitment and assembly of the contractile ring component necessary for cytokinesis and cdr2p was show to be important in the anchoring of mid1p to the cortex. In conjunction with Rho/Gef2, this complex is perhaps the most important of over a dozen proteins in the midsome in defining the site of division (Almonacid et al., 2009; Ye et al., 2012). These studies show that cdr2p has an important role function in defining the division plane.

The localization of cdr2p into these midsomes, a complex that contains many cell size and spatial regulators such as wee1 and blt1, suggests that there may be a link between defining division and sensing space (Moseley et al., 2009). Enticingly, pom1p, another protein that is involved in division plane regulation also has dual roles in cell size and division plane placement (Bahler and Pringle, 1998). Recent studies have proposed cdr2p as a sensor for a cell length signal originating from pom1p gradients (Martin and Berthelot-Grosjean, 2009; Moseley et al., 2009). In this model, cortical cdr2p localized in midsomes are fixed at the cell middle. During interphase, they are constantly inhibited from signaling downstream to initiate mitosis by a significant local concentration of pom1p that originates from gradients centered at the two cell tips. According to this model, as the cell grows in length, the sources of the gradients grow further in distance from the cdr2p midsomes, whose positions are fixed at the cell middle. This reduced the amount of pom1p that can diffuse to the middle and inhibit cdr2p. At some critical distance, the concentration of pom1p falls belong a threshold and the signal from cdr2p is now significant enough for mitosis to occur. To test this model, we have quantitatively analyzed the pom1p gradients at the cell middle as well as the concentration of cdr2p over the entire cell cycle. While we could not find evidence that the concentration of pom1p changes in the middle of the cell, we have found that the cdr2p concentration increases proportionally to the growth of cell length. In addition, we have shown that changing the expression of cdr2p can change cell size during division. These results suggest that cdr2p and not pom1p is the signal for cell size.

Results

Pom1p gradients do not differ significantly with cell length

According to the gradient length signal hypothesis, a gradient of pom1p is established from the cell tip to the cell middle where cdr2p is localized. As the cell grows local concentration of pom1p at the cell middle should decrease eventually to the point where enough cdr2p becomes activated to trigger mitosis. To test this model, we have quantitatively analyzed the pom1p gradients in living cells expressing a functional pom1-tomato fusion protein at near-endogenous levels (Hachet et al., 2011; Padte et al., 2006; Saunders et al., 2012). We previously found that pom1p cortical gradients exhibit large variability in intensity and distribution from cell to cell, fluctuate over time in individual cells, and show little change with cell length (Saunders et al., 2012). This variability plus a short decay length relative to cell length led us to question whether these gradients can function reliably as "rulers". Here, we tested this gradient model further by measuring the concentration of pom1-tomato in a 3μm region along the medial cortex, where cdr2p nodes are located. Using time averaged data (which reduces the effects of fluctuations in the gradient over time (Saunders et al., 2012)), we found low but detectable pom1 cortical levels (Figure 3.1A, Supplementary Figure 3.1A,B). One of the key predictions of the gradient-based model is that pom1p levels decrease on the medial cortex as cells grow. However, measurements of pom1-tomato at the medial cortex in a population of cells showed no detectable decrease with cell length (Figure 3.1B).

However, these results were of compiled from a population of cells. In the previous chapter I have discussed at length the high extrinsic variation we observed from cell to cell, and the complicated methods cells may use to filter out that noise. Since the decision to divide is made from a cell by cell basis, we wanted to eliminate extrinsic noise from the equation. Therefore, we then tracked pom1p expression in a number of individual cells over interphase growth, but detected no decrease in medial pom1-tomato levels in individual growing cells over time (Figure 3.1C, D). These cortical measurements improve on previously reported pom1p measurements that integrate intensities over the whole cell (Martin and Berthelot-Grosjean, 2009; Moseley et al., 2009). Instead we find that intensity at this location was in general very low and exhibited large fluctuations in concentration over time and absolute intensities varied from cell to cell. This confirmed our observations seen in our data compiled from a population of cells and demonstrated that the variations both from cell to cell and within a cell over time were larger than any differences between short and long cells. Even when fluctuation was reduced dramatically following a 90 sec time averaging step consistent with observations made during our previous work indicating that pom1p travel in fast moving clusters on the cortex, did not produced any trend of pom1p concentration between short and long cells but did reduced the extrinsic variation we observed from cell to cell(Figure S3.1B). In general, it seems that pom1p concentration is very low and pom1p cluster may move very quickly over the targeted area producing large temporal fluctuations that ultimately do not increase as the cell grows. Thus, our cortical measurements show that it is unlikely that the pom1p concentration at the medial cortex is responsible for conveying information about cell length.

Why were these results in stark contrast to previous observations? Previous studies reporting a decline in pom1p expression at the cell middle in long cells measured the total pom1p intensity in the medial section of the cell (Martin and Berthelot-Grosjean, 2009; Moseley et al., 2009). We found that these whole cell measurements have artifacts stemming from the normal exclusion of pom1p from the nucleus (Saunders et al., 2012) (Figure 3.1A, Figure S3.1C, D). In both of those studies, sample cells were selected and imaged with a z-series stack taking in the entirety of the cell and flattened into a two-dimensional image by a sum projection. Then these projections were further flattened into a one-dimensional image by averaging up the pixel intensities of pom1p along the long axis of the cell, producing a convenient line graph of the pom1p intensity along the X-axis. However, this method introduces two caveats. First is fact that the cortical surface, much like a globe, is a curved surface along three dimensional space, and projecting this onto a line twice distorts the spatial distribution of the pom1p concentration much as the projection of a globe onto a flat map will distort the geographic distance of the land. This is complicated further due to the differences in curvature along the cortex as the middle of the cell is curved along two dimensions like a cylinder, while the tips of the cell is curved along all three dimensions like the cap of a grain silo. It is especially problematic that the area of the most interesting gradient variation is at the area where the cap and the cylinder connect. Flattening this three-dimensional information down would serve to decrease the variations seen in the pom1p along the cortical surface and would distort the spatial distribution of its gradients.

The second issue is that the summing all the intensity of pom1p through the entire cell includes the small but significant levels of pom1p inside the cell. While the studies do subtract out this extemporaneous measurement by subtracting out the average cytoplasm pom1p intensity, the subtraction is done uniformly through the cell. This does not take in account the curvature of the cell, which makes the contribution of cytoplasmic pom1p non-uniform through the length of the cell (less cytoplasm is at the cross-section of the tip of the cell then is at the body), it also does not take in account the variation introduced by organelles in the cell which does not contain pom1p. The largest of these is the nucleus. The lack of pom1p localization in the nucleus is evident in the dark holes seen in images of confocal sections through the middle of the cell (Figure 3.1A). Since the nuclear size also grows with the cell length, we hypothesized that when this large absence of intensity is taken into account, it may produce an artificial decrease in pom1p.

A critical component of our quantification was that the images used were single confocal sections of the cells through the cell middle. Since intensity read out occurred around the cortical surface only, our analysis did not include any of the pom1p localized in the cellular interior nor did it distort distance. This is essentially a small refinement of the methods that were used in quantifying and analyzing the pom1p gradient distribution used in the previous chapter and they are elaborated in detail in the methods section. One consideration of our method is that due to the fact that we analyze pom1p along the cortical length of one confocal section through the middle of cells, we exclude the rest of the pom1p on the rest of the cell. We have extensively observed cells through different orientations and have seen no relationship through the different rotational sides of the cell along its long axis. While the distribution of pom1p along the cortex around that axis is neither uniform nor symmetric, it is random. Thus, we reasoned that sampling additional cells were just as good as sampling around the same cell, and while technical limitations prevent the former, we have gone through great pains to ensure we have gathered enough data by the latter method.

As a control we analyzed the same data set from our images with the same methods used in the previous studies and were able to replicate the trend that was previously noted (Figure S3.1C). We noted that pom1p was not present in the nucleus and hypothesized that the growth of the nucleus would take a large and large proportion in the cell middle could have acted to artificially deflate the average pom1p intensity at the middle of the cell (Neumann and Nurse, 2007). To see the effect of the nucleus we replaced in the nuclear space with the average pom1p intensity in the cytoplasm. As expected, we found that the relationship between concentration and cell length was largely removed (Figure S3.1C).

Manipulation of gradient shape does not change division length

If pom1p concentrations at the media cortex are not increasing the cell length, perhaps changes to the pom1p gradient outside of the immediate medial cortex can still signal cell length. To investigate further the proposal that change in the shape of the pom1p gradient can determine the length of the cell and trigger mitosis we constructed strains tagging pom1p with different fluorescent markers that produced pom1p gradients with different slopes. GFP, dTomato, and 3GFP (triple tandem GFP) all have a slight but different tendency of forming oligomers. A higher affinity for each other should have the effect of enhancing the natural ability of pom1p to cluster, which as demonstrated in the previous chapter, should alter the steepness of the gradient. Changing the slopes of these gradients should not alter the amount of pom1p at the medial cortex as previously we have shown that pom1p has an extremely ability to buffer high local levels of pom1p away from the media cortex.

We compared the gradient profiles of these three strains and found that pom1-tomato produced the shallowest sloped gradient while pom1-GFP and pom1-3GFP produced progressively steeper gradients (Figure 3.1E, F, Figure S3.2A,B). Quantitative analysis of many of these gradients show that even while the relative differences in the fluorescence levels have been normalized, a significant difference in the average gradient decays in terms of steepness can be detected, particularly in case of pom1-3GFP (Figure 3.1F). Using pom1-tomato as a standard we calculate that this change is significantly different and is outside the normal range of differences seen in the variance of pom1-tomato expressing wildtype cells. We hypothesize that this should produce a measureable difference in division length. In particular, we expect that the pom1-3GFP, which has the steepest gradients, would divide at the shortest length, followed by pom1-GFP and then by pom1-tomato. However, when we measured the length of these cells at division (defined by the presence of Calcofluor staining at the septum region), we detected no significant changed in the mean division length between the pom1p tagged strains and wildtype with untagged pom1p (Figure 3.1G, H).

Consistent with this result, we detected no differences in the intensity or number of cdr2p nodes (Figure S3.2C-G). Together, these data suggest that the precise shape of the pom1p gradient is not a critical factor in cell size control, and are therefore not consistent with the previously proposed cell size model based directly on the spatial distribution of pom1p gradients. However, when we performed statistical analyze of the differences between the distributions of division lengths seen in the different background, we did observe a small but significant change in the pattern between the pom1-3GFP and the pom1-tomato. However, it is difficult to interpret what this difference means and could indicate that changing pom1p gradients may have impacted division in some other manner.

Local cdr2p concentration at the medial cortex increase proportionately with cell length

To further investigate how this regulatory pathway may sense cell size, we focused on the next protein in the pathway, cdr2p. Cdr2p is a component of medial “nodes”, which are complexes of membrane proteins on the plasma membrane localized in a broad band surrounding the nucleus.

Pom1p may exert its effects on cdr2p in part by ensuring the proper localization of cdr2p nodes to this band (Celton-Morizur et al., 2006b; Martin and Berthelot-Grosjean, 2009; Moseley et al., 2009; Padte et al., 2006). However, how cell size affects cdr2p at the nodes is not known. We quantified the amount of cdr2p in cells by comparing fluorescent intensities with several previously published standards rlc1p, bzz1p, and the bacterial motor protein motB. We found that during interphase, a substantial amount of the total approximately 9000 molecules of cdr2p per cell is concentrated in the midsomes localized at the medial cortex, which each midsome averaging around 88 molecules (Figure 3.2A, S3.3A). Fluorescence intensity measurements in a population of cells revealed that the concentration of cdr2-GFP in the whole cell remained approximately constant in cells of various lengths (Figure 3.2B). Thus, the total number of cdr2-GFP molecules is approximately proportional to the cell volume as the cells grow (Figure S3.3D). Strikingly, however, total cdr2-GFP levels in the medial nodes approximately scaled with the length of the cells during interphase; this correlation is seen in analyses of a population of cells (Figure 3.2C) and in time-lapse imaging of individual cells over time (Figure 3.2E,F). Although the cortical area containing the nodes also increased with cell length, this rate of increase was slower than the rise in nodal cdr2p intensity (Figure 3.2C).

As cell length increase, the area where cdr2p midsomes localize also increases to a degree. Measurement of cortical cdr2p intensity within a fixed band of 3 μm in width showed directly that the local concentration of cdr2p in this cortical region rises approximately 2 fold as cells grow through interphase (Figure 3.2D, Figure S3.4). This suggested that cdr2p concentration was increasing in the area.

An increase in cdr2p levels in the cortical band can be due to an increase in the number of midsomes or an increase in cdr2p in each midsome, or a combination of these two factors. To differentiate this, the number and intensities of each midsome in each cell was compared with cell length. We found that the number of nodes in each cell increased as the cells grew (Figures 3.2G, S3.2E,G and S3.5). However, the cdr2-GFP intensity of each node remained similar (Figures 3.2H, S3.2D, F and S3.5), suggesting that the maximum number of cdr2p per node must be capped. This was confirmed when we compared the distributions of cdr2p intensity per midsome in long cells (over 12µm) and short cells (between 7 and 8µms). We found that when normalized for the additional number of midsomes, the distribution of the brightness of each midsome per cell was nearly identical (Figure 3.2H). In other words, midsomes were more numerous in longer cells but their brightness levels were preserved. Thus, instead of each node accumulating more cdr2p as cells grew, new nodes assemble, thereby leading to a higher density of nodes and an increase in the total cdr2p levels in the medial nodes. Further analysis revealed that cdr2p is a component of a system of dynamic cortical membrane proteins at the nodes. Time-lapse imaging showed that mature nodes are highly stable, as they moved only extremely slowly and exhibited little change over hours. Each node was estimated to contain an average of approximately 88 cdr2-GFP molecules (Figure S3.3B). However, FRAP studies revealed that cdr2-GFP within each node turned over with a $t_{1/2}$ of about 3 min (Figure S3.6). Imaging revealed a subpopulation of less intense and more motile cortical nodes that may be newly assembling ones.

We were curious to see if this relationship was seriously dependent on the pom1p gradient. Therefore, we returned to the strains that expressed with, pom1-GFP, and pom1-3GFP to see if the cdr2p marked midsomes respond to changes in the pom1p gradient. We quantified the cdr2-GFP midsome intensity in these cells and found the same relationship between cortical band intensity and cell length (Figure S3.2D, S3.2F). We also looked at midsome number and found that midsome number also increased with length in these cells as well (Figure S3.2E, S3.2G). In addition, we found that cdr2p marked midsome numbers were similar across all three pom1p tagged backgrounds for cell of similar length.

Modulating cdr2p expression in cells results in corresponding changes in division length

To investigate if surpassing a cdr2p concentration threshold would be sufficient for initiating mitosis we regulated the expression of cdr2p through the addition of an nmt81 promoter. Although it was previously shown that reduction in cdr2 causes cells to become longer, the ability of cdr2 to promote mitosis and produce shorter cells has not been demonstrated. We hypothesized that increasing total cellular levels of cdr2p may also increase cdr2p accumulation at the medial cortex in nodes. If this happened, then we may be able to preemptively trigger the division response if a simple threshold based system is the length sensing mechanism. Therefore, we induced a slight overexpression of cdr2 by the activation of the nmt81 promoter via thiamine treatment over a 16 hour period at 25^{o}C. As expected, division length of wildtype cells without the nmt81 promoter did not differ significantly upon the removal of thiamine from the growth media. However, upon the removal of thiamine, division length of cells with nmt81-cdr2 is dramatically reduced from the wildtype (Figure 3.3A).

Cells deprived of thiamine for 16 hours show a dramatic increase in cdr2p expression and in the number of cdr2p midsomes compared to cells of similar lengths of wildtype cells (Figure 3.3A). Furthermore, in the absence of thiamine for 16 hours, division length reduced to 12.3±1.2 µm (Figure 3.3B), suggesting that cdr2p concentration is the signal that trigger a cell division. Consistent with this hypothesis, we found that cell length at division is much longer at 16±2.4

μm in cells treated with thiamine than in wildtype cells which divide at 13.6±1 μm (Figure 3.3B). This response mimics the increase in division length seen in cdr2p deleted cells and seems to indicate that reduced levels of cellular cdr2p is enough to delay cellular entry into mitosis. Interestingly, the division lengths in cells underexpressing cdr2p is distributed over a much broader range, which may suggest that whatever remaining mechanism for triggering mitosis is much less sensitive to cell length. Image analysis of a nmt81-cdr2-GFP strain verified that both the intensity and the number of cdr2p midsomes are significantly reduced in the presence of thiamine, where even very long cells do not have the number of midsomes seen in wildtype cells of average length.

A critical issue in cell size regulation is whether cdr2p levels are indicative of cell size or passage of time (Turner et al., 2012): is cdr2p a “sizer” or a “timer?” To test these models, we first arrested cell growth by treating cells with the actin inhibitor Latrunculin A (Ayscough et al., 1997; Chang, 1999). A simple timer would be predicted to continue to increase over time, even without cell growth, while a sizer would not increase without cell growth. Over hours, Latrunculin A-treated cells exhibited no growth and showed no increase in cdr2-GFP levels at the nodes (Figure 3.3E). Next, we compared cells with different growth rates. We used formin *for3*Δ mutants, which exhibit highly variable growth rates (Feierbach and Chang, 2001). This mutant allowed us to measure cells with the same genotype and growth conditions in the same microscope field, but with growth rates that vary over 2-fold. Measurements of cdr2-GFP in these cells showed that the rate of cdr2-GFP accumulation at the nodes correlated with the rate of cell growth, but not with time elapsed (Figure 3.3F, Figure S3.7). Thus, cdr2p has properties of a “sizer” rather than a “timer.”

A model for cdr2p accumulation and length sensing

We next investigated the mechanism responsible for cdr2p-based sensing of cell size. Using time-lapse spinning disc confocal imaging, we detected three species of cdr2-GFP in interphase cells: those in medial membrane-bound nodes, a diffuse cytoplasmic haze, and interestingly, dim dots of cdr2-GFP all around the cortex (Figure 3.4A). This dim cortical population, which has not been observed previously, is highly dynamic, with the pattern of dots changing with every time frame (taken every 10s). Interestingly, the distribution of these cortical cdr2-GFP species did not vary over the cell tip, and thus did not correlate with levels of pom1p at cell tips. As described below, the presence of cdr2p all over the cortex suggests how cdr2p might function as a cell size sensor.

Although the above experiments have provided much information about the behavior of cdr2p, it remains unclear why the nodal cdr2p density scales with cell size. In order to provide mechanistic understanding, we used our data on cdr2-GFP to develop a quantitative model (Figure 3.4B, C). The model postulates that there is a dynamic flux of cdr2p from the cytoplasm to the plasma membrane, then to the nodes and then back to the cytoplasm. The model is based on the following assumptions, motivated by our experimental results: 1) the concentration of cdr2p in the cytoplasm is homogeneous and changes only slightly with cell length (Figure S3.8A); 2) cytoplasmic cdr2p molecules can bind all over the plasma membrane, and subsequently move rapidly by diffusion on the cortex (Figure 3.4A); 3) cortical cdr2p molecules can transition to associate with stationary node structures on the medial cortex; 4) both cortical and nodal cdr2p can then unbind and return cdr2p to the cytoplasm; 5) cytoplasmic cdr2p can then diffuse rapidly before rebinding to the membrane. As the timescale of cell growth (hours) is much slower than the timescale of the cdr2p dynamics (minutes, Figure S3.6), we assumed that the molecular system is, at any given time, effectively in steady state. These behaviors were represented by two mass-action equations for cortical and nodal cdr2p, and solved analytically. This model is shown in Figure 3.4B, along with its parameters, their experimental determination/constraints and analytic solutions in Figure 3.4C. Using the experimentally determined nodal/cortical areas, and with other parameters either measured or constrained from our experiments (see Description of Model in Methods), we then fitted total cdr2p levels in the medial nodes from the model as a function of cell length with those measured experimentally, with good results (Figure 3.4D). Note that the local cdr2p density in the medial nodes also then necessarily scales with cell length, due to the limited change in the nodal area (Figure 3.4E). A more sophisticated model with spatially-varying cdr2p on the cortex generated similar results (Figure S3.8B-F and Supplementary Materials).

This model has similar elements to a microtubule length control mechanism termed the “antennae model”, where longer microtubules bind more motor proteins, which then accumulate at the microtubule end in a length dependent manner (Varga et al., 2006). In the cell size sensing case, the whole surface area of the plasma membrane may be regarded as an “antennae,” so that cells accumulate more cdr2p bound on the plasma membrane as they grow, which leads to surface area-dependent accumulation of cdr2p at the nodes. Similar to the microtubule model, the property of cdr2p to first bind to the plasma membrane (as opposed to binding the nodes directly) is critical for this mechanism to read out cell size. If cdr2p bound to the nodes directly from the cytoplasm, the nodal cdr2p levels would not scale with cell size, as the cdr2p cytoplasmic concentrations themselves change only very slightly with cell size. Hence, our modeling has provided mechanistic understanding of how cdr2p can read out cell size, and elucidated which properties of cdr2p are key to its size-sensing capability.

The localization of a cdr2p sizer at cortical nodes provides several key advantages over other locales. First, as we have seen, it allows the local concentration of nodal cdr2p to increase as the cell grows. Other models have postulated sensing the nuclear concentration or the nuclear/cytoplasmic ratio of a sizer, but in many cell types (including in fission yeast), nuclear volume also increases as cells grow (Neumann and Nurse, 2007)(Figure S3.1D). Second, we speculate that the medial cortical placement of nodes surrounding the medial nucleus may allow cdr2p to communicate its local concentration to presumed targets such as wee1p and cdk1p on the nucleus. Although wee1p can be observed at some nodes upon overexpression (Moseley et al., 2009), its localization in late G2-phase is most clear at the spindle pole body (SPB) (Masuda et al., 2011), a structure on the nuclear envelope that is situated close (often < 0.5 μm) to the medial cortex, near the nodes. Cdk1/cyclin B and polo kinase are also located at the SPB (Alfa et al., 1990; Grallert et al., 2013; Masuda et al., 2011). Thus, we hypothesize that sensors on the SPB may detect local gradients of cdr2p (or other molecules) emanating from nearby nodes on the cortex. In this scenario, the proximity of the SPB to the medial nodes would be an additional critical geometric parameter in this system. Thus, a broad band of nodes encircling the whole nucleus may facilitate transfer of cell area information to the SPB and the nucleus.

Discussion

We have developed a new model for size control from a simple cdr2p concentration threshold based on our quantitative analysis of pom1p and cdr2p localization. From our analysis of the pom1p gradient, it seems unlikely that pom1p gradients are consistently different between cells of different sizes. Furthermore, differences in the pom1p concentration gradient do not seem to affect the pom1p concentration at the medial cortex overlapping the region of cdr2p marked midsomes. It is also unlikely that pom1p gradients affect the division cell length directly. While changing pom1p phosphorylation or kinase activity can affect its localization on the cortex, this may be only a secondary effect to how it signals division length. Our attempts to change gradient shape without altering the activity of pom1p show little measurable effect on the division length. However, it is difficult to separate pom1p activity and its localization as a gradient completely and our attempts are definitely limited in its success. Furthermore, the role of pom1p on cell polarity and division plane positioning may further complicate this matter as both these processes may have subtle effects on cell length as well. Further study is necessary to understand the role of pom1p on length control.

While it is certain that pom1p is necessary to restrict cdr2p midsomes from the tips of the cell, the ability for the pom1p gradient to affect cdr2p at the medial cortex is doubtful. There is evidence pointing to a direct interaction between pom1p and cdr2p that may affect cell division length, where this interaction is taking place is questionable. If this interaction directing cell length, then it’s unlikely that it’s taking place in the midsomes at the medial cortex. However, if the interaction is taken place elsewhere, it is unclear how the cell length can be transmitted given that a difference in expression levels cannot be detected anywhere else. If pom1p is acting through cdr2p to direct cell division length, it may only serve as a deterrent to prevent midsome localization to the tips of the cell. Once that has been accomplished, other factors may limit cdr2p midsomes to a certain band size. However, this does not preclude pom1p from acting in an independent manner to regulate division length.

Another critical issue is how different cells with widely varying cdr2p levels still reliably divide at an approximately fixed length. Model predictions for the cases of over and underexpression of cdr2p do not quite line up with our experimentally measured division lengths. In each cell the midsome cdr2p levels rise with cell size (Figure S3.7A) but to different absolute levels. This may be simply due to the fact that varying expression level in cells is an extremely unpredictable process, producing variable results from cell to cell. In fact we detected a significant increase in cytoplasmic cdr2-GFP levels in cells overexpressing cdr2-GFP. It could also mean that simply increasing the total cellular amount of cdr2p does not linearly impact the size sensing mechanism and other compensatory mechanisms, either passively or actively react to the dramatic increase in cdr2p levels. This is mostly likely the case due to the fact that cdr2p responsible for a variety of cellular processes and its regulators are many. In addition, there are already many known effectors of size sensing and division control whose impact on this simple threshold-based mechanism is completely unknown.

From our experiments with manipulating cdr2p levels in the cells, we can see that we are able to increase midsome numbers and drive a modest but significant decrease in division length. An important caveat to note is that the division length response was erratic and not replicated consistently in the cdr2-GFP strain even though overexpression of cdr2-GFP was consistent reproduced in the nmt81-cdr2-GFP strain. In some cases, cdr2-GFP cells became shorted when exposed to any type of EMM media. Given that the division length response to overexpression is consistent in cells not expressing a cdr2-GFP, it is possible that tagging cdr2 with GFP resulted in a partial gain of function. Interestingly, this is only seen in test conducted with minimal media and not YE5S, suggesting that nutrients may play a role in this early decision for mitosis.

While midsome numbers seem connected to cell length, it is still unclear how this is detected by the cell. If cdr2p concentration is the signal, what is the sensor? And by what mechanism the sensor detects cdr2p concentration? Genetic experiments tell us that the cdk1p pathway lay at the end of the road. Cdk1p is expressed in the nucleus and we have presumed that wee1p lying at the spindle pole body may act as the intermediary. However, how cdr2p signals wee1p is unknown and remains as an important question for future investigation.

Methods

S. pombe strain construction

Standard methods for *S. pombe* growth and genetics were used (Moreno et al., 1991). Strains are listed in Table S1. In general, strains were constructed using a PCR-based homologous recombination method to insert markers in the yeast chromosome (Bahler et al., 1998). Pom1-mGFP (pom1-1GFP) and pom1-3GFP strains were constructed by inserting mGFP and 3GFP constructs into the *pom1+* chromosomal locus from fragments amplified from pFA6a-mGFP-kanMX6 (monomeric GFP A206K mutation; Zacharias, 2002) and pFA6a-3GFP-kanMX6 (triple tandem GFP) (Martin and Chang, 2006; Wu and Pollard, 2005) , which were generously provided by JQ Wu.

For experiments to alter the expression of *cdr2+* (Figure 3.3) the nmt81 promoter (Basi et al., 1993). was inserted upstream of the *cdr2* chromosomal locus by homologous recombination using a PCR-generated DNA fragment derived from *pFA6a-kanMX6-P81nmt1* (Bahler et al., 1998). Correct insertion was verified by PCR of both sides of the construction using specific primers for the endogenous and inserted DNA. Multiple transformants showed the same cell size phenotypes. nmt81-cdr2 cells and the parental wildtype strain (FC15) were grown in EMM +5 μg/ml thiamine at 25ºC for two days, keeping the OD600 of the culture below 0.5 over the entire period. Cells were then washed 3 times by centrifugation at 2000 rpm with EMM, innoculated into EMM with or without 5 μg/ml thiamine, and then grown with shaking at 25ºC for 20 hr, and then samples were collected for micoscopy for cell length measurements. A *kanMX6-P81nmt1-cdr2-GFP-natMX* strain (KP268) was constructed by: starting with a *cdr2-*

GFP-kanMX strain (FC1441) and switching the *kanMX6* marker for *natMX* (Hentges et al., 2005); then inserting *kanMX6-P81nmt1* cassette at the N-terminus of *cdr2-GFP* in the genome using a fragment from *pFA6a-kanMX6-P81nmt1* . Constructs were verified by sequencing, and correct insertion was verified by PCR. Strains were backcrossed 4 times and checked for consistent expression levels and possible genetic modifiers.

Preparation of S. pombe cells

To prepare fission yeast cells for live cell imaging, cells were typically grown in liquid YE5S media at 25˚C with shaking in exponential phase for 18-24 hr. Cells were generally mounted in liquid YE5S media directly on glass. For long term imaging experiments, cells were plated on open 35mm glass bottom dishes (MatTek Corp.) with glass bottoms. To stick cells to the glass, dishes were coated with lectin by drying 5 µl of 1µg/µl lectin on the dishes; cells were applied and incubated for 5 min and then covered with 2 ml YE5S (Figures 3.1C, D, 3.2E, F).

For *cdr2+* dosage experiments (Figure 3.3), cells were first grown in YE5S cultures at 25ºC for two days, diluting them to keep their OD_{600} 0.2-0.8 over the entire period. Then they were washed by centrifugation in a microfuge at 4400 rpm with EMM + amino acid supplements and switched to EMM + amino acid supplements with or without the presence of 5 µg/ml thiamine. They were grown in 2.5 ml cultures in 25 X 100 mm Pyrex glass tubes with shaking for 16 hr at 25ºC, and then imaged live and assayed for length of septated cells and fluorescence intensity.

Pharmacological inhibitors and stains

Cycloheximide (Sigma) was used at a final concentration of 100 µg/ml from a stock of 10 mg/ml stock solution in ethanol and added to exponential phase cultures in YE at 25ºC (Polanshek, 1977). Samples were taken at indicated time intervals. Latrunculin A (LatA) was used at a final concentration of 200 µM from a 100X stock in DMSO (Chang, 1999). LatA was added in to cells plated onto a 35 mm glass bottom dish (described above) and the same cells were imaged for the next 2 hours. Cell lengths at division were generally measured from images of septated cells stained with 100µg/ml calcofluor or Blankophor.

Microscopy

Images were generally acquired using a spinning-disc confocal fluorescence NikonTI based microscope system (Nikon Instruments, Yokagawa, Solamere Technology) with an EM CCD camera (Hamamatsu Corp.) and a 100X 1.4 N.A. objective with a 1.5X magnifier (Saunders et al., 2012). A wide-field Nikon Eclipse 800 microscope and a 60X 1.4 N.A. objective was also used for some studies. FRAP studies were performed with a Zeiss 710 scanning confocal microscope.

Image Analysis

ImageJ (NIH) and custom MatLab (Mathworks) software were used for analysis.

Pom1 gradient analyses

For gradient profiles, generally, fluorescence intensity values around the cortex of cells were measured from images of cells in a medial focal plane, using custom MatLab software for the automated generation of a one-pixel wide mask around the cell cortex, followed by manual correction (Saunders et al., 2012). The single cell analysis of pom1-tomato (Figure 3.1C) used average projections of 5 0.5 sec continuous exposures. The average pom1-tomato intensity was measured in a 3-pixel wide by 3μm long rectangle over the medial cortex, and the mean background value outside of the cells was subtracted.

To measure the pom1p gradient decay lengths (Figures 3.1F, S3.2A,B), cells expressing the appropriate pom1-fusion were imaged for 3s at the mid plane. Cells segmented as described in Saunders *et al.,* 2012. Intensities normalized to one at the cell tip and background subtraction is performed such that the different fusions have zero intensity 5μm from the tip. Curves are fit to $\exp(-x/\lambda)$, where λ is the decay length of the profile (fitted λ shown in Figure S3.2A).

Cdr2 node analyses

Cdr2-GFP intensity was quantified using six different methods (Figure S3.4). (A) Maximum projections were made of 13 slices of confocal sections taken at 0.4 μm apart. A region of interest (ROI) was selected in ImageJ by hand around the cdr2p midsomes and excluding as much background as possible. The area and total intensity of the ROI was recorded, and the ROI width was determined by the spread of cdr2p midsomes along the long axis of the cell. (B) Simlar to A but the Maximum projection was taken from the top 3 slices consisting of the “top” cortical section of the cell. (C) Similar to A, except the ROI was selected by an image analysis program in Matlab (self-written) which selected only pixels over a predetermined threshold (approximately two times the mean background intensity). In this case, width was not determined. (D) Maximum projections were taken similar to A. We used the Find Maxima macro function in ImageJ to find the brightest pixel from a local intensity source (likely nodes), counting their number and totaling their intensity to estimate total intensity levels. In this case, width was also not determined. (E) We used a single confocal section through the middle of the cell and acquired images over 30 sec for a time averaged data set of 30 images. A region is then chosen from the averaged images that overlaps the cortical band (now see as a line on the perimeter of the cell) in a single pixel wide line that is 3 μm long. The intensity is measured from that line and is summed. (F) Maximum projections were made of 13 slices of confocal sections taken at 0.4 μm apart. Individual cells were then taken and rotated so their long axis was horizontal. A rectangular ROI was fixed at 3 μm wide and 3.72 μm tall for all cells and placed at the center of the cortical band. The mean intensity was the recorded in this fixed area.

In all these instances, the mean background intensity of an area outside of cells was subtracted for each pixel. These different methods all resulted in the same linear increase of cdr2-GFP intensity levels in the cortical band region in relation to increasing cell length. However, due to the fact that each method measured cdr2-GFP levels incompletely in different ways, the exact slope and variance of the correlation differed from method to method.

The single cell analysis of cdr2-GFP in wildtype and in the *for3Δ* background (Figure 3.2F, 3.3F) used a maximum projections of stacks comprised of 13 confocal sections 0.4 μm apart. Intensities were measured in a hand drawn ROI that contained the majority of cdr2 nodes and the mean background value outside of the cells was subtracted. In the measurements of rates of growth and cdr2 accumulation in *for3* mutants (Figure 3.3F), growth rates were calculated by a linear fit to the cell length as a function of time (images every 30 minutes), over 90-120 min.

The error in the fit is then calculated for each cell (as described http://mathworld.wolfram.com/LeastSquaresFitting.html). The change in intensity of cdr2p with time is also calculated by a least squares linear fitting. To test whether the positive correlation between growth and cdr2p accumulation rates was a statistical outlier, we performed numerical simulations using the distributions of the measured rates and their errors to create *in silico* data. We then performed a linear least squares fitting to find the level of correlation and test whether the level of correlation was equal or greater than that of the original data. Repeating this process 10^6 times, we found a probability of 0.0051 that the observed correlation in the data could have occurred by chance given the measured distributions of growth and cdr2p accumulation rates.

Protein counts were estimated by quantitative fluorescence intensity in ratios with standard proteins that had been quantitated previously (Coffman and Wu, 2012; Wu and Pollard, 2005) . GFP-MotB complexes in live bacteria were used as a standard at 22 GFP molecules/dot (Coffman et al., 2011; Laporte et al., 2011; Leake et al., 2006) .

To calculate the width of the nodal cdr2 region, we fitted Gaussian profiles ($ae^{-(x-x_0)/2\sigma^2}+b$) to time-averaged (90 second) mid plane images of the cdr2p profile (385 cells). We only analyzed cells with good quality of fit (so that the Gaussian fit is a reasonable approximation to the profile and hence the measured σ is meaningful) and $\sigma > 0.5$ µm (which excludes cells with distorted fits due to one very bright nodal region), leaving 237 cdr2p intensity profiles for analysis. Each cell was binned according to length (8-9µm, 9-10µm, …) and the mean and standard deviation calculated within each bin, Figure 3.2C. This data was used as the input to the model for the spread of cdr2p during cell growth.

Mathematical modeling

Cell morphology: Fission yeast geometry is approximated as a cylindrical body with hemispherical caps at either end. The cell has radius R and total length L, hence the cylindrical body has length $L\text{-}2R$. The total surface area of the cell is given by $A_{cor} = 2\pi RL$ and the total volume is $V = \pi R^2(L\text{-}2R/3)$. The radius of the cell is approximately constant at about R=1.5µm, while over the cell cycle the cell length grows from about L=7µm to L=14µm.

Different forms of cdr2p: In our modeling cdr2p is taken to have three forms: cytoplasmic, cortical and nodal. (1) Cytoplasmic cdr2p has a homogeneous concentration, $\rho_{cyt} = N_{cyt}/V$, which does not change significantly with cell size, as found experimentally, Figure S3.8A. (2) Cytoplasmic cdr2p can associate with the membrane. For this cortical cdr2p population, N_{cor} denotes the copy number and $\rho_{cor} = N_{cor}/A_{cor}$ is the corresponding concentration. (3) The cortical cdr2p can cluster in nodes at the midcell cortex in a cylindrical region defined by the length ω. For this nodal cdr2p population, N_{nod} denotes the copy number, with corresponding concentration $\rho_{nod} = N_{nod}/A_{nod}$, where $A_{nod} = 2\pi\omega R$ is the area of the cell membrane occupied by the nodes.

We employ two approaches in our analysis. First, guided by our experimental data, we take the cortical cdr2p population as diffusing rapidly and hence having an approximately uniform distribution around the cell membrane. The nodal cdr2p is taken to be uniformly distributed within the nodal region. In the second approach we explicitly consider diffusion of the cortical cdr2p population.

Timescales: From our cdr2p FRAP experiments, the lifetime of the nodal cdr2p is on the order of three minutes (Figure S3.6). From live imaging of cortical cdr2p (Figure 3.4A), cortical cdr2p dynamics are rapid, with a timescale on the order of seconds. However, cell growth is considerably slower (with doubling times on the order of hours) and hence we solve the subsequent equations for cdr2p with each cell size considered to be in quasi-steady-state.

Model I: Uniform cdr2p populations

Here the uniformly-distributed cdr2p populations in quasi-steady-state are described by the following equations:

$$0 = \beta \frac{A_{cor}}{V} N_{cyt} - \nu N_{cor} - \alpha \frac{A_{nod}}{A_{cor}} N_{cor}$$

$$0 = \alpha \frac{A_{nod}}{A_{cor}} N_{cor} - \eta N_{nod},$$

where β is the association parameter of cytoplasmic to cortical cdr2p, ν is the disassociation rate of cortical cdr2p back into the cytoplasm, α is the rate of uptake of cortical to nodal cdr2p and η is the disassociation rate of nodal cdr2p back into the cytoplasm. These equations can be solved exactly:

$$\rho_{nod} = \rho_{cyt} \frac{\beta}{\eta} \left(\frac{\nu}{\alpha} + \frac{\mathrm{A}_{nod}}{A_{cor}} \right)^{-1} \quad \text{and} \quad \rho_{cor} = \rho_{nod} \frac{\eta}{\alpha}.$$

The value of β is not important as it only enters our solutions as a constant prefactor. The rate of cdr2p disassociation from the nodes back into the cytoplasm, η, can be estimated from our FRAP experiments (Figure S3.6). We find that the cdr2p has a nodal occupancy time of around three minutes. We can therefore estimate $\eta = 5/10^{-3}\mathrm{s}^{-1}$.

Much higher concentrations of cdr2p in the nodes are experimentally observed than elsewhere on the cortex. From above, since $\rho_{nod}/\rho_{cor} = \alpha/\eta \gg 1$, we therefore require that the rate α of uptake of cortical cdr2p into the nodes be considerably greater than the rate η of nodal cdr2p disassociation back into the cytoplasm. This constraint places a lower bound on α, and consistently we choose $\alpha = 0.3\mathrm{s}^{-1}$.

Experimentally we observe significant scaling of ρ_{nod} with increasing A_{cor}. For this to occur, our model requires that two key criteria be met. Firstly, the cortical cdr2p must be much more likely to be taken up into the nodes than disassociate from the cortex, i.e. from above $v/\alpha \ll 1$. Since α is already constrained, we have a further restriction on v. Accordingly, we choose $v = 5/10^{-3}\mathrm{s}^{-1}$, meaning that the cdr2p disassociation rates from the nodes and cortex are the same. Secondly, A_{nod}, the area of the nodal region, must not scale proportionally with A_{cor}, the total cell area, as the cell size increases. Importantly, this model requirement was verified experimentally, see Figure 3.2C. In the model, the width ω of the nodal region was fitted to the observed width of the cdr2p membrane profile using $\omega = aL + b$ (for cells $9\mu\mathrm{m}<L<14\mu\mathrm{m}$). This experimentally determined increase in the area occupied by the cdr2p nodes, although small, was incorporated into the model output, as was the value of A_{cor}, through the ratio $A_{nod}/A_{cor} = \omega/L$. Note that as long as an overall cylindrical cell shape with hemispherical ends is maintained as the cell grows, the radius cancels out even if it is not constant.

Finally, the model also included the experimentally observed (slight) decrease in ρ_{cyt} as a function of cell length, Figure S3.8A black line (gradient = -0.01 after normalization to the average cytoplasmic intensity). However, there was little difference in our results between this case and when assuming a strictly constant ρ_{cyt}.

As shown in Figure 3.4D-E, the above model can recapitulate the observed cdr2p scaling. The larger the value of α, the stronger the scaling effect will be, as more cortical cdr2p - which effectively “measures” the cell area - is taken up into the nodes - which effectively “read-out” the spatial measurement.

Model II: Incorporating cortical cdr2p diffusion

Incorporating cortical diffusion into the model is straightforward, though solutions now need to be found numerically. We assume that the cytoplasmic cdr2p is still homogeneous and at an almost constant concentration, decreasing only slightly with cell length as described above. Assuming that on the membrane the cdr2p densities only depend on the long-axis coordinate, *x*, the equations become, at quasi-steady-state:

$$0 = D_{cor}\frac{\partial^2 \rho_{cor}}{\partial x^2} - \nu\rho_{cor} - \alpha(x)\rho_{cor} + \beta\rho_{cyt}$$

$$0 = D_{nod} \frac{\partial^2 \rho_{nod}}{\partial x^2} + \alpha(x)\rho_{cor} - \eta\rho_{nod},$$

with β, η and v taking the same values as before, Figure 3.4C. We now incorporate the width of the nodal region by using an association function $\alpha(x)$ for the uptake rate of cortical to nodal cdr2p. This scheme is, of course, a simplification of the true uptake dynamics, which presumably involve cdr2p aggregation and clustering. Nevertheless, this simplification is sufficient for understanding the mechanistic basis of size scaling. We take $\alpha(x) = \alpha_0 \exp(-x^2/2\omega^2)$, with $\alpha_0 = 0.5\ \text{s}^{-1}$, and where ω is the fitted width of the nodal region, as determined previously. In Figure 3.4A, we see that the nodal cdr2p does not move significantly over an extended period, suggesting $D_{nod}/D_{cor} \ll 1$. Therefore, we set $D_{nod} = 0$.

For the nodal cdr2p density to serve as a read-out of the entire cell membrane area, the typical cortical cdr2p diffusional displacement along the long cell axis must be at least 5µm. This requirement ensures that cortical cdr2p can diffuse along the long axis from the cell tips to the nodal region without first disassociating. Hence $\sqrt{(2D_{cor}\,\tau)} \gtrsim 5\mu\text{m}$, where τ is the lifetime of cortical cdr2p. Given a cortical cdr2p lifetime of around 3 minutes (see above), this implies that the diffusion constant should be greater than about $D_{cor} = 0.1\mu\text{m}^2\text{s}^{-1}$. In our simulations, we use $D_{cor} = 0.2\mu\text{m}^2\text{s}^{-1}$, but if the lifetime of the cortical cdr2p is shorter, then the cortical diffusion constant will need to be larger.

We solve the equations numerically in one-dimension with length L and hard wall boundary conditions, using Matlab. This model reproduces the profile of cortical/nodal cdr2p for different cell lengths (Figure S3.8B-D). The increase in nodal cdr2p concentration as the cell grows

(Figure 3.2F) is also captured (Figure S3.8E-F). In conclusion, within reasonable parameter ranges, the model prediction - that the concentration of cdr2p in the nodes increases with cell size - is robust to the inclusion of cortical cdr2p diffusion.

Cdr2p membrane localization without size control: If cytoplasmic cdr2p can only associate to the membrane by being directly taken up by nodes at midcell then we can simply leave out the cortical cdr2p form. In Model I, by balancing the cdr2p coming onto the nodes (parameter β) with that disassociating (rate η) we find $\rho_{nod} = (\beta/\eta)\ \rho_{cyt}$. The concentration of nodal cdr2p is now independent of cell size, assuming ρ_{cyt} is constant. A similar conclusion is reached if the nodes can form anywhere on the cortex by direct association of cdr2p from the cytoplasm.

For both these models, we see that the cdr2p nodal concentration no longer increases with the cell size. The system cannot sense cell size because both association and disassociation occur over the same region. To sense cell size we require one process, which here is the association of cdr2p anywhere onto the membrane, to scale proportionally with cell size. However, the second process, which here is the disassociation of cdr2p, must be localized over a region whose size does not scale proportionally with the total cell size as the cell grows.

Acknowledgements

I would like to thank the directors and students at the 2008 physiology course at the MBL for inspiring me to attempt more quantitative analysis of this work. Thanks also goes out to A. Kazatskaya for bring the right perspective to this project. As usual, additional thanks for the members of the Chang laboratory for thoughtful discussion and advice.

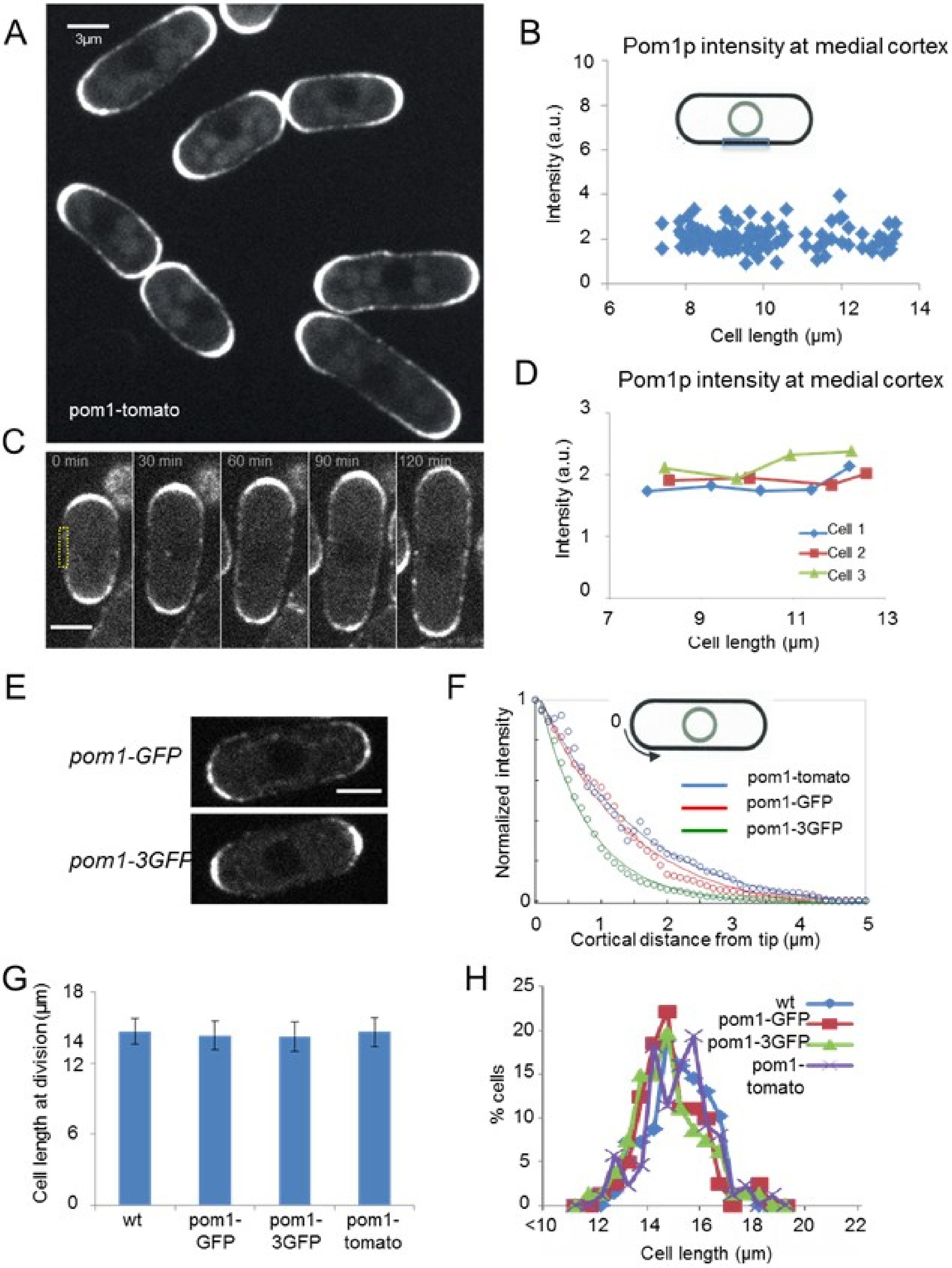
A
3μm
pom1-tomato
B
Pom1p intensity at medial cortex
Intensity (a.u.)
0
2
4
6
8
10
6
8
10
12
14
Cell length (μm)
C
0 min
30 min
60 min
90 min
120 min
D
Pom1p intensity at medial cortex
Intensity (a.u.)
0
1
2
3
7
9
11
13
Cell length (μm)
Cell 1
Cell 2
Cell 3
E
pom1-GFP
pom1-3GFP
F
Normalized intensity
1
0
0
1
2
3
4
5
Cortical distance from tip (μm)
pom1-tomato
pom1-GFP
pom1-3GFP
G
Cell length at division (μm)
18
14
12
6
0
wt
pom1-GFP
pom1-3GFP
pom1-tomato
H
% cells
25
20
15
10
5
0
<10
12
14
16
18
20
22
Cell length (μm)
wt
pom1-GFP
pom1-3GFP
pom1-tomato

Figure 3.1 Pom1p gradients do not differ significantly with cell length

A. Images of pom1-tomato gradients in wild-type fission yeast cells. Time-averaged image from spinning disc confocal images (60 frames over 3 min) of a medial focal plane is shown. Scale bar = 3 µm. Strain used was FC2054.
B. Measurements of pom1-tomato fluorescence intensity at the medial cortex using images like those in A. Total fluorescence intensities of a medial 3 µm segment along the cortical edge of interphase cells were measured (n = 50).
C. Time-lapse images of pom1-tomato in an individual cell. Time averaged image (5 frames over a 25 sec period) in a medial focal plane is shown in a single cell imaged every 30 min. Scale bar = 3 µm.
D. Total pom1-tomato intensities at the medial cortex (as measured in B) of representative individual growing interphase cells.
E. Confocal images (exposure 0.5 s) in a medial focal plane of pom1-GFP and the pom1-3GFP expressing cells. Strains used are FC1162 and FC2685. Scale bar = 3 µm.
F. Average normalized distribution of pom1p gradient profiles in cells expressing different fusions of pom1. Note that pom1-3GFP gradients have a shorter decay length than the other two (pom1-3GFP, pom1-GFP, pom1-tomato; n= 45, 31, 32 respectively). Peak absolute numbers of proteins of pom1-3GFP and pom1-1GFP gradients were similar, Figure S2A. Error bars not shown for clarity.
G. Average cell length at division for cells expressing no fusion or one of the indicated pom1-fusion proteins. (n > 100 septated cells for each). No differences between strains were found. Error bars = SDs.
H. Distribution of cell lengths at cell division in indicated strains.

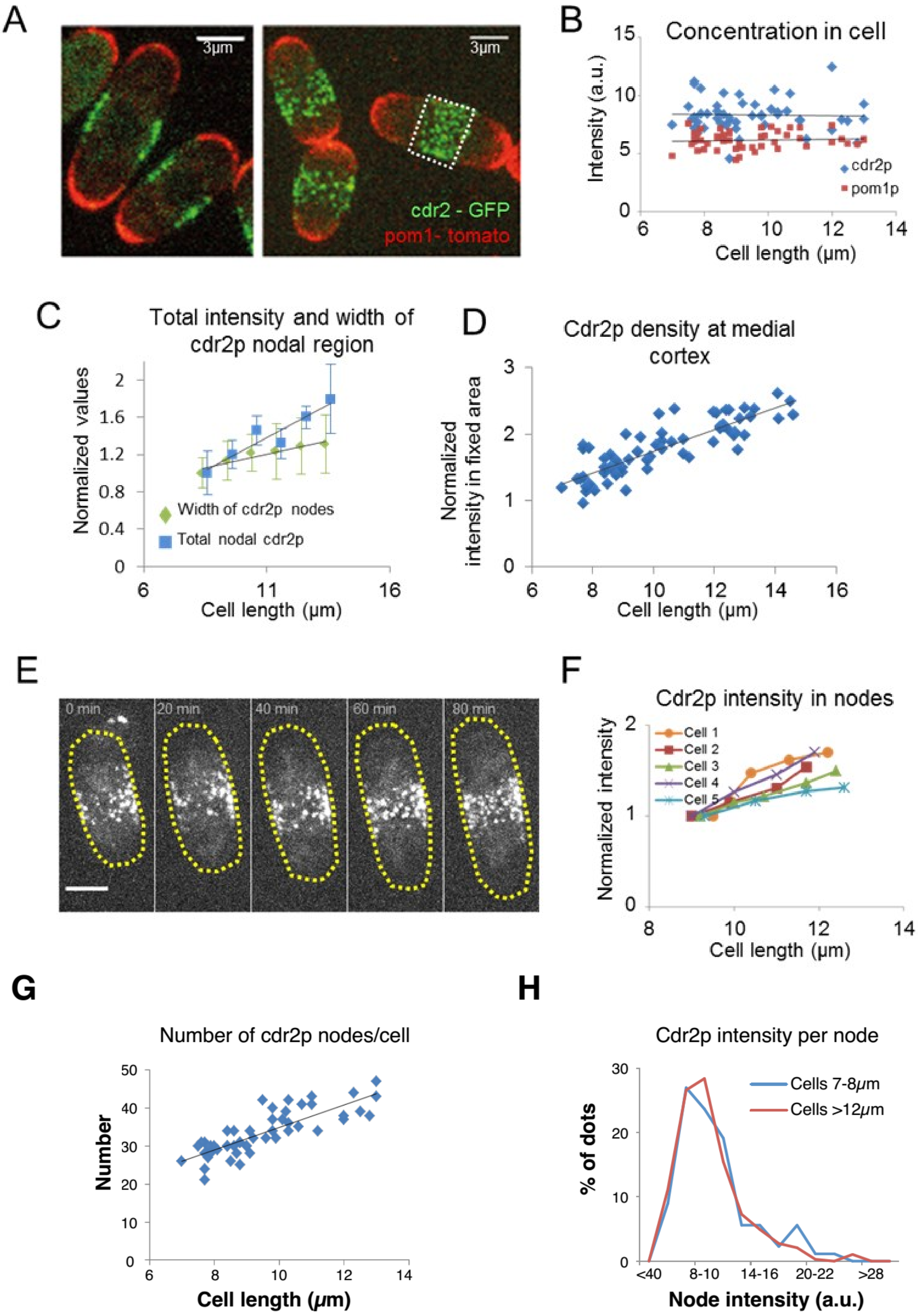
A
3µm
3µm
cdr2 - GFP
pom1- tomato
B
Concentration in cell
Intensity (a.u.)
15
10
5
0
6
8
10
12
14
Cell length (µm)
cdr2p
pom1p
C
Total intensity and width of cdr2p nodal region
Normalized values
2
1.6
1.2
0.8
0.4
0
6
11
16
Cell length (µm)
Width of cdr2p nodes
Total nodal cdr2p
D
Cdr2p density at medial cortex
Normalized intensity in fixed area
3
2
1
0
6
8
10
12
14
16
Cell length (µm)
E
0 min
20 min
40 min
60 min
80 min
F
Cdr2p intensity in nodes
Normalized intensity
2
1
0
8
10
12
14
Cell length (µm)
Cell 1
Cell 2
Cell 3
Cell 4
Cell 5
G
Number of cdr2p nodes/cell
Number
50
40
30
20
10
0
6
8
10
12
14
Cell length (µm)
H
Cdr2p intensity per node
% of dots
30
20
10
0
<40
8-10
14-16
20-22
>28
Node intensity (a.u.)
Cells 7-8µm
Cells >12µm

Figure 3.2 Local cdr2p concentrations at the medial cortex increase proportionately with cell length

A. Images of cells co-expressing pom1-tomato and cdr2-GFP. Left panel shows a medial confocal section, and right panel shows a maximum projection through the whole cell (13 images in each stack with 0.4 μm sections). Strain used was FC2678. Scale bar = 3 μm.
B. Concentrations of cdr2p and pom1p over the whole cell do not increase with cell length. Fluorescence intensity measurements of cdr2-GFP and pom1-tomato in the whole cell as a function of cell length. From maximum projections acquired as in A.
C. Cdr2p accumulates at the medial cortex as cell length increases. Cdr2p total intensity in the medial cortex (blue) was measured as described in Figure S4A (n = 51). Similar increases were observed using multiple approaches in image analyses (See Methods and Figure S4). Width of the cdr2p nodal band was measured along the long axis of the cell (see Methods). Error bars = standard error on the mean (n = 185). Black lines represent linear fits, r2 = 0.90 and 0.89 for width and intensity respectively.
D. Local concentration of cdr2p at the medial cortex increases as a function of cell length. Concentration was measured as total cdr2-GFP intensity in a fixed 3 μm wide medial band (see Figure S4E). n = 67. Black line represents linear fit with r2 = 0.71.
E. Time lapse images showing behavior of cdr2-GFP in an individual cell. From maximum projection acquired as in A. Scale bar = 3 μm.
F. Total normalized intensities of nodal cdr2-GFP in 5 cells tracked over time (measured from images such as E, see Figure S4A for method).
G. The number of cdr2-GFP nodes increases with cell length (n = 51). Black line represents linear best fit with r2 = 0.67. Nodes were determined after thresholding (Figure S4C), which provides a lower bound estimate.
H. The distributions of cdr2-GFP node intensities in short versus long cells. (n= 89 nodes in 9 cells, 286 nodes in 7 cells respectively). Nodes were determined as in G.

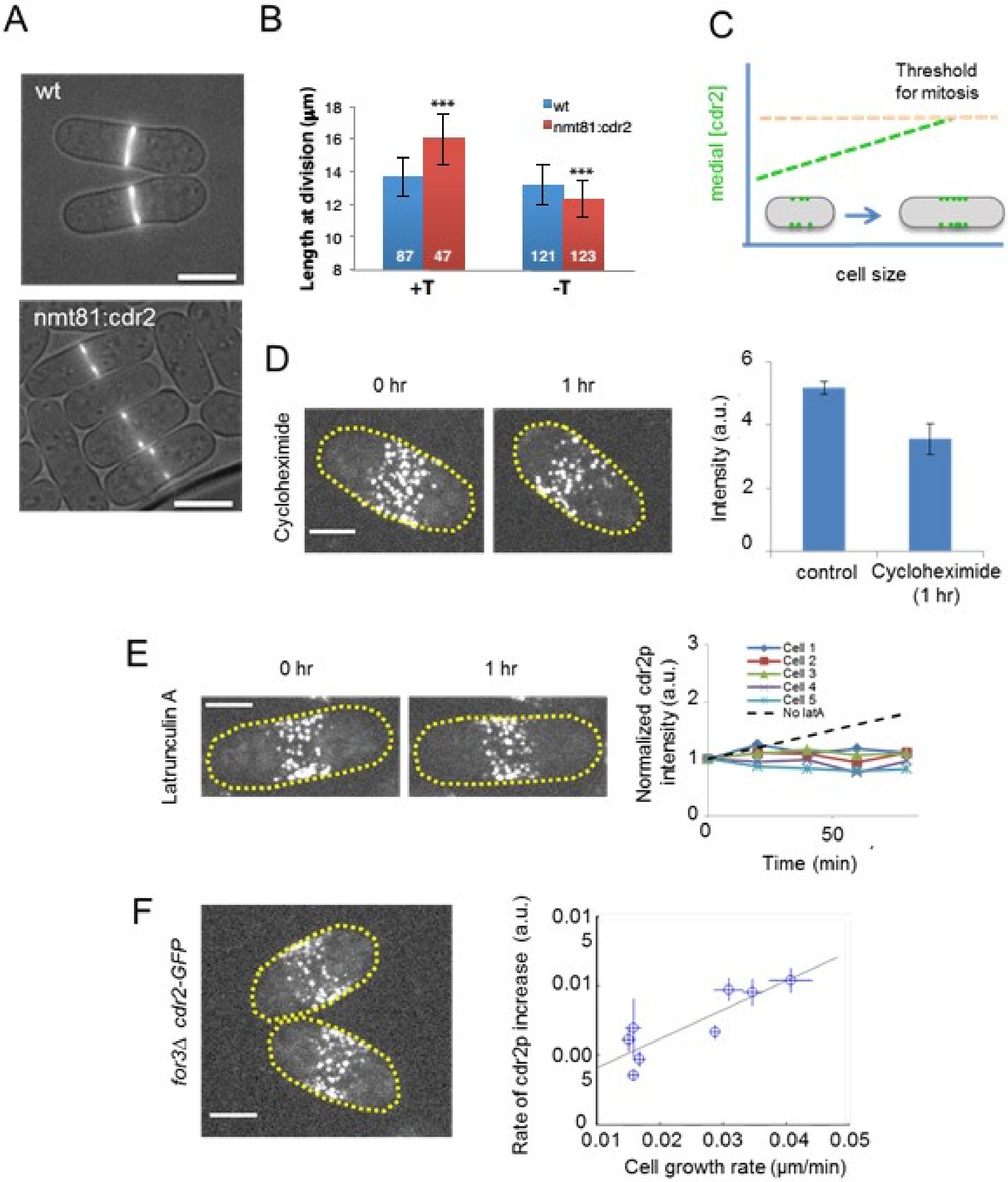
A
wt
nmt81:cdr2
B
Length at division (μm)
18
16
14
12
10
8
***
***
wt
nmt81:cdr2
87
47
121
123
+T
-T
C
Threshold for mitosis
medial [cdr2]
cell size
D
0 hr
1 hr
Cycloheximide
Intensity (a.u.)
6
4
2
0
control
Cycloheximide (1 hr)
E
0 hr
1 hr
Latrunculin A
Normalized cdr2p intensity (a.u.)
3
2
1
0
Cell 1
Cell 2
Cell 3
Cell 4
Cell 5
No latA
0
50
Time (min)
F
for3Δ cdr2-GFP
Rate of cdr2p increase (a.u.)
0.01 5
0.01
0.00 5
0
0.01
0.02
0.03
0.04
0.05
Cell growth rate (μm/min)

Figure 3.3 manipulation of cdr2p expression levels changes cell division length

A. Brightfield overlay with calcofluor stained wt cells after incubation in EMM AUL at 25^0C for 16 hours. (Experiment and analysis done by Ignacio Flor Parra)
B. Average cell length of dividing cells as visualized by calcofluor staining. N>85. (Experiment and analysis done by Ignacio Flor Parra)
C. Model that the local concentration of cdr2p in the region of the medial cortical nodes, which rises with cell length, is used to activate the G2/M transition.
D. Stability of cdr2-GFP protein. Measurements of cdr2-GFP in cells between 10 and 12 µm in length, treated with 100 µg/ml cycloheximide (Polanshek, 1977) or ethanol (control) for 1 hr, (n= 6 and 8 respectively). Images of two representative cells and measurements of cdr2 total nodal fluorescence intensities are shown. Scale bar = 3µm. Error bars = SD.
E. Cdr2-GFP at nodes does not accumulate without cell growth. Growth of wild-type cells was halted by treatment with 200 µM Latrunculin A, an actin inhibitor (Chang, 1999). Image of a single cell before and after 1 hr treatment. Graph shows total cdr2-GFP nodal fluorescence intensity in individual cells over time (measured as in Figure S4A). Dotted black line shows the observed average increase of total cdr2-GFP fluorescence in untreated cells (Figure 2F). Scale bar = 3µm
F. Rate of cdr2-GFP accumulation at nodes correlates with the rate of cell growth. Cdr2-GFP accumulation at nodes and cell growth were measured in time-lapse images of for3Δ mutant cells, which exhibit variable growth rates. Total cdr2-GFP nodal fluorescence intensity in individual cells was measured over time (as in Figure 2F and S4A). Image shows two representative cells. Graph shows a correlation of cell growth rate with the rate of accumulation of cdr2p in for3Δ mutant. Line is linear fit to the data (r2 = 0.75). The probability that the growth and cdr2 accumulation are more correlated than random is significant (p=0.005, see Supplementary Materials). Strain used was FC2690. Scale bar = 3 µm.

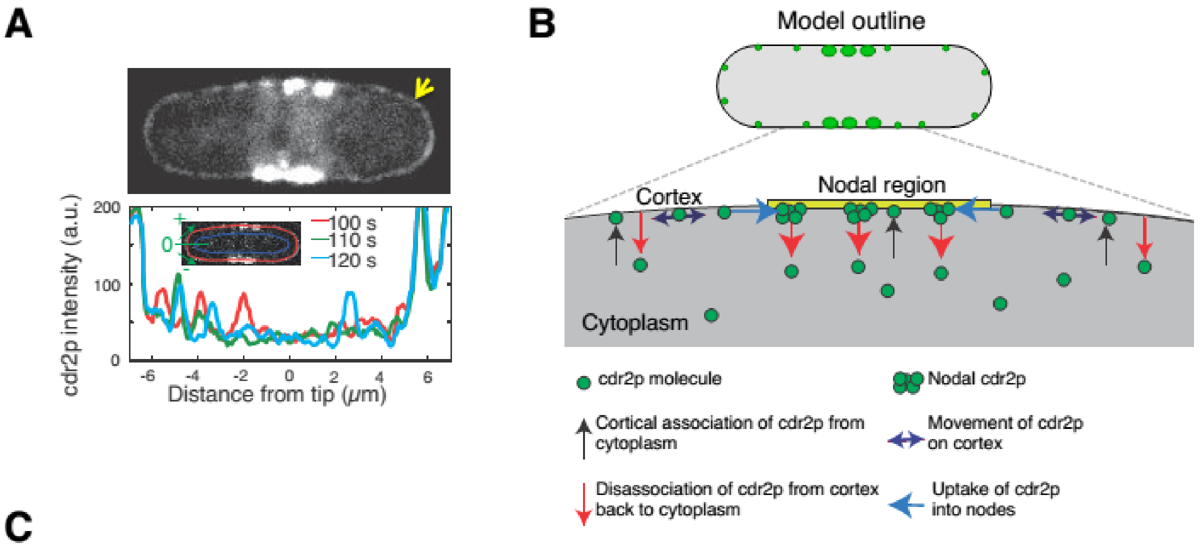

C

Model equations at quasi-steady state:

$$0 = \beta \frac{A_{cor}}{V} N_{cyt} - \nu N_{cor} - \alpha \frac{A_{nod}}{A_{cor}} N_{cor}$$

$$0 = \alpha \frac{A_{nod}}{A_{cor}} N_{cor} - \eta N_{nod}$$

where N_{cyt}, N_{cor} and N_{nod} are cdr2p molecule number in the cytoplasm, cortex and nodal regions respectively and V is the cytoplasm volume.

Solutions:

$$\rho_{nod} = \rho_{cyt} \frac{\beta}{\eta} \left(\frac{\nu}{\alpha} + \frac{A_{nod}}{A_{cor}} \right)^{-1} \propto \frac{A_{cor}}{A_{nod}} \quad \text{if } \frac{\nu}{\alpha} \ll 1$$

$$\rho_{cor} = \frac{\eta}{\alpha} \rho_{nod} \ll \rho_{nod} \quad \text{if } \frac{\eta}{\alpha} \ll 1$$

where $\rho_{cyt} = N_{cyt}/V$ is the cytoplasmic cdr2p concentration and
$\rho_{nod} = N_{nod}/A_{nod}$
$\rho_{cor} = N_{cor}/A_{cor}$

D

Parameter	Symbol	Value	
Cortical area	A_{cor}	~70–150μm²	Measured
Nodal area	A_{nod}	~20–25μm²	Measured
cdr2p cortical association	β	0.02μms⁻¹	Not important
cdr2p cortical disassociation	ν	0.005s⁻¹	Constrained
cdr2p nodal uptake	α	1.0s⁻¹	Constrained
cdr2p nodal disassociation	η	0.005s⁻¹	Measured

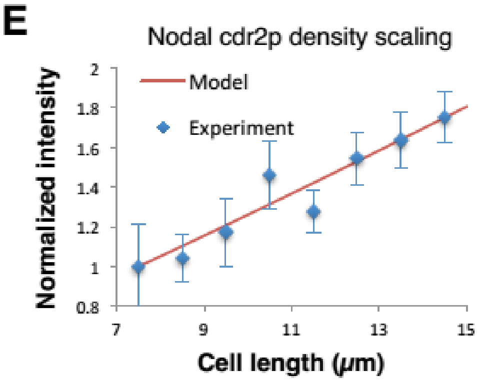

Figure 3.4. Model for cell size-sensing by cdr2p in fission yeast.

(Analysis and modeling were developed and performed by Tim Saunders)

A. Confocal time-averaged image (60 frames taken over a 10 minute period) in a medial focal plane of a cell expressing cdr2-GFP. Arrow highlights dim cdr2-GFP all around the cell cortex (see Supplementary Movie 1). The graph shows cdr2-GFP profiles on the cortex around one polar region at indicated time points. Cytoplasmic cdr2p appears brighter around the nodes because of out of focus nodal fluorescence. Scale bar = 3 µm. Strain used was FC2678.

B. Outline of model. The model employs three forms of cdr2p: cytoplasmic; cortex-bound; and bound to the cortex at a node. It assumes that cdr2p can associate anywhere on the cortex from the cytoplasm. Cortical cdr2p can either disassociate back into the cytoplasm or, if present in the nodal region, be taken up into nodes. Cdr2p can also disassociate from the nodes back into the cytoplasm.

C. Model details. Outline of equations describing cdr2p number on the cortex and in nodes, and the analytic solutions (within the approximations detailed in the Supplementary Materials). Parameters for the model are outlined in the table. "Measured" parameters are deduced from direct experiment, "constrained" parameters are limited by the requirements for scaling of total nodal cdr2 levels with cell length, and "not important" parameters do not play a role in determining scaling of total nodal cdr2 levels with cell length.

D. The model accurately reproduces the total nodal cdr2-GFP intensity as a function of cell length. Black line corresponds to the model. Parameters and equations are given in C. The model data was scaled by an arbitrary constant to overlap with the measured intensity data.

E. Model fit to the nodal cdr2-GFP density as a function of cell length. Parameters and equations are given in C. The model data was scaled by an arbitrary constant to overlap with the measured data.

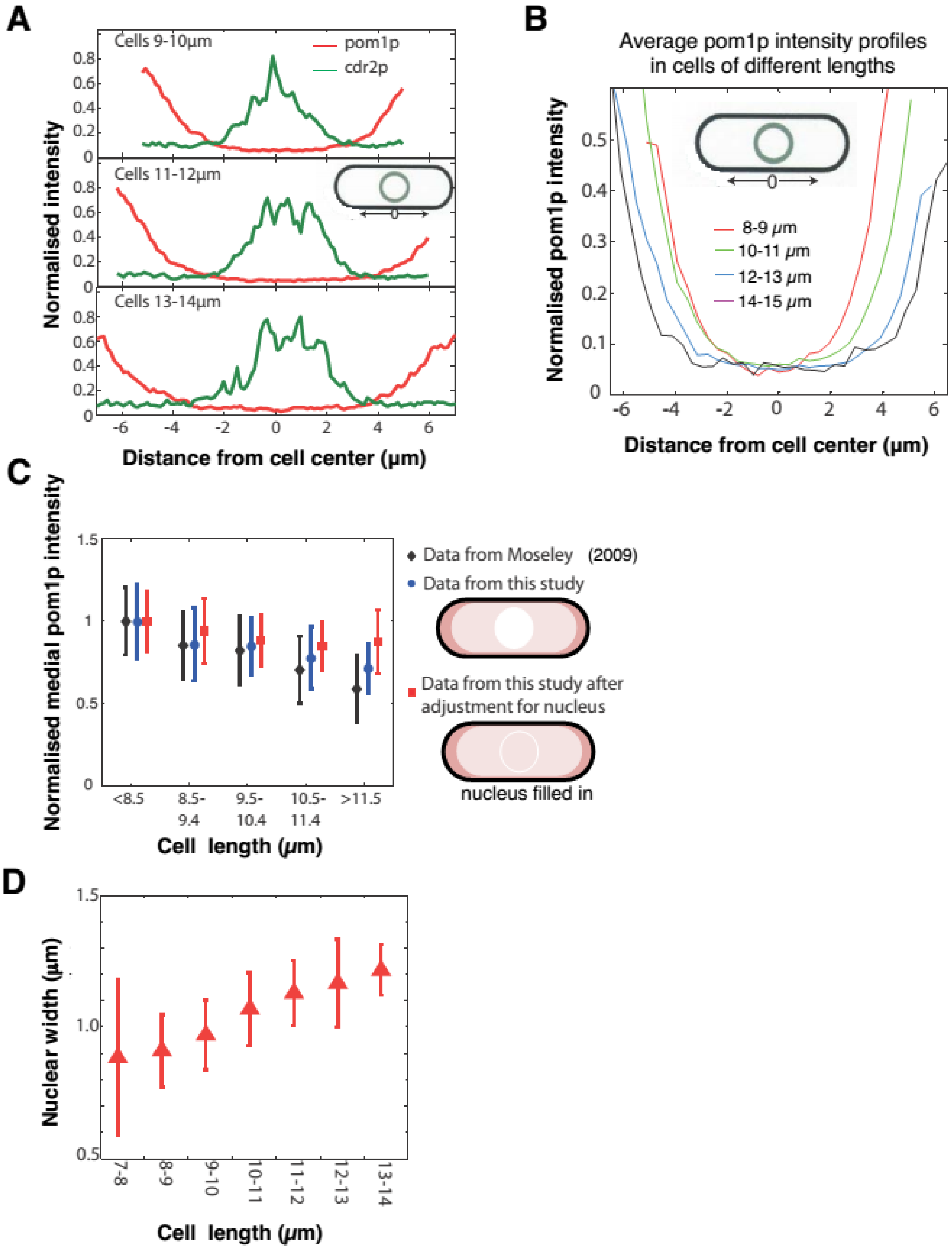
A
Normalised intensity
Cells 9-10µm
pom1p
cdr2p
Cells 11-12µm
Cells 13-14µm
0
0.2
0.4
0.6
0.8
-6
-4
-2
0
2
4
6
Distance from cell center (µm)
B
Average pom1p intensity profiles in cells of different lengths
Normalised pom1p intensity
8-9 µm
10-11 µm
12-13 µm
14-15 µm
0
0.1
0.2
0.3
0.4
0.5
-6
-4
-2
0
2
4
6
Distance from cell center (µm)
C
Normalised medial pom1p intensity
0
0.5
1
1.5
<8.5
8.5-9.4
9.5-10.4
10.5-11.4
>11.5
Cell length (µm)
◆ Data from Moseley (2009)
● Data from this study
■ Data from this study after adjustment for nucleus
nucleus filled in
D
Nuclear width (µm)
0.5
1.0
1.5
7-8
8-9
9-10
10-11
11-12
12-13
13-14
Cell length (µm)

Figure S3.1: Pom1p concentration at the medial cortex does not vary with cell length.

(Analysis and modelling were developed and performed by Tim Saunders)

A. Distributions of pom1p and cdr2p intensity around the cortex. Cells co-expressing pom1-tomato and cdr2-GFP were imaged for 3 seconds, with a 20 second interval between time points (30 measurements in total). Time-averaged intensities were measured around the cortex in the same cells as shown in the schematic. Normalized average pom1p (red) and cdr2p (green) profiles for varying cell lengths are shown. Top: n=78 cells, middle n=88 cells, bottom n=32 cells. Note that cdr2 nodes reside at the low point of pom1 gradients at all cell lengths.
B. Profile of pom1p intensity gradients at different cell lengths, based on data shown in (A). The measurement region is shown in the schematic.
C. Comparison of our data with previously published data. Moseley et al. (2009) and Martin and Berthelot-Grosjean M (2009) showed that in contrast to what we see, pom1p levels in the middle of the cell decrease with cell length. In the measurements of these papers, pom1p fluorescence in the whole cell was collapsed onto a single line. This method of image analysis differs from our approach of measuring pom1p intensity only on the cortex, where the gradient distribution is (Figure 1 and data above). We graphed measurements of pom1p in the middle of the cell as a function of cell length using different methods and data sets. The data from Moseley et al. is presented here as the black bars. We found that we found a similar trend using the same whole cell analysis on our own images of pom1-tomato cells (blue bars). pom1p is detectable at a low constant level all through the cytoplasm, but is not detectable in the nucleus (Saunders et al. 2011; Figure 1A). Therefore, we tested whether this difference between whole cell and cortical measurements may be due to lack of pom1p in the nucleus. We adjusted the effect of the nucleus by filling the nucleus with the average cytoplasmic intensity in silico. This adjustment largely abrogated the length dependent increase (red bars). We speculate that the decrease seen in the whole cell measurements may be due to slightly larger size of the nucleus in larger cells (Neumann and Nurse, 2007)(see Figure S1E below). Thus, the decrease seen in the previous publications may (partially) be an artifact of including cytoplasmic and nuclear fluorescence in addition to the cortical distribution.
D. Nuclear width as a function of cell length. Nuclear size was measured by the dark nuclear zone of pom1-tomato fluorescence. The width of the nucleus was determined as the maximum distance along the long axis of the cell. n=96 cells. Error bars = SD. Note that this method may provide a slight under estimate compared to measurements for instance of a nuclear envelope marker or a diffuse nuclear marker.

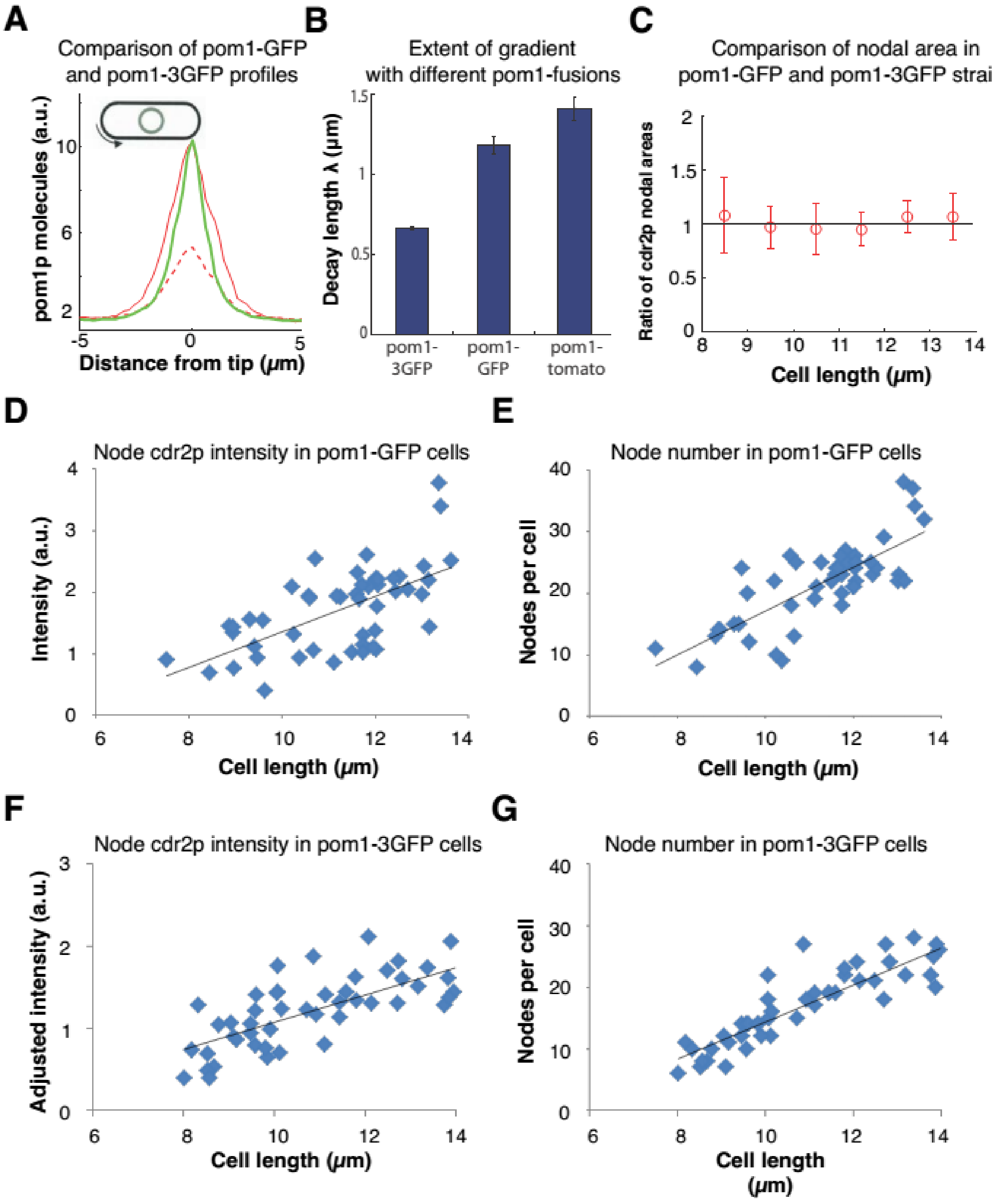
A
Comparison of pom1-GFP and pom1-3GFP profiles
pom1p molecules (a.u.)
10
6
2
-5
0
5
Distance from tip (μm)
B
Extent of gradient with different pom1-fusions
Decay length λ (μm)
1.5
1
0.5
0
pom1-3GFP
pom1-GFP
pom1-tomato
C
Comparison of nodal area in pom1-GFP and pom1-3GFP strains
Ratio of cdr2p nodal areas
2
1.5
1
0.5
0
8
9
10
11
12
13
14
Cell length (μm)
D
Node cdr2p intensity in pom1-GFP cells
Intensity (a.u.)
4
3
2
1
0
6
8
10
12
14
Cell length (μm)
E
Node number in pom1-GFP cells
Nodes per cell
40
30
20
10
0
6
8
10
12
14
Cell length (μm)
F
Node cdr2p intensity in pom1-3GFP cells
Adjusted intensity (a.u.)
3
2
1
0
6
8
10
12
14
Cell length (μm)
G
Node number in pom1-3GFP cells
Nodes per cell
40
30
20
10
0
6
8
10
12
14
Cell length (μm)

Figure S3.2: Pom1 gradients of different decay lengths do not affect cdr2 distribution.

A. Comparison of pom1-3GFP and pom1-GFP gradients. We compared the molecule number of pom1-3GFP with the pom1-GFP molecule numbers after adjusting for relative intensity difference (Intensity of adjusted pom1-GFP = Factor x ((raw pom1-GFP intensity) – (minimum pom1-GFP intensity)) + (minimum pom1-GFP intensity) where the red line corresponds to normalization to the total amount of pom1p in the cell and the dashed line represents the unscaled pom1-GFP number. These data show that these gradients have similar number of pom1p molecules at their peaks. (Analysis by Tim Saunders)
B. Fitted decay length of average pom1p intensity profile for three different fluorescent proteins (pom1-3GFP (n=45 cells), pom1-GFP (n=31 cells) and pom1-tomato (n=32 cells)). Note that these cells express the fusion as the only pom1p protein in the cell. Errors are the estimated from the fitting of an exponential curve to the average profile for each pom1p intensity profile. Intensity profiles are normalized to have the same intensity at the cell centers. We have confirmed that different normalizations (and also fitting to the raw data) do not significantly alter the measured decay lengths (Analysis by Tim Saunders).
C. Ratio of distributions of cdr2p nodes in cells with different pom1p gradient distributions. Maximum projection confocal images of cdr2-tomato in pom1-1GFP (49 cells) and pom1-3GFP (50 cells) strains were acquired and nodes were specified by a thresholding approach (see Methods). The ratio is defined as the area of the cdr2p nodes in the pom1-GFP strain divided by the area of the cdr2 nodes in the pom1-3GFP strain. Black line is guide to the eye.
D. Intensity of cdr2-tomato in nodes in pom1-1GFP strain. Black line is linear best fit (r2=0.39).
E. Number of cdr2-tomato nodes in pom1-1GFP strain. Black line is linear best fit (r2=0.61).
F. Intensity of cdr2-tomato in nodes in pom1-3GFP strain. Note that the intensities were adjusted to be on similar scale to (C). Black line is linear best fit (r2=0.55).
G. Number of cdr2-tomato nodes in pom1-1GFP strain. Black line is linear best fit (r2=0.80).

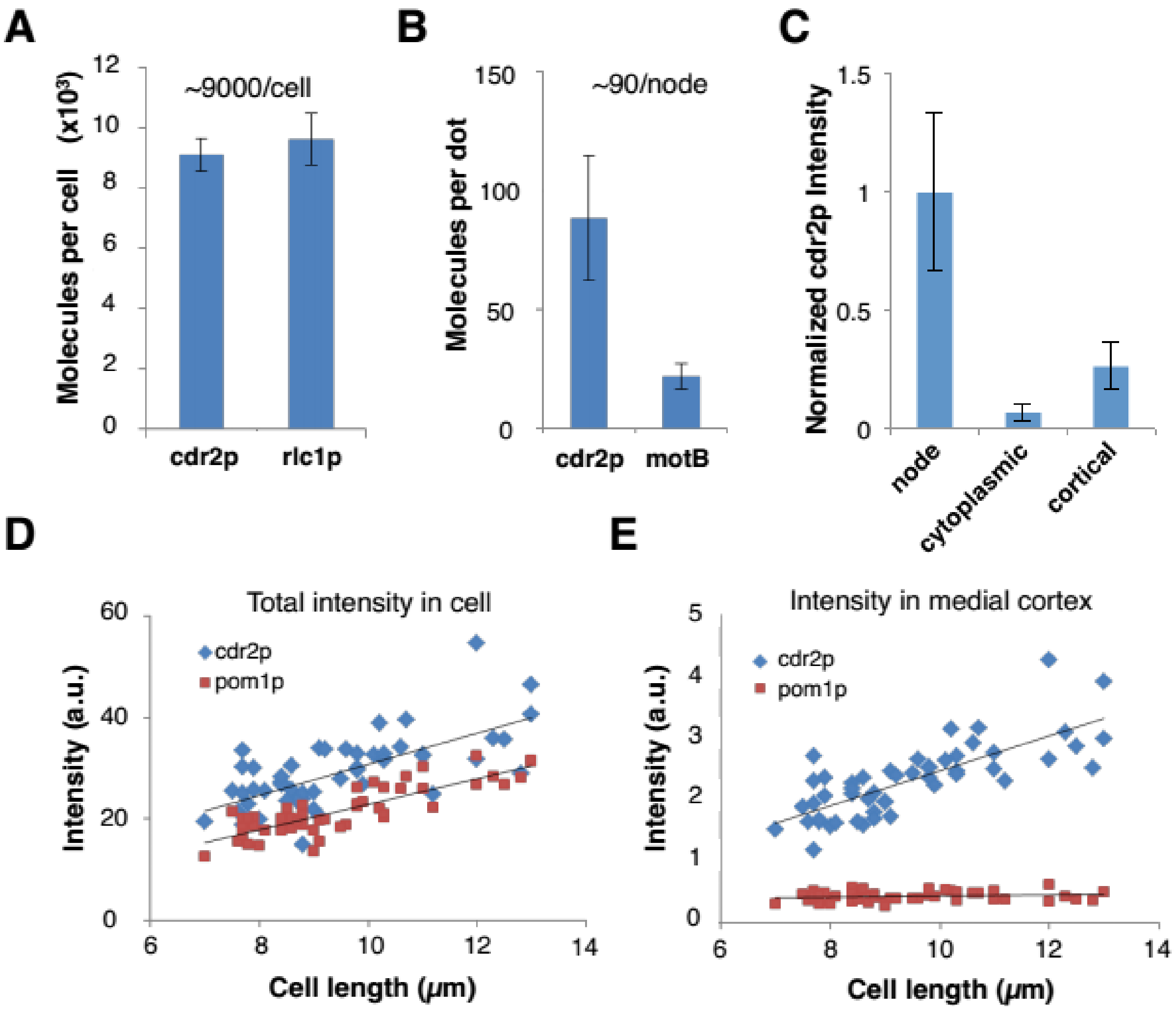
A
~9000/cell
Molecules per cell (x10³)
0
2
4
6
8
10
12
cdr2p
rlc1p
B
~90/node
Molecules per dot
0
50
100
150
cdr2p
motB
C
Normalized cdr2p Intensity
0
0.5
1
1.5
node
cytoplasmic
cortical
D
Total intensity in cell
cdr2p
pom1p
Intensity (a.u.)
0
20
40
60
6
8
10
12
14
Cell length (μm)
E
Intensity in medial cortex
cdr2p
pom1p
Intensity (a.u.)
0
1
2
3
4
5
6
8
10
12
14
Cell length (μm)

Figure S3.3: Measurement of cdr2p protein number.

A. Protein numbers were estimated by comparison of fluorescence intensity in living cells with standard fusion proteins that have been quantitated previously. Quantification of average cdr2p molecules in the whole cell were estimated by comparing total cell fluorescent intensity of cdr2-GFP with rlc1-GFP (regulatory light chain of myosin, which has been estimated around 9600 molecules/cell (Wu and Pollard, 2005) (N=50).
B. Quantification of cdr2p molecules in each node by comparing cdr2-GFP with the E. coli flagellar protein motB-GFP expressed in bacteria, estimated to be 22 molecules/ dot (Coffman et al., 2011) (N=200).
C. Comparison of fluorescence intensities of different cdr2-GFP species. Images of cdr2-GFP cells in a single medial slice. The cdr2-GFP mean intensities in a 12 pixel square area in a cdr2 node, cytoplasm, and dim motile cortical dots outside of the medial cortex were measured (see Figure 4A). Note that only the brighter, more discrete cortical dots were assayed. n= 20 measurements each in > 5 cells. Error bars = SD.
D. Total intensity of cdr2p and pom1p in the cell as a function of cell length. Black lines are linear best fits. Intensities were measured by an hand drawn ROI around the entire cell in a maximal projection of a stack of 13 confocal sections 0.4 μm apart.
E. Intensity of cdr2p and pom1p in the medial cortex as a function of cell length. Intensities were measured from the same Maximal projection as D but with a hand drawn ROI around the cortical band area.

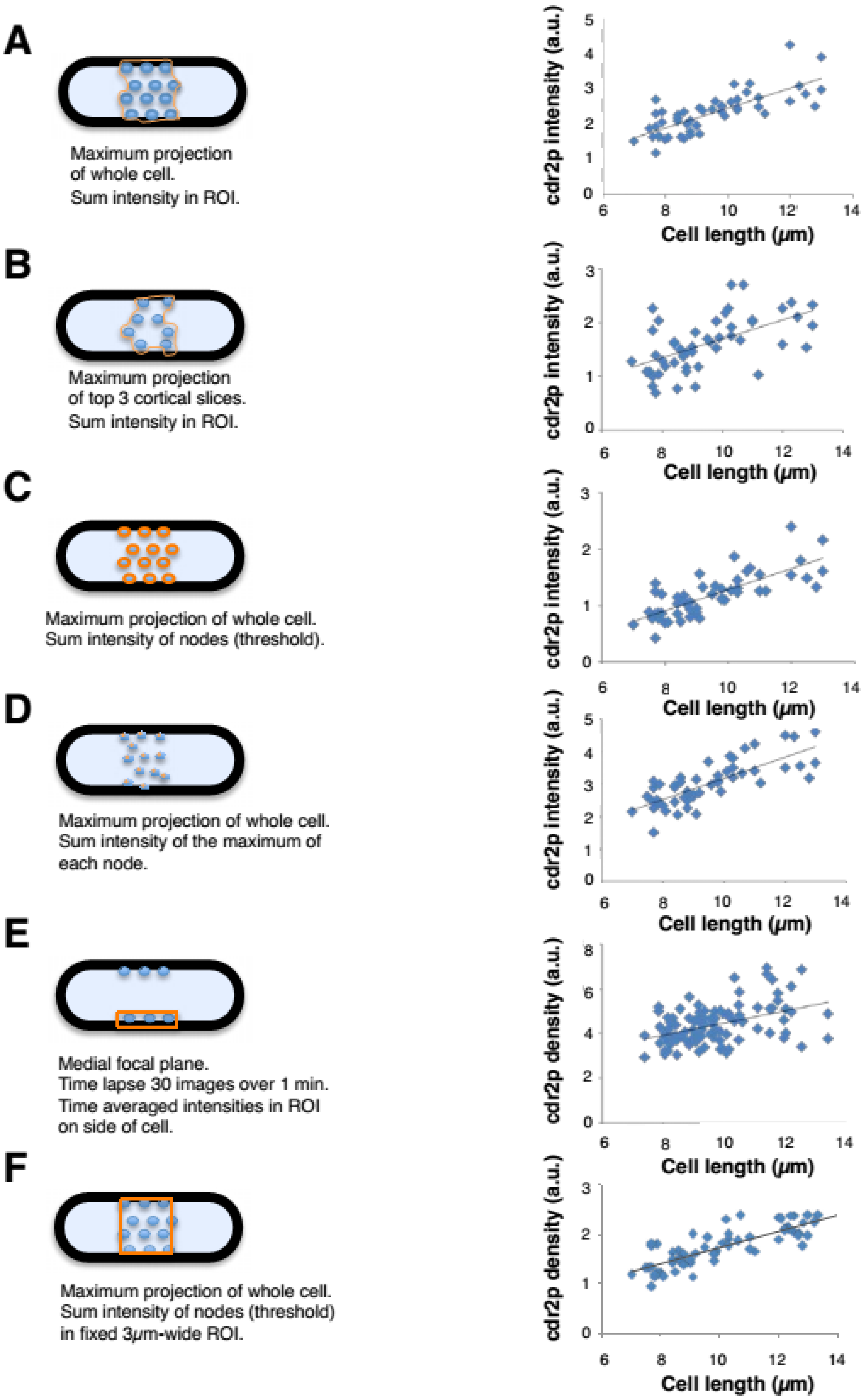
A
Maximum projection
of whole cell.
Sum intensity in ROI.
cdr2p intensity (a.u.)
0
1
2
3
4
5
6
8
10
12
14
Cell length (μm)
B
Maximum projection
of top 3 cortical slices.
Sum intensity in ROI.
cdr2p intensity (a.u.)
0
1
2
3
6
8
10
12
14
Cell length (μm)
C
Maximum projection of whole cell.
Sum intensity of nodes (threshold).
cdr2p intensity (a.u.)
0
1
2
3
6
8
10
12
14
Cell length (μm)
D
Maximum projection of whole cell.
Sum intensity of the maximum of
each node.
cdr2p intensity (a.u.)
0
1
2
3
4
5
6
8
10
12
14
Cell length (μm)
E
Medial focal plane.
Time lapse 30 images over 1 min.
Time averaged intensities in ROI
on side of cell.
cdr2p density (a.u.)
0
2
4
6
8
6
8
10
12
14
Cell length (μm)
F
Maximum projection of whole cell.
Sum intensity of nodes (threshold)
in fixed 3μm-wide ROI.
cdr2p density (a.u.)
0
1
2
3
6
8
10
12
14
Cell length (μm)

Figure S3.4: Comparison of image analysis methods on quantitating cdr2p fluorescence in the nodes.

We used four different methods to image and analyze cdr2p intensities. The details of each method are presented in the figure and described in detail in the Methods in Supplementary Information. Graphs show results of each method on cdr2p medial node intensity versus cell length in a population of cells. The intensities are normalized relative for each data set. All show a similar increased cdr2 intensity with longer cells. The graphs in E and F show in particular that the concentration of cdr2p, as measured as intensity in a fixed area, rises with cell length.

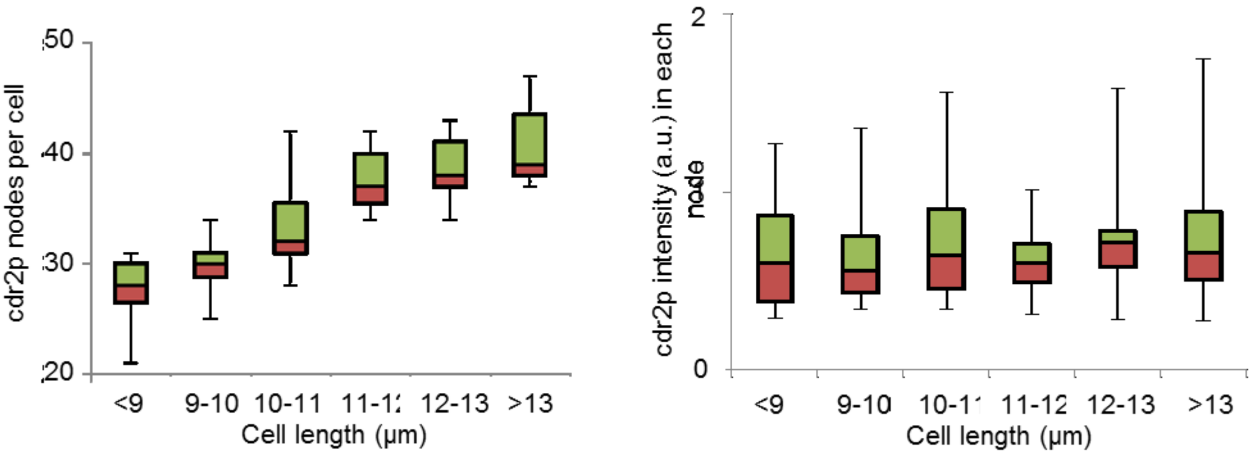

Figure S3.5: Cdr2p node number but not intensity increases with cell length.

Cdr2p was measured by the ImageJ “Find Maxima” function (Figure S4C), and data was graphed in bins according to cell length. A) shows a rise in the number of cdr2p nodes with cell length. B) shows the intensity of cdr2p in each node does not increase on average. Note that this thresholding method underestimates the number of nodes slightly. This data supports Figure 3.2G,H.

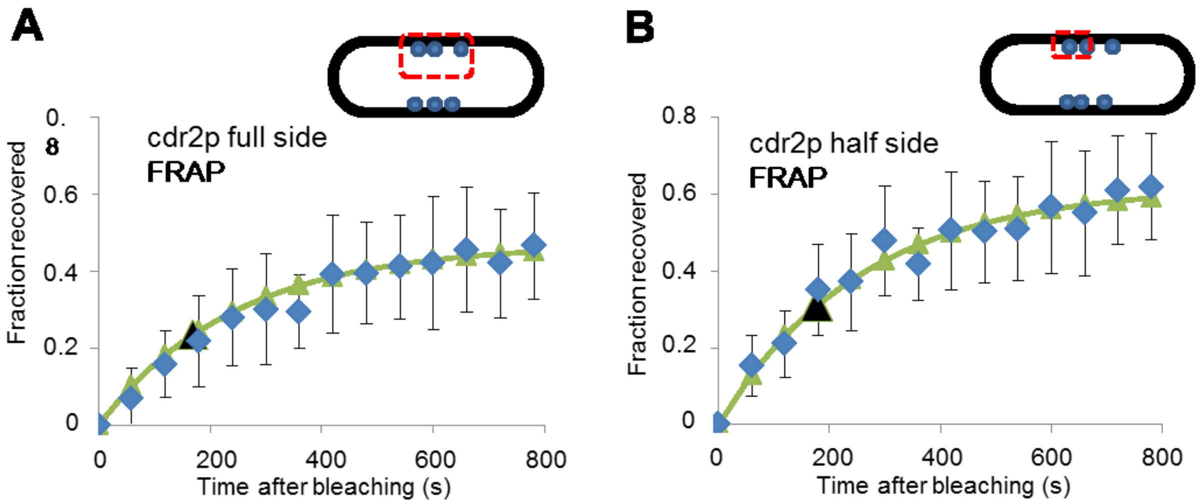

Figure S3.6: FRAP analysis of cdr2-GFP.

Cdr2-GFP in the nodes was photo-bleached in the indicated regions and fluorescence recovery was monitored over time. Cells were imaged in a single medial focal plane. Average data (blue) were fitted to exponential curves (green). The black arrows indicates the time of 50% recovery. t1/2 was about 3 min for both sets of data. This suggests that there is little exchange of cdr2 between nodes. n= 14 cells (A), 8cells (B). Error bars = SD.

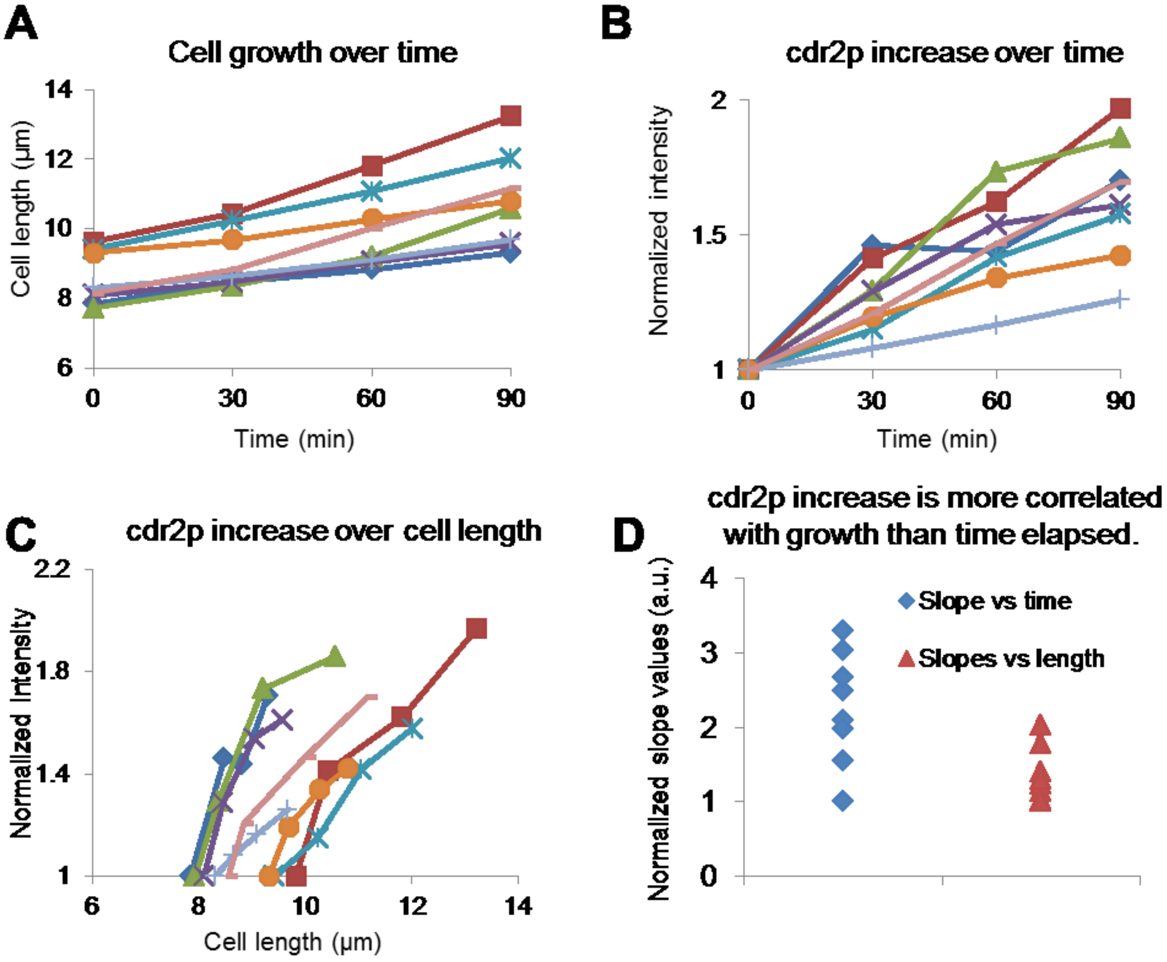
A
Cell growth over time
Cell length (µm)
14
12
10
8
6
0
30
60
90
Time (min)
B
cdr2p increase over time
Normalized intensity
2
1.5
1
0
30
60
90
Time (min)
C
cdr2p increase over cell length
Normalized Intensity
2.2
1.8
1.4
1
6
8
10
12
14
Cell length (µm)
D
cdr2p increase is more correlated with growth than time elapsed.
Normalized slope values (a.u.)
4
3
2
1
0
◆ Slope vs time
▲ Slopes vs length

Figure S3.7: Rate of cdr2p accumulation correlates with the rate of cell growth not time.

The effect of cell growth rate on cdr2p accumulation was examined by analyzing *for3* (formin) mutant, which lack actin cables and are defective in cell polarity. *for3*Δ cells exhibit highly variable growth rates, in part because one of the daughter cells grow from one cell tip while the other grows from both tips (Feierbach and Chang, 2001). The use of this mutant allowed us to analyze cells of very different growth rates but with the same genotype and growth conditions. These cells were grown on glass bottom dishes in YE5S liquid media and imaged in time lapse. The rate of cell growth and cdr2 nodal accumulation were measured at each indicated time point.

A. Rates of cell growth over time in 8 individual cells. Note a large variability in growth rates among the cell population.

B. Rates of cdr2-GFP nodal accumulation over time as measured by fluorescence intensity in the same individual cells (color scheme for each cell is the same as (A)). cdr2p measurement method described in Methods.

C. Rates of cdr2-GFP nodal accumulation as a function of cell length (color scheme for each cell is same as (A)).

D. Ratios of normalized cdr2 rates over time (blue), and ratios of normalized cdr2p rates over cell length increase (red). The correlation of cdr2p is tighter with cell growth than with time. Slopes calculated as described in Method.

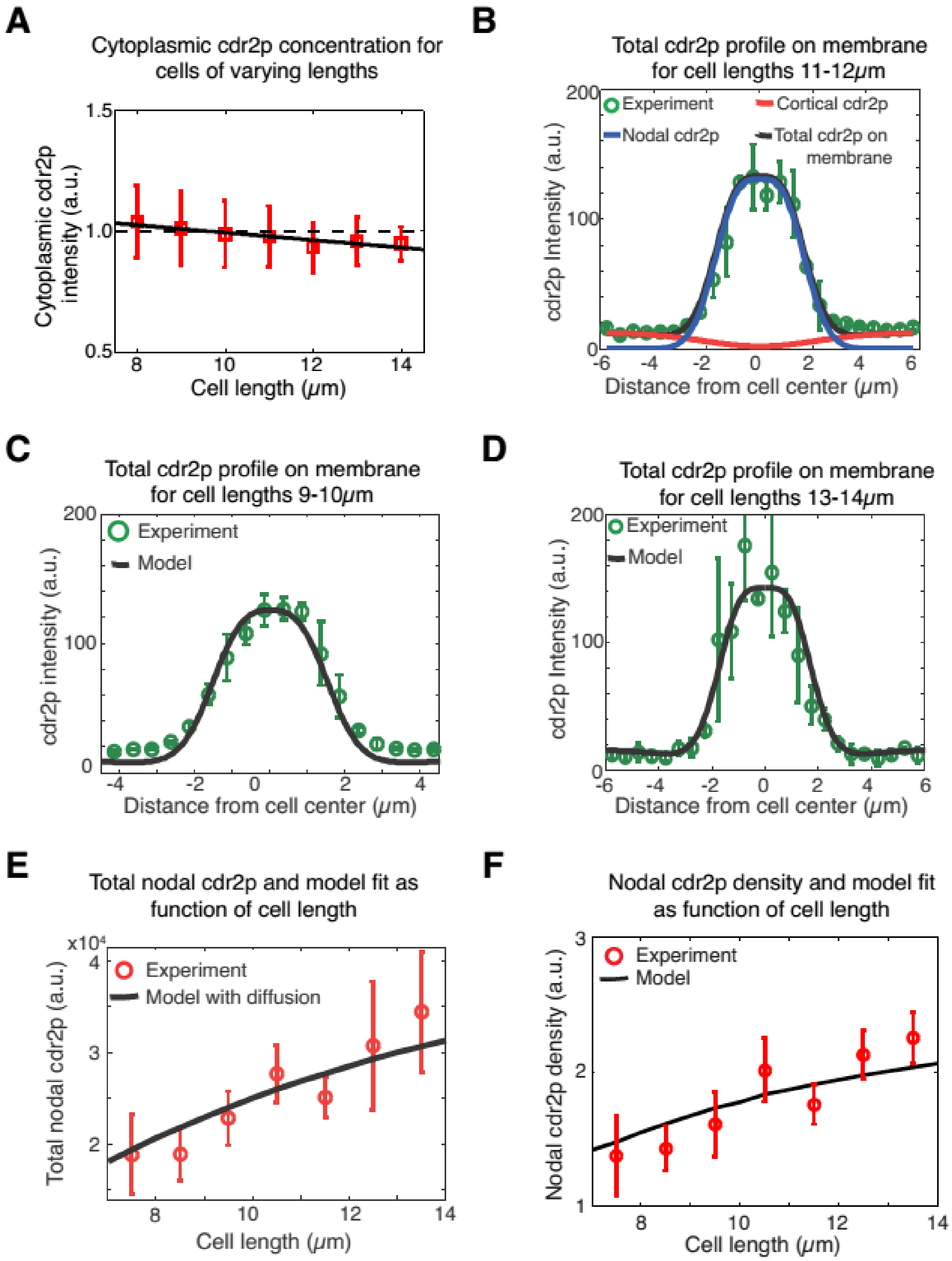
A
Cytoplasmic cdr2p concentration for cells of varying lengths
Cytoplasmic cdr2p intensity (a.u.)
1.5
1.0
0.5
8
10
12
14
Cell length (μm)
B
Total cdr2p profile on membrane for cell lengths 11-12μm
Experiment
Cortical cdr2p
Nodal cdr2p
Total cdr2p on membrane
cdr2p Intensity (a.u.)
200
100
0
-6
-4
-2
0
2
4
6
Distance from cell center (μm)
C
Total cdr2p profile on membrane for cell lengths 9-10μm
Experiment
Model
cdr2p intensity (a.u.)
200
100
0
-4
-2
0
2
4
Distance from cell center (μm)
D
Total cdr2p profile on membrane for cell lengths 13-14μm
Experiment
Model
cdr2p Intensity (a.u.)
200
100
0
-6
-4
-2
0
2
4
6
Distance from cell center (μm)
E
Total nodal cdr2p and model fit as function of cell length
x10⁴
Experiment
Model with diffusion
Total nodal cdr2p (a.u.)
4
3
2
8
10
12
14
Cell length (μm)
F
Nodal cdr2p density and model fit as function of cell length
Experiment
Model
Nodal cdr2p density (a.u.)
3
2
1
8
10
12
14
Cell length (μm)

Figure S3.8: Testing predictions of a spatial model for cdr2p distribution.

(Modeling and analysis were developed and performed by Tim Saunders)

A. Measured cytoplasmic cdr2p intensity (267 cells) as function of cell length. Solid black line is best linear fit and dashed line is best fit to data assuming constant cytoplasmic cdr2p levels. Error bars are SD.

B. Model fit (black line) to experimental measured cdr2p intensity profile on the membrane (for cells of length 11-12µm) (green circles) where the model contributions from the nodal (blue) and cortical (red) cdr2p are also shown.

C. As **C**, but for shorter cells (9-10µm)

D. As **C** but for longer cells (13-14µm).

E. As Figure 4D, except model prediction for the increase in total nodal cdr2p with cell growth including cortical cdr2p diffusion.

F. As Figure 4E, except model prediction for the increase in nodal cdr2p density (defined as mean concentration in 3µm region about cell centre) with cell growth including cortical cdr2p diffusion.

Chapter Four: Role of the endoplasmic reticulum on midsome localization and function

Kally Z. Pan[1] Timothy E. Saunders[2,3], Martin Howard[2] and Fred Chang[1]

1. Department of Microbiology and Immunology, Columbia University College of Physicians and Surgeons, New York, NY, 10032, USA
2. Department of Computational and Systems Biology, John Innes Centre, Norwich Research Park, Norwich NR4 7UH, United Kingdom
3. European Molecular Biology Laboratories, Meyerhofstrasse 1, 69117 Heidelberg, Germany

Abstract

Midsomes are important protein complexes that regulate the positioning of the division plane, construction of the cytokinetic machinery, and length sensing in fission yeast. The specific localization of important proteins such as the anillin-like mid1p and cdr2p to these midsomes at the media cortex of the cell are a critical part of their function. However, the mechanism of how these proteins become localized is unknown. We have observed that these midsomes are found at the intersection of the ER and the cortex. Imaging of fluorescent-tagged ER membrane proteins rtnp1 and ost1p has revealed discrete ER domains that are defined by their morphology. Furthermore, quantitative analysis of midsome positions indicates that they localize next to the boundaries defined by these ER domains. Physical disruption of the ER morphology by centrifugation leads to mis-localization of a mid1p-marked midsome, while deletion of rtn1p has a synthetic effect with cdr2p and pom1p in delocalizing mid1p-marked midsomes and results in defective cytokinetic rings. Taken together, this suggests that ER morphology has a parallel role, along with pom1p and cdr2p in positioning midsomes.

Introduction

The endoplasmic reticulum, or ER, is an organelle of eukaryotic cells that is generally known for the synthesis and processing of many cellular products including proteins, steroids, and lipids. Structurally, it is made up of a complex series of networked tubules, vesicles, and cisternae. Early electron micrographs have showed that the ER is divided into three distinctive domains, the nuclear envelope, smooth ER, and rough ER. Further work has led to the identification of subdomains with distinct morphologies responsible for distinct cellular functions. Exploring this relationship between shape and function have shed much light on how cellular components can affect physical morphological properties and in turn, can either limit or enhance cellular processes (Baumann and Walz, 2001).

Recently, one of the best examples of this approach has been the identification and characterization of a particular class of proteins called reticulons. Highly conserved throughout all eukaryotes studied, these proteins are confined mostly into the peripheral ER and are able to promote a distinctive and highly pronounced membrane curvature via a unique domain in its C-terminus (Shibata et al., 2006; Voeltz et al., 2006). This reticulon domain consists of two chains of hydrophobic residues thought to form hairpins that insert into membranes and define curvature through its own rigid shape (Figure 4.1a) (Oertle et al., 2003). These not only confer shape, but rising evidence suggests they form immobile oligomers that may serve as both structural anchors and help define semi-permanent locations at the cell cortex (Figure 4.1b) (Friedman and Voeltz, 2011; Hu et al., 2008). Though it has been show that human reticulons can cause defects in cell growth in neurons and CNS plasticity, work has just recently began to uncover the cell biology implications of reticulons and their role outside the ER (Chen et al., 2000).

In *pombe*, there may be an addition interest in the role of reticulons due to their genetic interactions with proteins that make up the midsomes. In *pombe* cells that have rtn1, the reticulon interaction protein yop1, and a third membrane protein tts1, ER membrane morphologies appear changed and distinct domain localization became dramatically altered (Zhang et al., 2010). Additionally, midsome proteins mid1 and cdr2 are mislocalized in these cells throughout the cortex. They both spread more broadly away from the medial cortical band and are more scattered and dynamic (Zhang et al., 2012). Cells exhibit a mid1-like phenotype in that they divide asymmetrically.

The evidence suggests that the ER may play a role in stabilizing and positioning midsome, and indirectly, provides a mechanism for the building of cdr2 concentration-dependent size measurement. The medial band where midsomes localize is indicated by the location of the nucleus and defines the future site of division via the actions of mid1p (Chang and Nurse, 1996; Chang et al., 1996). The localization is not set from the birth of the cell but is rather done dynamically, as midsome proteins localize on and off midsomes over the span of minutes (Paoletti and Chang, 2000; Zhang et al., 2010). Overexpression of mid1p leads to the development of karmellae-like structures that resemble extra stacks of nuclear envelope membranes as a result of overexpressing ER transmembrane proteins (Paoletti and Chang, 2000; Wright et al., 1988). Furthermore, highly curved ER tubules seem to connect the nuclear membrane with the peripheral membrane where midsomes are localized, suggesting that ER and midsomes may be connected (Brazer et al., 2000). We investigated this possibility by quantitatively examining the localization of midsome proteins with ER structures and measuring the spatial distribution and dynamics of midsome localization when rtn1 is deleted.

Results

Midsomes localize stably to specific regions adjacent to the cortical ER

Midsomes localize at the medial cortex in fairly large complexes with dozens of units. To investigate their proximity to ER structures, we generated a strain expressing ost1-tomato, rtn1-CFP, and mid1-GFP and imaged confocal sections at the cortical edge of the cells where the surface of the cell most resembles a two-dimensional area. In this field, ost1-tomato marked ER domains have the most diffused expression, which covers most of the cortical edges except for the very tips of the cell, where there are distinctive patches that lack ost1-tomato expression (Figure 4.2a). Meanwhile, rtn1-CFP domains are more discrete and cover the areas that had less intensive ost1-tomato expression, including the tips of the cell. These domains tend to snake into tubule like shapes through the medial cortex and then spread out more evenly at the tips. These domains are also dynamic, and significant re-organization could be seen in time-lapse images within a few minutes (Figure 4.2b). Rtn1-CFP tubules typically surround the edges of ost1-tomato regions and keep to this pattern as ost1-tomato dynamically changes shape. These results suggest that ER sheets dynamically shift and rtn1 regions may act as a cap around their perimeter and define an ER domain border.

Co-localization studies with mid1-GFP show that it localizes in stable clusters of various sizes scattered through the ER at the cortical section of the cell. Interestingly, mid1-GFP marked midsomes seem to favor certain locations in relation to the ER, and can be frequently seen decorating the ends of the rtn1-CFP ER domain (Figure 4.2c). Mid1-GFP intensity is often related to rtn1-CFP intensity as higher intensity clusters of mid1-GFP are often attached to higher intensity and or larger rtn1-CFP regions. However, larger rtn1-CFP regions did not necessitate the presence of mid1-GFP. Closer inspection of mid1-GFP midsomes show that there is partial but not complete overlap between the midsome and the tip of rtn1-CFP tubules, suggesting that the midsome may rest at the end of a ridge or tip of an rtn1-CFP border (Figure 4.2d).

Midsomes and ER domains do take up a significant amount of space in the media cortex. We wanted to determine statistically if the association of midsomes to rtn1p containing ER domains was likely due to chance. So we quantitatively analyzed midsome localization and ER domains within a pool of imaged cells. First, the intensity of rtn1-CFP and ost1-tomato were plotted and thresholds were applied to establish the positions of the different ER domains determined by the two markers and define their borders to pixel level accuracy. This created maps of the ER domains for each of the cells tested. Mid1-3GFP midsomes where then marked by their pixel intensity and position. This information was then plotted and the distance between each pixel of mid1-3GFP intensity and the nearest border of the ER domain was calculated. From initial plots, most of all the mid1-3GFP marked midsomes were within the boundaries of ER domains captured (Figure 4.3a)

As a control, a simulation was created where simulated midsomes were scattered randomly throughout the medial cortex on the ER domain maps. The simulated midsomes retained the exact same intensity profile as in the image, except that their positions were randomly distributed in the same area. The same distance analysis was then preformed on these cells. This analysis revealed that the experimental data differed significantly from the simulated data. While the simulation showed very little difference between the intensity of midsomes and their distance from ER domains, the experimental results showed that there is an inverse correlation between mid1-3GFP intensity and distance to an ER domain; the more intense a pixel is for mid1-3GFP, the closer its position was to a ER boundary (Figure 4.3b).

Mid1p requires rtn1p for proper localization

We next examined if rtn1p is involved in mid1p localization. In *rtn1Δ* cells, mid1-GFP expressing midsomes are able to localize to the medial cortical band. Mid1-GFP intensity and stability are not reduced in clusters with high intensity, suggesting that mature midsomes do not have difficulty forming and locating their normal positions (Figure4.4a). In addition, time-lapse analysis of mid1-GFP over the span of 30 min showed that mature, high intensity mid1-GFP expressing clusters have a similar range in movement in *rtn1Δ* cells as wildtype, suggesting that midsomes also do not have trouble staying in the same location.

It has been shown that mid1p requires cdr2p to localize properly and that several components in the midsome complex all contribute partly towards the proper localization of midsomes to the medial cortex by differentially binding to the cortex and to each other. Most of these bind via polybasic regions that favor membrane binding and have interactions that serve to bind themselves to other midsome complex, and are thought to be the prime method of midsome construction. Since these midsomes are so close to these specific ER domains, we wondered if rtn1 may be necessary for mid1p localization in some other manner.

In *cdr2Δ* cells, there is a small reduction in mid1-GFP expressing midsomes and midsome localization is more spread out in cells resulting in a wider cortical band. Therefore, we examined mid1-GFP localization in a *cdr2Δ rtn1Δ* double deletion background. Surprisingly, we found that this has an additive effect on mid1-GFP localization; there is a significant further reduction in mid1-GFP expressing midsomes (Figure 4.4a). Additionally, the few midsomes that were identified are spread out much further, and in some examples, they extend almost to the tips of the cell. Deleting cdr2 results in cells that divide at a longer length than wildtype and this was seen in the double deletion as well. It has been shown that the midsome band increases slightly in width as cells grow longer. We wanted to see if the increases in the spread of mid1-GFP in *cdr2Δ* cells or the double deleted cells were merely due to increased length of the average cell. We tracked the position of each mid1-GFP expressing midsome along the cell length in cells of all roughly the same size in wildtype, *cdr2Δ*, *rtn1Δ*, and *cdr2Δ rtn1Δ* cells and found that this spread is independent of cell length (Figure 4.4b). We then measured the distribution of the mid1-GFP expressing midsomes in the same backgrounds and found that the spread of the distribution in *cdr2Δ* cells are about double of that in wildtype and that the spread in *cdr2Δ rtn1Δ* is approximately doubled again (Figure 4.4c). Taken together, this indicates that rtn1p may serve as an additional but perhaps redundant mechanism for properly localizing mid1p to the cortex and for restricting this localization to its proper location at the cell middle.

Rtn1 tubules may connect the midsomes to the nucleus

Imaging confocal sections into the body of the cell reveal rtn1p ER tubules extend from the cortex into the interior of the cell, particularly towards the nucleus. Interestingly, it is not expressed in the nuclear envelope itself, suggesting that it may serve as a connector to the nucleus. Mid1p has been shown to respond to nuclear positioning and if the nucleus is moved, mid1 cortical band will re-localize to the area surrounding the new nuclear position (Daga and Chang, 2005; Paoletti and Chang, 2000). The mechanism for how this is accomplished remains a mystery, and we wondered if these rtn1p tubules may facilitate this positioning response.

To investigate this possibility, we imaged cells expressing mid1p fused with a triple tandem GFP so that we may visualize more clearly the lower levels of midsomes in the nucleus. In co-localization studies we found that many of the mid1-3GFP expressing midsomes can be seen attached to the rtn1-tomato tubules that connect the cortical ER with the nucleus (Figure 4.5a). We then repositioned the nucleus by centrifugation. Cell in certain orientations will have their nucleus repositioned to the cell tips upon centrifugation (see methods). Cells with displaced nuclei show heterogeneous mid1-3GFP localization. While some mid1-3GFP expressing midsomes could be seen localized where the nucleus would have been in the middle of the cell, some mid1-3GFP midsomes could be seen in areas around the new nuclear position (Figure 4.5b).

In addition, centrifuged cells show some rtn1-tomato expressing tubules attached to the nucleus but not to the peripheral ER along the cortex. Though these strands can be occasionally observed in wildtype cells, they seem to increase in frequency in centrifuged cells (Figure 4.5b, informally observed). Interestingly, mid1-3GFP expressing midsomes are found at the non-nuclear end of some of these unattached strands of rtn1 tubules (Figure 4.5c). These strands appear very briefly and are dynamic within the order of a few seconds. The same can be said about the mid1-3GFP midsomes that are seen in the cytoplasm in this manner. Due to this fast movement, it is unclear how the rtn1p tubules are reorganizing. It is also unclear whether the mid1-3GFP is being released from these strands, if they reattach very quickly back to the cortex, or if the midsome complex falls apart.

Nuclear localization of mid1 effects midsome stability

Mid1 is known to accumulate in the nucleus and its export is a major component of the ability of the nucleus to center the division plane (Almonacid et al., 2009). We wondered if rtn1p can affect mid1p localization in the nucleus. Therefore, we observed mid1-3GFP in the nucleus of cells that have an rtn1 deletion. While deleting rtn1 seems to have little effect directly on mid1-3GFP in midsomes, mid1-3GFP levels appear lower in the nucleus. Meanwhile, deleting cdr2 in cells seems to increase nuclear localization of mid13GFP (Figure 4.6). Nuclear accumulation of mid1 can be increased upon the treatment of Leptomycin B, a drug that effectively halts nuclear export. While initially at a significantly lower levels, the amount of mid1-3GFP accumulation in rtn1 deleted cells can be seen to approach that of wildtype cells after 90 minutes of treatment (Figure 4.7).

We wondered what would happen to mid1p if we forced it out of the nucleus so that there would be an excess of cytoplasmic mid1p. Therefore, we visualized a mutant mid1 that lacks the nuclear localization signal (Almonacid et al., 2009). This mid1-nls-4GFP cannot be seen in the nucleus but an increased amount can be seen localizing in small clusters all over the cortex. These clusters are significantly less intense than stable midsomes and are accordingly much more dynamic (Figure 4.8). Interestingly, regular, stable mid1p marked midsomes can still be seen and their stability, number, and intensity are significantly affected by the presence of these clusters. Nor are there any obvious effects on division plane placement, cytokinesis, or length of division immediately apparent from observation.

Discussion

Our quantitative analysis demonstrated that mid1p significantly associated with the edge of ER membrane domains marked by rtn1p. Specifically, midsomes are often found at links formed by distinct ER structures between the cortex and the nucleus, and that disruption of these links can lead to midsome displacement. The sum of this evidence suggests that the ER can influence the positioning and the stability of mid1p. However, measurements of molecular distances of midsome proteins seem to indicate binding with the plasma membrane (PM) (Laporte et al., 2011). This may indicate that control of these midsomes is due to some interplay at ER, PM junctions.

In addition, our results seem to indicate that changing the amount of nuclear mid1 does not drastically affect the setup of cytokinesis machinery and length-sensing. In addition, it only affects division plane placement insofar as it prevents the re-orientation of midsomes to nuclear movement inside the cell. However, in these examples, mid1 containing midsomes were never diminished in significant amounts when midsome accumulation was forced by drug treatment. Conversely, when cortical localization of midsomes is increased, the amount of stable midsomes also seems unaffected. This suggests that the experimental methods used to accumulate mid1p in the nucleus may not actually affect midsome assembly or function. This may be due to cytoplasmic mid1 acting as a buffer, setting the extra levels of mid1p trapped in the nucleus. It may also mean that high turnover of mid1p through the nucleus is not needed for stable midsomes, but may only be necessary for the nucleation of new midsomes. That nuclear accumulation can still occur in rtn1 deleted cells suggests that nuclear shuttling is not significantly dependent upon the ER. However, how these forces all come to play in terms of building the midsome is still unclear.

It is unknown if ER dynamics are an indication of membrane shifts, lipid movements, or a reorganization of the markers within the ER membrane. Given the likely scenario that these markers determine the ER structure, it may be that organized movement of these ER proteins leads to membrane movement. This movement may, in turn, allow the incorporation of additional elements into the cortical/membrane interspace. While both the players responsible for triggering this shift of ER proteins and their regulators remain unknown, these movements provide a likely additional mechanism of midsome positioning.

It remains to be seen whether rtn1 itself has any direct interaction with any of the proteins within the midsome, or if its effects on cytokinesis are secondary, due solely to the mis-positioning and decreased stability of the midsome. What seem clear is that deletion of rtn1 is not enough on its own to neither significantly impact either the behavior of midsomes nor change midsome effectiveness in directing cytokinesis or length sensing. In additional deletions of other ER membrane proteins, major defects in cytokinesis can be observed. It is not clear whether these defects are due to degradation of specific ER based interactions with midsome proteins, or due to changing the nature of ER organization.

However, there might be a clue that rtn1p is not just affecting midsomes through reducing its ability to stabilize on the cortex. While the number and intensity of mid1p midsomes on the cortex are the fewest and lowest in the double deletion, the strong defect in cytokinesis can be recapitulated in cells with both pom1 and rtn1 deleted. In these cells mid1p midsomes, while significantly spread throughout most of the cortex and all the way to the non-growing tip of the cell, show no significant decrease in numbers or intensity (Figure 4.9a). However, they still demonstrate an additive cytokinesis defect (Figure 4.9b). In this case, neither cdr2p nor mid1p have problems localizing to the cortex and clustering together. However, there is an increase in the localization of small patches of mid1p or cdr2p to the cortex for very brief amounts of time. These small patches are generally much smaller and less intense than mature stable midsomes and more significantly, unlike the more stable midsomes, often do not exhibit mid1p, cdr2p co-localized together (Figure 4.9c). Interestingly, while cytokinesis defects seem to worsen, there may be a slight rescue of the length defect seen in the pom1 rtn1 double deletion, suggesting that either cdr2p and mid1p interaction or midsome dynamics maybe important to length signaling. Perhaps deleting rtn1 reduces the chance that midsome proteins have of finding each other and "maturing", but normally, the restriction of these proteins to the cortex allows this to happen regardless. However, if something else comes to disturb this balance, like the deletion of pom1 or cdr2, midsome proteins are not restricted anymore and have a much more difficult time assembling.

What is the mechanism that allows rtn1 to accomplish this? The most likely explanation is that these ER proteins affect ER morphology and dynamics, which creates the conditions that allow midsome "maturing" to occur. The ER disruption seen in centrifuged cells suggests that even small, ephemeral changes in ER structure at the cortical membrane interphase can potentially affect midsome positioning. It is possible that this is due to direct interaction between ER membranes or proteins such as rtn1p, with midsome proteins such as mid1p or cdr2p. However, it may be that the ER simply acts as a corridor or mold of sorts that creates a space that midsome components can rest and assemble in relative isolation. In this way, the exact composition of membrane ridges and valleys that are carved out by the ER tubules created by rtn1p and other proteins may help determine where and how midsome nucleation or maturity can occur. The fact that these tubules are connect to the nucleus makes them ideal for defining the medial band. The relationship between medial band size and their fidelity in following the nucleus suggests that a physical connection such as the ER strains connecting the nucleus and the cortex may serve as the mechanism for this action.

Methods

S. pombe cell preparation

Standard methods for *S. pombe* growth and genetics were used (Moreno et al., 1991). Strains are listed in Table S1. Cells were grown in liquid YE5S media at 25˚C with shaking in exponential phase before imaging. Cells were generally mounted in liquid YE5S media directly on glass. 1% agarose YE5S pads were used for long-term imaging. Other long term imaging was conducted on 35mm non coated glass bottomed MatTek dishes. Dishes were treated with 5 μl of 1μg/μl of lectin, dried, cells were applied and incubated for 5 mins in RT and then 2 ml of YE was added.

For leptomyosin B treatment, cells were imcubated with 25 ng/ml leptomyosin B for in indicated time and then imaged (Almonacid et al., 2009).

Centrifugation experiments involved placing cells in a 0.5% agar mould in a 1.5ml tube and centrifuged at max speed for 1 minute (Daga and Chang, 2005).

Microscopy

Images were generally acquired using a spinning-disc confocal fluorescence microscope system (Nikon, Perkin-Elmer, Solamere Technology) with an ER CCD camera (Hamamatsu) and a 100x 1.4 N.A. objective. Triple co-localization was done using a DeltaVision Image Restoration Microscope on a Inverted Olumpus IX-70 platform. Images were processed by Huygens deconvolution software (SVI) at the Rockefeller Bioimaging Center.

Image Analysis

ImageJ (NIH) and custom MatLab (Mathworks) software were used for analysis. For intensity profiles, generally, fluorescence intensity values around the cortex of cells were measured from images of cells in a medial focal plane, using custom MatLab software for the automated generation of a one-pixel wide mask around the cell cortex, followed by manual correction.

Mid1p midsome positions were tracked by the following method. Maximum projections were made of 13 slices of confocal sections taken at 0.4 µm apart. Cells were then cropped out and rotated so that their long axis was horizontal. The Maxima detection in ImageJ was used to find the brightest pixel from midsomes and their positions were tracked for the X-axis, which corresponded to the long axis of the cell.

Acknowledgements

I would like to thank N. Padte for initiating this project, the creation of strains used here, and his contributions for my continued work. Thanks also go out to the Gould lab for strains and Z. North and the Rockefeller University Bio-imaging Resource for use of their equipment and software. As usual, additional thanks for the members of the Chang laboratory for thoughtful discussion and advice.

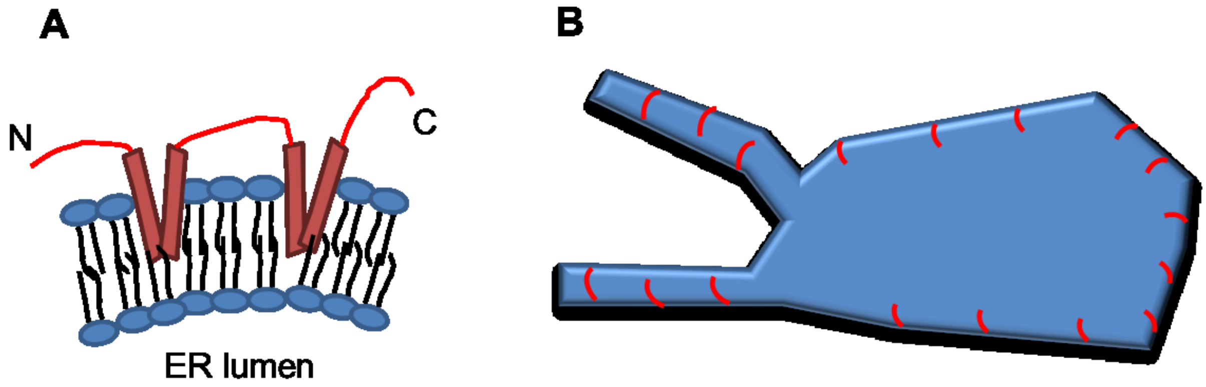

Figure 4.1 Model of reticulon proteins shape regions of high membrane curvature in the peripheral endoplasmic reticulum (ER).

A. Schematic of reticulon topology in the outer leaflet of the ER. Long transmembrane domains increase outer leaflet area relative to inner leaflet area, generating membrane curvature.
B. Schematic of ER cisternae and tubules (blue) indicating regions where reticulons (red) have been observed to localize and shown to regulate membrane curvature, including ER tubules and the edges of cisternae.

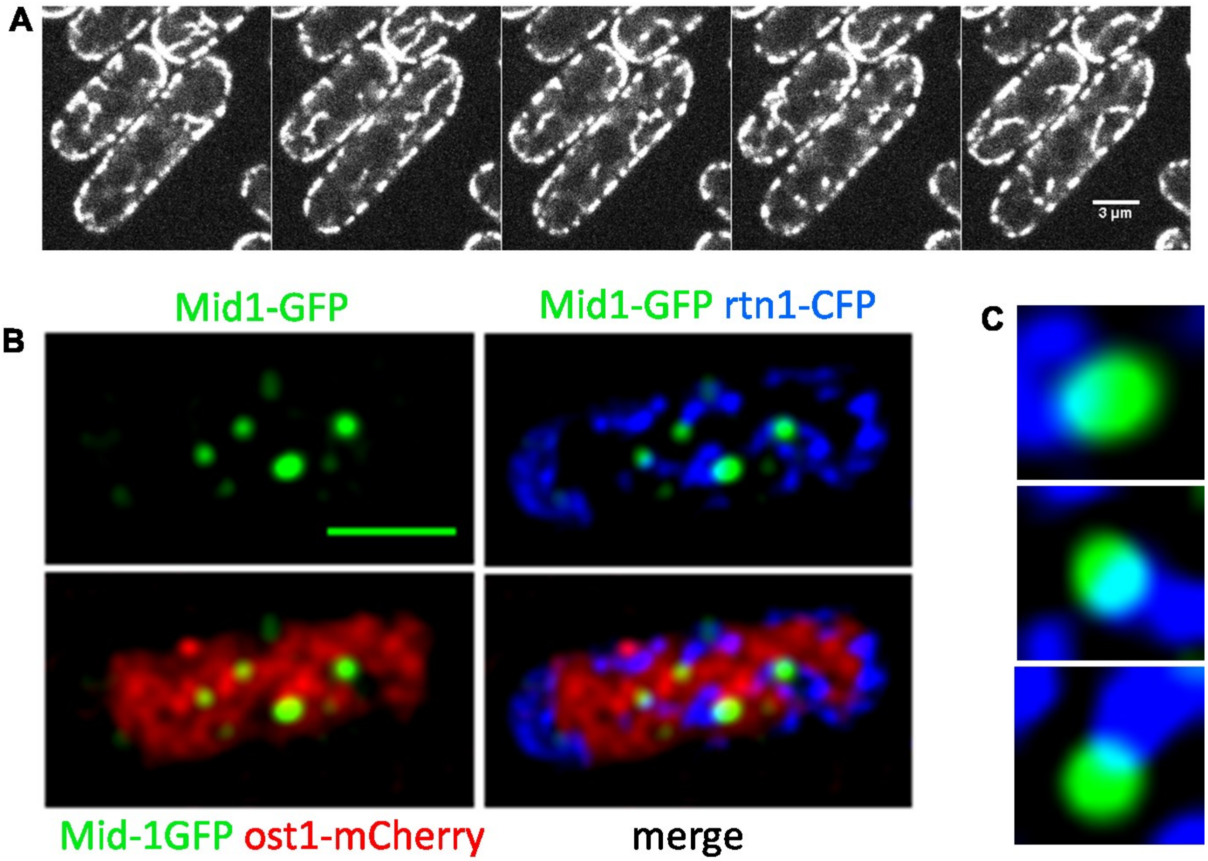

Figure 4.2 ER domains are highly dynamic but distinctive.

A. Confocal section through the middle of the cell body of cells expressing rtn1-GFP over 1 minute intervals.
B. Triple co-localization image of the cortical surface of a cell expressing rtn1-GFP, mid1-GFP, and ost1-mCherry taken with a Deltavision Widefield microscope with deconvolution with Huygens software.
C. Zoomed in images from a mid1-GFP, rtn1-CFP expressing cell.

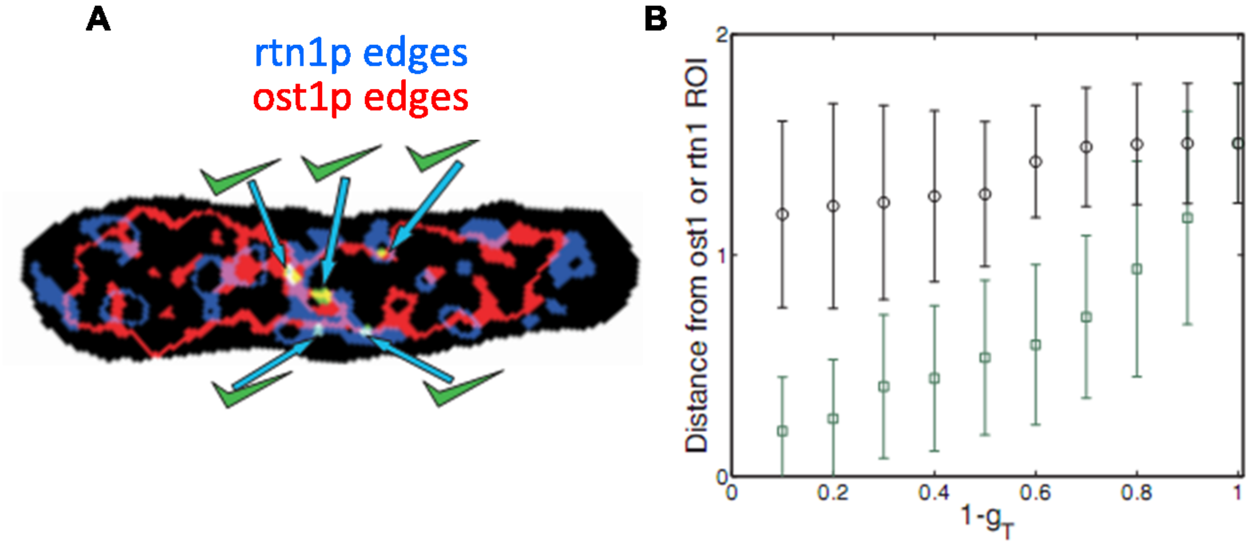

Figure 4.3 Quantitative analysis of mid1p association with the borders of ER domains.

(Modeling and analysis by Tim Saunders)

A. Pixel by pixel threshold generated positional map of the different ER domain boundaries and the location of mid1-GFP midsomes from cells imaged in figure above.
B. Average pixel distance between mid1-3GFP and the nearest ER boundary for mid1-3GFP midsomes positioned randomly in simulations (black) or in experimental data (green). X-axis is for decreasing levels of threshold of mid1-3GFP intensity with smaller values representing the highest thresholds and the brightest mid1-3GFP pixels. (See methods)

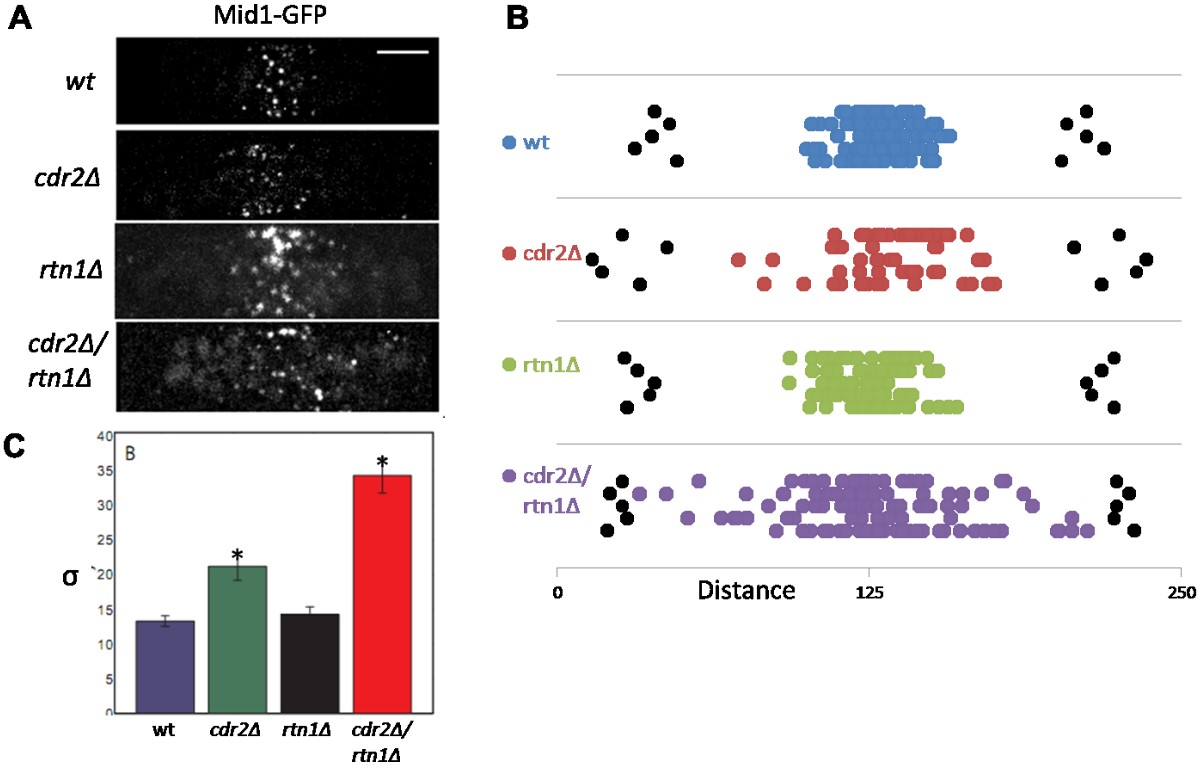

Figure 4.4 Rtn1p has an additive effect with cdr2p on the spread and localization of mid1p

A. Maximum projection confocal stack of 13 slices 0.4 µm of mid1-GFP in wildtype, *cdr2Δ*, *rtn1Δ*, and *cdr2Δ rtn1Δ* background. Bar = 3µm
B. Graph of mid1-GFP midsome position showing the spread of with the cell oriented in a horizontal position with the black dots marking the tips of the cells. Maximum projections of cells are re-oriented to the horizontal position, and only the X-axis position is recorded to indicate its spread over the length of the cell. N=5
C. The standard deviation of mid1p position from the center of the cell.

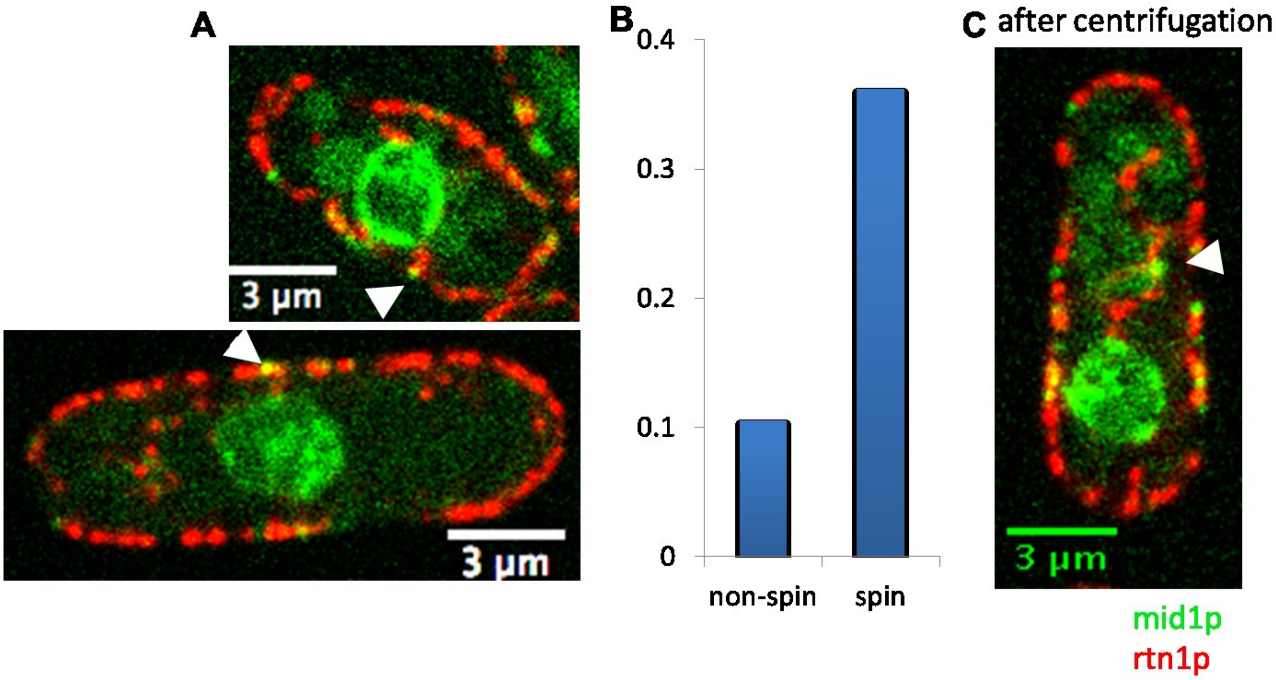

Figure 4.5 Some mid1p marked midsomes are attached to rtn1p tubules that connects to the nucleus.

A. Co-localization of mid1-3GFP and rtn1-tomato.
B. Fraction of cells with rtn1 attached to a midsome that is in the interior of the cells that were centrifuged at 13000 rpm speed for 1 min. N = 12 (see methods)
C. Image of a mid1-3GFP that is in the interior of the cell attached to an rtn1p tubule.

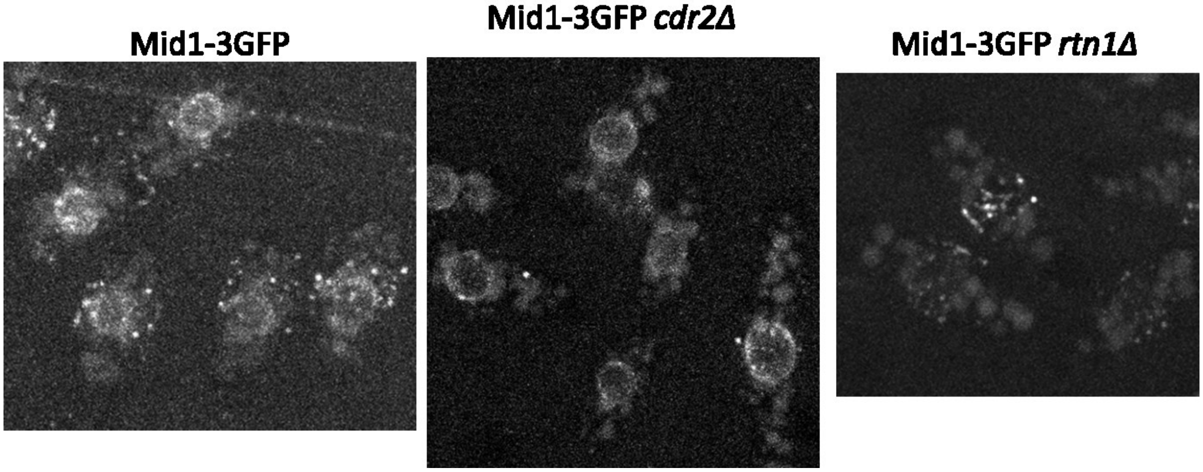

Figure 4.6 Nuclear localization of mid1 varies in *rtn1Δ* and *cdr2Δ*.

A. Maximum projection of a confocal stack of 13 sections at 0.4 µm apart of mid1-3GFP in wildtype, *cdr2Δ* and *rtn1Δ* cells.

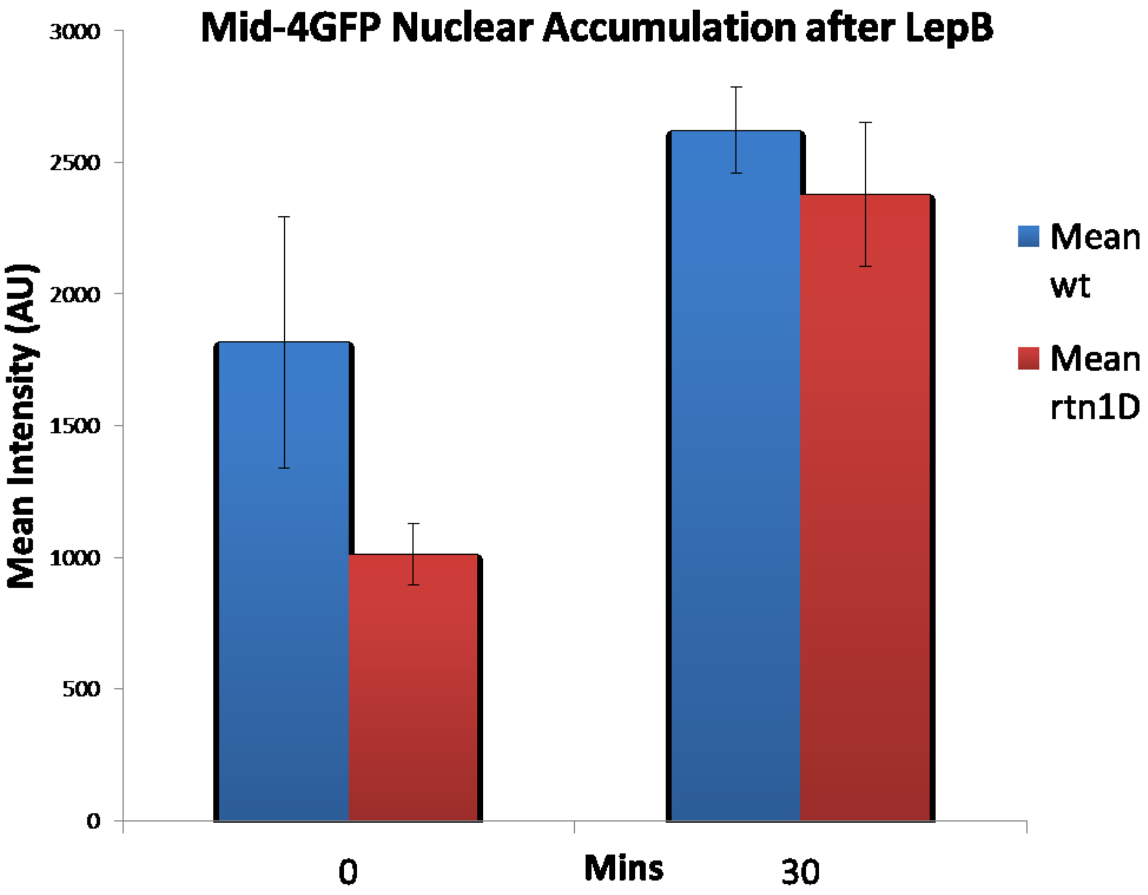

Figure 4.7 Nuclear accumulation of mid1p is unimpeded in *rtn1Δ*.

A. Average intensity of mid1-3GFP in the nucleus of cells treated with Leptomycin B taken from Maximum projections of complete cells of a confocal stack of 13 sections at 0.4 µm apart.

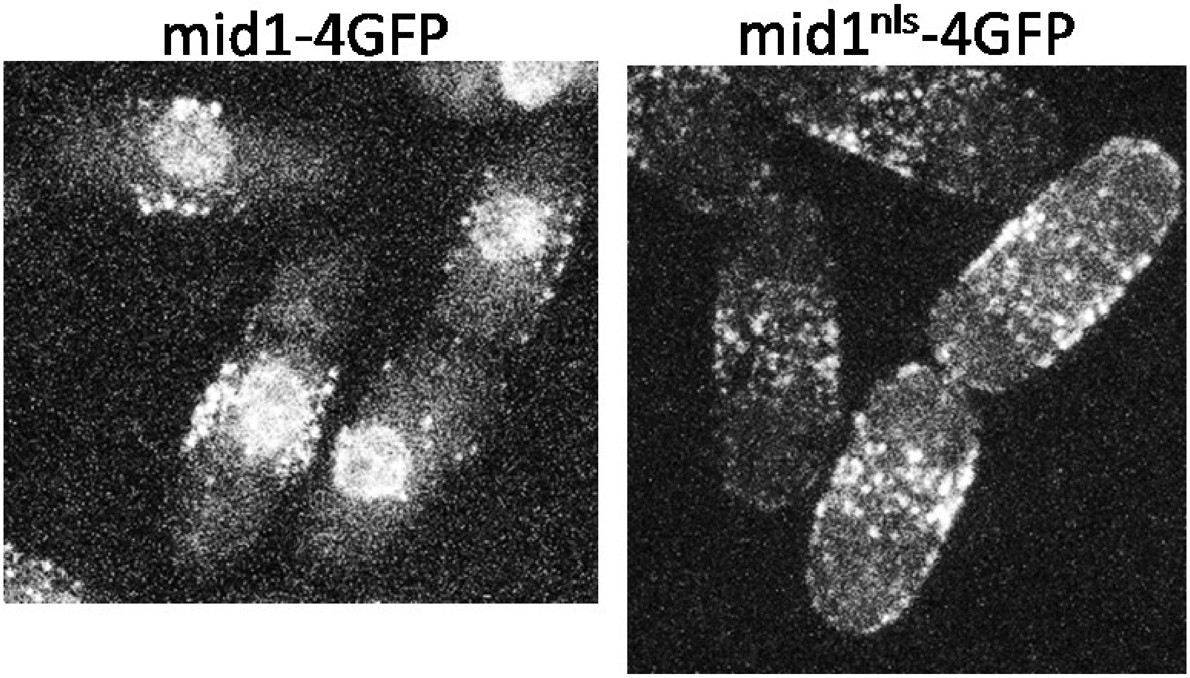

Figure 4.8 mid1p lacking the nuclear localization signal accumulate on the cortex

A. Maximum projection of a confocal stack of 13 sections at 0.4 µm apart of mid1-4GFP and in mid1-nls-4GFP cells.

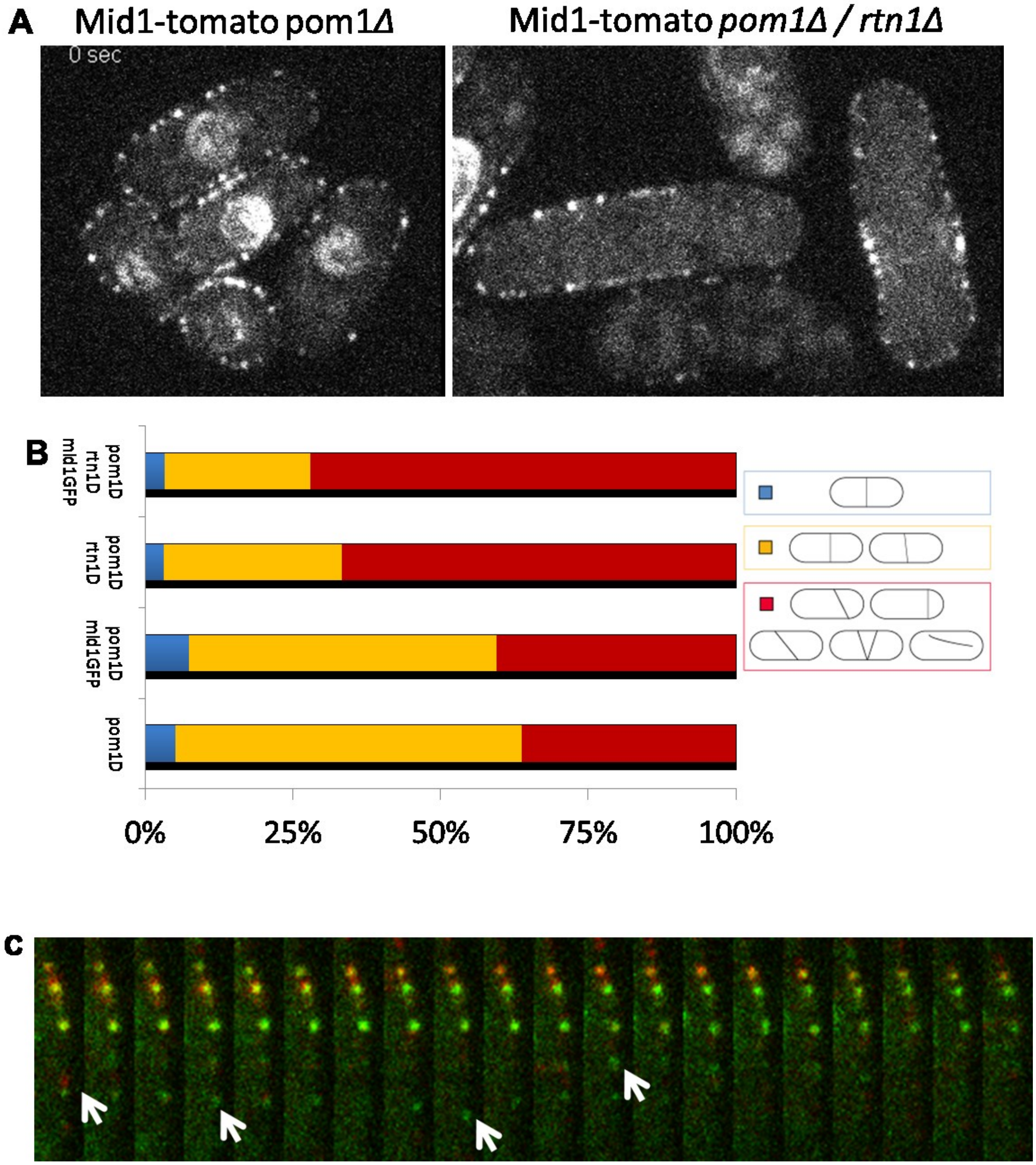

Figure 4.9 rtn1Δ exacerbates the division plane placement defect of pom1Δ and leads to midsome instability

A. Single confocal section of mid1-tomato in *pom1Δ*, and *pom1Δ rtn1Δ* cells.
B. Percentage of cells that show defects in division plane placement, divided by three classes: normal, minor, and severe. Division plane position was determined by calcoflor staining. N > 100
C. Time-lapse images of a single confocal section of mid1-tomato and cdr2-GFP at the cortex in the *pom1Δ rtn1Δ* cells over 5 second intervals.

Chapter 5: Conclusions

Introduction

In this thesis, I explored the question of cell size control by testing three different mechanisms that affect division length determination. The first is a noise reduction mechanism involved in the formation of pom1p clusters. The second is a threshold-based mechanism that signals cell division via an increase in the local concentration of cdr2p marked midsomes at the media cortex. The third is the manipulation of the ER morphology that allows the proper accumulation and assembly of midsome components. The findings presented in this thesis have added a more physical and quantitative perspective to the classic genetic and biochemical evidence for size control. This has allowed a re-examining of more traditional models by analyzing more specifically some of its predictions and has allowed us to refine or reconstruct them. In this final discussion, I will briefly overview these findings, discuss how they fit into our current understanding of division length, and speculate on what future directions may prove fruitful in uncovering the regulation of cell size control.

Current view

We have seen that the pom1p gradient is created and maintained by the formation of clusters of pom1p molecules freely diffusing on the cortex. The self-assembly of these clusters seems directly dependent on availability of free pom1p, and cluster size directly affects its dynamics, displaying an inverse relationship with its diffusion speed (Figure 5.1). However, we found no correlation with pom1p gradient shape or distribution with cell length; the buffering system worked so efficiently that gradients declined so steeply that pom1p concentration is negligible by the time it reached the medial cortex.

We believe that pom1p gradients act not directly on cell length as a length signal, but indirectly as an inhibitor of cdr2p. We hypothesize that pom1p localization to the tips inhibit cdr2p from becoming anchored to the cell tip region, possibly through its phosphorylation. Through our experiments, we have seen that cdr2p and even mid1p are not completely restricted from the cell tip area, but rather their localization at or near the cortical cell tip were always faint and transient. As, we have observed that pom1p gradients are extremely resilient to perturbations in cellular processes, being virtually immune to long-term disruption of cellular transport mechanisms, starvation, and cell polarity, to name a few, the same can be said about the ability to keep midsome formation from the cell tips. However, it seems that a pom1p gradient is probably not enough to produce such a sharp border of cdr2p midsomes by itself. We have suggested that ER components may be other such regulator of midsome positioning, but in light of the fact that midsomes proliferate to only one cell tip in a pom1 deletion background, the existence of other regulatory factors seem very likely.

The accumulation of cdr2p in midsomes allows it to build up a local concentration despite maintaining proportional expression levels with cell size. We believe this localized concentration allows the buildup of a signal that grows proportional to the cell size that is presumably sent through downstream signaling molecule wee1p at the spindle pole body, and into the nucleus to trigger mitosis through the activation of cdk1p (Figure 5.2). How this signal is delivered is still unknown. Genetic studies suggest that cdr2p, wee1p, cdc25, and cdk1p are involved and biochemical experiments show direct interactions between some of these kinases. But many questions remain about the mechanism of how size information is passed through this pathway

(Figure 5.3). If direct interactions between all the proteins are required, then why do our localization studies indicate that most of these proteins localize to different parts of the cell? While we may have some ideas as to why the inverse localization pattern of pom1p and cdr2p may help set up a rise in cdr2p midsome concentration, it is not clear how cdr2p can effectively signal to downstream elements like wee1p. While we have demonstrated that it is possible that a concentration gradient of cdr2p from midsomes can signal to the spindle pole body in silico, experimental evidence is still needed to test this hypothesis.

However, a model based on concentrating cdr2p midsomes suggests a solution to a long-standing mechanistic problem in size control. If molecular number increases in proportion with volume, then the concentration of this molecule stays constant, making a change difficult to detect (Figure 5.4a). By concentrating this increase in molecule number in a fixed volume, then the molecule effectively doubles in concentration locally (Figure 5.4b). Then as long as the sensor for this molecule is fixed, then the signal readout will be twice as strong.

The accumulation of cdr2p midsomes at the medial cortex may function under such a system. While not entirely fixed, the medial cortex is very limited and its increase in area is much slower than midsome accumulation, leading to an increase in the density of midsome occupation. The spindle pole body may contain a fixed number of elements such as wee1p that act as sensors for cdr2p, then limited numbers of wee1p molecules will be phosphorylated more frequently as cdr2p accumulates at the medial cortex and midsome density increases.

As an aside, the buffering nature of pom1p gradients prevents it from being able to act as a proxy for cell size. However, it could be an excellent system to buffer the cell from the excessive amounts of molecular noise seen in such small systems. It is likely that small levels of pom1p in the medial cortex do inhibit cdr2p function and the level of cdr2p required to pass the size threshold is determined by the amount of pom1p present. In this case, the ability of pom1p molecules to buffer themselves at the cell tip to keep medial concentrations of pom1p consistent and its ability to inhibit cdr2p at the cell middle would prove to be a critical refinement of the size signal and could explain how division length is so uniform compared with protein expression. Cellular variation in pom1p expression is buffered away to the cell tips, and variation of cdr2p expression is buffered by pom1p inhibition. Such large variability in protein levels is an unavoidable consequence of the stochastic nature of systems which deal in such small volumes and low numbers. This buffering could potentially be the mechanism involved in other biologically noisy systems (Huh and Paulsson, 2011).

If the pom1p gradient acts as a regulator that prevents midsome formation at the cell tips, the ER may act as a positive regulator that encourages midsome formation at the medial cortex. We have demonstrated that the deletion of ER membrane proteins can alter the ability for midsomes to localize properly on the medial cortex, perhaps through regulation of mid1p nuclear shuttling (Figure 5.5). We have also seen that ER disruption can have an effect on the function of midsomes through cytokinesis in addition to the effect seen with the deletion of the midsome protein cdr2p as well as pom1p. Other studies have demonstrated that deletion of more and more ER components lead to a deterioration of distinctive ER domains (Zhang et al., 2012), and that this is linked to increasingly unstable midsome localization. A possible explanation could be a spatial one: changes in ER morphology could create a physical pocket for midsomes to dock. Another possibility could be a direct interaction between these ER proteins and midsome function.

This ability to provide midsome cortical stability may impact length-sensing; a reduction of midsome localization to the cortex or even a reduction in the ability for midsomes to be sequestered in the medial region should in theory decrease the efficiency of length signaling. There is a hint that this may be the case as we have informally observed that *pom1Δ rtn1Δ* double mutants may have a significant number of cells divide at a longer length than *pom1Δ* alone. This may be due to the fact that cortical midsomes are spread further apart, reducing their effectiveness in signaling from the medial cortex and delaying entry into mitosis. This is complicated by the fact that midsomes are also spread out in *pom1Δ* cells yet these cell divide short, making the results difficult to interpret.

Further analysis is needed to determine if rtn1p has a significant impact on cell division length, and whether that impact is achieved through its effect on midsomes, or indirectly through other proteins such as pom1p. The ER is an organ that grows proportional with the cell size. In fact, regulation of ER membrane domains could theoretically be as sensitive to nutrient availability, or other regulators of growth, as a molecular cell size counter. Perhaps ER domains could shrink in size and allow the addition of more midsomes at the cortical surface, which would trigger an earlier entry into mitosis. It is entirely speculative but conceivable that the effect that the ER has on the localization and dynamic properties of midsome proteins could be the actual sizing mechanism.

Future Directions

One of the greatest challenges of answering the question of cell size control is the fact that this process is so multifaceted, with many different cellular functions and processes all having an effect on the end phenotype of abnormal division length. Many members of the pathway explored in this thesis have important roles to play in many cellular processes which, while different, may also affect division length. For example, pom1p is a critical component of polarity determination, which impacts growth. It is also a regulator of division plane positioning, helping to restrict midsomes from localizing at the cell tips. Cdr2p is not only a stabilizer of the midsome complex, it is also has a role in nutrient sensing.

As we have proposed a basic mechanism for length determination as a threshold-based model of cdr2p accumulation in midsomes in the medial cortex, this opens up a myriad of questions of the roles of pom1p, midsome proteins, and the ER in this regime. Adding to this difficulty is the near certainty that other systems must be working outside that of cdr2p and pom1p. In addition to genes like cdr1, which has been implicated as another actor in the wee1p pathway, a recent screen has unveiled a host of genes, seven of which have not been previously described as cell cycle regulators, and three of which regulate mitotic entry through an uncharacterized mechanism that does not involve the phosphorylation of cdk1p Tyr15 site that wee1p and cdc25p does (Coudreuse and Nurse, 2010; Navarro and Nurse, 2012). Do these new mechanisms offer a necessary overlap of regulation or are they just evidence of redundancies?

One interesting area to pursue is the question of the relation between the effects on cell length between pom1p and cdr2p. While genetic experiments confirm that deleting pom1 does not have an effect on cells lacking cdr2p, in our model it fails to explain why *pom1Δ* cells are shorter yet have midsomes localized in a more spread out manner. Preliminary observations seem to indicate that more midsomes are localized to the cortex in *pom1Δ* cells. However, is this due to an increase in the space that cdr2p is "allowed" to bind to the cortex or due to a more direct process where the cdr2p is recruited there more actively? Could the length reduction be due to unrelated effects that pom1p is having on growth rate due to its role in polarity? Do polarity mutants grow slower or have a measurable difference on division length that is independent of pom1p? To answer these questions, it is crucial to measure Cdr2p and mid1p concentrations and dynamics in midsomes in *pom1Δ* and other polarity and size mutants to differentiate the effect of loss of cell polarity verses change in cell size has on midsome properties.

Another area of interest is the midsome itself. Midsomes differ in size and intensity. They may also different in the balance of the different proteins that are found in the midsome. If these proteins form complex structures, do they exist in strict ratio to each other? We have some evidence from high resolution images of wildtype cells that midsome components like cdr2p and mid1p bind to the cortex ephemerally in small clusters that exhibit higher dynamics and a lower chance of co-localization with other midsome components. Do these "immature" midsomes contribute to size determination, and how are they regulated is it regulated? Is the kinase activity of cdr2p dependent on co-localizing with other midsome components? There is some evidence that wee1p may be present in midsomes. If that is the case, is it only present in the stable "mature" midsomes, and that is method by which cdr2p signals cell size?

The role of the ER in restricting midsomes to the medial cortex is another interesting area to pursue. In images reported by Zhang et. al., mid1p localizes in a more spread out area over the medial cortex, but generally does not spread all the way to the cell tips (Zhang et al., 2010). However, in pom1Δ cells, mid1p and cdr2p both spread all the way to the cell tip. It would be interesting to see if these ER mutants, which display mislocalized midsomes have any division length defects. It would be also be interesting to see if pom1p deletion and ER disruption have competing and opposing effects on division length. However, care must be taken in experiments conducted using mutant forms of pom1p, cdr2p, and the ER membrane proteins. Ideally, mutants could be found that only affect division length but not the other functions of these proteins. This would settle the question of whether division length is a primary product of this pathway, or a secondary product of several different pathways.

One caveat of these studies that bears discussion is the reliance upon fluorescent protein fusions. While they have proved extremely useful, an inherent risk in their use is the omnipresent possibility that fusing them to our protein of interest will change their localization or function. Additionally, different tags will behave differently in terms of its photoactivity, fold time, and steric hindrance. This tag heterogeneity will make comparisons between two differently tagged proteins difficult to make. Such an effect is observed in our strains that have pom1p tagged with different fluorescent proteins, though ironically, these slight differences helped us determine the effect of perturbing gradient shape on cell size. We have partially addressed this issue by generating strains with different tags and to confirm that they do not differ significantly in their phenotype and their molecular dynamics. We have also taken pains to ensure that all our quantitative comparisons are done using standards tagged with the exact same fluorescent tags and that multiple standards are used. These controls have yielded data that have been in rough agreement. However, it is virtually impossible to eliminate the possibility that the large variation we observe within each data set might be due to the effects of fluorescence tagging.

Another issue with these studies is the difficulty of defining the regulatory pathway. While on the surface, these kinases seem to follow in a linear signaling pathway, we have shown that many of these proteins are part of multiple biological functions, such as polarity, nutrient sensing, and cytokinesis that can indirectly affect cell size. It may be convenient for scientists to categorize and compartmentalize cellular processes into distinct and discrete functions. However, the cell is under no obligation to follow these rules and increasingly, we are finding out they do not. Perhaps we should not be so surprised at this fact considering that organisms, no matter the size, always have their internal processes intimately connect to each other. Interconnected processes help build redundancies and allow complexity and more refined biological responses without the need to build additional classes of proteins. This doubling-up of duties also reduces the amount of components needed to accomplish every task.

However, does this mean that an output such as division length is merely the sum of stochastic changes in a collection of flat processes, or is it a more directed and orchestrated event that are arranged in a hierarchy? In the former case, phenotype is an output of the entire network of genes that has but many connections to all the other components. In the latter case, division length is regulated by only a few players, which while sensitive to all the relevant genes in the network, dominate the process of division length control. It seems that the switch-like decision to divide is more hierarchal, and regulation all must flow through only a few components centered on cdk1. However, it seems likely that size determination is more flat, having many components that each contribute a small part to the overall signal. This difference makes some intuitive sense as division is a binary effect that the cell must commit entirely to, whereas cell need to be able to successfully divide at a spectrum of sizes. This mode of regulation may allow for greater flexibility and sensitivity so that size can be carefully gauged due to changing circumstances.

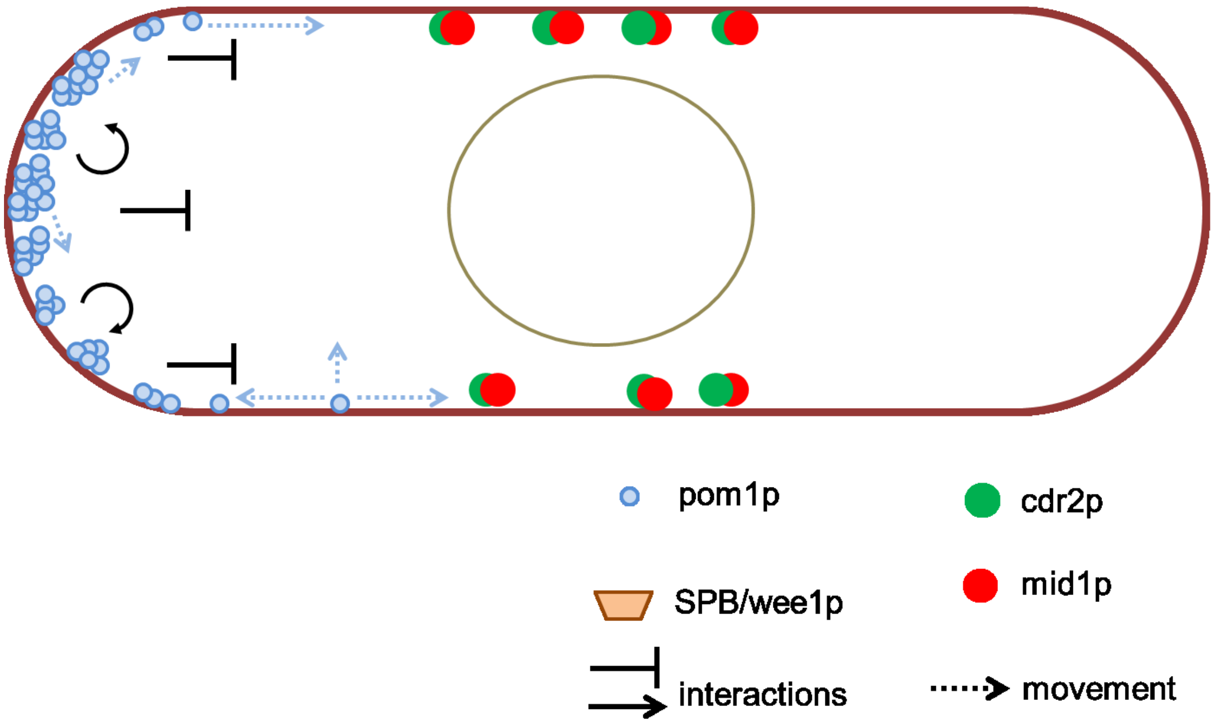

Figure 5.1 Model of the diffusion-based pom1p gradient

Pom1p can diffuse and self-organize into clusters, thereby buffering itself from the middle of the cell.

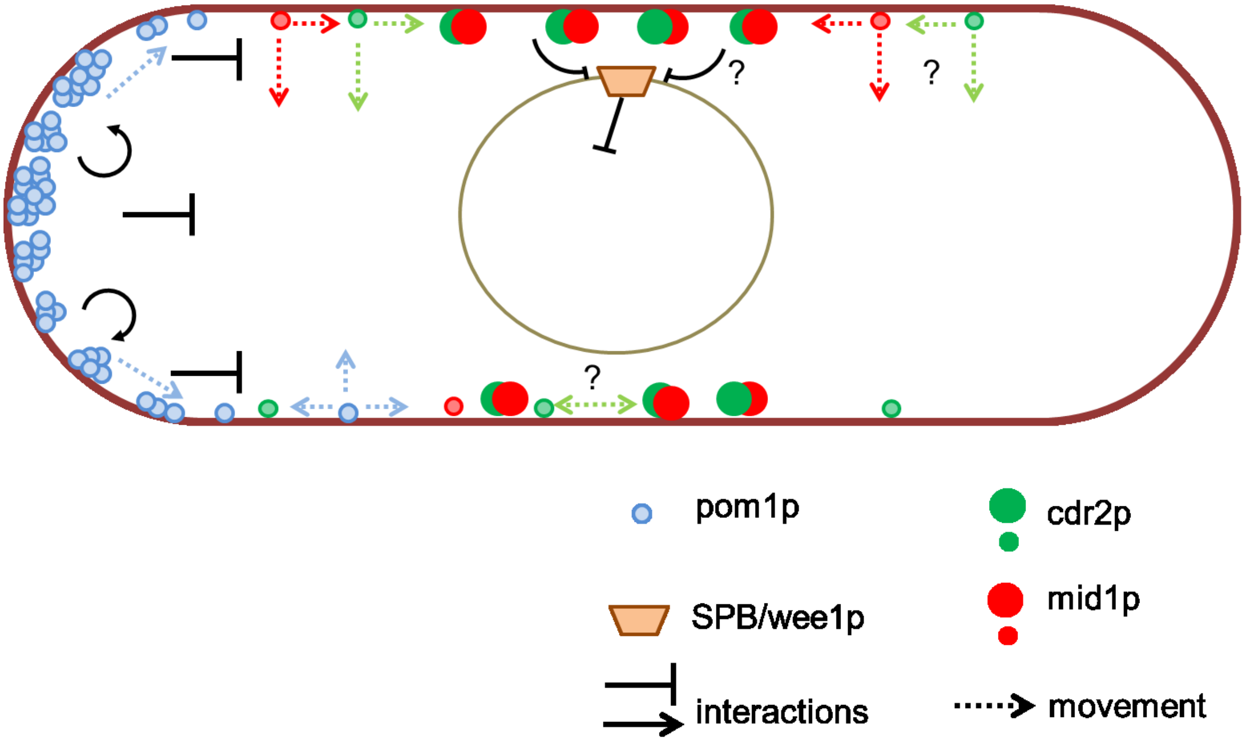

Figure 5.2 Model of the diffusion-based pom1p gradient and its potential downstream interactions

Pom1p gradients may provide a mechanism of localizing midsome proteins like cdr2p and mid1p by preventing its accumulation on the cortex at the cell tips. This allows accumulation at the middle where its proximity to the spindle pole body may allow for more efficient information transfer.

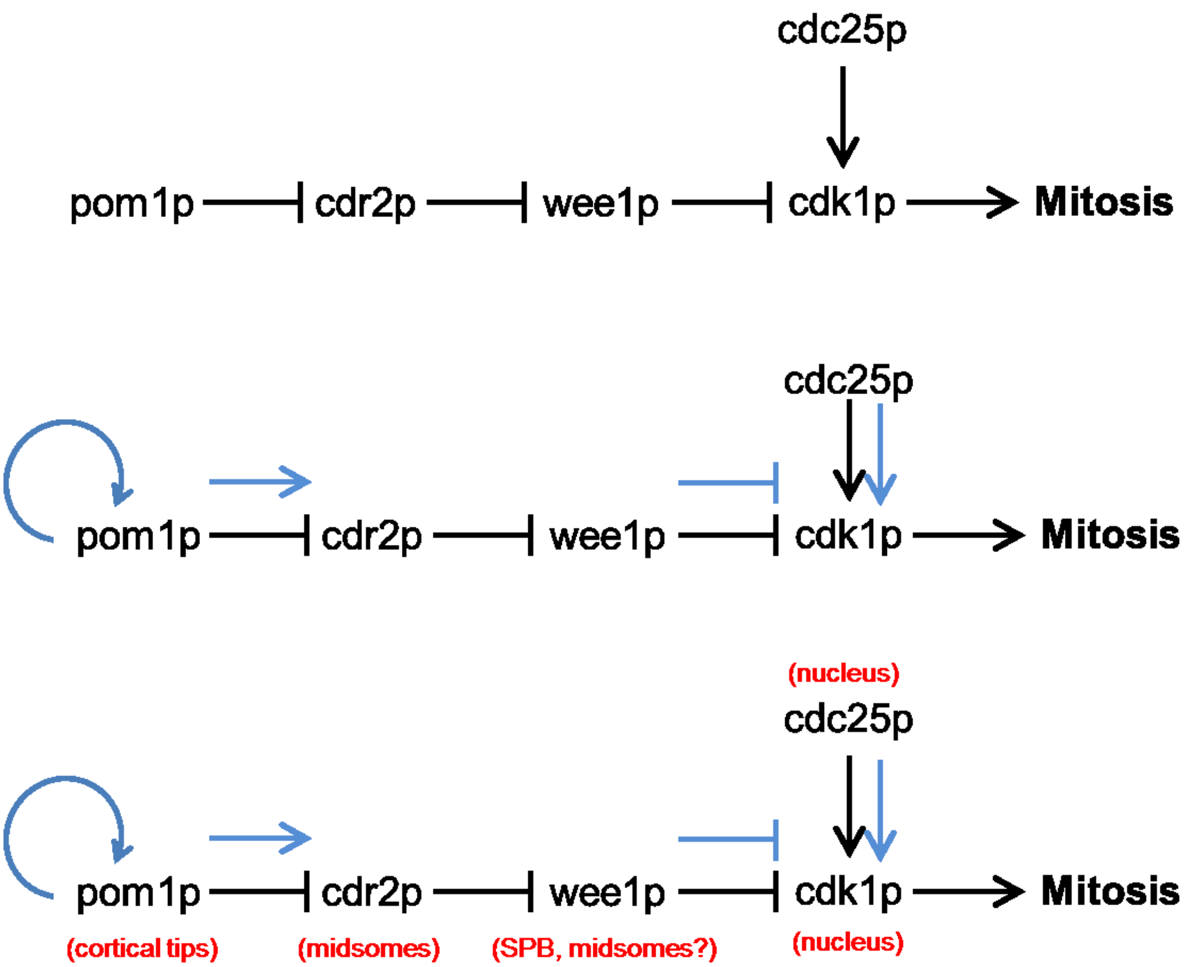

Figure 5.3 Regulatory pathway for activation of mitosis

Genetic pathway for size with phosphyilation interactions (blue arrows), and localizing information (red) overlayed.

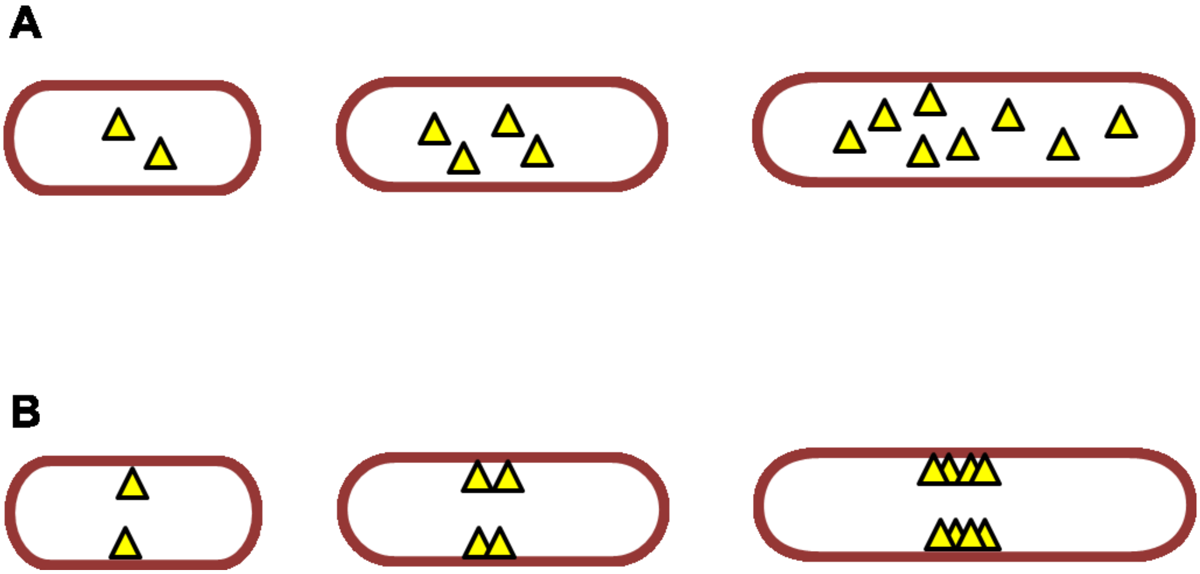

Figure 5.4 Mechanism for size sensing

A. Molecules increasing in number in proportion to cell size distributed randomly in cells do not increase in concentration.
B. Molecules increasing in number in proportion to cell size when restricted in localization can cause a local increase in concentration.

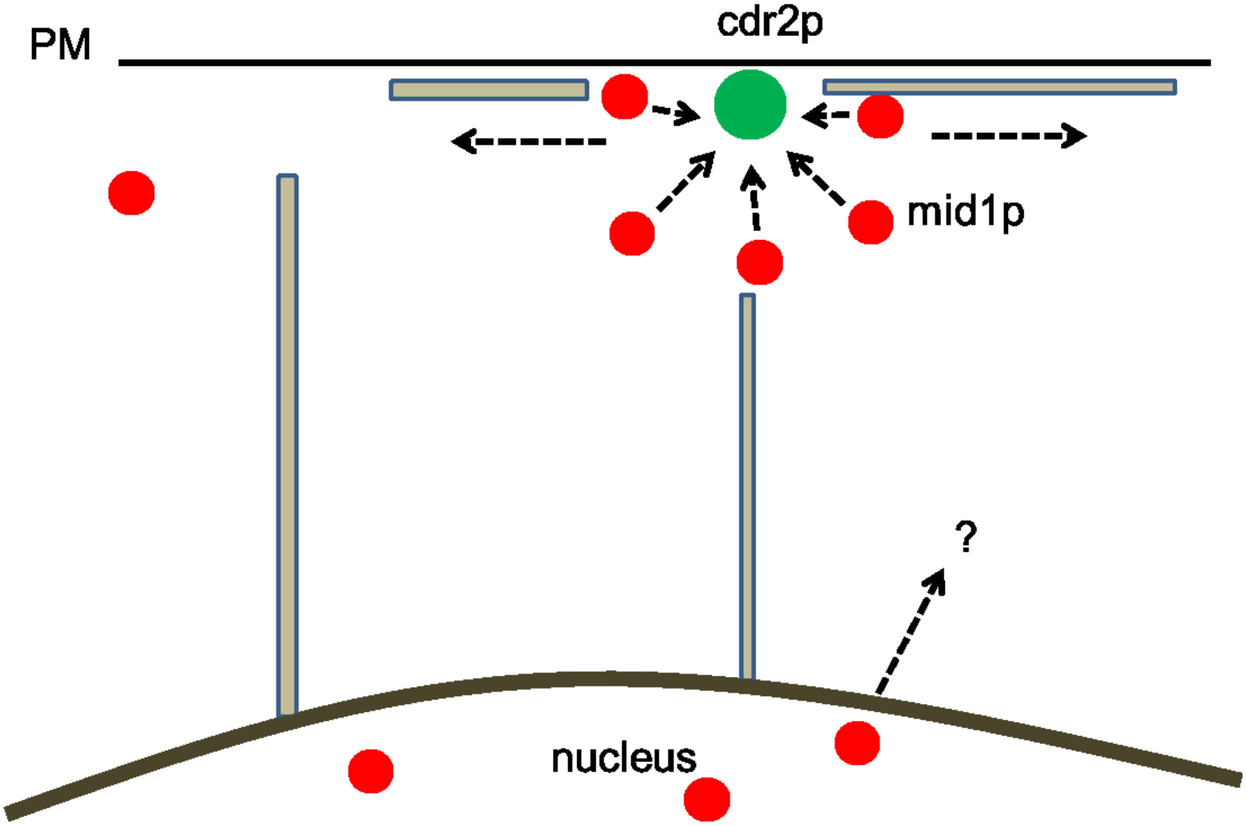

Figure 5.5 Model of the ER link to the nucleus

Cortical ER domains create “pockets” of ER/PM interphase that allow midsome localization and stabilization, while the tubular ER that connects the cortex and the nucleus may provide a way for mid1p to shuttle out of the nucleus.

Table 1 Yeast strains used in this study

Strains	**Genotype**	**References**
FC866	h^- *spn4-GFP:kanMX*	Lab collection
FC1162	h^- *pom1-GFP:kanMX*	(Bahler and Pringle, 1998)
FC1139	h^+ *rlc1-GFP:kanR ade6 leu1-32 ura4-D18*	Lab collection
FC2054	h^+ *pom1-tomato-dimer:natMX ade6 leu1-32 ura4-D18*	(Martin and Berthelot-Grosjean, 2009)
KP42	h^+ *pom1-tomato-dimer:natMX,tea1-3GFP:kanMX ade6-216 ura4-D18 leu1-32*	This study
KP189	h^- *pom1-tomato-dimer:natMX, end4::ura4 leu-*	This study
KP191	h^+ *pom1-tomato-dimer:natMX tea1::ura4 ade6 leu1-32 ura4-D18*	This study
KP193	h^+ *pom1-tomato-dimer:natMX tea4::ura4 ade6 leu1-32 ura4-D18*	This study
KP195	h^- *pom1-tomato-dimer:natMX leu-32::SV40-GFP-abt2(leu1+) ade6 leu1-32 ura4-D18*	This study
RB653	h^+ *dip1-GFP:kanMX ade6 leu1-32 ura4-D18*	Lab collection
FC2685	h^+ *pom1-3GFP:kanMX ade6 leu1-32 ura4-D18*	This study
FC2678	h^+ *pom1-tomato-dimer:natMX, cdr2-GFP:kanMX ade6 leu1-32 ura4-D18*	This study
FC2688	h^+ *cdr2-GFP:natMX ade6 leu1-32 ura4-D18*	This study
FC2689	h^+ *kanMX-P81nmt1-cdr2-GFP:natMX*	This study
FC2690	h^+ *cdr2-GFP:natMX, for3::kanMX*	This study
FC2686	h^- *pom1-monomeric-GFP:kanMX, cdr2-tomato-dimer:natMX ade6 leu1-32 ura4-D18*	This study
FC2687	h^- *pom1-3GFP:kanMX, cdr2-tomato-dimer:natMX ade6 leu1-32 ura4-D18*	This study
FC2683	h^+ *bzz1-GFP:kanMX ade6 leu1-32 ura4-D18*	(Saunders & Pan et al. 2012)
FC2046	h^- *cdr2-tomato-dimer:natMX ade6 leu1-32 ura4-D18*	Lab collection
	Complete collection	
KP0001	*ade6-216, ura4-D18, leu1-32*	personal collection
KP0002	*pom1-GFP-kanMX*	personal collection
KP0003	*pom1-3GFP-kanMX, ade6-216, ura4-D18, leu1-32*	personal collection
KP0004	*pom1-3GFP-kanMX, ade6-216, ura4-D18, leu1-32*	personal collection
KP0005	*pom1-3GFP-kanMX, ade6-216, ura4-D18,*	personal collection

	leu1-32	
KP0006	*pom1-3GFP-kanMX, ade6-216, ura4-D18, leu1-32*	personal collection
KP0007	*pom1-3GFP-kanMX, ade6-216, ura4-D18, leu1-32*	personal collection
KP0008	*ade6-216, ura4-D18, leu1-32*	personal collection
KP0009	*myo52Δ-ura4+, ura4-D18, leu32, ade6-216*	personal collection
KP0010	*end4Δ::Ura4+, leu-*	personal collection
KP0011	*myo1Δ::kanMX, leu1, his3, ura4, ade6*	personal collection
KP0012	*wsp1Δ::kanMX, leu1, his3, ura4, ade6*	personal collection
KP0013	*Pom1Δ::ura4, ura4-D18*	personal collection
KP0014	*pom1-tomato-natMX, ade6-216, ura4-D18, leu1-32*	personal collection
KP0015	*pom1-3GFP-kanMX, end4Δ-Ura4+, leu-*	personal collection
KP0016	*pom1-as1 ade6-216, ura4-D18, leu1-32*	personal collection
KP0017	*pom1-as1-GFP-KanMX ade6-216, ura4-D18, leu1-32*	personal collection
KP0018	*pom1-tomato-natMX, ade6-216, ura4-D18, leu1-32*	personal collection
KP0019	*pom1-drompa-KanMX ade6-216, ura4-D18, leu1-32*	personal collection
KP0020	*Mid1-tomato-KanMX ade6-216, ura4-D18, leu1-32*	personal collection
KP0021	*pom1-3GFP-kanMX, ade6-216, ura4-D18, leu1-32*	personal collection
KP0022	*pom1-3GFP-kanMX, ade6-216, ura4-D18, leu1-32 4th backcross*	personal collection
KP0023	*pom1-3GFP-kanMX, pom1-tomato-natMX Diploid*	personal collection
KP0024	*pom1-3GFP-kanMX, pom1-tomato-natMX Diploid*	personal collection
KP0025	*pom1-3GFP-kanMX, pom1-tomato-natMX Diploid*	personal collection
KP0026	*pom1-3GFP-kanMX, pom1-tomato-natMX Diploid*	personal collection
KP0027	*pom1-3GFP-kanMX, pom1-tomato-natMX Diploid*	personal collection
KP0028	*pom1-3GFP-kanMX, pom1-tomato-natMX Diploid*	personal collection
KP0029	*pom1-3GFP-kanMX, pom1-tomato-natMX Diploid*	personal collection
KP0030	*pom1-3GFP-kanMX, pom1-tomato-natMX Diploid*	personal collection
KP0031	*pom1-tomato-natMX, ade6-216, ura4-D18, leu1-32 (clone 1)*	personal collection

KP0032	*pom1-tomato-natMX, ade6-216, ura4-D18, leu1-32 (clone 2)*	personal collection
KP0033	*pom1-3GFP-kanMX, ade6-216, ura4-D18, leu1-32 5th backcross (clone 4)*	personal collection
KP0034	*pom1-3GFP-kanMX, ade6-216, ura4-D18, leu1-32 5th backcross (clone 5)*	personal collection
KP0035	*pom1-3GFP-kanMX, ade6-216, ura4-D18, leu1-32 5th backcross (clone 3)*	personal collection
KP0036	*pom1-3GFP-kanMX, ade6-216, ura4-D18, leu1-32 5th backcross (clone 6)*	personal collection
KP0037	*Tea1-3GFP-kanMX, ade6-216, ura4-D18, leu1-32*	personal collection
KP0038	*Tea1-3GFP-kanMX, ade6-216, ura4-D18, leu1-32*	personal collection
KP0039	*Tea1-3GFP-kanMX, ade6-216, ura4-D18, leu1-32*	personal collection
KP0042	*pom1-tomato-Nat, tea1-3GFP-kanMX ade6-216, ura4-D18, leu1-32*	personal collection
KP0043	*pom1-tomato-Nat, tea1-3GFP-kanMX ade6-216, ura4-D18, leu1-32*	personal collection
KP0044	*pom1-tomato-Nat, tea1-3GFP-kanMX ade6-216, ura4-D18, leu1-32*	personal collection
KP0045	*pom1-tomato-Nat, tea1-3GFP-kanMX ade6-216, ura4-D18, leu1-32*	personal collection
KP0046	*pom1-3GFP-kanMX, mid1-tomato-Nat ade6-216, ura4-D18, leu1-32*	personal collection
KP0047	*pom1-3GFP-kanMX rsp1-1 ade6-216, ura4+, leu1-32*	personal collection
KP0048	*pom1-3GFP-kanMX rsp1-1 ade6-216, ura4+, leu1-32*	personal collection
KP0049	*pom1-3GFP-kanMX tea1Δ::ura4+*	personal collection
KP0050	*pom1-3GFP-kanMX tea1Δ::ura4+*	personal collection
KP0051	*pom1-3GFP-kanMX tea1Δ::ura4+*	personal collection
KP0052	*pom1-3GFP-kanMX tea1Δ::ura4+*	personal collection
KP0053	*pom1-tomato-Nat, scd1-GFP-kanMX*	personal collection
KP0054	*pom1-tomato-Nat, scd1-GFP-kanMX*	personal collection
KP0055	*pom1-3GFP-kanMX, cdc25-22*	personal collection
KP0056	*pom1-3GFP-kanMX, tea1Δ::ura4+, cdc25-22*	personal collection
KP0057	*pom1-3GFP-kanMX, tea1Δ::ura4+, cdc25-22*	personal collection
KP0058	*pom1-tomato-Nat, wsp1Δ::his ade6-216, ura4+, leu1-32*	personal collection
KP0059	*pom1-tomato-Nat, wsp1Δ::his ade6-216, ura4+, leu1-32*	personal collection
KP0060	*pom1-tomato-Nat, wsp1Δ::his ade6-216, ura4+, leu1-32*	personal collection

KP0061	*pom1-tomato-Nat, wsp1Δ::his ade6-216, ura4+, leu1-32*	personal collection
KP0062	*pom1-GFP-kanMX, wsp1Δ::his ade6-216, ura4+, leu1-32*	personal collection
KP0063	*pom1-GFP-kanMX, wsp1Δ::his ade6-216, ura4+, leu1-32*	personal collection
KP0064	*pom1-3GFP-kanMX, cdr2-tomato-Nat ade6-216, ura4+, leu1-32*	personal collection
KP0065	*pom1-3GFP-kanMX, cdr2-tomato-Nat ade6-216, ura4+, leu1-32*	personal collection
KP0066	*pom1-tomato-Nat, cdr2-GFP-kanMX ade6-216, ura4+, leu1-32*	personal collection
KP0067	*pom1-tomato-Nat, cdr2-GFP-kanMX ade6-216, ura4+, leu1-32*	personal collection
KP0068	*pom1-tomato-Nat, cdr2-GFP-kanMX ade6-216, ura4+, leu1-32*	personal collection
KP0069	*pom1-tomato-Nat, cdr2-GFP-kanMX ade6-216, ura4+, leu1-32*	personal collection
KP0070	*pom1-as1-GFP ade6-216, ura4-D18, leu1-32*	personal collection
KP0071	*pom1-as1-GFP ade6-216, ura4-D18, leu1-32*	personal collection
KP0072	*cdr2-tomato-Nat ade6-216, ura4-D18, leu1-32*	personal collection
KP0073	*pom1-tomato-Nat, cdr2-tomato-Nat ade6-216, ura4-D18, leu1-32*	personal collection
KP0074	*mid1-GFP-KanMX, pom1-tomato-Nat ade6-216, ura4-D18, leu1-32*	personal collection
KP0075	*mid1-GFP-KanMX, pom1-tomato-Nat ade6-216, ura4-D18, leu1-32*	personal collection
KP0076	*cdr2-GFP-KanMX, pom1Δ::ura+*	personal collection
KP0077	*cdr2-GFP-KanMX, pom1Δ::ura+*	personal collection
KP0078	*leu-32::pSV40-GFP-atb2(leu1)*	personal collection
KP0079	*cdc25-22, leu-32::pSV40-GFP-atb2(leu1)*	personal collection
KP0080	*mat1:cyh, rpl42:cyhR*	personal collection
KP0081	*cdr2-GFP-KanMX ade6-216, ura4-D18, leu1-32*	personal collection
KP0082	*cdr2-GFP-KanMX ade6-216, ura4-D18, leu1-32*	personal collection
KP0083	*pom1-as1-tomato-Nat, cdr2-GFP-KanMX ade6-216, ura4-D18, leu1-32*	personal collection
KP0084	*pom1-as1-tomato-Nat, cdr2-GFP-KanMX ade6-216, ura4-D18, leu1-32*	personal collection
KP0085	*rlc1-GFP-kanMX ade6-216, ura4-D18, leu1-32*	personal collection
KP0086	*rlc1-GFP-kanMX ade6-216, ura4-D18, leu1-32*	personal collection
KP0087	*cdr2-GFP-kanMX, rlc1-tomato-Nat ade6-216, ura4-D18, leu1-32*	personal collection
KP0088	*cdr2-GFP-kanMX, rlc1-tomato-Nat ade6-216,*	personal collection

	ura4-D18, leu1-32	
KP0089	*cdr2-tomato-NatMX, mid1-3GFP-kanMX ade6-216, ura4-D18, leu1-32*	personal collection
KP0090	*cdr2-GFP-kanMX, mid1-tomato-kanMX ade6-216, ura4-D18, leu1-32*	personal collection
KP0091	*cdr2-GFP-kanMX, mid1-tomato-kanMX ade6-216, ura4-D18, leu1-32*	personal collection
KP0092	*cdr2-GFP-kanMX, cdc25-22 ade6-216, ura4-D18, leu1-32*	personal collection
KP0093	*cdr2-GFP-kanMX, rlc1-tomato-Nat, cdc25-22*	personal collection
KP0094	*cdr2-GFP-kanMX, rlc1-tomato-Nat, cdc25-22*	personal collection
KP0095	*mid1-YFP-kanMX ade6-216, ura4-D18, leu1-32*	personal collection
KP0096	*mid1-YFP-kanMX ade6-216, ura4-D18, leu1-32*	personal collection
KP0097	*rtn1-CFP-kanMX ade6-216, ura4-D18, leu1-32*	personal collection
KP0098	*rtn1-CFP-kanMX ade6-216, ura4-D18, leu1-32*	personal collection
KP0099	*mid1-YFP-kanMX, rtn1-CFP ade6-216, ura4-D18, leu1-32*	personal collection
KP0100	*mid1-YFP-kanMX, rtn1-CFP ade6-216, ura4-D18, leu1-32*	personal collection
KP0101	*mid1-YFP-kanMX, ost1mCherry-ura4+ ade6-216, ura4-D18, leu1-32*	personal collection
KP0102	*mid1-YFP-kanMX, ost1mCherry-ura4+ ade6-216, ura4-D18, leu1-32*	personal collection
KP0103	*mid1-3GFP-kan, ost1mCherry-ura4+ ade6-216, ura4-D18, leu1-32*	personal collection
KP0104	*mid1-3GFP-kan, ost1mCherry-ura4+ ade6-216, ura4-D18, leu1-32*	personal collection
KP0105	*mid1-YFP-kanMX, ost1mCherry-ura4+ rtn1-CFP-nat ade6-216, ura4-D18, leu1-32*	personal collection
KP0106	*mid1-YFP-kanMX, ost1mCherry-ura4+ rtn1-CFP-nat ade6-216, ura4-D18, leu1-32*	personal collection
KP0107	*mid1-YFP-kanMX, ost1mCherry-ura4+ rtn1-CFP-nat ade6-216, ura4-D18, leu1-32*	personal collection
KP0108	*mid1-YFP-kanMX, ost1mCherry-ura4+ rtn1-CFP-nat ade6-216, ura4-D18, leu1-32*	personal collection
KP0109	*rlc1-GFP-kanMX ade6-216, ura4-D18, leu1-32*	personal collection
KP0110	*rlc1-GFP-kanMX, cdr2::ura ade6-216, ura4-D18, leu1-32*	personal collection
KP0111	*rlc1-GFP-kanMX, rtn1::natMX ade6-216, ura4-D18, leu1-32*	personal collection
KP0112	*rlc1-GFP-kanMX, cdr2::ura, rtn1::natMX ade6-216, ura4-D18, leu1-32*	personal collection
KP0113	*pom1-tomato-natMX*	personal collection

KP0114	*mid1-3GFP-kanMX ade6-216, ura4-D18, leu1-32*	personal collection
KP0115	*mid1-3GFP-kanMX, cdr2::ura ade6-216, ura4-D18, leu1-32*	personal collection
KP0116	*mid1-3GFP-kanMX, rtn1::natMX ade6-216, ura4-D18, leu1-32*	personal collection
KP0117	*mid1-3GFP-kanMX, cdr2::ura, rtn1::natMX ade6-216, ura4-D18, leu1-32*	personal collection
KP0118	*mid1-tomato-KanMX ade6-216, ura4-D18, leu1-32*	personal collection
KP0119	*rlc1-tomato-NatMX ade6-216, ura4-D18, leu1-32*	personal collection
KP0120	*sad1-GFP-KanMX ade6-216, ura4-D18, leu1-32*	personal collection
KP0121	*mid1-GFP-KanMX, pcp1-RFP-KanMX ade6-216, ura4-D18, leu1-32*	personal collection
KP0122	*pom1-tomato-natMX, cdr2-GFP-kanMX ade6-216, ura4-D18, leu1-32*	personal collection
KP0123	*pom1-tomato-natMX, cdr2-GFP-kanMX ade6-216, ura4-D18, leu1-32*	personal collection
KP0124	*rtn1-tomato-natMX ade6-216, ura4-D18, leu1-32*	personal collection
KP0125	*rtn1-tomato-natMX ade6-216, ura4-D18, leu1-32*	personal collection
KP0126	*sec24-GFP-kanMX, cdr2-tomato-natMX ade6-216, ura4-D18, leu1-32*	personal collection
KP0127	*sec24-GFP-kanMX, cdr2-tomato-natMX ade6-216, ura4-D18, leu1-32*	personal collection
KP0128	*sec24-GFP-kanMX, pom1-tomato-natMX ade6-216, ura4-D18, leu1-32*	personal collection
KP0129	*sec24-GFP-kanMX, pom1-tomato-natMX ade6-216, ura4-D18, leu1-32*	personal collection
KP0130	*sad1-GFP-KanMX, rlc1-GFP-kanMX ade6-216, ura4-D18, leu1-32*	personal collection
KP0131	*sad1-GFP-KanMX, rlc1-GFP-kanMX ade6-216, ura4-D18, leu1-32*	personal collection
KP0132	*rtn1-GFP-kanMX, pom1-tomato-natMX ade6-216, ura4-D18, leu1-32*	personal collection
KP0133	*rtn1-GFP-kanMX, pom1-tomato-natMX ade6-216, ura4-D18, leu1-32*	personal collection
KP0134	*sad1-GFP-KanMX ade6-216, ura4-D18, leu1-32*	personal collection
KP0135	*sad1-GFP-KanMX ade6-216, ura4-D18, leu1-32*	personal collection
KP0136	*rtn1-GFP-kanMX, cdr2-tomato-natMX ade6-216, ura4-D18, leu1-32*	personal collection

KP0137	*rtn1-GFP-kanMX, cdr2-tomato-natMX, pom1-tomato-natMX ade6-216, ura4-D18, leu1-32*	personal collection
KP0138	*sad1-GFP-KanMX, rlc1-GFP-kanMX, cdr2::ura ade6-216, ura4-D18, leu1-32*	personal collection
KP0139	*sad1-GFP-KanMX, rlc1-GFP-kanMX, cdr2::ura ade6-216, ura4-D18, leu1-32*	personal collection
KP0140	*sad1-GFP-KanMX, rlc1-GFP-kanMX, rtn1::natMX ade6-216, ura4-D18, leu1-32*	personal collection
KP0141	*sad1-GFP-KanMX, rlc1-GFP-kanMX, cdr2::ura, rtn1::natMX ade6-216, ura4-D18, leu1-32*	personal collection
KP0142	*sad1-GFP-KanMX, rlc1-GFP-kanMX, cdr2::ura, rtn1::natMX ade6-216, ura4-D18, leu1-32*	personal collection
KP0143	*rtn1::natMX ade6-216, ura4-D18, leu1-32*	personal collection
KP0144	*rtn1::natMX ade6-216, ura4-D18, leu1-32*	personal collection
KP0145	*pom1::kanMX ade6-216, ura4-D18, leu1-32*	personal collection
KP0146	*pom1::kanMX ade6-216, ura4-D18, leu1-32*	personal collection
KP0147	*rtn1::natMX, pom1::kanMX ade6-216, ura4-D18, leu1-32*	personal collection
KP0148	*rtn1::natMX, pom1::kanMX ade6-216, ura4-D18, leu1-32*	personal collection
KP0149	*rtn1::natMX, pom1::kanMX ade6-216, ura4-D18, leu1-32*	personal collection
KP0150	*rtn1::natMX, pom1::kanMX ade6-216, ura4-D18, leu1-32*	personal collection
KP0151	*mid1-tomato-KanMX sec24-GFP-kanMX ade6-216, ura4-D18, leu1-32*	personal collection
KP0152	*mid1-tomato-KanMX sec24-GFP-kanMX ade6-216, ura4-D18, leu1-32*	personal collection
KP0153	*mid1-tomato-KanMX yop1-GFP-kanMX ade6-216, ura4-D18, leu1-32*	personal collection
KP0154	*mid1-tomato-KanMX yop1-GFP-kanMX ade6-216, ura4-D18, leu1-32*	personal collection
KP0155	*mid1-tomato-KanMX pom1::ura, rtn1::natMX ade6-216, ura4-D18, leu1-32*	personal collection
KP0156	*mid1-tomato-KanMX pom1::ura, rtn1::natMX ade6-216, ura4-D18, leu1-32*	personal collection
KP0157	*mid1-tomato-KanMX pom1::ura, rtn1::natMX ade6-216, ura4-D18, leu1-32*	personal collection
KP0158	*mid1-tomato-KanMX pom1::ura, rtn1::natMX ade6-216, ura4-D18, leu1-32*	personal collection
KP0159	*rtn1::natMX, dmf1::kanMX, [mid1-4GFP-leu] integrated ade6-216, ura4-D18, leu1-32*	personal collection
KP0160	*rtn1::natMX, dmf1::kanMX, [mid1-4GFP-leu]*	personal collection

	integrated ade6-216, ura4-D18, leu1-32	
KP0161	*rtn1::natMX, dmf1::kanMX, [mid1-4GFP-leu] integrated ade6-216, ura4-D18, leu1-32*	personal collection
KP0162	*rtn1::natMX, dmf1::kanMX, [mid1-4GFP-leu] integrated ade6-216, ura4-D18, leu1-32*	personal collection
KP0163	*rtn1::natMX, dmf1::kanMX, [mid1nsm-4GFP-leu] integrated ade6-216, ura4-D18, leu1-32*	personal collection
KP0164	*rtn1::natMX, dmf1::kanMX, [mid1nsm-4GFP-leu] integrated ade6-216, ura4-D18, leu1-32*	personal collection
KP0165	*rtn1::natMX, dmf1::kanMX, [mid1nsm-4GFP-leu] integrated ade6-216, ura4-D18, leu1-32*	personal collection
KP0166	*rtn1::natMX, dmf1::kanMX, [mid1nsm-4GFP-leu] integrated ade6-216, ura4-D18, leu1-32*	personal collection
KP0167	*rtn1::natMX, dmf1::kanMX, [nls-mid1-4GFP-leu] integrated ade6-216, ura4-D18, leu1-32*	personal collection
KP0168	*rtn1::natMX, dmf1::kanMX, [nls-mid1-4GFP-leu] integrated ade6-216, ura4-D18, leu1-32*	personal collection
KP0169	*rtn1::natMX, dmf1::kanMX, [nls-mid1-4GFP-leu] integrated ade6-216, ura4-D18, leu1-32*	personal collection
KP0170	*rtn1::natMX, dmf1::kanMX, [nls-mid1-4GFP-leu] integrated ade6-216, ura4-D18, leu1-32*	personal collection
KP0171	*rtn1-tomato-natMX, dmf1::kanMX, [mid1-4GFP-leu] integrated ade6-216, ura4-D18, leu1-32*	personal collection
KP0172	*rtn1-tomato-natMX, dmf1::kanMX, [mid1-4GFP-leu] integrated ade6-216, ura4-D18, leu1-32*	personal collection
KP0173	*rtn1-tomato-natMX, dmf1::kanMX, [mid1nsm-4GFP-leu] integrated ade6-216, ura4-D18, leu1-32*	personal collection
KP0174	*rtn1-tomato-natMX, dmf1::kanMX, [mid1nsm-4GFP-leu] integrated ade6-216, ura4-D18, leu1-32*	personal collection
KP0175	*rtn1-tomato-natMX, dmf1::kanMX, [nls-mid1-4GFP-leu] integrated ade6-216, ura4-D18, leu1-32*	personal collection
KP0176	*rtn1-tomato-natMX, dmf1::kanMX, [nls-mid1-4GFP-leu] integrated ade6-216, ura4-D18, leu1-32*	personal collection
KP0177	*cdr2-tomato-natMX, dmf1::kanMX, [mid1-4GFP-leu] integrated ade6-216, ura4-D18, leu1-32*	personal collection
KP0178	*cdr2-tomato-natMX, dmf1::kanMX, [mid1-4GFP-leu] integrated ade6-216, ura4-D18, leu1-32*	personal collection
KP0179	*cdr2-tomato-natMX, dmf1::kanMX, [mid1nsm-*	personal collection

	4GFP-leu] integrated ade6-216, ura4-D18, leu1-32	
KP0180	*cdr2-tomato-natMX, dmf1::kanMX, [mid1nsm-4GFP-leu] integrated ade6-216, ura4-D18, leu1-32*	personal collection
KP0181	*cdr2-tomato-natMX, dmf1::kanMX, [nls-mid1-4GFP-leu] integrated ade6-216, ura4-D18, leu1-32*	personal collection
KP0182	*cdr2-tomato-natMX, dmf1::kanMX, [nls-mid1-4GFP-leu] integrated ade6-216, ura4-D18, leu1-32*	personal collection
KP0183	*rtn1::natMX, cdr2::ura dmf1::kanMX, [nls-mid1-4GFP-leu] integrated ade6-216, ura4-D18, leu1-32*	personal collection
KP0184	*rtn1::natMX, cdr2::ura dmf1::kanMX, [nls-mid1-4GFP-leu] integrated ade6-216, ura4-D18, leu1-32*	personal collection
KP0185	*rtn1-GFP-kanMX ade6-216, ura4-D18, leu1-32*	personal collection
KP0186	*rtn1-GFP-kanMX ade6-216, ura4-D18, leu1-32*	personal collection
KP0187	*rtn1::natMX, pom1-tomato-NatMX ade6-216, ura4-D18, leu1-32*	personal collection
KP0188	*rtn1::natMX, pom1-tomato-NatMX ade6-216, ura4-D18, leu1-32*	personal collection
KP0189	*pom1-tomato-natMX, end4::ura ade6-216, ura4-D18, leu1-32*	personal collection
KP0190	*pom1-tomato-natMX, end4::ura ade6-216, ura4-D18, leu1-32*	personal collection
KP0191	*pom1-tomato-natMX,tea1::kanMX ade6-216, ura4-D18, leu1-32*	personal collection
KP0192	*pom1-tomato-natMX,tea1::kanMX ade6-216, ura4-D18, leu1-32*	personal collection
KP0193	*pom1-tomato-natMX,tea1::kanMX ade6-216, ura4-D18, leu1-32*	personal collection
KP0194	*pom1-tomato-natMX,tea1::kanMX ade6-216, ura4-D18, leu1-32*	personal collection
KP0195	*pom1-tomato-natMX, leu-32::pSV40-GFP-atb2(leu1)*	personal collection
KP0196	*pom1-tomato-natMX, rtn1-GFP-kanMX ade6-216, ura4-D18, leu1-32*	personal collection
KP0197	*pom1-tomato-natMX, rtn1-GFP-kanMX ade6-216, ura4-D18, leu1-32*	personal collection
KP0198	*mid1-3GFP-natMX ade6-216, ura4-D18, leu1-32*	personal collection
KP0199	*pom1-tomato-natMX, cdr2::ura ade6-216, ura4-D18, leu1-32*	personal collection
KP0200	*pom1-tomato-natMX, cdr2::ura ade6-216,*	personal collection

	ura4-D18, leu1-32	
KP0201	*pom1-tomato-natMX, cdc25-22 ade6-216, ura4-D18, leu1-32*	personal collection
KP0202	*pom1-tomato-natMX, cdc25-22 ade6-216, ura4-D18, leu1-32*	personal collection
KP0203	*[pom1-poly+ GFP:leu] ade6-216, ura4-D18, leu1-32*	personal collection
KP0204	*[pom1-poly+ GFP:leu] ade6-216, ura4-D18, leu1-32*	personal collection
KP0205	*pom1-tomato-NatMX, [pom1-poly+ GFP:leu] ade6-216, ura4-D18, leu1-32*	personal collection
KP0206	*pom1-tomato-NatMX, [pom1-poly+ GFP:leu] ade6-216, ura4-D18, leu1-32*	personal collection
KP0207	*pom1::ura, [pom1-poly+ GFP:leu] ade6-216, ura4-D18, leu1-32*	personal collection
KP0208	*pom1::ura, [pom1-poly+ GFP:leu] ade6-216, ura4-D18, leu1-32*	personal collection
KP0209	*pom1-as1-tomato-NatMX ade6-216, ura4-D18, leu1-32*	personal collection
KP0210	*pom1-as1-tomato-NatMX ade6-216, ura4-D18, leu1-32*	personal collection
KP0211	*cdr2-tomato-NatMX, mid1-3GFP-kanMX ade6-216, ura4-D18, leu1-32*	personal collection
KP0214	*sad1-GFP-KanMX, pom1-tomato-NatMX ade6-216, ura4-D18, leu1-32*	personal collection
KP0215	*sad1-GFP-KanMX, pom1-3GFP-KanMX ade6-216, ura4-D18, leu1-32*	personal collection
KP0216	*sad1-GFP-KanMX, pom1-3GFP-KanMX ade6-216, ura4-D18, leu1-32*	personal collection
KP0217	*pom1-2*	personal collection
KP0218	*pom1-2*	personal collection
KP0219	*pom1-tomato-NatMX, cdr2-GFP-kanMX, cdc25-22 ade6-216, ura4-D18, leu1-32*	personal collection
KP0220	*pom1-tomato-NatMX, cdr2-GFP-kanMX, cdc25-22 ade6-216, ura4-D18, leu1-32*	personal collection
KP0221	*pom1-as1-GFP-kanMX, cdr2-GFP-kanMX, mid1-tomato-kanMX ade6-216, ura4-D18, leu1-32*	personal collection
KP0222	*pom1-mGFP-KanMX ade6-216, ura4-D18, leu1-32*	personal collection
KP0223	*pom1ΔC-mGFP-KanMX ade6-216, ura4-D18, leu1-32*	personal collection
KP0224	*cdr2-GFP-kanMX, mid1-tomato-kanMX ade6-216, pom1-2 ade6-216, ura4-D18, leu1-32*	personal collection
KP0225	*cdr2-GFP-kanMX, mid1-tomato-kanMX ade6-*	personal collection

	216, pom1-2 ade6-216, ura4-D18, leu1-32	
KP0226	*mid1-tomato-kanMX ade6-216, pom1-as1-GFP-kan ade6-216, ura4-D18, leu1-32*	personal collection
KP0227	*mid1-tomato-kanMX ade6-216, pom1-as1-GFP-kan ade6-216, ura4-D18, leu1-32*	personal collection
KP0228	*cdr2-GFP-kanMX, mid1-tomato-kanMX ade6-216, pom1-as1-GFP-kan ade6-216, ura4-D18, leu1-32*	personal collection
KP0229	*cdr2-GFP-kanMX, mid1-tomato-kanMX ade6-216, pom1-as1-GFP-kan ade6-216, ura4-D18, leu1-32*	personal collection
KP0230	*cdr2-tomato-natMX, mid1-3GFP-kanMX ade6-216, pom1Δ::ura ade6-216, ura4-D18, leu1-32*	personal collection
KP0231	*cdr2-tomato-natMX, mid1-3GFP-kanMX ade6-216, pom1Δ::ura ade6-216, ura4-D18, leu1-32*	personal collection
KP0232	*cdr2-GFP-kanMX, mid1-tomato-kanMX ade6-216, pom1Δ::ura ade6-216, ura4-D18, leu1-32*	personal collection
KP0233	*cdr2-GFP-kanMX, mid1-tomato-kanMX ade6-216, pom1Δ::ura ade6-216, ura4-D18, leu1-32*	personal collection
KP0234	*pom1-mGFP-KanMX ade6-216, ura4-D18, leu1-32*	personal collection
KP0235	*cdr2-tomato-natMX ade6-216, ura4-D18, leu1-32*	personal collection
KP0236	*[pREP41X-GFP-leu]*	personal collection
KP0237	*cdr2-GFP-kan (GOOD) ade6-216, ura4-D18, leu1-32*	personal collection
KP0238	*cdr2-tomato-natMX, pom1-mGFP-kanMX*	personal collection
KP0239	*cdr2-tomato-natMX, pom1-mGFP-kanMX*	personal collection
KP0240	*cdr2-tomato-natMX, pom1ΔC-mGFP-kanMX*	personal collection
KP0241	*cdr2-tomato-natMX, pom1ΔC-mGFP-kanMX*	personal collection
KP0242	*cdr2-GFP-kan (GOOD), ade6-216, pom1Δ::natMX ura4-D18, leu1-32*	personal collection
KP0243	*cdr2-GFP-kan (GOOD), ade6-216, pom1Δ::natMX ura4-D18, leu1-32*	personal collection
KP0244	*cdr2-GFP-kan (GOOD) ade6-216, ura4-D18, leu1-32*	personal collection
KP0245	*alp14-GFP-kanMX, klp2-tomato-kanMX ade6-216, mal3Δ::natMX ade6-216, ura4-D18, leu1-32*	personal collection
KP0246	*alp14-GFP-kanMX, klp2-tomato-kanMX ade6-216, mal3Δ::natMX ade6-216, ura4-D18, leu1-32*	personal collection
KP0247	*mto1Δ::kanMX ade6-216, ura4-D18, leu1-32*	personal collection
KP0248	*cdr2-GFP-natMX ade6-216, ura4-D18, leu1-32*	personal collection
KP0249	*cdr2-GFP-natMX ade6-216, ura4-D18, leu1-32*	personal collection

KP0250	*cdr2-GFP-natMX ade6-216, ura4-D18, leu1-32*	personal collection
KP0251	*cdr2-GFP-natMX ade6-216, ura4-D18, leu1-32*	personal collection
KP0252	*cdr2-GFP-natMX ade6-216, ura4-D18, leu1-32*	personal collection
KP0253	*cut11-GFP-ura ade6-216, ura4-D18, leu1-32*	personal collection
KP0254	*cut11-GFP-ura ade6-216, ura4-D18, leu1-32*	personal collection
KP0255	*pom1-tomato-NatMX, cdr2-GFP-natMX, cdc25-22 ade6-216, ura4-D18, leu1-32*	personal collection
KP0256	*kanMX-P3nmt1-cdr2-GFP-natMX ade6-216, ura4-D18, leu1-32*	personal collection
KP0257	*kanMX-P3nmt1-cdr2-GFP-natMX ade6-216, ura4-D18, leu1-32*	personal collection
KP0258	*kanMX-P3nmt1-cdr2-GFP-natMX ade6-216, ura4-D18, leu1-32*	personal collection
KP0259	*kanMX-P3nmt1-cdr2-GFP-natMX ade6-216, ura4-D18, leu1-32*	personal collection
KP0260	*kanMX-P3nmt1-cdr2-GFP-natMX ade6-216, ura4-D18, leu1-32*	personal collection
KP0261	*kanMX-P3nmt1-cdr2-GFP-natMX ade6-216, ura4-D18, leu1-32*	personal collection
KP0262	*kanMX-P41nmt1-cdr2-GFP-natMX ade6-216, ura4-D18, leu1-32*	personal collection
KP0263	*kanMX-P41nmt1-cdr2-GFP-natMX ade6-216, ura4-D18, leu1-32*	personal collection
KP0264	*kanMX-P41nmt1-cdr2-GFP-natMX ade6-216, ura4-D18, leu1-32*	personal collection
KP0265	*kanMX-P41nmt1-cdr2-GFP-natMX ade6-216, ura4-D18, leu1-32*	personal collection
KP0266	*kanMX-P41nmt1-cdr2-GFP-natMX ade6-216, ura4-D18, leu1-32*	personal collection
KP0267	*kanMX-P41nmt1-cdr2-GFP-natMX ade6-216, ura4-D18, leu1-32*	personal collection
KP0268	*kanMX-P81nmt1-cdr2-GFP-natMX ade6-216, ura4-D18, leu1-32*	personal collection
KP0269	*kanMX-P81nmt1-cdr2-GFP-natMX ade6-216, ura4-D18, leu1-32*	personal collection
KP0270	*kanMX-P81nmt1-cdr2-GFP-natMX ade6-216, ura4-D18, leu1-32*	personal collection
KP0271	*kanMX-P81nmt1-cdr2-GFP-natMX ade6-216, ura4-D18, leu1-32*	personal collection
KP0272	*kanMX-P81nmt1-cdr2-GFP-natMX ade6-216, ura4-D18, leu1-32*	personal collection
KP0273	*kanMX-P81nmt1-cdr2-GFP-natMX ade6-216, ura4-D18, leu1-32*	personal collection
KP0274	*kanMX-P81nmt1-cdr2-GFP-natMX ade6-216, ura4-D18, leu1-32*	personal collection

KP0275	*cdr2-GFP-natMX ade6-216, 2Kbp-cdr2-GFP-kanMX [intergrated in leu] ura4-D18, leu1-32*	personal collection
KP0276	*cdr2-GFP-natMX ade6-216, 2Kbp-cdr2-GFP-kanMX [intergrated in leu] ura4-D18, leu1-32*	personal collection
KP0277	*cdr2-GFP-natMX ade6-216, 2Kbp-cdr2-GFP-kanMX [intergrated in leu] ura4-D18, leu1-32*	personal collection
KP0278	*cdr2-GFP-natMX ade6-216, 2Kbp-cdr2-GFP-kanMX [intergrated in leu] ura4-D18, leu1-32*	personal collection
KP0279	*cdr2-GFP-natMX ade6-216, 2Kbp-cdr2-GFP-kanMX [intergrated in leu] ura4-D18, leu1-32*	personal collection
KP0280	*cdr2-GFP-natMX ade6-216, 2Kbp-cdr2-GFP-kanMX [intergrated in leu] ura4-D18, leu1-32*	personal collection
KP0281	*cdr2-GFP-natMX ade6-216, 2Kbp-cdr2-GFP-kanMX [intergrated in leu] ura4-D18, leu1-32*	personal collection
KP0282	*cdr2-GFP-natMX ade6-216, 2Kbp-cdr2-GFP-kanMX [intergrated in leu] ura4-D18, leu1-32*	personal collection
KP0283	*cdr2-GFP-natMX ade6-216, 2Kbp-cdr2-GFP-kanMX [intergrated in leu] ura4-D18, leu1-32*	personal collection
KP0284	*cdr2-GFP-natMX ade6-216, 2Kbp-cdr2-GFP-kanMX [intergrated in leu] ura4-D18, leu1-32*	personal collection
KP0285	*cdr2-GFP-natMX ade6-216, 2Kbp-cdr2-GFP-kanMX [intergrated in leu] ura4-D18, leu1-32*	personal collection
KP0286	*cdr2-GFP-natMX ade6-216, 2Kbp-cdr2-GFP-kanMX [intergrated in leu] ura4-D18, leu1-32*	personal collection
KP0287	*mto1::kanMX ade6-216, ura4-D18, leu1-32*	personal collection
KP0288	*mto1::kanMX ade6-216, ura4-D18, leu1-32*	personal collection
KP0289	*pom1-tomato-natMX, mto1::kanMX ade6-216, ura4-D18, leu1-32*	personal collection
KP0290	*pom1-tomato-natMX, mto1::kanMX ade6-216, ura4-D18, leu1-32*	personal collection
KP0291	*pom1-tomato-natMX, cdr2-GFP-kanMX, mto1::kanMX ade6-216, ura4-D18, leu1-32*	personal collection
KP0292	*pom1-tomato-natMX, cdr2-GFP-kanMX, mto1::kanMX ade6-216, ura4-D18, leu1-32*	personal collection
KP0293	*cdr2-GFP-kanMX, sid2-tomato-natMX*	personal collection
KP0294	*pom1-tomato-natMX, cdr2-GFP-kanMX, sid2-tomato-natMX*	personal collection
KP0295	*pom1-tomato-natMX, cdr2-GFP-kanMX, sid2-tomato-natMX*	personal collection
KP0296	*pom1-tomato-natMX, cdr2-GFP-kanMX, sid2-tomato-kanMX*	personal collection
KP0297	*cdr2-GFP-kanMX, pom1-tomato-natMX, cut7-24, leu-32::pSV40-GFP-atb2(leu1)*	personal collection
KP0298	*cdr2-GFP-kanMX, pom1-tomato-natMX, cut7-24*	personal collection

KP0299	*cdr2-GFP-kanMX, pom1-tomato-natMX, cut7-24, cut11-GFP-kan, leu-32::pSV40-GFP-atb2(leu1)*	personal collection
KP0300	*pom1-tomato-natMX, cut7-24, cut11-GFP-kan, leu-32::pSV40-GFP-atb2(leu1)*	personal collection
KP0301	*cdr2-GFP-kanMX, cut7-24, cut11-GFP-kan, leu-32::pSV40-GFP-atb2(leu1)*	personal collection
KP0302	*cut7-24, cut11-GFP-kan, leu-32::pSV40-GFP-atb2(leu1)*	personal collection
KP0303	*pom1-tomato-kanMX, rga4::ura*	personal collection
KP0304	*pom1-tomato-kanMX, rga4::ura*	personal collection
KP0305	*pom1-tomato-kanMX, cdr2-GFP-kanMX, rga4::ura*	personal collection
KP0306	*pom1-tomato-kanMX, cdr2-GFP-kanMX, rga4::ura*	personal collection
KP0307	*pom1-tomato-kanMX, rga2::ura*	personal collection
KP0308	*pom1-tomato-kanMX, rga2::ura*	personal collection
KP0309	*pom1-tomato-kanMX, cdr2-GFP-kanMX, rga2::ura*	personal collection
KP0310	*pom1-tomato-kanMX, cdr2-GFP-kanMX, rga2::ura*	personal collection
KP0311	*cdr2-GFP-kanMX, rga4::ura*	personal collection
KP0312	*cdr2-GFP-kanMX, rga4::ura*	personal collection
KP0313	*cdr2-GFP-kanMX, rga2::ura*	personal collection
KP0314	*pom1-tomato-kanMX, cdr2-GFP-kanMX, rga2::ura*	personal collection
KP0315	*cdr2-tomato-natMX*	personal collection
KP0316	*pom1-GFP-kanMX, cdr2-tomato-natMX*	personal collection
KP0317	*pom1-GFP-kanMX, cdr2-tomato-natMX*	personal collection
KP0318	*pom1::natMX*	personal collection
KP0319	*pom1::natMX*	personal collection
KP0320	*cdr2-GFP-kanMX, for3::kanMX ade6-216, ura4-D18, leu1-32*	personal collection
KP0321	*cdr2-GFP-kanMX, for3::kanMX ade6-216, ura4-D18, leu1-32*	personal collection
KP0322	*cdr2-tomato-natMX, for3::kanMX ade6-216, ura4-D18, leu1-32*	personal collection
KP0323	*cdr2-tomato-natMX, for3::kanMX ade6-216, ura4-D18, leu1-32*	personal collection
KP0324	*cdr2-GFP-natMX, for3::kanMX ade6-216, ura4-D18, leu1-32*	personal collection
KP0325	*cdr2-GFP-natMX, for3::kanMX ade6-216, ura4-D18, leu1-32*	personal collection

Bibliography

Abu-Arish, A., Porcher, A., Czerwonka, A., Dostatni, N., and Fradin, C. (2010). High mobility of bicoid captured by fluorescence correlation spectroscopy: implication for the rapid establishment of its gradient. Biophys J *99*, L33-35.

Alfa, C.E., Ducommun, B., Beach, D., and Hyams, J.S. (1990). Distinct nuclear and spindle pole body population of cyclin-cdc2 in fission yeast. Nature *347*, 680-682.

Almonacid, M., Moseley, J.B., Janvore, J., Mayeux, A., Fraisier, V., Nurse, P., and Paoletti, A. (2009). Spatial control of cytokinesis by Cdr2 kinase and Mid1/anillin nuclear export. Curr Biol *19*, 961-966.

Altafaj, X., Martin, E.D., Ortiz-Abalia, J., Valderrama, A., Lao-Peregrin, C., Dierssen, M., and Fillat, C. (2012). Normalization of Dyrk1A expression by AAV2/1-shDyrk1A attenuates hippocampal-dependent defects in the Ts65Dn mouse model of Down syndrome. Neurobiol Dis.

Ashe, H.L., and Briscoe, J. (2006). The interpretation of morphogen gradients. Development *133*, 385-394.

Ayscough, K.R., Stryker, J., Pokala, N., Sanders, M., Crews, P., and Drubin, D.G. (1997). High rates of actin filament turnover in budding yeast and roles for actin in establishment and maintenance of cell polarity revealed using the actin inhibitor latrunculin-A. J Cell Biol *137*, 399-416.

Bahler, J., and Pringle, J.R. (1998). Pom1p, a fission yeast protein kinase that provides positional information for both polarized growth and cytokinesis. Genes Dev *12*, 1356-1370.

Bahler, J., Wu, J.Q., Longtine, M.S., Shah, N.G., McKenzie, A., 3rd, Steever, A.B., Wach, A., Philippsen, P., and Pringle, J.R. (1998). Heterologous modules for efficient and versatile PCR-based gene targeting in Schizosaccharomyces pombe. Yeast *14*, 943-951.

Basi, G., Schmid, E., and Maundrell, K. (1993). TATA box mutations in the Schizosaccharomyces pombe nmt1 promoter affect transcription efficiency but not the transcription start point or thiamine repressibility. Gene *123*, 131-136.

Baumann, O., and Walz, B. (2001). Endoplasmic reticulum of animal cells and its organization into structural and functional domains. Int Rev Cytol *205*, 149-214.

Bean, J.M., Siggia, E.D., and Cross, F.R. (2005). High functional overlap between MluI cell-cycle box binding factor and Swi4/6 cell-cycle box binding factor in the G1/S transcriptional program in Saccharomyces cerevisiae. Genetics *171*, 49-61.

Becker, W., and Sippl, W. (2011). Activation, regulation, and inhibition of DYRK1A. FEBS J *278*, 246-256.

Behrens, R., and Nurse, P. (2002). Roles of fission yeast tea1p in the localization of polarity factors and in organizing the microtubular cytoskeleton. J Cell Biol *157*, 783-793.

Bicho, C.C., Kelly, D.A., Snaith, H.A., Goryachev, A.B., and Sawin, K.E. (2010). A catalytic role for Mod5 in the formation of the Tea1 cell polarity landmark. Curr Biol *20*, 1752-1757.

Botvinick, E.L., and Shah, J.V. (2007). Laser-based measurements in cell biology. Methods Cell Biol *82*, 81-109.

Brazer, S.C., Williams, H.P., Chappell, T.G., and Cande, W.Z. (2000). A fission yeast kinesin affects Golgi membrane recycling. Yeast *16*, 149-166.

Breeding, C.S., Hudson, J., Balasubramanian, M.K., Hemmingsen, S.M., Young, P.G., and Gould, K.L. (1998). The cdr2(+) gene encodes a regulator of G2/M progression and cytokinesis in Schizosaccharomyces pombe. Mol Biol Cell *9*, 3399-3415.

Brown, G.C., and Kholodenko, B.N. (1999). Spatial gradients of cellular phospho-proteins. FEBS Lett *457*, 452-454.

Calonge, T.M., Eshaghi, M., Liu, J., Ronai, Z., and O'Connell, M.J. (2010). Transformation/transcription domain-associated protein (TRRAP)-mediated regulation of Wee1. Genetics *185*, 81-93.

Caudron, M., Bunt, G., Bastiaens, P., and Karsenti, E. (2005). Spatial coordination of spindle assembly by chromosome-mediated signaling gradients. Science *309*, 1373-1376.

Celton-Morizur, S., Racine, V., Sibarita, J.B., and Paoletti, A. (2006a). Pom1 kinase links division plane position to cell polarity by regulating Mid1p cortical distribution. Journal of Cell Science *119*, 4710-4718.

Celton-Morizur, S., Racine, V., Sibarita, J.B., and Paoletti, A. (2006b). Pom1 kinase links division plane position to cell polarity by regulating Mid1p cortical distribution. J Cell Sci *119*, 4710-4718.

Chang, F. (1999). Movement of a cytokinesis factor cdc12p to the site of cell division. Curr Biol *9*, 849-852.

Chang, F. (2001). Establishment of a cellular axis in fission yeast. Trends Genet *17*, 273-278.

Chang, F., and Martin, S.G. (2009). Shaping fission yeast with microtubules. Cold Spring Harb Perspect Biol *1*, a001347.

Chang, F., and Nurse, P. (1996). How fission yeast fission in the middle. Cell *84*, 191-194.

Chang, F., Woollard, A., and Nurse, P. (1996). Isolation and characterization of fission yeast mutants defective in the assembly and placement of the contractile actin ring. J Cell Sci *109 (Pt 1)*, 131-142.

Chen, M.S., Huber, A.B., van der Haar, M.E., Frank, M., Schnell, L., Spillmann, A.A., Christ, F., and Schwab, M.E. (2000). Nogo-A is a myelin-associated neurite outgrowth inhibitor and an antigen for monoclonal antibody IN-1. Nature *403*, 434-439.

Chen, Y.E., Tropini, C., Jonas, K., Tsokos, C.G., Huang, K.C., and Laub, M.T. (2011). Spatial gradient of protein phosphorylation underlies replicative asymmetry in a bacterium. Proc Natl Acad Sci U S A *108*, 1052-1057.

Cobrinik, D. (2005). Pocket proteins and cell cycle control. Oncogene *24*, 2796-2809.

Coffman, V.C., and Wu, J.Q. (2012). Counting protein molecules using quantitative fluorescence microscopy. Trends in biochemical sciences *37*, 499-506.

Coffman, V.C., Wu, P., Parthun, M.R., and Wu, J.Q. (2011). CENP-A exceeds microtubule attachment sites in centromere clusters of both budding and fission yeast. J Cell Biol *195*, 563-572.

Coleman, A.W. (1982). The Nuclear-Cell Cycle in Chlamydomonas (Chlorophyceae). J Phycol *18*, 192-195.

Conlon, I., and Raff, M. (1999). Size control in animal development. Cell *96*, 235-244.

Conlon, I.J., Dunn, G.A., Mudge, A.W., and Raff, M.C. (2001). Extracellular control of cell size. Nat Cell Biol *3*, 918-921.

Coudreuse, D., and Nurse, P. (2010). Driving the cell cycle with a minimal CDK control network. Nature *468*, 1074-1079.

Craigie, R.A., and Cavaliersmith, T. (1982). Cell-Volume and the Control of the Chlamydomonas Cell-Cycle. Journal of Cell Science *54*, 173-191.

Cranna, N., and Quinn, L. (2009). Impact of steroid hormone signals on Drosophila cell cycle during development. Cell Div *4*, 3.

Crick, F. (1970). Diffusion in embryogenesis. Nature *225*, 420-422.

Cross, F.R. (1988). DAF1, a mutant gene affecting size control, pheromone arrest, and cell cycle kinetics of Saccharomyces cerevisiae. Mol Cell Biol *8*, 4675-4684.

Daga, R.R., and Chang, F. (2005). Dynamic positioning of the fission yeast cell division plane. Proc Natl Acad Sci U S A *102*, 8228-8232.

Dannenberg, J.H., van Rossum, A., Schuijff, L., and te Riele, H. (2000). Ablation of the retinoblastoma gene family deregulates G(1) control causing immortalization and increased cell turnover under growth-restricting conditions. Genes Dev *14*, 3051-3064.

David-Pfeuty, T. (2006). The flexible evolutionary anchorage-dependent Pardee's restriction point of mammalian cells: how its deregulation may lead to cancer. Biochim Biophys Acta *1765*, 38-66.

Di Talia, S., Skotheim, J.M., Bean, J.M., Siggia, E.D., and Cross, F.R. (2007). The effects of molecular noise and size control on variability in the budding yeast cell cycle. Nature *448*, 947-951.

Di Talia, S., Wang, H., Skotheim, J.M., Rosebrock, A.P., Futcher, B., and Cross, F.R. (2009). Daughter-specific transcription factors regulate cell size control in budding yeast. PLoS Biol *7*, e1000221.

Dimova, D.K., and Dyson, N.J. (2005). The E2F transcriptional network: old acquaintances with new faces. Oncogene *24*, 2810-2826.

Dirick, L., and Nasmyth, K. (1991). Positive feedback in the activation of G1 cyclins in yeast. Nature *351*, 754-757.

Dolznig, H., Grebien, F., Sauer, T., Beug, H., and Mullner, E.W. (2004). Evidence for a size-sensing mechanism in animal cells. Nat Cell Biol *6*, 899-905.

Donachie, W.D. (1968). Relationship between cell size and time of initiation of DNA replication. Nature *219*, 1077-1079.

Doncic, A., Falleur-Fettig, M., and Skotheim, J.M. (2011). Distinct interactions select and maintain a specific cell fate. Mol Cell *43*, 528-539.

Donnan, L., and John, P.C. (1983). Cell cycle control by timer and sizer in Chlamydomonas. Nature *304*, 630-633.

Draetta, G., Piwnica-Worms, H., Morrison, D., Druker, B., Roberts, T., and Beach, D. (1988). Human cdc2 protein kinase is a major cell-cycle regulated tyrosine kinase substrate. Nature *336*, 738-744.

Dungrawala, H., Hua, H., Wright, J., Abraham, L., Kasemsri, T., McDowell, A., Stilwell, J., and Schneider, B.L. (2012). Identification of new cell size control genes in S. cerevisiae. Cell Div *7*, 24.

Dunphy, W.G., Brizuela, L., Beach, D., and Newport, J. (1988). The Xenopus cdc2 protein is a component of MPF, a cytoplasmic regulator of mitosis. Cell *54*, 423-431.

Eldar, A., Dorfman, R., Weiss, D., Ashe, H., Shilo, B.Z., and Barkai, N. (2002). Robustness of the BMP morphogen gradient in Drosophila embryonic patterning. Nature *419*, 304-308.

Eldar, A., Rosin, D., Shilo, B.Z., and Barkai, N. (2003). Self-enhanced ligand degradation underlies robustness of morphogen gradients. Dev Cell *5*, 635-646.

Elowitz, M.B., Levine, A.J., Siggia, E.D., and Swain, P.S. (2002). Stochastic gene expression in a single cell. Science *297*, 1183-1186.

Enserink, J.M., and Kolodner, R.D. (2010). An overview of Cdk1-controlled targets and processes. Cell Div *5*, 11.

Erdmann, T., Howard, M., and ten Wolde, P.R. (2009). Role of spatial averaging in the precision of gene expression patterns. Phys Rev Lett *103*, 258101.

Evans, T., Rosenthal, E.T., Youngblom, J., Distel, D., and Hunt, T. (1983). Cyclin: a protein specified by maternal mRNA in sea urchin eggs that is destroyed at each cleavage division. Cell *33*, 389-396.

Fang, S.C., de los Reyes, C., and Umen, J.G. (2006). Cell size checkpoint control by the retinoblastoma tumor suppressor pathway. PLoS Genet *2*, e167.

Fang, S.C., and Umen, J.G. (2008). A suppressor screen in chlamydomonas identifies novel components of the retinoblastoma tumor suppressor pathway. Genetics *178*, 1295-1310.

Fantes, P., and Nurse, P. (1977). Control of cell size at division in fission yeast by a growth-modulated size control over nuclear division. Exp Cell Res *107*, 377-386.

Fantes, P.A., and Nurse, P. (1978). Control of the timing of cell division in fission yeast. Cell size mutants reveal a second control pathway. Exp Cell Res *115*, 317-329.

Feierbach, B., and Chang, F. (2001). Roles of the fission yeast formin for3p in cell polarity, actin cable formation and symmetric cell division. Curr Biol *11*, 1656-1665.

Feierbach, B., Verde, F., and Chang, F. (2004). Regulation of a formin complex by the microtubule plus end protein tea1p. J Cell Biol *165*, 697-707.

Feilotter, H., Nurse, P., and Young, P.G. (1991). Genetic and molecular analysis of cdr1/nim1 in Schizosaccharomyces pombe. Genetics *127*, 309-318.

Friedman, J.R., and Voeltz, G.K. (2011). The ER in 3D: a multifunctional dynamic membrane network. Trends Cell Biol *21*, 709-717.

Fuller, B.G., Lampson, M.A., Foley, E.A., Rosasco-Nitcher, S., Le, K.V., Tobelmann, P., Brautigan, D.L., Stukenberg, P.T., and Kapoor, T.M. (2008). Midzone activation of aurora B in anaphase produces an intracellular phosphorylation gradient. Nature *453*, 1132-1136.

Gautier, J., Norbury, C., Lohka, M., Nurse, P., and Maller, J. (1988). Purified maturation-promoting factor contains the product of a Xenopus homolog of the fission yeast cell cycle control gene cdc2+. Cell *54*, 433-439.

Gladfelter, A.S., Zyla, T.R., and Lew, D.J. (2004). Genetic interactions among regulators of septin organization. Eukaryot Cell *3*, 847-854.

Gould, K.L., Moreno, S., Tonks, N.K., and Nurse, P. (1990). Complementation of the mitotic activator, p80cdc25, by a human protein-tyrosine phosphatase. Science *250*, 1573-1576.

Grallert, A., Patel, A., Tallada, V.A., Chan, K.Y., Bagley, S., Krapp, A., Simanis, V., and Hagan, I.M. (2013). Centrosomal MPF triggers the mitotic and morphogenetic switches of fission yeast. Nat Cell Biol *15*, 88-95.

Gregor, T., Tank, D.W., Wieschaus, E.F., and Bialek, W. (2007a). Probing the limits to positional information. Cell *130*, 153-164.

Gregor, T., Wieschaus, E.F., McGregor, A.P., Bialek, W., and Tank, D.W. (2007b). Stability and nuclear dynamics of the bicoid morphogen gradient. Cell *130*, 141-152.

Gurdon, J.B., and Bourillot, P.Y. (2001). Morphogen gradient interpretation. Nature *413*, 797-803.

Guzman-Vendrell, M., Baldissard, S., Almonacid, M., Mayeux, A., Paoletti, A., and Moseley, J.B. (2013). Blt1 and mid1 provide overlapping membrane anchors to position the division plane in fission yeast. Mol Cell Biol *33*, 418-428.

Hachet, O., Berthelot-Grosjean, M., Kokkoris, K., Vincenzetti, V., Moosbrugger, J., and Martin, S.G. (2011). A phosphorylation cycle shapes gradients of the DYRK family kinase Pom1 at the plasma membrane. Cell *145*, 1116-1128.

Hammerle, B., Ulin, E., Guimera, J., Becker, W., Guillemot, F., and Tejedor, F.J. (2011). Transient expression of Mnb/Dyrk1a couples cell cycle exit and differentiation of neuronal precursors by inducing p27KIP1 expression and suppressing NOTCH signaling. Development *138*, 2543-2554.

Hartwell, L.H., Culotti, J., and Reid, B. (1970). Genetic control of the cell-division cycle in yeast. I. Detection of mutants. Proc Natl Acad Sci U S A *66*, 352-359.

Haustein, E., and Schwille, P. (2007). Fluorescence correlation spectroscopy: novel variations of an established technique. Annual review of biophysics and biomolecular structure *36*, 151-169.

Hentges, P., Van Driessche, B., Tafforeau, L., Vandenhaute, J., and Carr, A.M. (2005). Three novel antibiotic marker cassettes for gene disruption and marker switching in Schizosaccharomyces pombe. Yeast *22*, 1013-1019.

Hu, J., Shibata, Y., Voss, C., Shemesh, T., Li, Z., Coughlin, M., Kozlov, M.M., Rapoport, T.A., and Prinz, W.A. (2008). Membrane proteins of the endoplasmic reticulum induce high-curvature tubules. Science *319*, 1247-1250.

Huang, Y., Chew, T.G., Ge, W., and Balasubramanian, M.K. (2007). Polarity determinants Tea1p, Tea4p, and Pom1p inhibit division-septum assembly at cell ends in fission yeast. Dev Cell *12*, 987-996.

Huh, D., and Paulsson, J. (2011). Non-genetic heterogeneity from stochastic partitioning at cell division. Nat Genet *43*, 95-100.

Jorgensen, P., Nishikawa, J.L., Breitkreutz, B.J., and Tyers, M. (2002). Systematic identification of pathways that couple cell growth and division in yeast. Science *297*, 395-400.

Jorgensen, P., and Tyers, M. (2004). How cells coordinate growth and division. Curr Biol *14*, R1014-1027.

Kalab, P., and Heald, R. (2008). The RanGTP gradient - a GPS for the mitotic spindle. J Cell Sci *121*, 1577-1586.

Kanoh, J., and Russell, P. (1998). The protein kinase Cdr2, related to Nim1/Cdr1 mitotic inducer, regulates the onset of mitosis in fission yeast. Mol Biol Cell *9*, 3321-3334.

Kerichevsky, O., and Bonnet, G. (2002). Fluorescence-Correlation Spectroscopy: The technique and its applications. Reports on Progress in Physics.

La Carbona, S., and Le Goff, X. (2006). Spatial regulation of cytokinesis by the Kin1 and Pom1 kinases in fission yeast. Curr Genet *50*, 377-391.

Lander, A.D. (2007). Morpheus unbound: reimagining the morphogen gradient. Cell *128*, 245-256.

Laporte, D., Coffman, V.C., Lee, I.J., and Wu, J.Q. (2011). Assembly and architecture of precursor nodes during fission yeast cytokinesis. J Cell Biol *192*, 1005-1021.

Leake, M.C., Chandler, J.H., Wadhams, G.H., Bai, F., Berry, R.M., and Armitage, J.P. (2006). Stoichiometry and turnover in single, functioning membrane protein complexes. Nature *443*, 355-358.

Lee, I.J., and Wu, J.Q. (2012). Characterization of Mid1 domains for targeting and scaffolding in fission yeast cytokinesis. J Cell Sci *125*, 2973-2985.

Lee, M.G., and Nurse, P. (1987). Complementation used to clone a human homologue of the fission yeast cell cycle control gene cdc2. Nature *327*, 31-35.

Lee, P., Cho, B.R., Joo, H.S., and Hahn, J.S. (2008). Yeast Yak1 kinase, a bridge between PKA and stress-responsive transcription factors, Hsf1 and Msn2/Msn4. Mol Microbiol *70*, 882-895.

Lopez, A.D., Tar, K., Krugel, U., Dange, T., Ros, I.G., and Schmidt, M. (2011). Proteasomal degradation of Sfp1 contributes to the repression of ribosome biogenesis during starvation and is mediated by the proteasome activator Blm10. Mol Biol Cell *22*, 528-540.

Lundgren, K., Walworth, N., Booher, R., Dembski, M., Kirschner, M., and Beach, D. (1991). mik1 and wee1 cooperate in the inhibitory tyrosine phosphorylation of cdc2. Cell *64*, 1111-1122.

Marco, E., Wedlich-Soldner, R., Li, R., Altschuler, S.J., and Wu, L.F. (2007). Endocytosis optimizes the dynamic localization of membrane proteins that regulate cortical polarity. Cell *129*, 411-422.

Martin, S.G., and Berthelot-Grosjean, M. (2009). Polar gradients of the DYRK-family kinase Pom1 couple cell length with the cell cycle. Nature *459*, 852-856.

Martin, S.G., and Chang, F. (2006). Dynamics of the formin for3p in actin cable assembly. Curr Biol *16*, 1161-1170.

Martin, S.G., McDonald, W.H., Yates, J.R., 3rd, and Chang, F. (2005). Tea4p links microtubule plus ends with the formin for3p in the establishment of cell polarity. Dev Cell *8*, 479-491.

Masuda, H., Fong, C.S., Ohtsuki, C., Haraguchi, T., and Hiraoka, Y. (2011). Spatiotemporal regulations of Wee1 at the G2/M transition. Mol Biol Cell *22*, 555-569.

Masui, Y., and Markert, C.L. (1971). Cytoplasmic control of nuclear behavior during meiotic maturation of frog oocytes. J Exp Zool *177*, 129-145.

Mata, J., and Nurse, P. (1997). tea1 and the microtubular cytoskeleton are important for generating global spatial order within the fission yeast cell. Cell *89*, 939-949.

Meyers, J., Craig, J., and Odde, D.J. (2006). Potential for control of signaling pathways via cell size and shape. Curr Biol *16*, 1685-1693.

Mitchison, J.M., and Nurse, P. (1985). Growth in cell length in the fission yeast Schizosaccharomyces pombe. J Cell Sci *75*, 357-376.

Miyata, H., Miyata, M., and Ito, M. (1978a). Cell-Cycle in Fission Yeast, Schizosaccharomyces-Pombe .1. Relationship between Cell-Size and Cycle Time. Cell Structure and Function *3*, 39-46.

Miyata, H., Miyata, M., and Ito, M. (1978b). Cell-Cycle in the Fission Yeast, Schizosaccharomyces-Pombe .2. Recovery Mode of the Period of a Cycle Extended by Pulse Treatment with Hydroxyurea. Cell Structure and Function *3*, 153-159.

Moore, S.A. (1988). Kinetic evidence for a critical rate of protein synthesis in the Saccharomyces cerevisiae yeast cell cycle. J Biol Chem *263*, 9674-9681.

Moreno, S., Klar, A., and Nurse, P. (1991). Molecular genetic analysis of fission yeast Schizosaccharomyces pombe. Methods Enzymol *194*, 795-823.

Morgan, D. (2007). The Cell Cycle: Principles of Cell Control (London: New Science Press Ltd.).

Morrell, J.L., Nichols, C.B., and Gould, K.L. (2004). The GIN4 family kinase, Cdr2p, acts independently of septins in fission yeast. J Cell Sci *117*, 5293-5302.

Moseley, J.B., Mayeux, A., Paoletti, A., and Nurse, P. (2009). A spatial gradient coordinates cell size and mitotic entry in fission yeast. Nature *459*, 857-860.

Moseley, J.B., and Nurse, P. (2010). Cell division intersects with cell geometry. Cell *142*, 184-188.

Mueller, P.R., Coleman, T.R., and Dunphy, W.G. (1995). Cell cycle regulation of a Xenopus Wee1-like kinase. Mol Biol Cell *6*, 119-134.

Nash, R., Tokiwa, G., Anand, S., Erickson, K., and Futcher, A.B. (1988). The WHI1+ gene of Saccharomyces cerevisiae tethers cell division to cell size and is a cyclin homolog. EMBO J *7*, 4335-4346.

Navarro, F.J., and Nurse, P. (2012). A systematic screen reveals new elements acting at the G2/M cell cycle control. Genome Biol *13*, R36.

Neufeld, T.P., de la Cruz, A.F., Johnston, L.A., and Edgar, B.A. (1998). Coordination of growth and cell division in the Drosophila wing. Cell *93*, 1183-1193.

Neumann, F.R., and Nurse, P. (2007). Nuclear size control in fission yeast. J Cell Biol *179*, 593-600.

Niccoli, T., Arellano, M., and Nurse, P. (2003). Role of Tea1p, Tea3p and Pom1p in the determination of cell ends in Schizosaccharomyces pombe. Yeast *20*, 1349-1358.

Niethammer, P., Bastiaens, P., and Karsenti, E. (2004). Stathmin-tubulin interaction gradients in motile and mitotic cells. Science *303*, 1862-1866.

Ninomiya-Tsuji, J., Nomoto, S., Yasuda, H., Reed, S.I., and Matsumoto, K. (1991). Cloning of a human cDNA encoding a CDC2-related kinase by complementation of a budding yeast cdc28 mutation. Proc Natl Acad Sci U S A *88*, 9006-9010.

Nishi, Y., and Lin, R. (2005). DYRK2 and GSK-3 phosphorylate and promote the timely degradation of OMA-1, a key regulator of the oocyte-to-embryo transition in C. elegans. Dev Biol *288*, 139-149.

Nishi, Y., Rogers, E., Robertson, S.M., and Lin, R. (2008). Polo kinases regulate C. elegans embryonic polarity via binding to DYRK2-primed MEX-5 and MEX-6. Development *135*, 687-697.

Novak, B., and Tyson, J.J. (1993). Modeling the Cell Division Cycle: M-phase Trigger, Oscillations, and Size control. J Theor Biol *165*, 34.

Nurse, P. (1975). Genetic control of cell size at cell division in yeast. Nature *256*, 547-551.

Nurse, P. (1990). Universal control mechanism regulating onset of M-phase. Nature *344*, 503-508.

Nurse, P. (2002). Cyclin dependent kinases and cell cycle control (nobel lecture). Chembiochem *3*, 596-603.

Oertle, T., Merkler, D., and Schwab, M.E. (2003). Do cancer cells die because of Nogo-B? Oncogene *22*, 1390-1399.

Padte, N.N., Martin, S.G., Howard, M., and Chang, F. (2006). The cell-end factor pom1p inhibits mid1p in specification of the cell division plane in fission yeast. Curr Biol *16*, 2480-2487.

Pan, K.Z., and Chang, F. (2009). Cell-cycle control: don't supersize me. Curr Biol *19*, R517-519.

Pang, K.M., Ishidate, T., Nakamura, K., Shirayama, M., Trzepacz, C., Schubert, C.M., Priess, J.R., and Mello, C.C. (2004). The minibrain kinase homolog, mbk-2, is required for spindle positioning and asymmetric cell division in early C. elegans embryos. Dev Biol *265*, 127-139.

Paoletti, A., and Chang, F. (2000). Analysis of mid1p, a protein required for placement of the cell division site, reveals a link between the nucleus and the cell surface in fission yeast. Mol Biol Cell *11*, 2757-2773.

Park, J., Song, W.J., and Chung, K.C. (2009). Function and regulation of Dyrk1A: towards understanding Down syndrome. Cell Mol Life Sci *66*, 3235-3240.

Pellettieri, J., Reinke, V., Kim, S.K., and Seydoux, G. (2003). Coordinate activation of maternal protein degradation during the egg-to-embryo transition in C. elegans. Dev Cell *5*, 451-462.

Petersen, J., and Nurse, P. (2007). TOR signalling regulates mitotic commitment through the stress MAP kinase pathway and the Polo and Cdc2 kinases. Nat Cell Biol *9*, 1263-1272.

Piel, M., and Tran, P.T. (2009). Cell shape and cell division in fission yeast. Curr Biol *19*, R823-827.

Polanshek, M.M. (1977). Effects of heat shock and cycloheximide on growth and division of the fission yeast, Schizosaccharomyces pombe. With an Appendix. Estimation of division delay for S. pombe from cell plate index curves. J Cell Sci *23*, 1-23.

Popolo, L., Vanoni, M., and Alberghina, L. (1982). Control of the yeast cell cycle by protein synthesis. Exp Cell Res *142*, 69-78.

Pyronnet, S., and Sonenberg, N. (2001). Cell-cycle-dependent translational control. Curr Opin Genet Dev *11*, 13-18.

Raj, A., Rifkin, S.A., Andersen, E., and van Oudenaarden, A. (2010). Variability in gene expression underlies incomplete penetrance. Nature *463*, 913-918.

Raser, J.M., and O'Shea, E.K. (2004). Control of stochasticity in eukaryotic gene expression. Science *304*, 1811-1814.

Ries, J., and Schwille, P. (2008). New concepts for fluorescence correlation spectroscopy on membranes. Physical chemistry chemical physics : PCCP *10*, 3487-3497.

Riley, K.F., Hobson, M.P., and Bence, S.J. (1998). Mathematical Methods for Physics and Engineering.

Rowley, R., Hudson, J., and Young, P.G. (1992). The wee1 protein kinase is required for radiation-induced mitotic delay. Nature *356*, 353-355.

Rupes, I. (2002). Checking cell size in yeast. Trends Genet *18*, 479-485.

Rupes, I., Jia, Z., and Young, P.G. (1999). Ssp1 promotes actin depolymerization and is involved in stress response and new end take-off control in fission yeast. Mol Biol Cell *10*, 1495-1510.

Russell, P., and Nurse, P. (1987). Negative regulation of mitosis by wee1+, a gene encoding a protein kinase homolog. Cell *49*, 559-567.

Saucedo, L.J., and Edgar, B.A. (2002). Why size matters: altering cell size. Curr Opin Genet Dev *12*, 565-571.

Saunders, T.E., and Howard, M. (2009). Morphogen profiles can be optimized to buffer against noise. Phys Rev E Stat Nonlin Soft Matter Phys *80*, 041902.

Saunders, T.E., Pan, K.Z., Angel, A., Guan, Y., Shah, J.V., Howard, M., and Chang, F. (2012). Noise reduction in the intracellular pom1p gradient by a dynamic clustering mechanism. Dev Cell *22*, 558-572.

Schmidt, E.E., and Schibler, U. (1995). Cell size regulation, a mechanism that controls cellular RNA accumulation: consequences on regulation of the ubiquitous transcription factors Oct1 and NF-Y and the liver-enriched transcription factor DBP. J Cell Biol *128*, 467-483.

Schneider, B.L., Zhang, J., Markwardt, J., Tokiwa, G., Volpe, T., Honey, S., and Futcher, B. (2004). Growth rate and cell size modulate the synthesis of, and requirement for, G1-phase cyclins at start. Mol Cell Biol *24*, 10802-10813.

Shibata, Y., Voeltz, G.K., and Rapoport, T.A. (2006). Rough sheets and smooth tubules. Cell *126*, 435-439.

Sirotkin, V., Berro, J., Macmillan, K., Zhao, L., and Pollard, T.D. (2010). Quantitative analysis of the mechanism of endocytic actin patch assembly and disassembly in fission yeast. Mol Biol Cell *21*, 2894-2904.

Slaughter, B.D., Das, A., Schwartz, J.W., Rubinstein, B., and Li, R. (2009). Dual modes of cdc42 recycling fine-tune polarized morphogenesis. Dev Cell *17*, 823-835.

Smith, L.D., and Ecker, R.E. (1971). The interaction of steroids with Rana pipiens Oocytes in the induction of maturation. Dev Biol *25*, 232-247.

Son, S., Tzur, A., Weng, Y., Jorgensen, P., Kim, J., Kirschner, M.W., and Manalis, S.R. (2012). Direct observation of mammalian cell growth and size regulation. Nat Methods *9*, 910-912.

Spirov, A., Fahmy, K., Schneider, M., Frei, E., Noll, M., and Baumgartner, S. (2009). Formation of the bicoid morphogen gradient: an mRNA gradient dictates the protein gradient. Development *136*, 605-614.

Sveiczer, A., Novak, B., and Mitchison, J.M. (1996). The size control of fission yeast revisited. J Cell Sci *109 (Pt 12)*, 2947-2957.

Tatebe, H., Nakano, K., Maximo, R., and Shiozaki, K. (2008). Pom1 DYRK regulates localization of the Rga4 GAP to ensure bipolar activation of Cdc42 in fission yeast. Curr Biol *18*, 322-330.

Tatebe, H., Shimada, K., Uzawa, S., Morigasaki, S., and Shiozaki, K. (2005). Wsh3/Tea4 is a novel cell-end factor essential for bipolar distribution of Tea1 and protects cell polarity under environmental stress in S. pombe. Curr Biol *15*, 1006-1015.

Tcherniak, A., Reznik, C., Link, S., and Landes, C.F. (2009). Fluorescence correlation spectroscopy: criteria for analysis in complex systems. Anal Chem *81*, 746-754.

Tejedor, F., Zhu, X.R., Kaltenbach, E., Ackermann, A., Baumann, A., Canal, I., Heisenberg, M., Fischbach, K.F., and Pongs, O. (1995). minibrain: a new protein kinase family involved in postembryonic neurogenesis in Drosophila. Neuron *14*, 287-301.

Tostevin, F. (2011). Precision of sensing cell length via concentration gradients. Biophys J *100*, 294-303.

Tostevin, F., ten Wolde, P.R., and Howard, M. (2007). Fundamental limits to position determination by concentration gradients. PLoS Comput Biol *3*, e78.

Turner, J.J., Ewald, J.C., and Skotheim, J.M. (2012). Cell size control in yeast. Curr Biol *22*, R350-359.

Tyers, M., Fitch, I., Tokiwa, G., Dahmann, C., Nash, R., Linskens, M., and Futcher, B. (1991). Characterization of G1 and mitotic cyclins of budding yeast. Cold Spring Harb Symp Quant Biol *56*, 21-32.

Tyers, M., Tokiwa, G., and Futcher, B. (1993). Comparison of the Saccharomyces cerevisiae G1 cyclins: Cln3 may be an upstream activator of Cln1, Cln2 and other cyclins. EMBO J *12*, 1955-1968.

Tyers, M., Tokiwa, G., Nash, R., and Futcher, B. (1992). The Cln3-Cdc28 kinase complex of S. cerevisiae is regulated by proteolysis and phosphorylation. EMBO J *11*, 1773-1784.

Ubersax, J.A., Woodbury, E.L., Quang, P.N., Paraz, M., Blethrow, J.D., Shah, K., Shokat, K.M., and Morgan, D.O. (2003). Targets of the cyclin-dependent kinase Cdk1. Nature *425*, 859-864.

Umen, J.G. (2005). The elusive sizer. Curr Opin Cell Biol *17*, 435-441.

Umen, J.G., and Goodenough, U.W. (2001). Control of cell division by a retinoblastoma protein homolog in Chlamydomonas. Genes Dev *15*, 1652-1661.

Unger, M.W., and Hartwell, L.H. (1976). Control of cell division in Saccharomyces cerevisiae by methionyl-tRNA. Proc Natl Acad Sci U S A *73*, 1664-1668.

van Zon, J.S., Tzircotis, G., Caron, E., and Howard, M. (2009). A mechanical bottleneck explains the variation in cup growth during FcgammaR phagocytosis. Molecular systems biology *5*, 298.

Varga, V., Helenius, J., Tanaka, K., Hyman, A.A., Tanaka, T.U., and Howard, J. (2006). Yeast kinesin-8 depolymerizes microtubules in a length-dependent manner. Nat Cell Biol *8*, 957-962.

Verges, E., Colomina, N., Gari, E., Gallego, C., and Aldea, M. (2007). Cyclin Cln3 is retained at the ER and released by the J chaperone Ydj1 in late G1 to trigger cell cycle entry. Mol Cell *26*, 649-662.

Vilela, M., Morgan, J.J., and Lindahl, P.A. (2010). Mathematical model of a cell size checkpoint. PLoS Comput Biol *6*, e1001036.

Voeltz, G.K., Prinz, W.A., Shibata, Y., Rist, J.M., and Rapoport, T.A. (2006). A class of membrane proteins shaping the tubular endoplasmic reticulum. Cell *124*, 573-586.

Watanabe, N., Broome, M., and Hunter, T. (1995). Regulation of the human WEE1Hu CDK tyrosine 15-kinase during the cell cycle. EMBO J *14*, 1878-1891.

Wattis, J.A.D. (2006). An introduction to mathematical models of coagulation-fragmentation processes: A discrete deterministic mean-field approach. Physica D-Nonlinear Phenomena *222*, 1-20.

Wightman, R., Bates, S., Amornrrattanapan, P., and Sudbery, P. (2004). In Candida albicans, the Nim1 kinases Gin4 and Hsl1 negatively regulate pseudohypha formation and Gin4 also controls septin organization. J Cell Biol *164*, 581-591.

Wright, R., Basson, M., D'Ari, L., and Rine, J. (1988). Increased amounts of HMG-CoA reductase induce "karmellae": a proliferation of stacked membrane pairs surrounding the yeast nucleus. J Cell Biol *107*, 101-114.

Wu, J.Q., and Pollard, T.D. (2005). Counting cytokinesis proteins globally and locally in fission yeast. Science *310*, 310-314.

Wu, L., and Russell, P. (1993). Nim1 kinase promotes mitosis by inactivating Wee1 tyrosine kinase. Nature *363*, 738-741.

Ye, Y., Lee, I.J., Runge, K.W., and Wu, J.Q. (2012). Roles of putative Rho-GEF Gef2 in division-site positioning and contractile-ring function in fission yeast cytokinesis. Mol Biol Cell *23*, 1181-1195.

Young, P.G., and Fantes, P.A. (1987). Schizosaccharomyces pombe mutants affected in their division response to starvation. J Cell Sci *88 (Pt 3)*, 295-304.

Zhang, D., Vjestica, A., and Oliferenko, S. (2010). The cortical ER network limits the permissive zone for actomyosin ring assembly. Curr Biol *20*, 1029-1034.

Zhang, D., Vjestica, A., and Oliferenko, S. (2012). Plasma membrane tethering of the cortical ER necessitates its finely reticulated architecture. Curr Biol *22*, 2048-2052.